Influence of the fluid structure and elasticity on motions in a yield-stress material - Implications for geological systems

Nicolò Rubens Sgreva

université
PARIS-SACLAY

Influence of the fluid structure and elasticity on motions in a yield-stress material - Implications for geological systems

Thèse de doctorat de l'université Paris-Saclay

École doctorale n°579 Sciences mécaniques et énergétiques, matériaux et géosciences (SMEMaG)
Spécialité de doctorat: Structure et évolution de la terre et des autres planètes
Unité de recherche: Université Paris-Saclay, CNRS, FAST, 91405, Orsay, France
Référent: Faculté des sciences d'Orsay

Thèse présentée et soutenue à Orsay, le 25/09/2020, par

Nicolò Rubens SGREVA

Composition du Jury

Andréa TOMMASI Directeur de recherche, Université Montpellier II, CNRS	Présidente
Muriel GERBAULT Chargé de recherche, Obs. Midi-Pyrénées, Université P. Sabatier	Rapporteur
Christel MÉTIVIER Maîtres de conférences, Université de Lorraine, CNRS	Rapporteur
Boris KAUS Professeur, Johannes Gutenberg University Mainz	Examinateur
Philippe GONDRET Professeur, Université Paris-Saclay	Examinateur
Anne DAVAILLE DR1, Université Paris-Saclay, CNRS	Directrice de thèse

Thèse de doctorat

NNT : 2020UPASJ002

université PARIS-SACLAY

ÉCOLE DOCTORALE
Sciences mécaniques et énergétiques, matériaux et géosciences (SMEMAG)

Titre : Influence de la structure du fluide et de l'élasticité sur les mouvements dans un matériau avec contrainte-seuil – Implications pour les systèmes géologiques.

Mots clés : Yield-stress ; Mécanique des Fluides ; Panaches ; Géodynamique ; Rhéologie

Abstract : Cette thèse étudie la transition solide/fluide dans les fluides à contrainte-seuil, en utilisant des expériences de laboratoire et des simulations numériques. Les résultats obtenus à partir de l'étude de mécanique des fluides sont ensuite appliqués à la dynamique des systèmes magmatiques. Les objectifs sont d'évaluer comment la transition dépend de la structure du fluide et de son élasticité, quels sont les ingrédients nécessaires pour décrire mathématiquement cette transition et le mouvement du fluide, et dans quelles conditions cette description n'est plus valide. Deux systèmes ont été choisis pour la simplicité de leur dynamique dans le cas Newtonien et leur pertinence pour les systèmes géologiques: (1) le mouvement d'une sphère solide, et (2) le développement des panaches thermiques. Dans le premier cas, on a caractérisé expérimentalement la chute libre d'une shère dans un mélange aqueux de gels superabsorbants. L'objectif est ici d'étudier l'influence de la taille des grains de gel qui constituent la structure du fluide sur la dynamique de l'intrusion sphérique. Dans le second cas, l'approche utilisée est numérique, avec des simulations combinant les effets viscoplastiques et viscoélastiques. Le rôle de l'élasticité sur la déformation du fluide est ainsi caractérisé. Les résultats sont ensuite appliqués aux réservoirs magmatiques dans la croûte terrestre, où sont examinés les phénomènes à petite échelle (le mouvement des bulles de gaz et des poches de liquide fondu dans la chambre magmatique) et à grande échelle (la remontée d'un diapir magmatique et la déformation de la croûte au dessus de la chambre magmatique).

Title : Influence of the fluid structure and elasticity on motions in a yield-stress material - Implications for geological systems.

Keywords : Yield-stress ; Fluid mechanics ; Thermal Plumes ; Geodynamics ; Rheology

Abstract : In this thesis, the solid/flowing transition in yield-stress fluids is investigated using laboratory experiments and numerical simulations. The results obtained from the fluid mechanics study are then applied to the dynamics of magmatic systems. The aims are to evaluate how the transition depends on the fluid structure and its elasticity, what ingredients are needed to describe mathematically this transition and fluid motion, and when this description will break down. Two systems have been chosen for the simplicity of their dynamics in Newtonian fluids and their relevance to geological systems: (1) the motion of a solid sphere, and (2) the development of thermal plumes. Case (1) regards the experimental work on the free-fall of a sphere through a mixture of water and superabsorbent gel grains. The aim here is to investigate the influence that the size of particles which build up the structure of the fluid has on the dynamics of a spherical intruder. Case (2) is instead approached through numerical simulations that combine viscoelasticity and viscoplasticity together. The role of elasticity on the overall deformation of the fluid is characterized. Results are afterwards applied to crustal magmatic reservoirs in which both small scale phenomena (such as the motion of bubbles and melt pockets) and larger scale phenomena (deformation on the top of an entire magmatic chamber) are examined.

Université Paris-Saclay
Espace Technologique / Immeuble Discovery
Route de l'Orme aux Merisiers RD 128 / 91190 Saint-Aubin, France

This project has received funding from the European Unions Horizon 2020 research and innovation programme under the Marie Sklodowska-Curie grant agreement No 642029 - ITN CREEP.

Thèse de Doctorat
École doctorale de "Sciences mécaniques et énergétiques, matériaux, géosciences" (SMEMaG)

INFLUENCE OF THE FLUID STRUCTURE AND ELASTICITY ON MOTIONS IN A YIELD-STRESS MATERIAL
-
IMPLICATIONS FOR GEOLOGICAL SYSTEMS

Auther: M. Nicolò Rubens SGREVA

Directeur de thèse: Mme Anne DAVAILLE

Université Paris-Saclay, 2020

Contents

Chapter 1

Introduction

Yield-stress fluids are a broad category of fluids which have recently been increasingly studied due to their key roles both in industry (e.g. drilling fluids, cement pastes, foams) and in natural phenomena (e.g. lava and mud flows, avalanches, landslides). A so-called yield-stress fluid does flow only when the applied stresses become larger than a threshold value, the yield stress (σ_y). The fluid structure can sustain stresses smaller than σ_y, and the fluid retains a solid behaviour in those conditions. A key-question when studying the dynamics of yield-stress fluids is therefore how it transitions from the solid state to the flowing state: how does this transition depend on the fluid structure? what ingredients do we need to describe mathematically this transition? when will this mathematical description break down?

We shall focus here on the influence of the fluid structure and elasticity on the fluid dynamics, using laboratory experiments and numerical simulations. Our main applications are the geological systems, since the solid/flowing transition is present on a large range of time- and length- scales.

1.1 The solid/flowing behaviour of geological systems

The bulk Earth's interior is made of polycrystalline aggregates of several different compositions and physical properties. All processes that have shaped the planet during its history and made it as it is now had them as main players. These materials form major rock units (e.g. crust and mantle), which are extended continuous geological bodies. On a macro-scale, the continuum assumption means that the matter inside these domains is continuously distributed and do not contain mass-free voids and gaps. As continuous body they can be subjected to motion. As portions of the body move relative to each other, their relative position change, leading to deformation and flow of matter. On Earth, motion and deformation span a wide range of dimensions and time scales.

The fluid behaviour that these solid domains show under load directly comes from the rheological properties of the medium in question. On Earth's surface an example is glacier and sea ice. In this case the solid ice flows freely and deform. Different rheological models

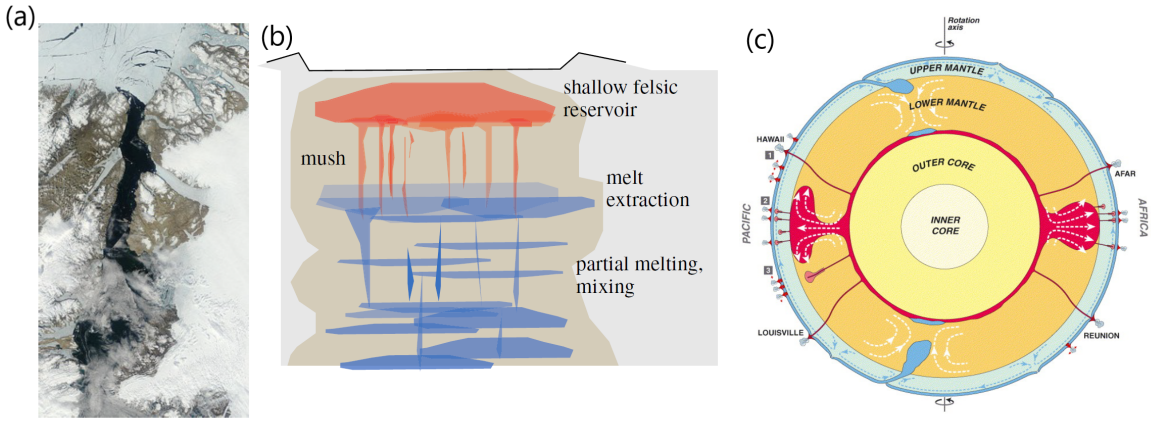

Figure 1.1: (a) Ice bridge at the entrance of Nares Strait (July 8, 2010). Presence of arc-like channels upstream the bridge before a break event. From *NASA/GSFC MODIS Rapid Response at http://rapidfire.sci.gsfc.nasa.gov/imagery/*. (b) Sketch of transcrustal magmatic reservoir, modified from Edmonds et al. (2019). (c) Dynamical cross section of the Earth showing the main features involved in mantle dynamics (Courtillot et al., 2003).

can be used to model ice behaviour, each of them gives a different stress-strain relationship. A traditional approach to deal with sea ice dynamics is based on visco-plastic models (Hibler, 1977, 1979) which prescribe that ice creeps very slowly as a viscous fluid for small stress, and deforms plastically above a certain stress threshold σ_y. However, a simple visco-plastic approach is found to be inconsistent with the observed mechanical behaviour of ice. Recent works have then started to consider continuum models that are also consistent with brittle mechanical observations (Fig. 1.1a), such as multiscale fracturing and frictional sliding (Dansereau et al., 2016).

Moving to Earth's crust, a proper rheological framework is fundamental to model and interpret igneous processes in magma chambers or in larger magmatic reservoirs (Fig. 1.1b). Transcrustal magmatic systems are dominated by crystal mush (Cashman et al., 2017), i.e. large regions of partially molten rocks where rheology is controlled by deformation of the solid crystalline framework. However, since eruptible magma is a fluid-like suspension of crystals in melt, there exists a rheological transition in which the solid-like mush domain develops fluid-like behaviour and can be quickly erupted (Sparks et al., 2019; Cashman et al., 2017).

Moving deeper in Earth's interior, a third example regards mantle rocks. The mechanical behaviour of Earth's mantle and crust strongly depends on the time scale of deformation. At short ("human") time scales, the mantle is rigid (e.g. it transmits elastically seismic shear waves) and has a solid answer to motion. For instance, a subducting lithospheric slab sinking in the sub-lithospheric mantle produces earthquakes when the amount of regional stresses becomes sufficiently large to activate faults (Fig. 1.2). On the other hand, looking at the same system on geodynamic time scales (millions of years) the entire slab moves downward a few centimeters per year and the mantle deforms as a viscous fluid. As the mantle is cooled at the surface by the cold universe, and heated from within and from below, it undergoes thermal

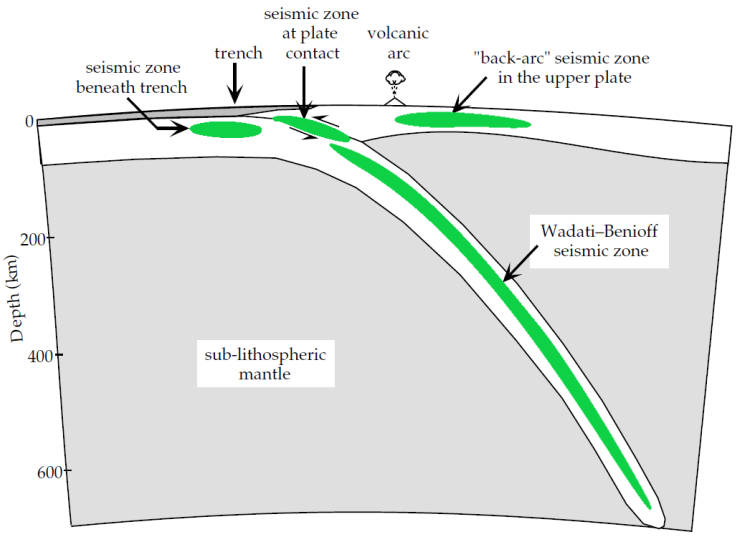

Figure 1.2: Seismic active zones (green) in subduction zone. The most active region is at plate contact at depths of 10−60 km. Below about 70 km depth the seismic zone is confined within the subducting slab. Modified from Lowrie (2007).

convection (Fig. 1.1c). From this perspective, the subducting slab in Fig. 1.2 appears as the unstable cold thermal boundary layer of mantle convection. Volcanism, formation of plates at the mid-ocean ridges, their movements and sinking at subduction zones, are all signatures of mantle convection. However, convection in the mantle is definitely more complex than in an isoviscous fluid. For instance, plate tectonics cannot develop in convection of Newtonian fluids because the latter do not allow the strong strain localization needed for plate boundary formation. With a newtonian viscosity that strongly increases with decreasing temperature, a stiffer plate may form at the mantle surface, but it will never break, leading to convection under a stagnant lid (Davaille and Jaupart, 1994) . Plate-like behaviour can be addressed by using a different stress-strain relationship: viscoplastic rheology is in fact a way to localize deformation and to generate weak zones (Tackley, 2000; Rolf and Tackley, 2011).

In all these cases, material bulk behaviour involves a number of processes spanning from an elastic response to the involvement of different creep models. However, the use of fluids with complex rheology is not free from pitfalls. One is the prediction of how much deformation is localized. That is how large is the region that mainly responds as a fluid with respect to the one which still deforms elastically. And how thermal structures and their evolution are affected by this. A second regards the onset of motion. Indeed, in the example of mantle convection, the transition from a solid-like to a fluid-like behaviour strongly depends on the thermal structure of the lithosphere and clearly on the rheology of mantle material (Tackley, 2000).

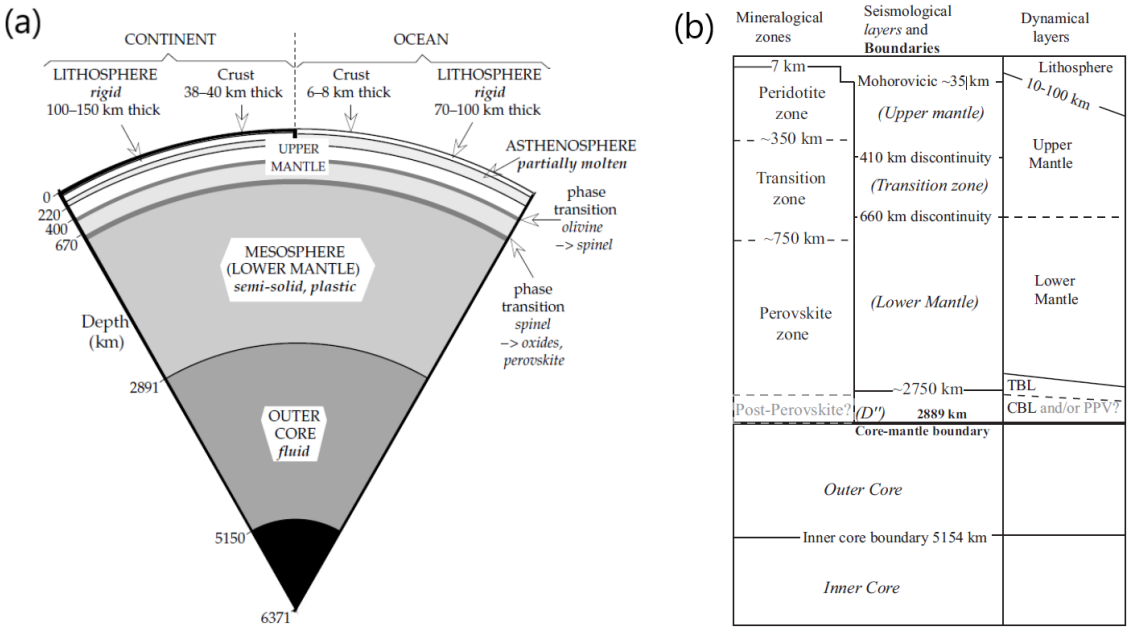

Figure 1.3: Structure of Earth's interior. (a) Principal layers and associated seismic discontinuities, from Lowrie (2007). (b) Mineralogical zones, seismological layers and dynamical layers, from Davies (2001); Massmeyer (2013).

1.2 Earth's internal structure

Earth is one of the rocky planets in the Solar System together with Mercury, Venus and Mars. These planets share the same basic internal structure: a central metallic core surrounded by a silicate mantle and crust. A schematic structure of Earth's interior is given in Fig. 1.3.

The separation between radial layers is based on the study of seismic waves and experiments on minerals under high-pressure and high-temperature. The principal layers are crust, mantle, outer and inner core. Each of them are characterized by specific properties such as composition and phases. Earth's inner core is the innermost spherical layer of the planet with a radius of about 1200 km (Engdahl et al., 1974), is solid and composed predominantly of iron-nickel alloy (Birch, 1964). Above there is the outer core, a liquid ∼2400-km-thick layer with similar composition. The transition between inner and outer core is located at ∼5150 km from Earth's surface (Lowrie, 2007). From a seismological point of view, the whole mantle extends then from the outer Core-Mantle Boundary (CMB), located at ∼2890 km depth, up to the crust. The mantle can also be divided in sub-layers which reflect mineral phase changes. In fact, olivine, which is the primary component of peridotite rocks, undergoes a phase transition and becomes wadsleyite at 410 km of depth. The phase change results in a denser crystal structure and therefore it is recorded as a seismic discontinuity. Similarly, wadsleyite transforms in ringwoodite at 520 km which, in turn, transforms in silicate perovskite at 660 km (Davies, 2001). So, one can identify within the mantle a first layer (upper mantle) primarily made up of peridotite rocks; a transition zone in between 410 and 660 km where the described phase transitions take places; and a bottom layer (lower mantle) made

up of perovskite (Fig. 1.3b). Within the latter, an additional seismic discontinuity near the CMB, the so-called D" discontinuity, may be related to perovskite to post-perovskite phase transition (Murakami et al., 2004; Dobson et al., 2013). Mantle and overlaid crust are also separated by a density discontinuity, namely the Mohorovičić (Moho) discontinuity. Crustal rocks differ in composition from those of the mantle. They are less dense and hence gravitationally stable with respect to heavier mantle rocks. Beneath continental crust, the Moho is 20-90 km deep, whereas beneath oceanic crust, its depth ranges in between 5-10 km.

In geodynamics, layers are identified by their rheological behaviour rather than by the speed of seismic waves passing through it (Fig. 1.3b). Therefore, the subdivision slightly differs from the seismological one. In this view, the shallowest part of Earth's interior which is made by relatively cold rocks and does not flow during intervals of geological time scales (up to 10^9 years) takes the name of lithosphere. It is composed of the crust and part of the upper mantle down to depth about 70-100 km under ocean basins and down to 200-250 km under continents. The lithosphere constitutes the upper cold thermal boundary layer of the mantle convective system. The ∼200 km-thick layer which lies below the lithosphere is called the asthenosphere. At a typical temperature of 1600 K, rocks there can deform and flow with solid-state creep (Turcotte and Schubert, 2002).

1.3 Deformation in Earth's systems and rheology

As described in the previous section, there are several circumstances in which rocks and minerals behaves as a ductile material. An important aspect in geological systems is therefore the characterization of the fluid rheology, as a function of temperature, pressure, composition, stress, or strain rate. We first introduce below some basic rheological concepts.

1.3.1 Solids deformation

We start from the simple and relatively common scenario of simple shear (Fig. 1.4). If a material is located in between two plates of area A and at distance H from each other, the application of a force $\boldsymbol{F}$ to the top surface, as indicated in Fig. 1.4, generates a deformation in which parallel planes of material translate relative to each other. The stress parallel to the surface (shear stress) is defined as force per unit area:

$$\tau = F/A, \tag{1.1}$$

whereas the deformation (shear strain) is defined as the ratio between the relative lateral displacement of the plane (Δx) to the distance between plates, H:

$$\gamma = \Delta x/H. \tag{1.2}$$

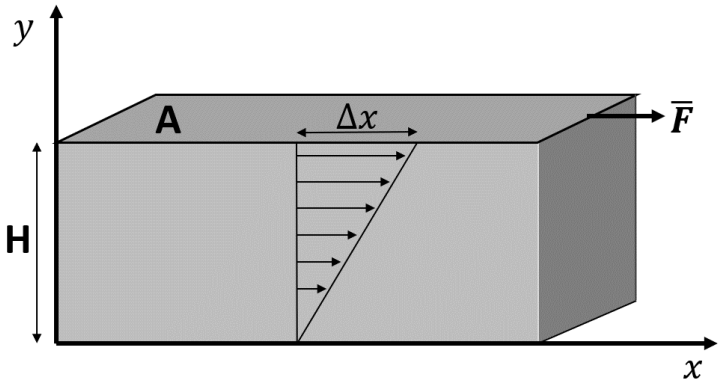

Figure 1.4: Principle of a simple shear. The upper plate of area A is subjected to a force $\boldsymbol{F}$, as indicated. The underlying material experienced a relative displacement of Δx.

The way stress and strain are linked together describes the intrinsic rheological behaviour of the material. This relation defines the constitutive equations (or rheological relationships). In the case in which the material in Fig. 1.4 is a solid, the rheological relationship is given by Hooke's law:

$$\tau = G\gamma, \tag{1.3}$$

where G is a proportional constant, namely the shear modulus, which depends on the material itself.

Within the (τ, γ)-plane, eq. (1.3) is not always valid. For instance, for sufficiently large stresses, the response of the solid is not linear any more but rather it deforms widely (Fig. 1.5). For a solid, one can distinguishes two different (ideal) behaviours: ductile behaviour and brittle behaviour. Above a certain stress threshold, in the case of a ductile material, the deformation is localized in specific portions of the material; whereas a brittle material breaks into several parts.

1.3.2 Flow curves

If the material in Fig. 1.4 is a liquid rather than a solid, the application of a shear stress will generate a time dependent strain. The simplest constitutive equation in this case writes

$$\tau = \eta\dot{\gamma}, \tag{1.4}$$

where η is the viscosity, that is the resistance of a fluid to flow under applied stress, and $\dot{\gamma}$ is the shear strain-rate, that is the temporal derivative of shear strain. By plotting the relationship between shear stress (τ) and shear strain-rate ($\dot{\gamma}$) in simple shear, one obtains the so called "flow curve". In the simplest case of a constant viscosity, the flow curve obtained by plotting $\tau(\dot{\gamma})$ is the one of a Newtonian fluid. In this case, the curve represents a fluid

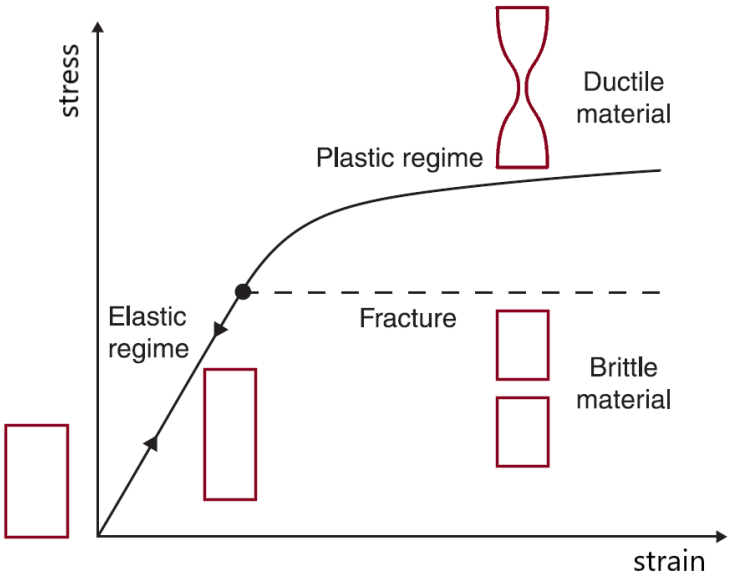

Figure 1.5: Two types of solid behaviours. In one case the material fractures, whereas in the other it plastically deforms beyond a critical deformation. Cartoons represent a block of material at its initial state, the homogeneous deformation in the elastic regime, then either a ductile or brittle behaviour. Modified from Coussot (2012).

which flows as soon as stress is applied. Moreover, the subsequent rate of deformation is proportional to applied stress and during deformation there is no accumulation of energy. Examples of Newtonian fluids are water, syrup and other usual liquids composed by small molecules.

The behaviour of a liquid can deviate from this first case once viscosity depends on strain, strain rate or stress. In this case the material is a non-Newtonian fluid. The stress-strain relationship becomes non-linear. But an effective viscosity can always be defined by:

$$\eta_{eff} = \tau/\dot{\gamma}. \tag{1.5}$$

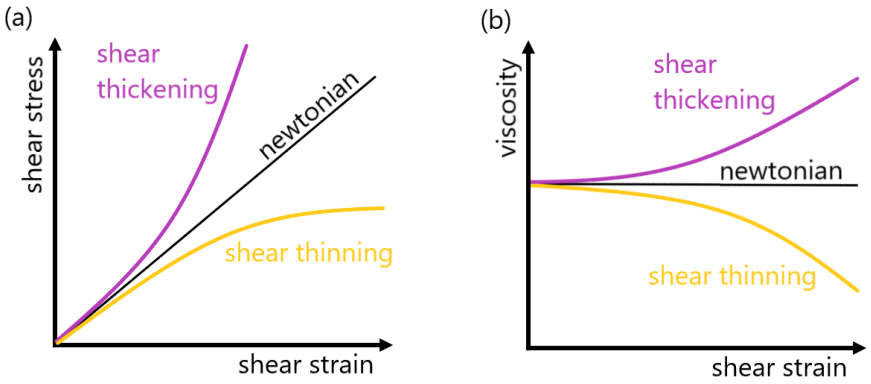

Figure 1.6: Example of flow curves for different fluids.

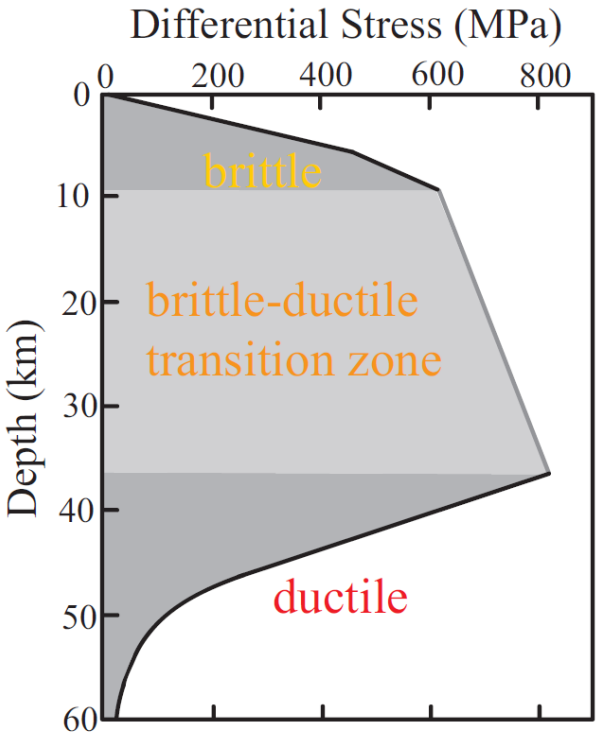

Figure 1.7: Deformation mechanisms in the Earth's mantle with the estimated depths of brittle ductile transitions. From Kohlstedt et al. (1995); Massmeyer (2013).

This effective viscosity depends on applied stress and can either increase under current shear rate (shear thickening fluids, e.g. cornstarch) or decrease (shear thinning fluids, e.g. mayonese, hair gel) (Fig. 1.6).

1.3.3 Creep in the mantle

Although most of the mantle deformation occurs under ductile flow at geological time scales, deformation in the first few kilometers of depth remains brittle and takes form of fractures. The transition from brittle to ductile deformation with depth depends on several parameters: local geothermal gradient, rocks composition, crustal thickness and the strain rate.

For an oceanic lithosphere we show the hypothetical vertical profile in Fig. 1.7. In the ductile regime the flow takes place by diffusion creep or dislocation creep. In diffusion creep, thermally activated defects in the mineral lattice migrate in the presence of a stress field. Because of this diffusion, crystal grains deform leading to rock strain. In Nabarro-Herring diffusion creep defects move through the body of the grain, whereas in Coble creep they move along grain boundaries. In both cases the flow is associated with a Newtonian rheology because stress and strain are proportional:

$$\dot{\gamma} \propto A_{diff}\sigma, \tag{1.6}$$

where $\dot{\gamma}$ is the strain rate, σ is the stress, and A_{diff} is a proportional coefficient that depends

on grain size, pressure, temperature, oxygen and water fugacity but is independent of stress (Gerya, 2019).

In dislocation creep the strain is generated by the propagation of time defects through the crystal lattice. The resulting creep has a non-linear (non-Newtonian) stress-strain relationship:

$$\dot{\gamma} \propto A_{disl}/\sigma^{n_E}, \tag{1.7}$$

where A_{disl} is a proportional coefficient that does not depend on stress and grain size but does depend on pressure, temperature, oxygen and water fugacity (Gerya, 2019). n_E is the stress exponent and for rocks ranges between 2 and 4.5 (Ranalli, 1995).

For both diffusion and dislocation creep mechanisms, the deformation rate can be written as (Hirth and Kohlstedf, 2003; Ranalli, 1995; Gerya, 2019)

$$\dot{\gamma} = A_D d^{-m} (\sigma_d)^{n_E} e^{\left(-\frac{E_a + V_a P}{RT}\right)}, \tag{1.8}$$

with T being the temperature; P the pressure; R the universal gas constant; E_a and V_a the activation energy and volume, respectively; n_E the stress exponent; σ_d the difference between maximal and minimal applied stress; d the grain size; m the grain size exponent and A_D a material constant. Dislocation creep is grain size independent so then m=0 and d^m=1. Moreover in dislocation creep n_E, E_a and V_a are larger than in the case of diffusion creep. Hence, at small grain size, low stresses, low temperature and high pressure, the dominant creep mechanism is diffusion.

1.3.4 Viscoelasticity

A number of materials have an intermediate behaviour with respect to a purely viscous liquid and a purely elastic solid, whereby they behave elastically on short time scales and viscously on long time scales. They are called viscoelastic mediums. In this case the rheological law combines linear elasticity (eq. (1.3)) with linear (eq. (1.4)) or non-linear viscosity. Therefore, a viscoelastic material exhibits a time-dependent strain due to its viscous part.

The difference with a purely elastic solid can be noticed from stress-strain curves in Fig. 1.8. Purely elastic materials do not dissipate energy in a loading and unloading cycle, whereas viscoelastic materials do. The amount of energy lost during this process is given by the area within the hysteresis loop in Fig. 1.8b.

The ability of a material to deform by viscous creep is measured by the dimensionless Deborah number, De. It is the ratio between two characteristic time scales: the relaxation time, t_c, that is the time it takes for a material to deform or adjust to applied stress, and the time scale of observation (e.g. experiment, numerical simulation, etc.), t_p:

$$De = t_c/t_p. \tag{1.9}$$

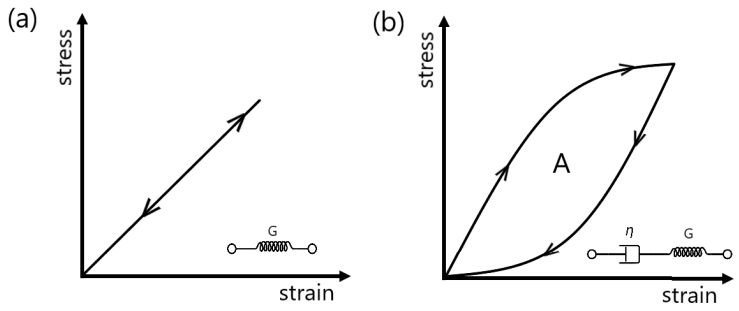

Figure 1.8: Stress−strain curves for a purely elastic solid (a) and for a viscoelastic material (b). The area A within the hysteresis loop represents the amount of energy lost in a loading and unloading cycle.

For a purely elastic solid the relaxation time is t_c=∞ and hence $De \rightarrow \infty$. For a Newtonian fluid, t_c=0 and hence $De \rightarrow$0.

There exist many mechanical models that determine the stress-strain interactions for viscoelastic material. The more common are the Maxwell model and the Kelvin-Voigt model.

In a Maxwell model an elastic Hooke element (spring) and a Newtonian element (dashpot) are combined in series. Strain (γ) is additive and stress (σ) is uniform, that is:

$$\gamma = \gamma_{spring} + \gamma_{dashpot} \tag{1.10}$$

$$\sigma = \sigma_{spring} = \sigma_{dashpot}. \tag{1.11}$$

The rheological equation for a Maxwell element is given by

$$\dot{\gamma} = \frac{1}{G}\dot{\sigma} + \frac{1}{\eta}\sigma. \tag{1.12}$$

The response of a Maxwell element under constant stress (i.e. σ=σ_c in Fig. 1.9 and hence $\dot{\sigma}$=0) is

$$\gamma = \frac{\sigma_c}{G} + \frac{\sigma_c}{\eta}t, \tag{1.13}$$

where t is time. Hence, when a constant stress is applied to a Maxwell body, an instantaneous elastic deformation is followed by a linear viscous strain. When the stress is removed, only the elastic strain is recovered and therefore the body remains deformed (a Maxwell material is in fact referred as Maxwell *fluid*). This strain-time curve is shown in Fig. 1.9a.

In a Kelvin-Voigt model the elastic and viscous elements are disposed in parallel (Fig. 1.9b). In this case is the stress to be additive while strain is uniform:

$$\sigma = \sigma_{spring} + \sigma_{dashpot} \tag{1.14}$$

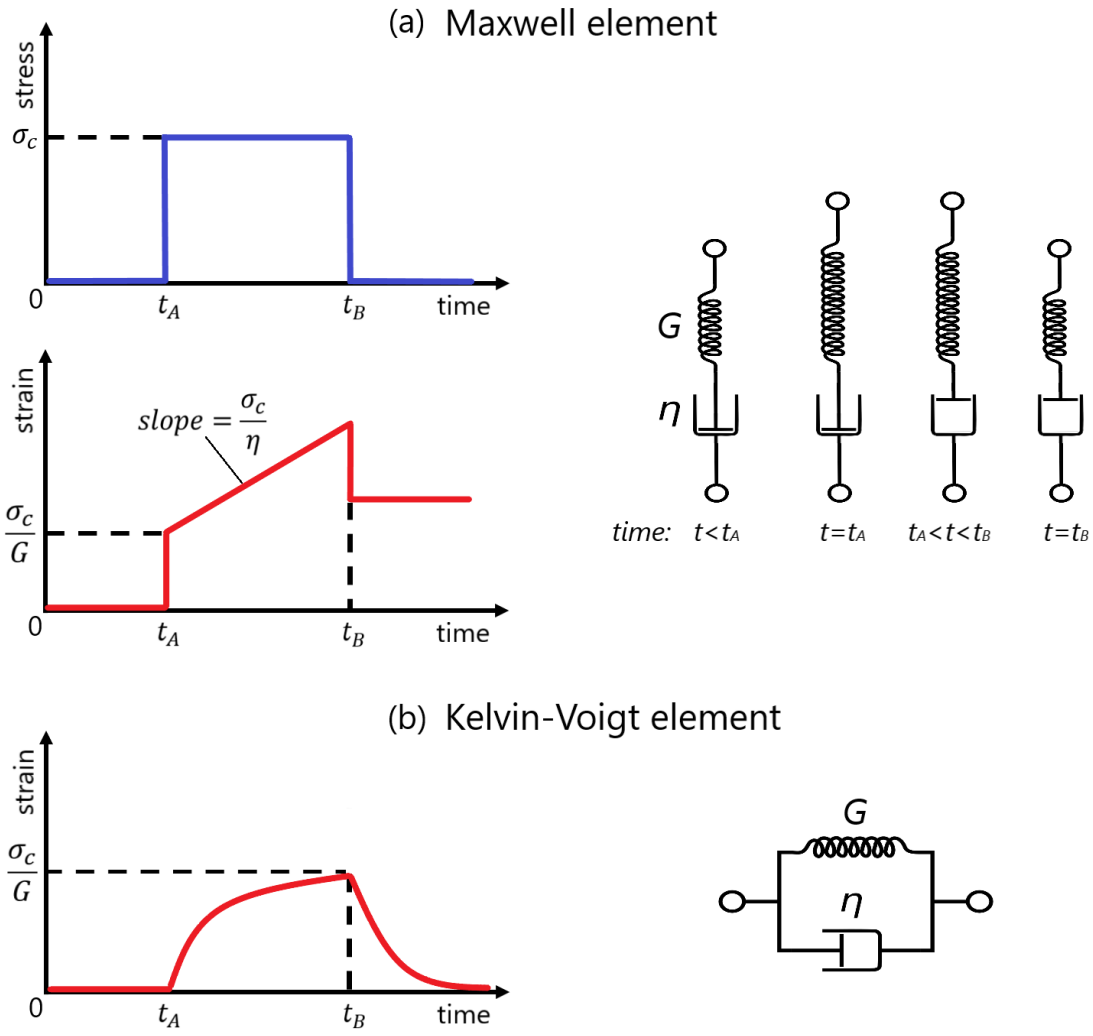

Figure 1.9: Strain−time diagrams for (a) Maxwell fluid and (b) Kelvin-Voigt solid with the relative rheological model. The elastic contribution is indicated by a spring whereas the dashpot indicates the linear viscous part.

$$\gamma = \gamma_{spring} = \gamma_{dashpot}. \tag{1.15}$$

The rheological equation write then

$$\sigma = G\gamma + \eta\dot{\gamma} \tag{1.16}$$

and the strain-time curve (Fig. 1.9b) is characterized by a response during constant load of

$$\gamma = \frac{\sigma_c}{G}\left[1 - e^{\left(-\frac{G}{\eta}t\right)}\right]. \tag{1.17}$$

When load is released the strain goes exponentially to zero, that is the material gradually relaxes to its underformed state. The recovered deformation is

$$\gamma = \left\{\frac{\sigma_c}{G}\left[1 - e^{\left(-\frac{G}{\eta}t_A\right)}\right]\right\} e^{\left[-\frac{G}{\eta}(t-t_A)\right]}. \tag{1.18}$$

The Kelvin-Voigt body is therefore basically a *solid* that undergoes reversible, viscoelastic strain.

1.3.5 Viscoplasticity: yield Stress fluids

Visco-plastic fluids (synonym of yield stress fluids) differs from the previous ones because of the presence of a yield stress (σ_y). A typical example is a suspension of particles in a liquid. When the particle volume fraction increases, the particles become in close contact with one another, and the material can face jamming. In this jammed state, the material can support stresses without flowing. A so-called yield-stress fluid does not flow if the applied stresses are not high enough to unjam the structure, but it does flow when the stresses become larger than σ_y. This introduces a non-linearity into the material rheology, which strongly impacts on its dynamics (Makse et al., 2005; Bonn et al., 2017; Coussot, 2005; Barnes, 1995).

Simple yield stress fluids are those described by popular fluid models such as the Bingham model or the Hershel-Bulkley model. Once the local stresses exceeds the yield stress, a Bingham fluid exhibits Newtonian behaviour through a linear flow curve and a constant value of viscosity. If a fluid shows a non-linear flow curve, i.e. $\eta(\dot{\gamma})$, it can be approximated by the Hershel-Bulkley model that is written as

$$\begin{cases} \sigma = \sigma_y + K_v\dot{\gamma}^n & \text{if} \quad \sigma > \sigma_y \\ \dot{\gamma} = 0 & \text{if} \quad \sigma \leq \sigma_y \end{cases} \tag{1.19}$$

where K_v is the consistency and n the power-law exponent. Note that the exponent n defined here is the reverse of the power law index usually used in geophysics (e.g. n_E in eq. (1.7)), that is $n = 1/n_E$. Unless otherwise indicated, in what follows we will use this latter definition when refering to the power-law index (i.e. n and not n_E). For n <1 the fluid is shear thinning and the effective viscosity η_{eff} decreases as $\dot{\gamma}$ increases. For n >1 the

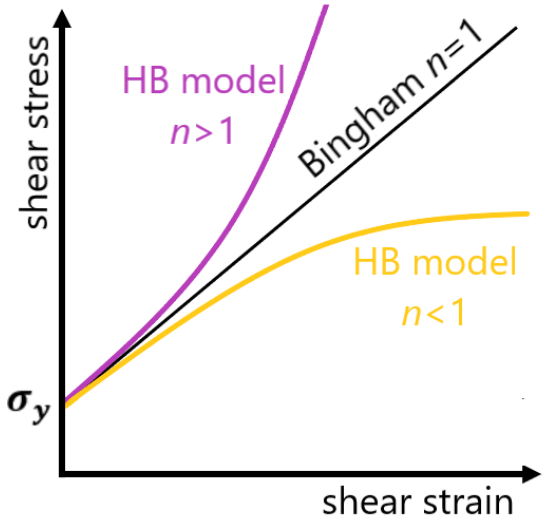

Figure 1.10: Flow curves for different yield stress fluids. Black line refers to a Bingham fluid. Blue line for a Hershel-Bulkley fluid with power law exponent n >1. Yellow lines is for a Hershel-Bulkley fluid with n <1.

fluid is shear thickening. For n=1 it reduces to the Bigham model (Fig. 1.10) and for n=1 and σ_y=0 to Newtonian fluid. Through a broad variety of fluids and systems, the power law index is found to range more often in between n=0.2-0.8 rather than n=1 as it is in the Bingham model (Bonn et al., 2017). Moreover, the exponent n seems to be a relevant material parameter that does not change much with fluid density and temperature (Bonn et al., 2017).

Fig. 1.11a shows the example of Carbopol, an aqueous mixture of a polymeric microgels and one of the most commonly used "yield stress" fluid in experiments. Fig. 1.11b reports a steady-state rheometry analysis. It shows the presence of a yield stress at very low strain rates and highlights the good fit of the Hershel-Bulkley model to the experimental flow curve. However, steady state measurements can investigate only the flow of the material (i.e. its viscous response). The viscoelastic behaviour of the material, considering also its solid-like regime (i.e. for $\sigma < \sigma_y$), can be probed by using oscillatory rheometry (Fig. 1.11c). The measured stress response is made up by the contribution of the storage modulus, G', and the loss modulus, G". Fig. 1.11c shows that at the lowest accessible strains the fluid response is solid-like, with a storage modulus much larger than the loss modulus, while at higher strains, it is the loss modulus to predominate, showing the liquid-like bahaviour.

1.4 Fluid flow and thermal convection

In the continuum assumption, flow and deformation of a body are the results of the balance of the internal and external forces acting on this media. To relate forces and flow, motion

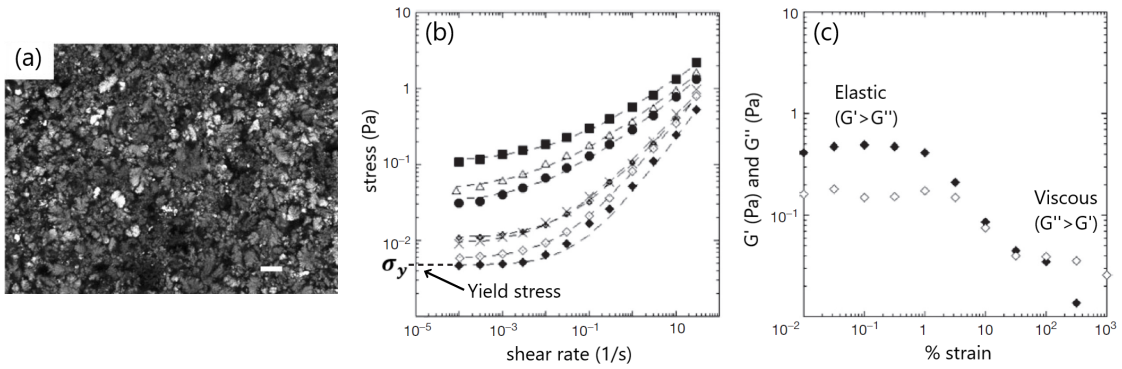

Figure 1.11: (a) Structure of Carbopol gels. The length of the scale bar is 20 μm. From Gutowski et al. (2012). (b) and (c) are an example of rheological properties of Carbopol gels at T=293 K from Darbouli et al. (2013). (b) Steady-state rheometry: shear stress as a function of strain rate. (Black diamonds: σ_y=0.0047 Pa, diamonds: σ_y=0.006 Pa, plus: σ_y=0.01 Pa, crosses: σ_y=0.009 Pa, black circles: σ_y=0.031 Pa, triangles: σ_y=0.045 Pa, black squares: σ_y=0.104 Pa, dashed lines: Herschel Bulkley model). (c) Oscillatory rheometry: variation of the elastic G' (black diamonds) and loss G" (white diamonds) moduli as a function of the strain for a Carbopol gel with σ_y=0.006 Pa and a frequency f=0.1 Hz.

equations have to be used. We introduce those equations below, in the first place for an athermal system and consequently for the case in which heat transport is coupled to material deformation.

1.4.1 Equations of motion

We consider that the flow is incompressible. The conservation of mass and conservation of momentum (Navier-Stokes equation) then write, respectively:

$$\nabla \cdot \boldsymbol{v} = 0 \tag{1.20}$$

$$\underbrace{\rho}_{\text{I}} \underbrace{\left(\frac{\partial \boldsymbol{v}}{\partial t} + \boldsymbol{v} \cdot \nabla \boldsymbol{v} \right)}_{\text{II}} = \underbrace{-\nabla P}_{\text{III}} + \underbrace{\nabla \cdot \boldsymbol{\tau}}_{\text{IV}} + \underbrace{\boldsymbol{F}}_{\text{V}}. \tag{1.21}$$

where $\boldsymbol{v}$ is the velocity vector, P the pressure and $\boldsymbol{\tau}$ the deviatoric shear stress tensor. Eq. (1.21) is set up in accordance with Newton's second law of motion. Its differ terms represent: (I) the density of the fluid; (II) the acceleration expressed by the local rate of change of velocity and advection; (III) the internal pressure gradient of the fluid; (IV) the internal viscous forces. For a Newtonian fluid, $\boldsymbol{\tau} = 2\eta\dot{\boldsymbol{\gamma}}$ with viscosity η constant and this term can also be written as $\eta\nabla^2\boldsymbol{v}$; (V) other external body forces acting on the fluid, for example gravity leads to $\boldsymbol{F} = \Delta\rho\boldsymbol{g}$.

Considering the simple case of a solid body of spherical shape with characteristic diameter d moving in a very viscous Newtonian fluid, a relatively simple solution of eq. (1.21) can be

obtained. If from initial and boundary conditions the characteristic scales of velocity and time, U and T, respectively, are known, the dimensionless (hatted) variables involved in eq. (1.21) are

$$\hat{t} = \frac{t}{T_i}, \quad \hat{\boldsymbol{v}} = \frac{\boldsymbol{v}}{U}, \quad \hat{P} = \frac{PL}{\eta U}, \quad \hat{x} = \frac{x}{L}. \tag{1.22}$$

Ignoring the external forces, the Navier-Stokes equations in terms of these variables, and dropping the $\hat{}$, are:

$$\nabla \cdot \boldsymbol{v} = 0 \tag{1.23}$$

$$\left(\frac{d^2}{T_i \nu}\right) \frac{\partial \boldsymbol{v}}{\partial t} + \left(\frac{Ud}{\nu}\right) \boldsymbol{v} \cdot \nabla \boldsymbol{v} = -\nabla P + \nabla^2 \boldsymbol{v} \tag{1.24}$$

where ν is the kinematic viscosity or momentum diffusivity, $\nu = \eta/\rho$. Three different time scales hide in eq. (1.24): T_i=t_{flow}, the inherent time scale of flow; d/U=$t_{advection}$, the time to travel a distance d at speed U; and d^2/ν=$t_{diffusion}$, the time for viscous diffusion over a distance d. The two dimensionless groups that appear are then

$$\frac{d^2}{T_i \nu} = \frac{t_{diffusion}}{t_{flow}} \tag{1.25}$$

$$\frac{Ud}{\nu} = \frac{t_{diffusion}}{t_{advection}} = Re \tag{1.26}$$

where Re is the Reynold number. When both eq. (1.25) and eq. (1.26) are smaller than 1, the resulting (slow) flow is the Stokes flow. Therefore, returning to dimensional variables, the equation of motion for Stokes flow are

$$\nabla \cdot \boldsymbol{v} = 0; \qquad 0 = -\nabla P + \eta \nabla^2 \boldsymbol{v} + \boldsymbol{F} \tag{1.27}$$

where $\boldsymbol{F} = \Delta\rho \boldsymbol{g}$ in flows driven by density differences.

Given the large values of magma and rock viscosities, Stokes flow usually applies in geological contexts. For example, magma ascent velocity in the lithosphere can be estimated by the size of the largest xenoliths (solid rock fragments) carried with it and erupted on Earth's surface, if magma viscosity and density contrast are known (Turcotte and Schubert, 2002). Stokes flow can also be used to estimate the size and velocity of hot plume heads rising in the mantle (e.g. plumes in Fig. 1.1c). With typical sizes of L ∼1000 km, mantle kinematic viscosity ν=10^{18} m^2/s (Lowrie, 2007), and characteristic velocity U ∼10 cm/yr, Re ∼10^{-21} and the inertial force can be neglected. So that Stokes flow becomes a good framework.

1.4.2 Thermal convection

In isoviscous fluids

The Earth's mantle is internally heated by radioactive decay, heated from below at the core-mantle boundary (CMB) and cooled from above. If we neglect internal heating, this is the same configuration as the classical Rayleigh-Bénard convection. Assuming that all density differences can be ignored except those linked to the buoyancy term and caused by thermal expansion, the governing equations for convection (RBC), in their dimensionless form, write as:

$$\nabla \cdot \hat{\boldsymbol{v}} = 0 \tag{1.28}$$

$$\frac{1}{Pr}\left(\frac{\partial \hat{\boldsymbol{v}}}{\partial \hat{t}} + \hat{\boldsymbol{v}} \cdot \nabla \hat{\boldsymbol{v}}\right) = -\nabla \hat{P} + \nabla \cdot \hat{\boldsymbol{\tau}} + Ra\hat{T}\boldsymbol{e}_y \tag{1.29}$$

$$\frac{\partial \hat{T}}{\partial \hat{t}} + \hat{\boldsymbol{v}} \cdot \nabla \hat{T} = \kappa \nabla^2 \hat{T} + H \tag{1.30}$$

where $\boldsymbol{e}_y$ is the unit vector in vertical direction, κ the thermal diffusivity and H the internal heating. Here we use a characteristic length d, dimensionless time $\hat{t} = t(\kappa/d^2)$, dimensionless velocity $\hat{\boldsymbol{v}} = \boldsymbol{v}(k/d)$ and dimensionless temperature $\hat{T} = T/\Delta T$, where ΔT is the temperature gradient between the hot and cold plates. In addition to the conservations of mass and momentum, already introduced, eq. (1.30) represents the conservation of energy.

The two parameters that govern the system are the Prandtl number, Pr, and the Rayleigh number, Ra. The Prandtl number compares momentum diffusivity with thermal diffusivity

$$Pr = \frac{\nu}{\kappa}. \tag{1.31}$$

For Earth's mantle, $Pr \sim 10^{23}$, meaning that momentum diffuses much faster than heat. So convection will stop as soon as ΔT (i.e. the engine of convection) disappears, and inertia is negligible ($Re \sim 10^{-21}$).

The Rayleigh number compares the thermal buoyancy forces and the effects of thermal diffusion and viscous dissipation

$$Ra = \frac{\alpha g \Delta T d^3}{k\nu}, \tag{1.32}$$

where α is the thermal expansion and d the thickness of the fluid layer. For Newtonian fluids a regime diagram of thermal convection as function of Pr and Ra is shown in Fig. 1.12. There exists a critical value of Rayleigh number, Ra_c, below which convection is not observed and heat is transferred by conduction. For free-slip boundary conditions Ra_c=657, whereas for no-slip Ra_c=1708 (Chandrasekhar, 2013). For Pr >100 and increasing Ra, convection

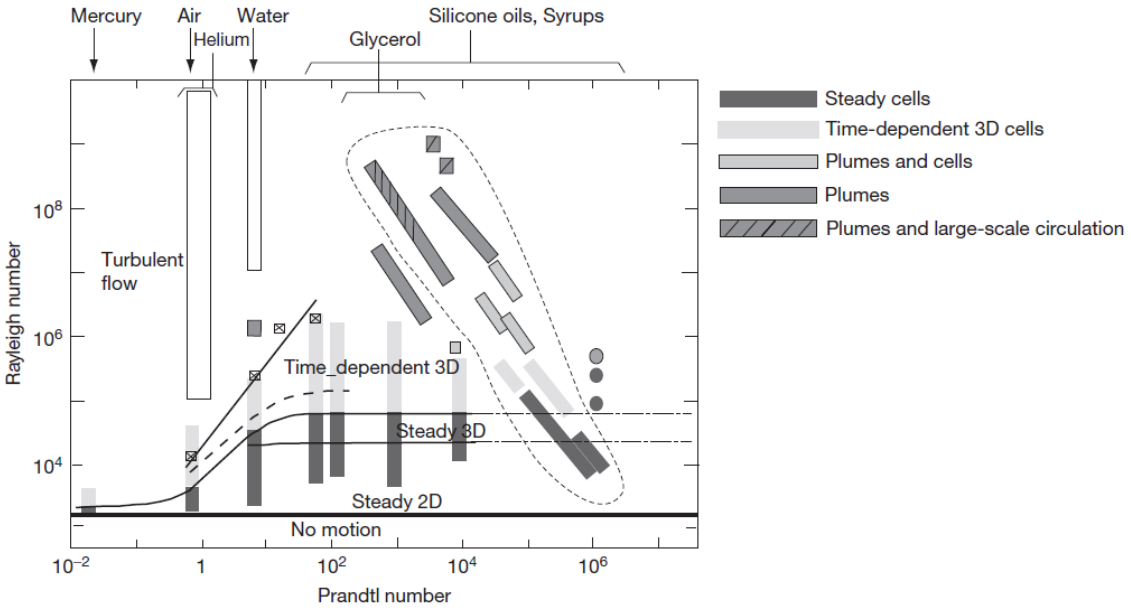

Figure 1.12: RBC regime diagram. Modified from Davaille and Limare (2015). Data from Krishnamurti (1970a,b, 1979); Whitehead Jr and Parsons (1977); Nataf et al. (1984); Guillou and Jaupart (1995); Zhang et al. (1997); Manga and Weeraratne (1999); Xi et al. (2004)

progressively passes from steady convective rolls, to time-dependent cells, to hot and cold plumes. In Earth's mantle, the typical value of Ra varies between 10^6 and 10^9.

Temperature dependence of the viscosity

A first complication with respect to the simple case of RBC described above occurs when considering a temperature-dependent viscosity. The main impact of a strongly temperature-dependent viscosity is to break the symmetry in the convection cell typical of fluids with constant viscosity. The system is now characterized by Ra, Pr and ξ, where ξ is the viscosity ratio: $\xi = \eta(T_{top})/\eta(T_{bot})$. $\eta(T_{top})$ is the viscosity at the surface cold temperature and $\eta(T_{bot})$ the viscosity at the hot bottom temperature. Three main regimes are observed (Solomatov, 1995). For small ξ <2-5, the flow behaves as in isoviscous fluids. At intermediate ξ (5< ξ <10^4), the asymmetry between cold and hot instabilities increases, as well as the resistance to motion of the cold thermal boundary layer. For sufficiently large Ra, the resulting convection pattern is determined by the local characteristics of these cold and hot thermal boundary layers (Androvandi et al., 2011; Davaille and Limare, 2015). Three scales of convection can be distinguished . A large cellular convection characterized by cold downwelling which encloses several smaller upwelling plumes. Within the latter, cold rings are formed when the plume reaches the cold boundary layer. At large ξ >10^4, convection develops below a stagnant lid, which encompasses most of the viscosity variations. Only the bottom part of the cold thermal boundary layer can become unstable, and heat transfer through the stagnant lid is conductive. For Earth-like parameters (i.e. Ra ~10^6-10^7 and a

viscous contrast across the lithosphere of $\xi \geq 10^7$), mantle convection should be in the stagnant lid regime and plate tectonics should not exist. However, what is actually observed on Earth is more similar to the regime described for intermediate viscosity contrast (Androvandi et al., 2011). Therefore, although a $\eta(T)$ plays an important role in the formation of a single stagnant lid, is not sufficient to break it down and create different plates that participate in convection sinking in the subduction zones.

Complex rheology

Plate tectonics requires mechanisms that allow strain localization and weak zones formation (Bercovici, 2003; Tackley, 2000). The use of plastic yielding in models of mantle dynamics is one of the possible ways to weaken and break down the stagnant lid (Tackley, 2000; Rolf and Tackley, 2011; Trompert and Hansen, 1998; Stein et al., 2004, 2011, 2013). The deformation mechanisms used are similar to the rheology of yield stress fluids presented in section 1.3.5. Briefly, these models consider an effective viscosity η^* consisting of two contributions: $\eta^* = f(\eta_T, \eta_\sigma)$, where f indicates the minimum or a specific average function, depending on the model; η_T is a temperature-dependent viscosity and η_σ is the stress-dependent contribution. The latter is calculated as for a Bingham fluid, i.e. $\eta_\sigma = A + \sigma_y(z)/\dot{\gamma}$, where A is a constant that depends on the model and $\sigma_y(z)$ is a depth-dependent yield stress.

From a rheological point of view, the implementation of a viscoplastic model to describe the stress-strain relationship, however, brings also some complications. For example, a theoretical difficulty appears when the rate of strain, $\dot{\gamma}$, is close to zero and the viscosity approaches infinity (e.g. in eq. (1.5)). Contrary to the Newtonian case, the conductive regime in a viscoplastic fluid is always stable to infinitesimally small perturbations and spontaneous motion is inhibited by the presence of the yield stress (Zhang et al., 2006; Balmforth and Rust, 2009; Vikhansky, 2009). However, RBC experiments in Carbopol (Darbouli et al., 2013; Kebiche et al., 2014; Metivier et al., 2017) observed convective motions even though no finite amplitude perturbations were applied, contrary to what theory predicts.

Different avenues have been proposed to solve this paradox and deal with the onset of motion in yield stress fluids. For instance, a classical way to proceed in numerical modeling is through regularized models (e.g. Massmeyer et al., 2013; Li et al., 2016) where a finite high effective viscosity is introduced for small values of strain rate. In this way, the fluid is simply treated as a highly viscous material in regions where it should not deform. But this is at odds with the rheological measurements which show that Carbopol rheology at low stress is not viscous (Dinkgreve et al., 2017; Møller et al., 2009). These models also have issues regarding the location of yield surfaces due to their dependence on regularized parameters (Saramito and Wachs, 2017; Karimfazli et al., 2016). They can also give results different from exact solutions (Frigaard and Nouar, 2005), making the investigation of the onset of motion even more complicated.

An extension of this approach is to consider the fluid as elasto-visco-plastic, so that, below the yield stress, the elasticity of the fluid is taken into account through a visco-elastic

effective viscosity (Darbouli et al., 2013; Saramito, 2007, 2009).

A third scenario is proposed by Metivier et al. (2017). They consider Carbopol solution as a porous media made of aggregates of microgel particles and pools filled with water. The motion is supposed to start in these pools, building stresses through Darcy flow in the porous media, until they are able to destabilize the entire system. However, their measurements indicate permeability values too small for the process to be efficient if Carbopol is considered as a classic porous media. Hence, they suggest that this approach failure could be due to two main aspects: (i) the onset of convection in Carbopol is not only due to the motion of water in the gel pores, but should be considered in the entire bulk material, and (ii) Carbopol may have different properties from the ideal non-deformable porous media used to make the analogy.

As we can see, both the RBC onset of motion in natural yield-stress fluids, and the influence of the fluid structure, are still debated and needs better description and understanding.

1.4.3 The fall of a sphere

A first approach to large scale features of mantle convection is to treat them in the simplest way possible. For instance, hot mantle plumes, with heads made by hotter, less dense and less viscous rocks than the surrounding mantle rocks, can be modeled as spherical bodies whose velocities are given by the Stoke law. Therefore we introduce here the problem of a falling (or rising) buoyant spherical body in fluids with different rheology.

In a Newtonian fluid

Stokes equations can be solved for the classical case of a sphere falling in a infinite expanse of viscous Newtonian fluid. A solid sphere of diameter d_s will rise or fall through a viscous fluid if its density ρ_s is different from the density of the fluid ρ_f. For Stokes flow, sphere density only enters in the buoyancy term $\Delta\rho g$, where $\Delta\rho = \rho_s - \rho_f$. The sphere is subjected to the drag force F_D:

$$F_D = 6\pi\eta v_s \left(\frac{d_s}{2}\right), \tag{1.33}$$

where η is the constant viscosity of the fluid. The force balance only requires buoyancy to be balanced by drag:

$$\frac{1}{2}C_D\rho_f v_s^2 \pi \left(\frac{d_s}{2}\right)^2 = \Delta\rho g \left(\frac{1}{6}\pi d_s^3\right) \tag{1.34}$$

where C_D is the dimensionless drag coefficient:

$$C_D = \frac{F_D}{\frac{1}{2}\rho_f v_s^2 \pi \left(\frac{d_s}{2}\right)^2} = \frac{24}{\left(\rho_f v_s d_s\right)/\eta} = \frac{24}{Re}. \tag{1.35}$$

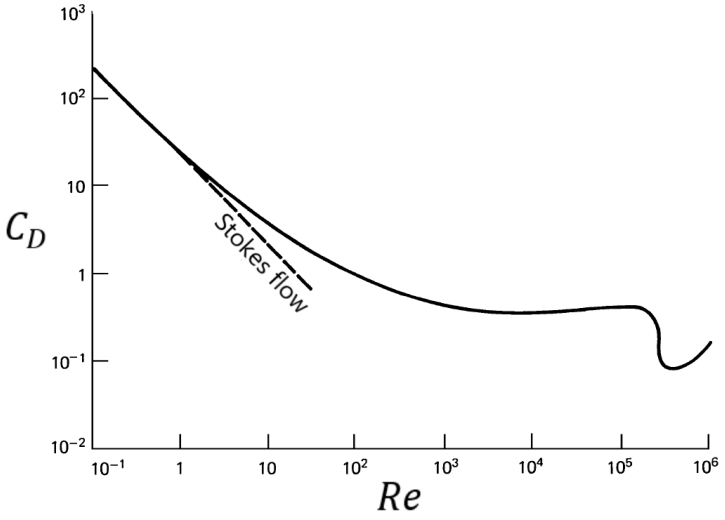

Figure 1.13: Dependence of the drag coefficient for a sphere on Reynolds number. Modified from Turcotte and Schubert (2002). The solid line is the measured dependence whereas the dashed line is eq. (1.35).

Thus, the Stokes solution for slow motion is formulated by two dimensionless groups, the drag coefficient C_D and the Reynold number Re. Eq. (1.35) is valid only for laminar flow. At large values of Re, vortices are generated and flow becomes unsteady. This is shown in Fig. 1.13 where the relationship between Re and C_D is plotted for a wide range of Reynold numbers. The result for Stokes flow, eq. (1.35), is a valid approximation only for Re <1.

In a yield stress fluid

Considering a shear-thinning yield-stress fluid modeled by the Hershel-Bulkley model (eq.1.19), the total number of independent variables that characterize the sphere motion is 7. They are: the fluid density through which the sphere is settling, ρ_f; sphere characteristic diameter d_s, terminal velocity v_s and buoyancy $\Delta\rho g$; and the rheological parameters present in eq. (1.19): consistency, K_v, shear-thinning index, n, and the yield stress, σ_y. The number of parameters with independent dimensions is 3. According to the Buckingham Π theorem, there exist 7-3=4 dimensionless groups that parameterize the problem. They are the shear thinning index (n), the Reynold number (Re), the Bingham number (Bi) and the drag coefficient (C_D). Taking into account that for a Hershel-Bulkley fluid; viscous stress writes as $K_v(v_s/d_s)^n$, the Reynold number becomes

$$Re = \frac{\rho_f v_s^2}{K_v \left(v_s/d_s\right)^n}. \tag{1.36}$$

The Bingham number compares the yield stress with viscous stress:

$$Bi = \frac{\sigma_y}{K_v \left(v_s/d_s\right)^n}. \tag{1.37}$$

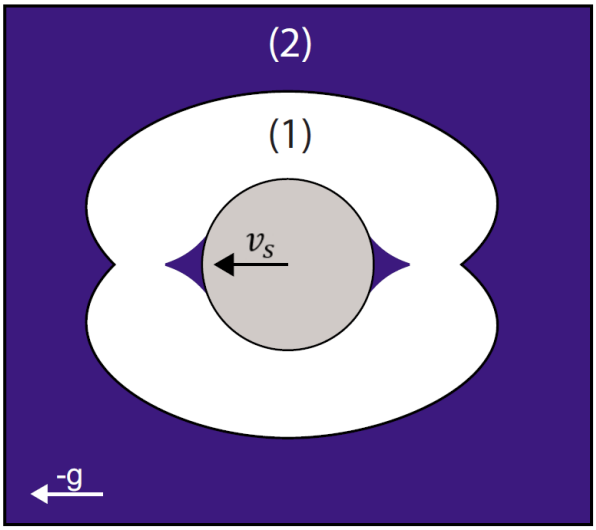

Figure 1.14: Shape of yielded (in white) and unyielded (in blue) flow regions for a sphere moving from right to left. Modified from Putz et al. (2008).

The drag coefficient remains the same one obtained rearranging eq. (1.34), that is the ratio of buoyancy to drag. From the dimensional analysis, C_D can be also expressed as a relationship among the other dimensionless groups, that is C_D=$f(Re, Bi, n)$. Ansley and Smith (1967) proposed the expression

$$C_D = 24X(n)\left(1 + \frac{kBi}{Re}\right). \tag{1.38}$$

Here $X(n)$ is a correction factor and depends on the power-law index n. In shear thinning fluids where n ranges between 0 and 1, $X(n)$ takes values between 1 and 1.5. For Newtonian fluids, $X(n = 1) = 1$. The parameter k is a numerical coefficient acting on Bi which indicates how much the yield stress is significant relatively to viscous stress. Ansley and Smith (1967) suggested a value of k equal to 1. More recent numerical simulations find k=0.823 (Beaulne and Mitsoulis, 1997). Eq. (1.38) can be rewritten by the introduction of another dimensionless number: the Yield number, Y. It is the ratio between yield stress and buoyancy stress, that is

$$Y = \frac{3\sigma_y}{\Delta\rho g d_s}. \tag{1.39}$$

Eq. (1.38) then becomes

$$C_D = \frac{4}{Y}\frac{Bi}{Re}. \tag{1.40}$$

By substituting eq. (1.40) in eq. (1.38) and knowing $X(n)$ and k, one finds that the motion of a sphere in a yield stress fluid is described by an expression of form $Y^{-1}(Bi^{-1})$. A detailed discussion about it will be given in section 3.3.

Beside the determination of the drag coefficient, another crucial aspect regards the determination of the shape and position of the yield surface that separates the solid-like region (where $\sigma < \sigma_y$) from the fluid-like one ($\sigma > \sigma_y$). It was first determined numerically and analytically for a Bingham fluid by Beris et al. (1985) (Fig. 1.14). Recent studies in Hershel-Bulkley fluid (Carbopol) have shown that, within the yielded region, the flow in Carbopol is asymmetric and confined nearby the sphere, within an area which size depends on the yield stress of the fluid (Putz et al., 2008; Holenberg et al., 2012; Fraggedakis et al., 2016). Similar results had been found for Laponite, a very thixotropic colloidal suspensions (Gueslin et al., 2009), where the asymmetry of the flow pattern increases with the age of the fluid through the appearance of a negative wake (i.e. upward fluid motion in the sphere's wake (Hassager, 1979)), and in viscoelastic aqueous polyacrylamide solutions (Arigo and McKinley, 1998). Another peculiar characteristic of a falling sphere in yield stress fluids or in viscoelastic materials is that its velocity can depart from a constant value and show oscillations and irregularities. One of the first observations of an oscillating particle settling has been in hydroxyl propyl guar (HPG) polymer gels (Mollinger et al., 1999), a yield-stress power-law family of fluids (Jiang et al., 1986). In this work, the authors suggested that the irregularities in the descending motion were linked to the elasticity of the gel. Something similar is reported in entangled wormlike micellar fluids (Jayaraman and Belmonte, 2003; Kumar et al., 2012), in Laponite (Fazilati et al., 2017), where the vertical velocity can oscillate in bursts and, again, in HPG (Weidman et al., 2012). In cornstarch suspensions (shear thickening fluid) (von Kann et al., 2011; Von Kann et al., 2013), the sphere velocity never approaches a steady terminal velocity but instead it oscillates, decreases with time, to reach a series of stop-go cycles as the sphere becomes close to the experimental tank bottom. In wormlike micellar fluids, the cause of non-transient oscillations is to be found in the formation and subsequent breakage of flow-induced structures; in cornstarch suspensions, in the formation and dissolution of a jammed layer that, under sufficient stress, increases drag and slows the sphere down; while the irregular motion in laponite is due to the existence of flow instabilities and shear banding.

1.5 Thesis outline

In this thesis, we investigate the transition solid/flowing in yield-stress fluids, using laboratory experiments and numerical simulations. The results obtained from the fluid mechanics study are then applied to the dynamics of magmatic systems. Our aims are to evaluate how the transition depends on the fluid structure and its elasticity, what ingredients are needed to describe mathematically this transition and fluid motion, and when this description will break down. Two systems have been chosen for the simplicity of their dynamics in newtonian fluids, and their relevance to geological systems: the motion of a solid sphere, and the development of thermal plumes.

The manuscript is organized as follows:

- We carried out experiments on the free-fall of a sphere through an elasto-viscoplastic mixture of water and superabsorbent gel grains. In Chapter 2 I first describe the fluid preparation and properties, and afterwards the experimental set up and techniques used during the experiments. A control case by using a Newtonian fluid is also reported. At the end of the chapter all experiments and relevant parameters needed throughout the thesis are listed.

- Chapter 3 holds the main experimental results. I first describe the different regimes that we observed for the motion of the falling sphere. Then I show how we can infer the fluid effective rheology determined from the falling sphere experiment within the framework of a simple yield stress fluid. The second part presents PIV measurements and the analysis of the yielded portion of fluid that surrounds the sphere. The last part discusses the differences and deviations from what is expected for a simple yield stress fluid, and in particular the influence of the fluid structure on the dynamics. This study has been done in collaboration with Professors Ichiro Kumagai (Dept of Engineering, Meisei Univ., Tokyo) and Kei Kurita (Earthquake Research Institiute, Univ. of Tokyo, Japan). A first manuscript is in revision for Journal of Non-Newtonian Fluid Mechanics, and a second one is in preparation.

- Chapter 4 presents the results of numerical simulations for thermal instabilities in elasto-viscoplastic fluids. Deformation patterns and thermal evolution are compared with previous laboratory experiments in Carbopol (Davaille et al., 2013), and numerical simulations using a regularized viscoplastic formulation (Massmeyer et al., 2013). We explore how the addition of elasticity influences plume dynamics. This work was done in collaboration with Prof. P. J. Tackley (Institute of Geophysics, Department of Earth Sciences, ETH Zurich, Switzerland) and Dr. V. Patočka (Institute for Planetary Research, German Aerospace Center, Berlin, Germany). Ultimately, we wanted to apply this work to plume dynamics in the Earth's mantle, but more simulations are still needed to do that.

- In Chapter 5, I move to a larger, - geological-, scale, applying the scaling laws found in the laboratory to magma chambers. A special care is given to the interpretation of the rheological magma-mush transition which characterizes the deformation in transcrustal magmatic reservoirs. Several scenarios on remobilization of a crystal mush are discussed. A manuscript for Journal of Volcanology and Geothermal Research is in preparation.

- I end by the conclusions and perspectives.

- I have included in the appendices the revised version of the paper to JNNFM, a list of the oral and poster presentations in international workshops and conferences, as well as the internships at other institutions that I have done during my thesis.

Chapter 2

Experimental details

This chapter introduces the fluids and the set up used during the experiments. We have carried out an experimental study using mixture of superabsorbent polymers (SAP) where the interaction between a falling sphere and the fluid structure has been examined. SAP are constituted of polymer grains that in water can sell up to 100 times and form gels grains whose size can be controlled by controlling the size of the initial powder. High particle fractions are easy to reach, making the system a promising analog for complex and heterogeneous geological systems. The rheology of this mixture (water and touching grains) combines viscous, elastic and plastic aspects and can be characterized using the free-fall of spheres of different diameters and densities. After describing the fluid preparation and the experimental apparatus, we report a first analysis for Newtonian fluids in order to test the reproducibility and accuracy of the experimental techniques. The chapter ends by a list of tables in which all experiments and their relevant parameters are summarized.

2.1 Fluid preparation and properties

According to the product company (Omiya Green Service Co., Ltd), the experimental fluid we used is a superabsorbent polymer (polyacrylamide) made by copolymerization of acrylic acid and acrylamide. It is part of the family of aqueous dispersions of polymeric materials with large capacity of water absorption (Zohuriaan-Mehr and Kabiri, 2008; Ramazani-Harandi et al., 2006), which are used in many different water absorbing applications in agriculture (Guilherme et al., 2015), in health care industry (e.g. in sanitary pads and baby diapers), in sealants and in air-fresheners (Po, 1994; Graham and Buchholz, 1998) (Fig. 2.1).

The original material, a dry powder with sugar-like particles, reaches its final swollen stage when left to react with water for a few days (2-3 days, depending on the fluid sample) (Fig. 2.1). During this period, the powder absorbs a very large quantity of water: 1 g of powder can entrap up to 200 g of water and grains swell up to 100 times their original size.

The final gel is an aqueous mixture of soft viscoelastic grains (Ramazani-Harandi et al.,

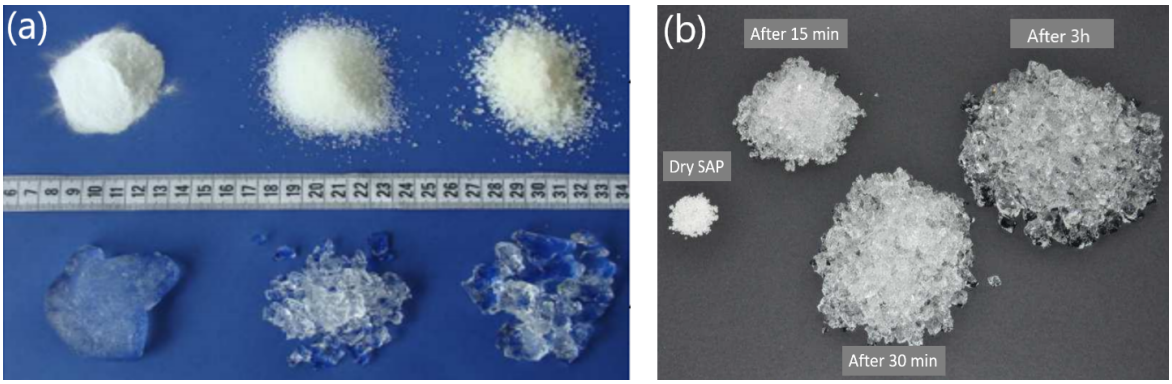

Figure 2.1: Photos modified from geosap.up.wroc.pl (Lejcuś et al., 2015). (a) Example of raw dry powder on the top and corresponding swollen gel on the bottom. Different powder sizes are obtained by grinding the original material. The swollen state is reached after absorption of the water. (b) Volume of swollen SAP during water absorption.

2006) with irregular shapes but a general homogeneous size that can be controlled by controlling the original dimension of the dry powder (Fig. 2.1a). Even though the general behaviour of this material in its swollen state is proved to combine viscoelastic (Ramazani-Harandi et al., 2006) and shear-thinning aspects (Zhang et al., 2010), the rheological properties may vary due to sample preparation and to the amount of powder and water used. Moreover, their measurement is still quite complicated as typical commercial SAP have large (up to a few millimetres) and irregular swollen particles that render classical rheological methods difficult to use (Ramazani-Harandi et al., 2006).

Depending on the initial powder mass (m_p) and mass of added water (W_{in}), grains may not be able to absorb and entrap in their structure more than a fraction of W_{in}. The water mass conservation writes:

$$W_{in} = W_{gel} + W_{free} + W_{wet} \tag{2.1}$$

where W_{gel} indicates the water absorbed by the polymer, that is the water contained inside the grains, W_{free} the free water which flows between grains and W_{wet} the water wetting the grains surface. We have measured the weight of the free water by pouring the mixture in a tea strainer and the weight of W_{wet} from the amount of absorbed water in a tissue paper. The water content of the fluid can be estimated then by three parameters, namely the the swelling factor, the total water number and the free water number.

The swelling factor is the ratio between the water absorbed by the gel and the initial amount of dry powder, W_{gel}/m_p. The maximum swelling occurs for wt% of powder between 0.45 and 0.55 (Fig. 2.2a) where powder grains swell up to around 100 times their original size, but it drops afterwards if too much powder is used to prepare the fluid sample. Given that, all the fluid samples used in experiments are obtained by letting 17.5 $\pm$ 0.1 g of dry product to react with 3.5 l of distilled water for a wt% of powder equal 0.50 in order to guarantee the maximum swelling factor. They were left to react for one night. The preparation ended by

stirring gently (200 rpm) the resulting swollen mixture for 2-3 days with an electric stirrer to remove air bubbles and to homogenize the mixture.

The total water number expresses the total weight of recovered water on the one initially added, $(W_{free}+W_{wet})/W_{in}$. For wt%=0.5 of powder, the total water in excess not caught by the polymer structure is almost 50% of the initial added water (Fig. 2.2b) that would result in a solid volume fraction for our mixture of ϕ=0.50. However, since each grain contains water, during the measurement of W_{wet}, it will release some of it on the tissue paper by capillary effect. The presence of a certain amount of mobilized water that can escape from the grain structure is also observed in grains that are under load. When we attempted to measure normal forces and penetration depth in a single SAP grain by using a microindenter, we have not been able to get any reliable measurement since slip of the grain always occurred. This occurs because, when squeezed, a grain releases a small amount of water that makes it glide. Hence, the presence of mobilized water leads to overestimate the amount of water not absorbed by the polymer structure and, in turn, to underestimate ϕ.

The rough estimate of the solid fraction is then obtained from the last parameter, the free water number, defined as W_{free}/W_{in}. Under a certain threshold of wt% of powder, it is found to increase linearly with decreasing quantity of powder present in the fluid (Fig. 2.2c). For wt%=0.5 of powder, W_{free}/W_{in} is around 0.30-0.37, leading to a solid volume fraction of $\phi \sim$ 0.63-0.70.

Experiments of a falling sphere have been carried out in six different fluids prepared at constant wt% powder equal to 0.5. The difference between them only regards the size of the grains which constitute the fluid structure: finer dry powder obtained by grinding the original material will give thinner compounds whereas for larger powders the final fluids will be made of coarser grains (Fig. 2.1).

To obtain the grains size distribution of the swollen gel samples, we analyzed several high resolution images (4288 x 2848 pixels) of a laser-illuminated vertical cross-section of the experimental tank by using Multispec, an image analysis software (Biehl and Landgrebe, 2002). The sample was stirred between each image, so that each image shows a different organization of the fluid structure. Fig. 2.6b shows an example of how the fluid structure looks like. The arrangement of the grains is easily recognizable and the sampling of each of them during the images analysis can be automatically or manually done directly from black and white images without needing more complex adjustments. Once the outline of the grains is defined from the image, the grain surface comes by counting the number of pixels of which it is composed. We describe each grain by the equivalent diameter, d_g, of a disk with the same area as the measured surface. Fig.2.3 presents the measured 2-D grains size distributions, $h(d)$, and their characteristics are given in Table 2.1. The distributions can be fitted by normal distributions (Fig.2.3a). To infer the real 3-D parent size distribution from the the 2-D measurements is a tricky problem, because it is under-determined if the shape of the particles is unknown. Assuming that the gel grains are spheres, we estimate the numerical density histograms of these spheres diameters, $h(d^*)$, from $h(d)$, using the software StripStar

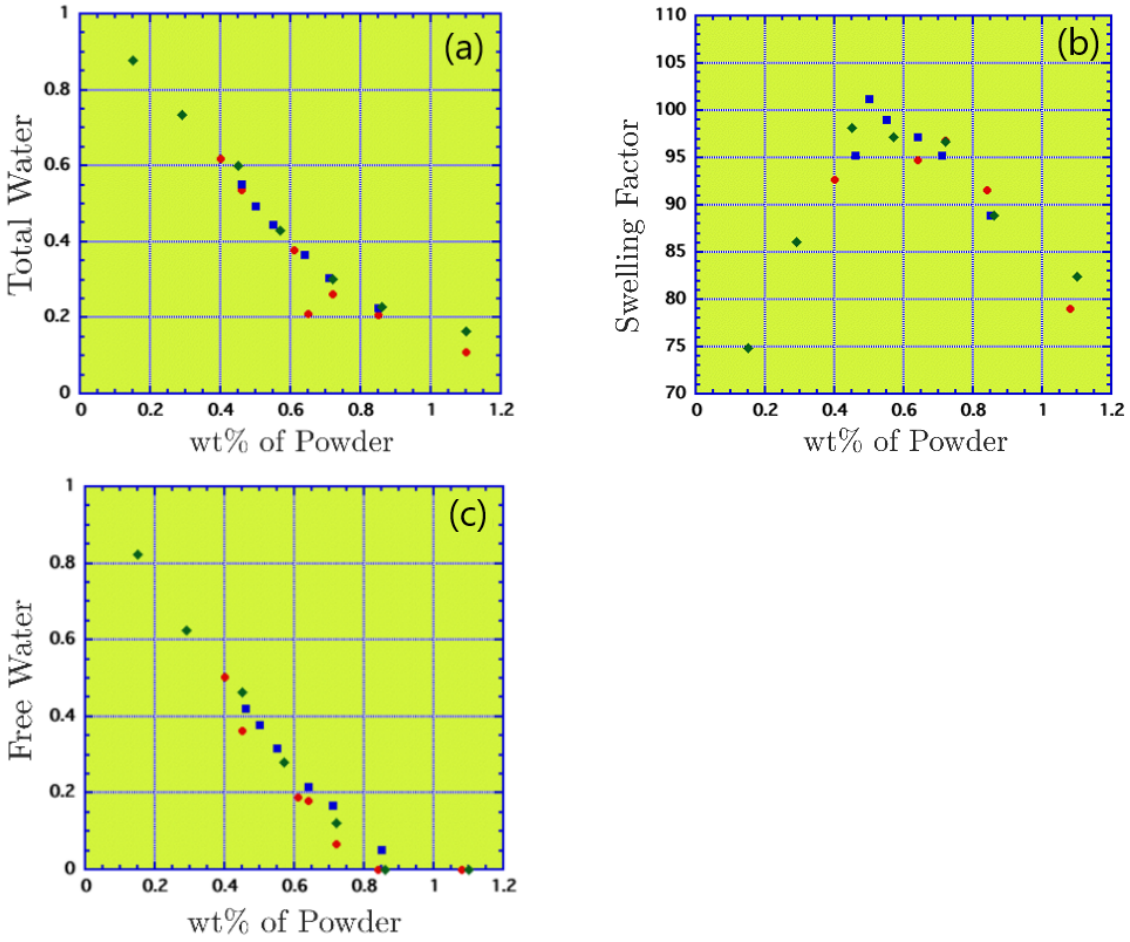

Figure 2.2: Parameters that define the water content as function of powder mass fraction. Symbols refer to fluid samples prepared at different times. Samples are here obtained mixing the same dry powder (i.e. same powder size) with different amounts of water. (a) Swelling factor. (b) Total water number. (c) Free water number. (Courtesy of Prof. Kei Kurita)

name	Mean d_g (mm)	std (mm)	Median (mm)	Max d_g (mm)	Mean d_g^* (mm)
Gel A	1.4	0.3	1.4	2.3	1.4
Gel B	2.1	0.5	2.1	3.5	2.2
Gel C	3.3	0.9	3.0	5.8	3.4
Gel D	4.8	1.2	4.5	9.5	4.9
Gel E	5.7	1.2	5.5	9.6	5.8
Gel F	6.2	1.6	5.7	10.6	6.4

Table 2.1: Characteristics of the gels, obtained from image analysis: the mean grain diameter d_g, the standard deviation (std), the median and the maximum diameter for the 2-D distributions of circles; and the mean diameter d_g^* for the calculated 3-D grain size distributions.

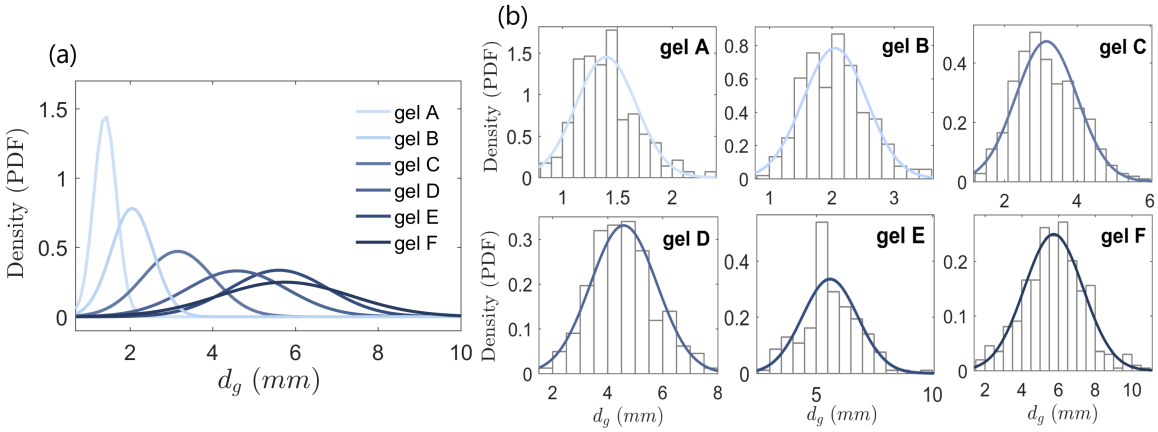

Figure 2.3: (a) Plot of probability density functions (PDF) of 2-D grain diameters, d_g, for all gels. Lines indicate a normal distribution. For the grain diameter we refer to the equivalent diameter of a disk having the same area as the measured grain surface. (b) Histogram representation of 2-D grain size with a normal distribution curve on top for each gel.

(Heilbronner and Barrett, 2013) (Fig.2.4). To obtain the equivalent diameter of spheres, the measured $h(d)$ is compared to an ideal distribution $h_I(d)$ of disks obtained from an known distribution $h_I(d^*)$ of uniform distributed spheres of diameter d^*. The software derives the distribution of $h(d^*)$ by creating a proportionally higher or lower number of spheres in it, depending on the difference between the ideal distribution $h_I(d)$ and the measured distribution $h(d)$ (for details, see Heilbronner and Barrett (2013); Heilbronner and Bruhn (1998)). Table 2.1 shows that the 3-D estimates are quite close to the 2D-measurements. In what follows, we take as the "gel grain size" the mean value of the 2-D measurements for each gel.

In similar way, we analyzed the grains aspect ratio β, where $\beta = MajorAxis/MinorAxis$. In the case of our SAP fluids, grains do not have high aspect ratios (i.e. grains are not fibers and they do not have any others very elongated shapes) even though they are not perfectly spherical (Fig. 2.5). The aspect ratio is found to be a random variable and the histograms

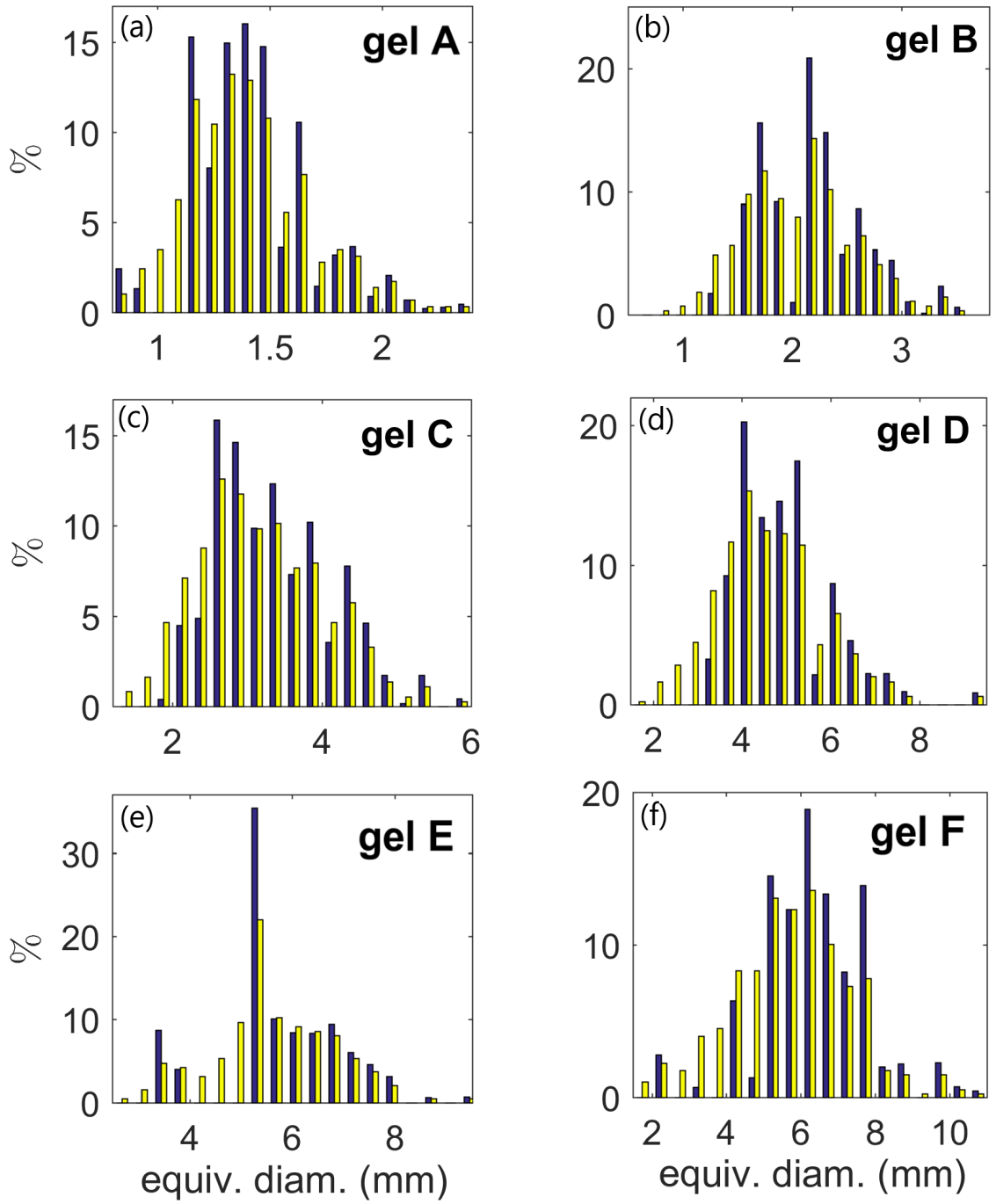

Figure 2.4: Histograms of measured 2-D grain size (yellow) and of calculated 3-D grain size (blue) for the gels used in the experiments: gel A (a), gel B (b), gel C (c), gel D (d), gel E (e) and gel F (f).

are fitted both by the log-normal distribution and the generalized-extreme-value distribution in Fig. 2.5. The log-normal distribution is a probability distribution of a random variable, the logarithm of which is normally distributed. In this case, for the fit of all gels together we found an arithmetical average of 1.81 and an geometrical one of 1.75. For a log-normal distribution, the latter average is the more appropriate to use. However, by comparison, a generalized-extreme-value (GEV) distribution seems to be a more appropriate probability density functions (PDF) of the aspect ratio. The GEV distribution unites three simpler distributions (i.e. the Gumbel, Frechet and Weibull distributions) into a single form to permit a continuous range of possible shapes. It is usually used to model the smallest or largest values among a large set of identically distributed, independent random values. Examples are the particle aspect ratio of concrete material (Ruan et al., 2019), the area of inclusions in steel (Sakaguchi et al., 2020) and size of other defects in specific alloys (Tiryakioğlu, 2008). The PDF of GEV writes

$$F(x;\mu,\sigma,k) = \frac{1}{\sigma}\exp\left[-\left\{1+k\left(\frac{x-\mu}{\sigma}\right)\right\}^{-\frac{1}{k}}\right]\left\{1+k\left(\frac{x-\mu}{\sigma}\right)\right\}^{-1-\frac{1}{k}}, \tag{2.2}$$

where the three parameters k, μ and σ represent a shape, location, and scale of the distribution function, respectively. For the fit in Fig. 2.5a they are k=0.0488, μ=1.5710 and σ=0.3863. For the generalized-extreme-value distribution in Fig. 2.5a the mean aspect ratio is 1.81 with a variance of 0.28. Unless otherwise indicated, in what follows we will refer to the latter as the mean aspect ratio. Grain aspect ratio is also found to be independent of the gel size since we do not see any significant variation even between the thinner and the coarser samples (Fig. 2.5b).

An estimation of the grain aspect ratio is vital because, in addition to solid fraction, the particles shape also affects the rheology of a suspension (Mader et al., 2013; Mueller et al., 2009). Particles aspect ratio controls the maximum packing fraction ϕ_m which, for smooth particles, writes

$$\phi_m = 0.656\exp\left[-\frac{(\log_{10}\beta)^2}{2.33}\right]. \tag{2.3}$$

For an aspect ratio β=1.81 we found ϕ_m=0.638, very close to the classical close packing density for hard spheres ϕ_c=0.64 (e.g. Seth et al., 2011). With the solid volume fraction estimated above, i.e. ϕ ∼0.63-0.70, our gels are above the limit of ϕ_m, meaning that grains are deformed and compressed together (that is, they overlap each others).

2.2 Experimental apparatus

We analyzed the free fall of a sphere through SAP within a cylindrical Plexiglas vessel of height H=50 cm and width D=10 cm filled with approximately 3.5 liters of fluid and placed in a rectangular tank filled with water (Fig. 2.6a). The external tank is necessary to reduce

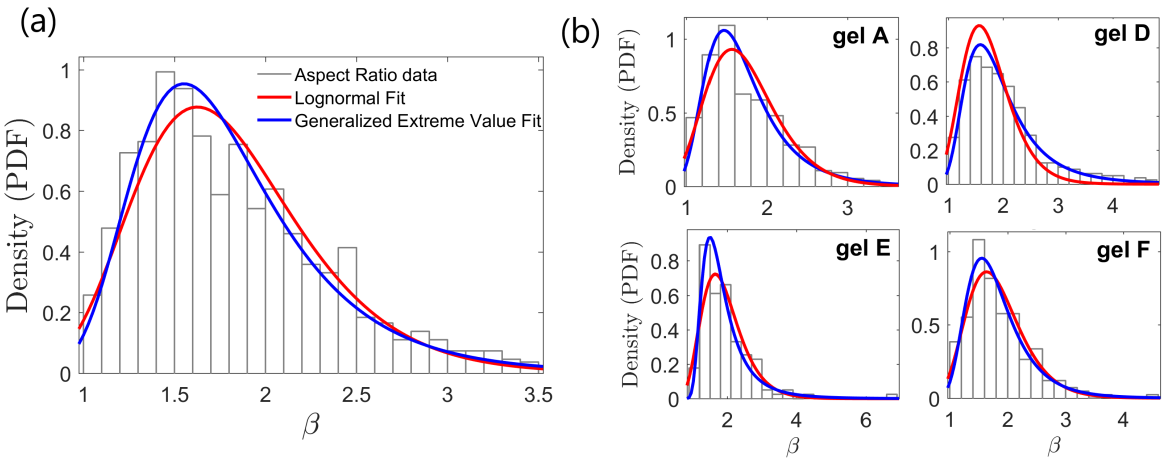

Figure 2.5: Plot of the PDF distribution of the particle aspect ratios, β. Red line indicates a lognormal fit. Blue line is the fit of a generalized extreme value (GEV) distribution. (a) Histograms for the entire data set in which aspect ratio analysis has been carried out, that is for gel A, gel D, gel E and gel F. For the GEV distribution, the mean aspect ratio is $\bar{\beta}$=1.81 with variance Var(β)=0.28. (b) Distributions for single gels. For gel A: $\bar{\beta}$=1.77; Var(β)=0.35. For gel D: $\bar{\beta}$=1.89; Var(β)=0.29. For gel E: $\bar{\beta}$=1.83; Var(β)=0.26. For gel F: $\bar{\beta}$=1.83; Var(β)=0.30.

ρ_s (kg/m^3)	d_s (mm)
14952	6.00
7980	6.00; 12.00; 14.00; 16.00; 18.00
7970	3.00; 4.00; 5.00; 7.00; 8.00; 10.00; 20.00; 22.00; 25.00
7799	6.00
7782	14.00
7621	8.00
7519	3.20
3227	6.00
2200	15.66; 15.81

Table 2.2: Spheres density ρ_s and diameter d_s.

strong optical distortions once the cylinder is illuminated laterally by a vertical 532 nm laser sheet (Fig. 2.6b). Single spheres were released by hand from the center of the fluid top surface. We used spheres of different materials and densities (from glass spheres, ρ_s=2200 kg/m^3, to tungsten spheres, ρ_s=14952 kg/m^3) and with diameters, d_s, in between 3 and 25 mm. Their characteristics are summarized in Table 2.2 and in the following sections we will indicate ρ_s and d_s case by case.

All the spheres with density of 7980 and 7970 kg/m^3 have been painted with black spray paint to avoid strong reflections, while the other spheres have been left with their original surfaces. The use of spray paint could have increased the surface roughness that in turn can affect the velocity field in the fluid around the object as well as the shape of the yielded region (Holenberg et al., 2012). However, we did not observe any discrepancies between the

painted and the bare spheres.

Before each experiment, we stirred gently the fluid to remove any possible preferential path that might have been formed during previous runs. SAP, in fact, shows some hysteresis where the fluid structure does not recover completely its original state after it has been deformed. This aspect is observed when a second sphere is dropped from the same position as the previous one without stirring the fluid in between the two runs. For identical spheres, we have always measured higher velocities for those released in second and falling through an already deformed path. Stirring the fluid between runs prevents this issue and allowed us to get reproducible velocities for identical spheres.

Motion of spheres were captured by a 25 frames-per-second video camera (Canon Legria HF S21 1080p) placed in front of the tube and perpendicularly to the laser sheet. Two different techniques of visualization have been used: shadowgraph for most of the experiments, and particle image velocimetry (PIV) for a few of them (see tables in section 2.4). Shadowgraph revels non-uniformities in transparent media (like our SAP samples) and only requires a good light source. Movies recorded in this way are then used to obtain the velocity of the sphere. The position of the center of the sphere on each frame was determined by plotting the spatio-temporal evolution of a pixel line centered on the sphere, or by using the blob analysis method in Matlab (MathWorks, 2019). Both methods allow the derivation of the local vertical velocity of the sphere through time. The blob analysis also provides the measurements of the horizontal position and velocity of the sphere. PIV, instead, is used to calculate the velocity field of the fluid around the sphere and requires the setup to be laterally illuminated by the laser sheet. We use the software DaVis from LaVision. Here frames are divided with a grid in several small windows and in each grid-window, the position of the maximum of light intensity is compared between n subsequent frames. In our case we usually have n=2 except when motion was very slow and the comparison of images was made every 5 frames. Thus, the displacement field (pixels) is calculated by cross correlation and is subsequently converted in velocity field (mm/s) by knowing both pixel length and the time in between frames. More details about parameters used during PIV analysis are given in the sections where the results are discussed.

2.3 Control case with a Newtonian fluid

As a first step, it is useful to test the reproducibility and the accuracy of the experimental techniques and the possible limits arising from the dimension of our setup. To do so, we measured the terminal velocities, v_y, of spheres settling in a Newtonian fluid, namely glucose syrup (Glucor 60/80).

To reduce the high viscosity of the original syrup, we mixed 3.5 l of it with 250 g of distillate water at T=60 °C by using a magnetic stirrer. Subsequently, we used an Anton Paan MCR501 rheometer to measure the fluid viscosity (Fig. 2.7a). We used a cone-plate geometry and also a Couette-cylinder geometry. The final viscosity is taken by averaging the

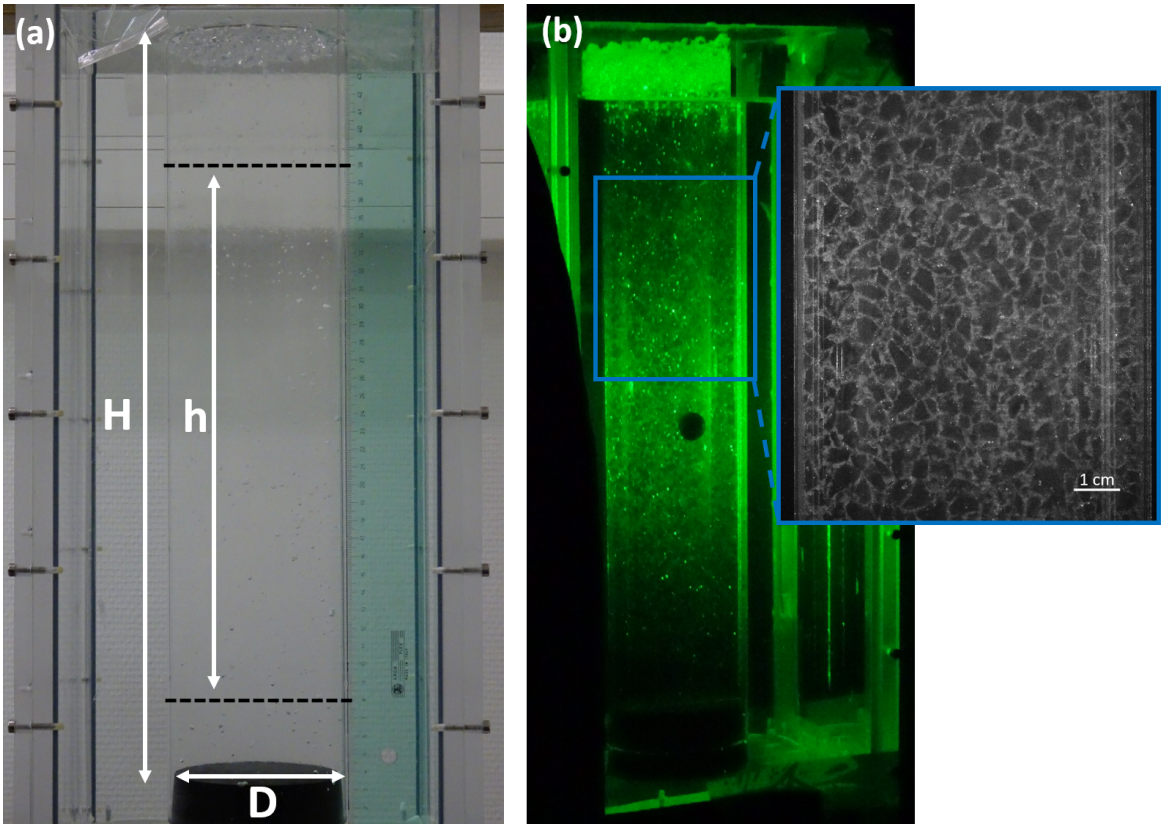

Figure 2.6: Experimental set up. (a) Cylindrical vessel of height H=50 cm and diameter D=10 cm. Videos are recorded in the tube section between the two black dotted lines (h). (b) Set up illuminated by a laser sheet. The zoomed box shows the fluid structure: in black the SAP grains and in bright color the water film between them.

values at the plateau for the Couette-cylinder geometry. For the case shown in Fig. 2.7a, measurements at ambiant temperature T=15.8 °C lead to a viscosity of 12.20±0.49 Pa.s. Both density and viscosity are temperature-dependent. Fig. 2.7b shows the exponential temperature dependence of the viscosity where data fit $\eta(T) = a\, e^{bT}$, with a=77.35 and b=-0.1198. Unfortunately, due to technical issues we had no temperature control in laboratory room. The temperature at which experiments were carried out differs a little from the one of Fig. 2.7a and is around 15.2 °C. Given the impossibility to keep the temperature completely under control during all experiments, small variations of it (around 0.2-0.3 °C) are expected. At temperature of T=15.2±0.3 °C the measured fluid viscosity is η_{syrup}=12.33±0.65 Pa.s and its density is ρ_{syrup}=1394.66 kg/m^3 (measured with an Anton Paar DMA 5000 densimeter).

Spheres settling in a Newtonian fluid at low Reynolds number reach a terminal velocity given by the Stokes velocity

$$v_{Stokes} = \frac{2}{9}\frac{R_s^2(\rho_s - \rho_{fluid})g}{\eta}, \tag{2.4}$$

where R_s and ρ_s are radius and density of the sphere, respectively, and g the acceleration due to gravity. In Fig. 2.7c we plot the velocities measured for spheres of same density and diameters in between 3 and 18 mm. Larger spheres are subjected to wall effects and in this case the sphere terminal velocity can be corrected by a coefficient that writes

$$K_1^{-1} = 1 + \alpha_1\left(\frac{d_s}{D}\right) + \alpha_2\left(\frac{d_s}{D}\right)^3 + \alpha_3\left(\frac{d_s}{D}\right)^5, \tag{2.5}$$

where $\alpha_1 = -2.104443$, $\alpha_2 = 2.08877$, $\alpha_3 = -0.94813$ and D is the tube diameter (Happel and Howard, 2012).

Experiments we carried out in syrup show that the measured settling velocities are in good agreement with the corresponding corrected Stokes velocities, that is $v_y/(v_{Stokes}K_1^{-1}) = 1$ (Fig. 2.7c), ensuring that our measurement system is accurate.

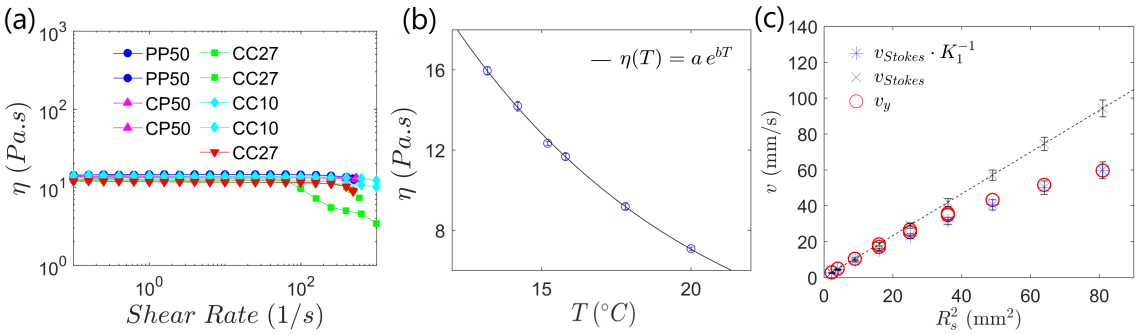

Figure 2.7: Newtonian case. (a) Measurement of syrup viscosity at T=15.8 °C. Different lines refer to different rheometer geometries (PP: plate-plate; CP: cone-plate; CC: Couette cylinder). (b) Syrup viscosity as function of temperature. Black line is the exponential fit for a=77.35 and b=-0.1198. (c) Measured terminal velocities, v_y, in syrup (circles) and Stokes velocities, v_{Stokes}, (crosses and dashed line) as function of spheres squared radius, R_s^2. Uncertainties for Stokes velocities come from the uncertainties in determining the syrup viscosity whereas the error for v_y is 0.25 mm/s, smaller than the symbols. Star symbols are the ideal velocities considering the wall correction, eq. (2.5).

2.4 Tables of experiments

We carried out and analyzed in total 99 experiments. In five of them we also measured the fluid velocity field with PIV (as indicated by the label "PIV" in the following tables). Almost every experiment was duplicated to test reproducibility. Following the definition given for the dimensionless numbers in the Introduction, the Reynolds number, Re, is here always small. It ranges in between 10 and 10^{-4} but for those relevant experiments described in next chapters is always less than 1. The Bingham number, Bi, is between 10 and 10^{-2}. As it will be discussed later, for experiments in the logarithmic regime, a steady-state velocity is never reached. Instead, it progressively decreases until the sphere stops. This would result in Bi=0. However, we report anyway the average velocity within the interval of depth h for this case whereas we report v=0 for those cases where the sphere gets stuck or never moves. The Yield number Y (and consequently its reverse, Y_{inv}=$1/Y$), is found in between 5x10^{-1} and 5x10^{-3}. The Deborah number De is defined in section 3.3. At given gel properties, it depends on the sphere diameter and density. It ranges between 10 and 10^{-1} and its largest values are for the large spheres.

Below is the list of all experiments together with relevant parameters needed for the discussion in the next sections. Table's columns refer to: sphere's diameter, d_s; density difference between sphere and fluid, $\Delta\rho$; average sphere falling velocity, v, and standard deviation, *std*; Reynolds number; Bingham number; Yield number and its reverse; Deborah number; the motion regime observed and whether PIV has been carried out.

Table 2.3: Experiments carried out in gel A.

d_s (mm)	$\Delta\rho$ (kg/m^3)	v (mm/s)	std (mm/s)	Re	Bi	Y	Y_{inv}	De	$Regime$	
18	6980	5.40x10^{2}	3.11x10^{1}	6.31	4.48x10^{-2}	5.04x10^{-3}	1.98x10^{2}	1.19x10^{1}	linear	
16	6980	4.77x10^{2}	2.61x10^{1}	4.94	4.49x10^{-2}	5.67x10^{-3}	1.76x10^{2}	1.06x10^{1}	linear	
14	6980	2.53x10^{2}	2.34x10^{1}	1.79	5.77x10^{-2}	6.48x10^{-3}	1.54x10^{2}	9.26	linear	
14	6980	1.78x10^{2}	3.35x10^{1}	1.05	6.88x10^{-2}	6.48x10^{-3}	1.54x10^{2}	9.26	LOG	
12	6980	1.10x10^{2}	7.49	4.72x10^{-1}	8.11x10^{-2}	7.56x10^{-3}	1.32x10^{2}	7.94	linear	
12	6980	1.41x10^{2}	2.50x10^{1}	6.85x10^{-1}	7.16x10^{-2}	7.56x10^{-3}	1.32x10^{2}	7.94	irregular	
10	6970	9.68x10^{1}	1.70x10^{1}	3.57x10^{-1}	7.88x10^{-2}	9.08x10^{-3}	1.10x10^{2}	6.61	LOG	
10	6970	6.39x10^{1}	3.45	1.91x10^{-1}	9.70x10^{-2}	9.08x10^{-3}	1.10x10^{2}	6.61	linear	
8	6970	4.76x10^{1}	8.00	1.10x10^{-1}	1.01x10^{-1}	1.14x10^{-2}	8.81x10^{1}	5.29	irregular	
8	6970	5.68x10^{1}	4.24	1.43x10^{-1}	9.20x10^{-2}	1.14x10^{-2}	8.81x10^{1}	5.29	linear	PIV
8	6970	3.88x10^{1}	5.76	8.10x10^{-2}	1.11x10^{-1}	1.14x10^{-2}	8.81x10^{1}	5.29	linear	
7	6970	3.07x10^{1}	4.59	5.33x10^{-2}	1.17x10^{-1}	1.30x10^{-2}	7.71x10^{1}	4.62	linear	
7	6970	3.83x10^{1}	5.21	7.44x10^{-2}	1.05x10^{-1}	1.30x10^{-2}	7.71x10^{1}	4.62	linear	
6	6980	2.44x10^{1}	3.57	3.51x10^{-2}	1.22x10^{-1}	1.51x10^{-2}	6.62x10^{1}	3.97	linear	
6	6980	2.27x10^{1}	3.93	3.14x10^{-2}	1.26x10^{-1}	1.51x10^{-2}	6.62x10^{1}	3.97	irregular	
5	6970	1.12x10^{1}	2.64	9.93x10^{-3}	1.64x10^{-1}	1.82x10^{-2}	5.51x10^{1}	3.30	irregular	
5	6970	8.69	2.20	6.78x10^{-3}	1.86x10^{-1}	1.82x10^{-2}	5.51x10^{1}	3.30	LOG	
4	6970	5.15	1.69	2.77x10^{-3}	2.16x10^{-1}	2.27x10^{-2}	4.40x10^{1}	2.64	irregular	
4	6970	4.64	1.54	2.37x10^{-3}	2.28x10^{-1}	2.27x10^{-2}	4.40x10^{1}	2.64	irregular	
3	6970	9.54x10^{-1}	8.08x10^{-1}	1.91x10^{-4}	4.35x10^{-1}	3.03x10^{-2}	3.30x10^{1}	1.98	stop&go	
3	6970	1.80	1.38	4.98x10^{-4}	3.16x10^{-1}	3.03x10^{-2}	3.30x10^{1}	1.98	LOG	
15.66	1200	5.71	1.06x10^{1}	6.40x10^{-3}	4.06x10^{-1}	3.37x10^{-2}	2.97x10^{1}	1.78	LOG	
15.81	1200	5.05	1.57x10^{1}	5.35x10^{-3}	4.34x10^{-1}	3.34x10^{-2}	3.00x10^{1}	1.80	LOG	

Table 2.4: Experiments carried out in gel B.

d_s (mm)	$\Delta\rho$ (kg/m^3)	v (mm/s)	std (mm/s)	Re	Bi	Y	Y_{inv}	De	$Regime$
8	6621	$4.08\text{x}10^{1}$	3.59	$9.27\text{x}10^{-2}$	$1.60\text{x}10^{-1}$	$1.66\text{x}10^{-2}$	$6.01\text{x}10^{1}$	3.61	linear
3.2	6519	1.49	1.03	$4.09\text{x}10^{-4}$	$5.31\text{x}10^{-1}$	$4.22\text{x}10^{-2}$	$2.37\text{x}10^{1}$	1.42	LOG
3.2	6519	1.71	$9.58\text{x}10^{-1}$	$5.03\text{x}10^{-4}$	$4.96\text{x}10^{-1}$	$4.22\text{x}10^{-2}$	$2.37\text{x}10^{1}$	1.42	irregular
3.2	6519	1.71	$9.81\text{x}10^{-1}$	$5.02\text{x}10^{-4}$	$4.96\text{x}10^{-1}$	$4.22\text{x}10^{-2}$	$2.37\text{x}10^{1}$	1.42	irregular
3.2	6519	1.41	$8.48\text{x}10^{-1}$	$3.77\text{x}10^{-4}$	$5.46\text{x}10^{-1}$	$4.22\text{x}10^{-2}$	$2.37\text{x}10^{1}$	1.42	irregular
3.2	6519	2.22	1.46	$7.47\text{x}10^{-4}$	$4.34\text{x}10^{-1}$	$4.22\text{x}10^{-2}$	$2.37\text{x}10^{1}$	1.42	LOG
3.2	6519	1.79	1.09	$5.39\text{x}10^{-4}$	$4.84\text{x}10^{-1}$	$4.22\text{x}10^{-2}$	$2.37\text{x}10^{1}$	1.42	irregular
3.2	6519	1.68	$9.59\text{x}10^{-1}$	$4.91\text{x}10^{-4}$	$5.00\text{x}10^{-1}$	$4.22\text{x}10^{-2}$	$2.37\text{x}10^{1}$	1.42	irregular

Table 2.5: Experiments carried out in gel F.

d_s (mm)	$\Delta\rho$ (kg/m^3)	v (mm/s)	std (mm/s)	Re	Bi	Y	Y_{inv}	De	$Regime$	
19	6869	$2.14\text{x}10^{1}$	2.17	$2.02\text{x}10^{-2}$	1.52	$8.06\text{x}10^{-2}$	$1.24\text{x}10^{1}$	$7.45\text{x}10^{-1}$	linear	PIV
19	6869	$1.77\text{x}10^{1}$	6.76	$1.52\text{x}10^{-2}$	1.67	$8.06\text{x}10^{-2}$	$1.24\text{x}10^{1}$	$7.45\text{x}10^{-1}$	linear	
16	6869	7.57	3.85	$3.91\text{x}10^{-3}$	2.35	$9.57\text{x}10^{-2}$	$1.05\text{x}10^{1}$	$6.27\text{x}10^{-1}$	linear	
14	6782	1.96	1.06	$4.82\text{x}10^{-4}$	4.31	$1.11\text{x}10^{-1}$	9.03	$5.42\text{x}10^{-1}$	irregular	

Table 2.6: Experiments carried out in gel C.

d_s (mm)	$\Delta\rho$ (kg/m^3)	v (mm/s)	std (mm/s)	Re	Bi	Y	Y_{inv}	De	$Regime$	
22	6970	$4.97\text{x}10^{2}$	$4.22\text{x}10^{1}$	4.58	$7.03\text{x}10^{-2}$	$7.56\text{x}10^{-3}$	$1.32\text{x}10^{2}$	7.94	linear	
20	6970	$3.98\text{x}10^{2}$	$4.94\text{x}10^{1}$	3.13	$7.50\text{x}10^{-2}$	$8.31\text{x}10^{-3}$	$1.20\text{x}10^{2}$	7.22	linear	
20	6970	$3.87\text{x}10^{2}$	$4.70\text{x}10^{1}$	3.00	$7.60\text{x}10^{-2}$	$8.31\text{x}10^{-3}$	$1.20\text{x}10^{2}$	7.22	linear	
18	6980	$2.60\text{x}10^{2}$	$5.31\text{x}10^{1}$	1.57	$8.79\text{x}10^{-2}$	$9.22\text{x}10^{-3}$	$1.08\text{x}10^{2}$	6.50	LOG	
18	6980	$3.61\text{x}10^{2}$	$8.41\text{x}10^{1}$	2.57	$7.46\text{x}10^{-2}$	$9.22\text{x}10^{-3}$	$1.08\text{x}10^{2}$	6.50	LOG	
16	6980	$2.44\text{x}10^{2}$	$4.17\text{x}10^{1}$	1.34	$8.57\text{x}10^{-2}$	$1.04\text{x}10^{-2}$	$9.64\text{x}10^{1}$	5.78	LOG	
16	6980	$2.20\text{x}10^{2}$	$3.00\text{x}10^{1}$	1.15	$9.01\text{x}10^{-2}$	$1.04\text{x}10^{-2}$	$9.64\text{x}10^{1}$	5.78	linear	PIV
16	6980	$2.05\text{x}10^{2}$	$5.15\text{x}10^{1}$	1.03	$9.34\text{x}10^{-2}$	$1.04\text{x}10^{-2}$	$9.64\text{x}10^{1}$	5.78	LOG	
14	6980	$1.39\text{x}10^{2}$	$1.49\text{x}10^{1}$	$5.42\text{x}10^{-1}$	$1.06\text{x}10^{-1}$	$1.19\text{x}10^{-2}$	$8.43\text{x}10^{1}$	5.06	linear	
14	6980	$1.49\text{x}10^{2}$	$4.18\text{x}10^{1}$	$6.01\text{x}10^{-1}$	$1.02\text{x}10^{-1}$	$1.19\text{x}10^{-2}$	$8.43\text{x}10^{1}$	5.06	LOG	
12	6980	$1.12\text{x}10^{2}$	$2.94\text{x}10^{1}$	$3.62\text{x}10^{-1}$	$1.09\text{x}10^{-1}$	$1.38\text{x}10^{-2}$	$7.23\text{x}10^{1}$	4.34	LOG	
12	6980	$9.28\text{x}10^{1}$	$1.75\text{x}10^{1}$	$2.73\text{x}10^{-1}$	$1.20\text{x}10^{-1}$	$1.38\text{x}10^{-2}$	$7.23\text{x}10^{1}$	4.34	irregular	
10	6970	$4.37\text{x}10^{1}$	8.58	$8.06\text{x}10^{-2}$	$1.60\text{x}10^{-1}$	$1.66\text{x}10^{-2}$	$6.01\text{x}10^{1}$	3.61	irregular	
10	6970	$4.07\text{x}10^{1}$	8.12	$7.25\text{x}10^{-2}$	$1.66\text{x}10^{-1}$	$1.66\text{x}10^{-2}$	$6.01\text{x}10^{1}$	3.61	irregular	
8	6970	$2.17\text{x}10^{1}$	6.87	$2.51\text{x}10^{-2}$	$2.03\text{x}10^{-1}$	$2.08\text{x}10^{-2}$	$4.81\text{x}10^{1}$	2.89	irregular	
8	6970	$2.20\text{x}10^{1}$	9.86	$2.57\text{x}10^{-2}$	$2.02\text{x}10^{-1}$	$2.08\text{x}10^{-2}$	$4.81\text{x}10^{1}$	2.89	LOG	
7	6970	$1.34\text{x}10^{1}$	6.48	$1.14\text{x}10^{-2}$	$2.42\text{x}10^{-1}$	$2.38\text{x}10^{-2}$	$4.21\text{x}10^{1}$	2.53	LOG	
7	6970	$1.48\text{x}10^{1}$	7.51	$1.33\text{x}10^{-2}$	$2.30\text{x}10^{-1}$	$2.38\text{x}10^{-2}$	$4.21\text{x}10^{1}$	2.53	LOG	
6	6980	5.03	3.67	$2.44\text{x}10^{-3}$	$3.65\text{x}10^{-1}$	$2.77\text{x}10^{-2}$	$3.61\text{x}10^{1}$	2.17	LOG	
6	6980	7.48	4.26	$4.42\text{x}10^{-3}$	$2.99\text{x}10^{-1}$	$2.77\text{x}10^{-2}$	$3.61\text{x}10^{1}$	2.17	LOG	
5	6970	2.45	2.66	$7.58\text{x}10^{-4}$	$4.77\text{x}10^{-1}$	$3.33\text{x}10^{-2}$	$3.01\text{x}10^{1}$	1.80	stop&go	
5	6970	3.62	2.71	$1.36\text{x}10^{-3}$	$3.93\text{x}10^{-1}$	$3.33\text{x}10^{-2}$	$3.01\text{x}10^{1}$	1.80	stop&go	
4	6970	0	-	-	-	$4.16\text{x}10^{-2}$	$2.41\text{x}10^{1}$	1.44	no motion	
15.81	1200	1.72	$7.04\text{x}10^{-1}$	$7.91\text{x}10^{-4}$	1.01	$6.11\text{x}10^{-2}$	$1.64\text{x}10^{1}$	$9.82\text{x}10^{-1}$	linear	
15.66	1200	1.40	1.19	$5.77\text{x}10^{-4}$	1.12	$6.17\text{x}10^{-2}$	$1.62\text{x}10^{1}$	$9.73\text{x}10^{-1}$	linear	

Table 2.7: Experiments carried out in gel D.

d_s (mm)	$\Delta\rho$ (kg/m^3)	v (mm/s)	std (mm/s)	Re	Bi	Y	Y_{inv}	De	$Regime$
25	6970	5.77x10^{2}	1.31x10^{1}	6.11	1.41x10^{-1}	1.35x10^{-2}	7.43x10^{1}	4.46	linear
20	6970	3.45x10^{2}	4.02	2.53	1.63x10^{-1}	1.68x10^{-2}	5.94x10^{1}	3.57	linear
18	6980	2.52x10^{2}	2.25x10^{1}	1.50	1.81x10^{-1}	1.87x10^{-2}	5.36x10^{1}	3.21	linear
16	6980	1.92x10^{2}	1.50x10^{1}	9.37x10^{-1}	1.95x10^{-1}	2.10x10^{-2}	4.76x10^{1}	2.86	linear
14	6980	1.30x10^{2}	2.66x10^{1}	4.87x10^{-1}	2.22x10^{-1}	2.40x10^{-2}	4.17x10^{1}	2.50	irregular
14	6980	1.10x10^{2}	2.88x10^{1}	3.78x10^{-1}	2.42x10^{-1}	2.40x10^{-2}	4.17x10^{1}	2.50	irregular
12	6980	7.33x10^{1}	1.86x10^{1}	1.92x10^{-1}	2.73x10^{-1}	2.80x10^{-2}	3.57x10^{1}	2.14	irregular
12	6980	7.47x10^{1}	2.33x10^{1}	1.97x10^{-1}	2.71x10^{-1}	2.80x10^{-2}	3.57x10^{1}	2.14	LOG
10	6970	3.35x10^{1}	1.04x10^{1}	5.41x10^{-2}	3.69x10^{-1}	3.37x10^{-2}	2.97x10^{1}	1.78	irregular
10	6970	3.67x10^{1}	1.26x10^{1}	6.20x10^{-2}	3.53x10^{-1}	3.37x10^{-2}	2.97x10^{1}	1.78	irregular
8	6970	1.04x10^{1}	6.16	8.37x10^{-3}	5.92x10^{-1}	4.21x10^{-2}	2.38x10^{1}	1.43	irregular
8	6970	1.65x10^{1}	9.53	1.67x10^{-2}	4.70x10^{-1}	4.21x10^{-2}	2.38x10^{1}	1.43	irregular
7	6970	3.98	5.09	1.85x10^{-3}	8.97x10^{-1}	4.81x10^{-2}	2.08x10^{1}	1.25	stop&go
7	6970	6.86	5.06	4.18x10^{-3}	6.83x10^{-1}	4.81x10^{-2}	2.08x10^{1}	1.25	irregular
5	6970	5.11x10^{-1}	1.29	7.21x10^{-5}	2.11	6.73x10^{-2}	1.49x10^{1}	8.91x10^{-1}	stop&go
6	13952	2.96x10^{1}	2.00x10^{1}	3.47x10^{-2}	3.04x10^{-1}	2.80x10^{-2}	3.57x10^{1}	2.14	irregular
6	13952	2.92x10^{1}	1.47x10^{1}	3.40x10^{-2}	3.06x10^{-1}	2.80x10^{-2}	3.57x10^{1}	2.14	irregular
6	6799	2.47	4.23	8.36x10^{-4}	1.05	5.75x10^{-2}	1.74x10^{1}	1.04	stop&go
6	6799	2.07	3.74	6.41x10^{-4}	1.15	5.75x10^{-2}	1.74x10^{1}	1.04	stop&go
4	6970	0	-	-	-	8.41x10^{-2}	1.19x10^{1}	7.13x10^{-1}	no motion
6	2227	0	-	-	-	1.76x10^{-1}	5.70	3.42x10^{-1}	no motion
15.81	1200	6.36x10^{-1}	3.83x10^{2}	1.78x10^{-4}	3.37	1.24x10^{-1}	8.09	4.85x10^{-1}	LOG
15.66	1200	6.52x10^{-1}	3.66x10^{2}	1.84x10^{-4}	3.31	1.25x10^{-1}	8.01	4.81x10^{-1}	LOG

Table 2.8: Experiments carried out in gel E.

d_s (mm)	$\Delta\rho$ (kg/m^3)	v (mm/s)	std (mm/s)	Re	Bi	Y	Y_{inv}	De	$Regime$	
30	6970	$2.12\text{x}10^{2}$	$2.04\text{x}10^{1}$	$8.67\text{x}10^{-1}$	$5.69\text{x}10^{-1}$	$4.33\text{x}10^{-2}$	$2.31\text{x}10^{1}$	1.38	linear	
25	6980	$1.44\text{x}10^{2}$	8.45	$4.40\text{x}10^{-1}$	$6.32\text{x}10^{-1}$	$5.19\text{x}10^{-2}$	$1.93\text{x}10^{1}$	1.16	linear	
22	6970	$5.75\text{x}10^{1}$	9.67	$1.04\text{x}10^{-1}$	$9.37\text{x}10^{-1}$	$5.91\text{x}10^{-2}$	$1.69\text{x}10^{1}$	1.02	irregular	
20	6970	$6.60\text{x}10^{1}$	8.80	$1.23\text{x}10^{-1}$	$8.34\text{x}10^{-1}$	$6.50\text{x}10^{-2}$	$1.54\text{x}10^{1}$	$9.23\text{x}10^{-1}$	linear	PIV
20	6970	$6.17\text{x}10^{1}$	$1.44\text{x}10^{1}$	$1.11\text{x}10^{-1}$	$8.63\text{x}10^{-1}$	$6.50\text{x}10^{-2}$	$1.54\text{x}10^{1}$	$9.23\text{x}10^{-1}$	irregular	
18	6980	$2.73\text{x}10^{1}$	9.78	$3.09\text{x}10^{-2}$	1.23	$7.21\text{x}10^{-2}$	$1.39\text{x}10^{1}$	$8.32\text{x}10^{-1}$	irregular	
18	6980	$3.19\text{x}10^{1}$	$1.14\text{x}10^{1}$	$3.90\text{x}10^{-2}$	1.14	$7.21\text{x}10^{-2}$	$1.39\text{x}10^{1}$	$8.32\text{x}10^{-1}$	LOG	
16	6980	$1.43\text{x}10^{1}$	6.05	$1.11\text{x}10^{-2}$	1.60	$8.11\text{x}10^{-2}$	$1.23\text{x}10^{1}$	$7.40\text{x}10^{-1}$	irregular	
16	6980	$1.45\text{x}10^{1}$	6.33	$1.13\text{x}10^{-2}$	1.59	$8.11\text{x}10^{-2}$	$1.23\text{x}10^{1}$	$7.40\text{x}10^{-1}$	LOG	
14	6980	5.16	4.63	$2.24\text{x}10^{-3}$	2.49	$9.27\text{x}10^{-2}$	$1.08\text{x}10^{1}$	$6.47\text{x}10^{-1}$	stop&go	
14	6980	5.24	3.91	$2.29\text{x}10^{-3}$	2.48	$9.27\text{x}10^{-2}$	$1.08\text{x}10^{1}$	$6.47\text{x}10^{-1}$	LOG	
12	6980	$4.01\text{x}10^{-1}$	1.34	$4.49\text{x}10^{-5}$	8.29	$1.08\text{x}10^{-1}$	9.24E+00	$5.55\text{x}10^{-1}$	log-stop&go	
12	6980	1.34	1.90	$2.75\text{x}10^{-4}$	4.53	$1.08\text{x}10^{-1}$	9.24	$5.55\text{x}10^{-1}$	stop&go	PIV
12	6980	$5.27\text{x}10^{-1}$	1.04	$6.77\text{x}10^{-5}$	7.23	$1.08\text{x}10^{-1}$	9.24	$5.55\text{x}10^{-1}$	log-stop&go	
10	6970	0	-	-	-	$1.30\text{x}10^{-1}$	7.69	$4.62\text{x}10^{-1}$	no motion	
15.81	1200	0	-	-	-	$4.78\text{x}10^{-1}$	2.09	$1.26\text{x}10^{-1}$	no motion	

Chapter 3

Experimental results of a falling sphere in SAP

In this chapter we report the main experimental results regarding the fall of a sphere in SAP. As seen above, the complex rheology of SAP can be characterized using the free-fall of spheres of different diameters and densities. As the typical size of the gel grains was varied, there is a range where it becomes comparable to the size of the falling spheres. We observe five different regimes of motion . (1) A linear regime where the sphere has a rapid and linear fall and reaches a constant terminal velocity. (2) An irregular regime where the sphere's velocity varies around a constant value. (3) A intermittent regime where periods of no-motion and periods of irregular falls follow one another. (4) A slow fall regime where the sphere's speed progressively decreases in a logarithmic way. And (5) a no-motion regime when spheres are not heavy enough to overcome the yield stress of the mixture, or are too small compared to the grain size. We also analyze the fluid flow around the sphere and the deformation that occurs within it in order to estimate the portion of fluid that undergoes fluidization.

Besides these five regimes, we find that the effective yield stress and effective consistency of the mixtures always increase with the grain size. Moreover, the critical Yield number (Y_c) above which there is no motion decreases as the sphere to grain diameters ratio becomes smaller than 2.5. This shows the control of the fluid structure on the validity of the viscoplastic rheological model.

3.1 Motion regimes

We now move to the case where the fluid through which spheres fall is one of the SAP mixture described in the previous chapter. In Fig. 3.1 we report a selection of falling profiles in gel E and gel C (grains mean diameter d_g=5.72 mm and d_g=3.28 mm, respectively) for four spheres with same density but different diameters. The same type of plot is also showed

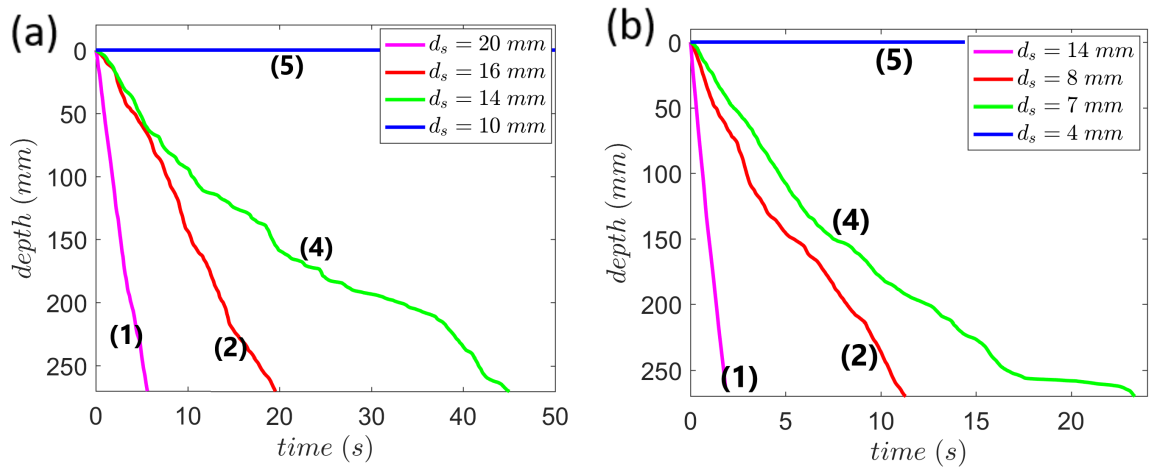

Figure 3.1: Depth of spheres settling through gel E (a) and gel C (b) as function of time. Spheres have constant density ($\Delta\rho$=6980±10 kg/m^3). Varying sphere's diameter, one can recognize the following motion regimes: linear regime (1), irregular motion superimposed to a linear trend (2), logarithmic regime (4) and no-motion (5).

in Fig. 3.2a where this time we track spheres having same size but different densities settling in gel D (d_g=4.79 mm). In both figures, the starting position value along y-axis (h=0) does not refer to the top fluid surface but to the upper limit of the camera view at which we recorded the movies (Fig. 2.6a). This is a consequence of the fact that all movies have been taken for a magnified portion of tube h=300 mm, starting from 70 mm under the surface. Camera position and therefore size of the view are kept constant for each serie of runs done within the same fluid.

For each gel, depending on the diameter and density of the sphere, we distinguish the following five regimes (Fig. 3.1 and Fig. 3.2):

1. A linear regime: rapid and linear fall in which spheres reach a constant terminal velocity.

2. An irregular regime superimposed to a linear one where spheres never stop during their way down (v_y >0) but their local velocity fluctuates around a constant value.

3. A intermittent regime: another irregular regime but here periods of no-motion, where the sphere's vertical velocity goes to zero, and periods of irregular falls follow one another (see also Fig. 3.3 that highlights this specific regime in other gels).

4. A logarithmic regime where the sphere's speed progressively decreases.

5. A no-motion regime in which spheres do not move at all from their initial positions.

Regimes (1) and (5) are typical of a yield stress fluid (Tabuteau et al., 2007; Fazilati et al., 2017; Ferroir et al., 2004) and one can interpret them based on the state of the medium that surrounds the object. In the linear regime (1) the fluid around the sphere has a liquid-like

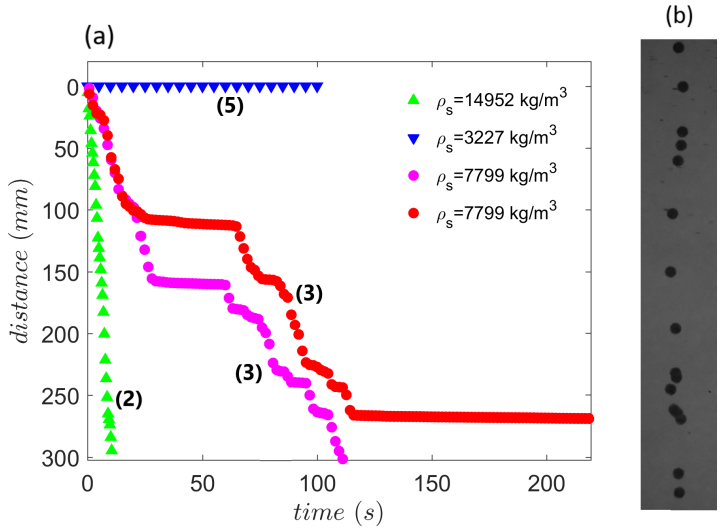

Figure 3.2: (a) Depth of spheres settling through gel D as function of time. Here spheres have constant diameter (d_s=6 mm) but different densities. As in Fig. 3.1, we report the case of irregular regime (2), no-motion (5) and, in addition, the intermittent regime (3). (b) Sequence of snapshots every 100 frames showing the irregular motion in gel D for a sphere with d_s=7 mm and ρ_s=7970 kg/m^3.

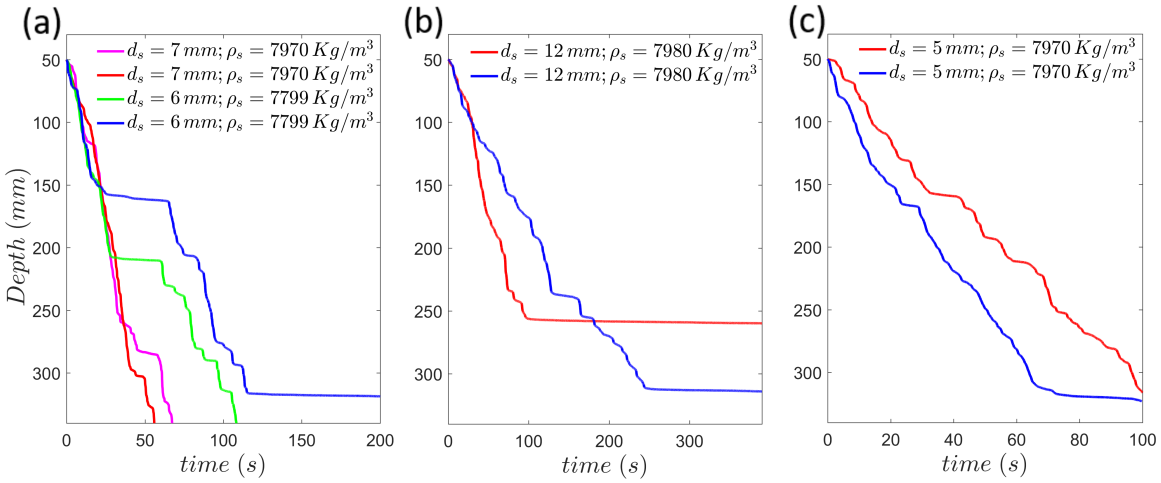

Figure 3.3: Depth of falling spheres as a function of time for different fluids: in gel D (a), gel E (b) and gel C (c). In this case we observe irregular and consecutive cycles of "stop" and "go" periods. In two cases we got the complete arrest of the sphere (blue line in (a) and red in (b)).

	Regimes				
	(1)	*(2)*	*(3)*	*(4)*	*(5)*
$\overline{v}_y = 0 \pm err(v_y)$					x
$\mathrm{MSE}_{lin} > \mathrm{MSE}_{log}$				x	
$\mathrm{MSE}_{lin} < \mathrm{MSE}_{log}$ & $std(v_y)/\overline{v}_y < 0.15$	x				
$\mathrm{MSE}_{lin} < \mathrm{MSE}_{log}$ & $std(v_y)/\overline{v}_y \geqslant 0.15$		x	x		
$\mathrm{MSE}_{lin} < \mathrm{MSE}_{log}$ & $t_s/t_0 \geq 5\%$			x		

Table 3.1: Summary of the observed motion regimes and the way they are classified.

behaviour that allows spheres to go down, whereas in regime (5) local stresses are below the yield stress value, σ_y. In this case the material around the sphere remains in the solid state, leading to the no motion of the object. Here the stress field is generated by the sphere buoyancy and the no-motion regime is always observed for the smallest d_s (Fig. 3.1) or $\Delta\rho$ (Fig. 3.2a, as in Tabuteau et al. (2007)). We have had no-motion whether the sphere was placed on the surface or it was gently pushed in the fluid column and released deeper in the fluid. In both cases, we left the spheres in that position for days (up to a week for one run) and they never moved away from their starting positions.

Although the distinction between the two end-member cases (1) and (5) is easy to establish, to discern quantitatively between the first steady-state motion regime (1) and the more irregular ones is more delicate. We summarize how we define the different motion regimes in Table 3.1. From the falling profiles one can notice that, although sometimes it is still possible to identify an almost constant falling speed superimposed on the oscillations (e.g. red lines in Fig. 3.1), in some other cases, spheres seem to slow down logarithmically during their way to the bottom (e.g. green lines in Fig. 3.1), making impossible to determine any constant terminal velocity. We report this aspect in Fig. 3.4a by plotting the mean squared variations (MSE) obtained by fitting the falling profiles with a linear or a semilog fit as function of spheres buoyancy. In this way, we define the logarithmic regime (4) for $\mathrm{MSE}_{linear} > \mathrm{MSE}_{log}$, that is when falls are better represented with a logarithmic fit. From Fig. 3.4a, even though it is evident how such logarithmic behaviour appears more often at lower buoyancies, the distinction between a linear regime and a non linear one is not straightforward: in a few cases at same buoyancy, these two behaviours coexist.

Once the separation between the stoppage cases (logarithmic regime (4) and no-motion (5)) and the other cases is established, one can identify the differences between the steady-state motion (regime (1)) and the more irregular and chaotic regimes (2) and (3). Depending on the buoyancy of the object and hence on its velocity, the irregularities show up as fluctuations in the sphere local vertical velocity and as a progressive increase in its horizontal motion (Fig. 3.2b). Regimes (2) and (3) show some similarities: in both of them, spheres have a long term constant falling velocity on which is superimposed a more complex and ir-

regular pattern of fluctuations. The latter are characterized by accelerations and subsequent decelerations in a short period of time and, in some cases, they can result in a succession of stops of the sphere. In the most drastic cases, we observe the complete arrest of the sphere after it has passed through most of the fluid (Fig. 3.2a).

To determine the boundaries between the irregular regimes (2) and (3) and regime (1), one can look, as a first approximation, at the ratio between the standard deviation (std) of the local falling velocity and its mean value. Variations of the local velocity for spheres within these irregular regimes are much larger than the experimental uncertainty (Fig. 3.4c-d). The latter is due to the precision of the technique we used to detect the sphere position in time (hereafter $err(v_y)$). It is estimated to be 0.25 mm/s from the syrup-case measurements, where $std(v_y)/\overline{v}_y$ always remains smaller than 0.15 (Fig. 2.7c), and from local velocity measurements in the no motion regime. We take this value to define the linear regime (1) when $std(v_y)/\overline{v}_y < 0.15$ (dashed line in Fig. 3.4c-d) and thus to use it as a limit between what is steady-state motion and does not show irregularities and what instead shows a broader distribution of velocities.

Once the linear regime is bounded in this way, we distinguish between the irregular regime (2) and the intermittent regime (3) as follows. In the intermittent case, the sphere remains during a certain cumulative amount of time, t_s, at $v_y \leqslant err(v_y)$. We then compare t_s to the total time, t_0, the sphere takes to descend 30 cm. The intermittent regime is defined as $t_s/t_0 \geq 5\%$ (cross symbols in Fig. 3.4e-f). The remaining irregular regime (2) is therefore defined as $t_s/t_0 < 5\%$ and $std(v_y)/\overline{v}_y > 0.15$ (square symbols in Fig. 3.4e-f).

3.2 Horizontal motion

Oscillations, accelerations and subsequent decelerations and the resulting general complex set of behaviours of the moving sphere that have been shown in section 3.1, characterize the motion both in the direction of fall and in the one perpendicular to it. In fact, the irregular motion we have observed is not only present and visible in the vertical direction but it also affects the horizontal movement of spheres. This happens in a such a way that they collect along this latter direction a certain amount of traveled distance, L_x, with respect to their initial position, depending on their diameter (Fig. 3.5a), on the gel grains size (Fig. 3.5b), and on the vertical falling distance h (Fig. 3.6a).

Fig. 3.6b shows that for each run, L_x is roughly proportional to h. Fig. 3.5 shows that small spheres change frequently their horizontal position, oscillating continuously around the vertical axis, and travelling for larger distances L_x than the large spheres. If we normalize L_x by h and d_s by the diameter of the gel grains (d_g), we achieve a good collapse for all our data along a line with slope -2. That is

$$L_x/h = C_{exp}\,(d_s/d_g)^{-2}\,, \tag{3.1}$$

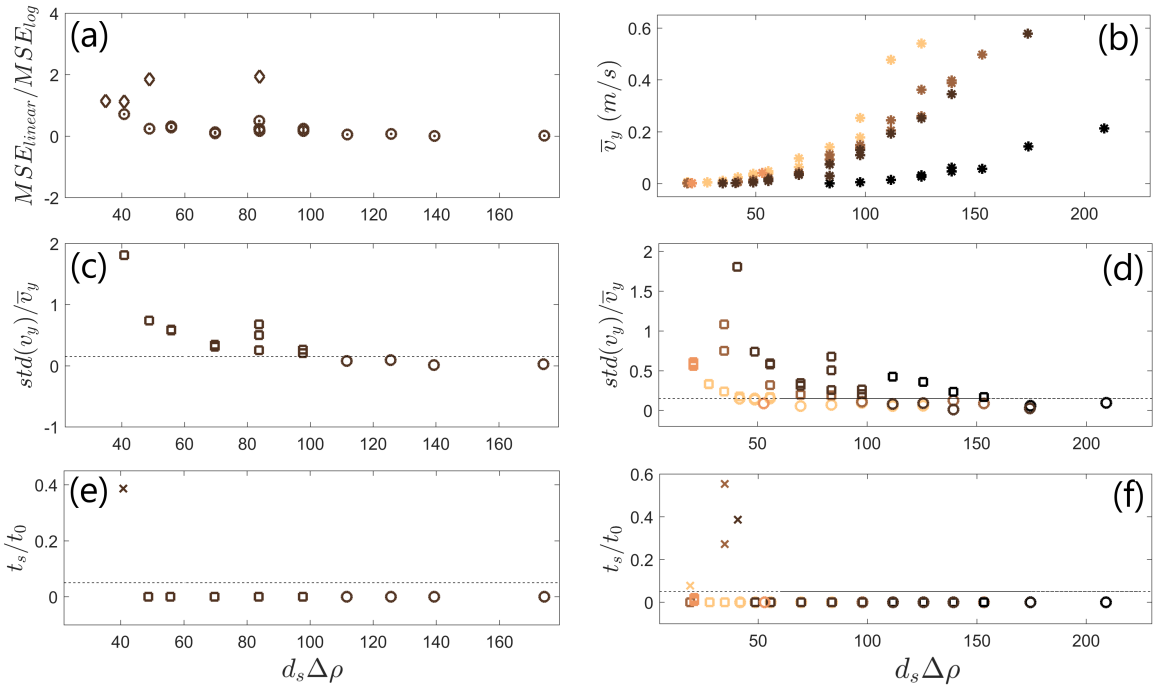

Figure 3.4: Determination of the different regimes of motion. In (a), (c) and (e) data refer to experiments carried out in gel D. In (b), (d) and (f) data are for all fluids. Colours indicate the grain size: lighter colors for thinner gels, darker for more coarse ones. (a) Best fit (MSE_{linear}/MSE_{log}) of the falling profiles. $\odot$ indicates a better linear fit whereas $\Diamond$ a better semi-log fit (logarithmic regime (4)). (b) Mean falling velocities ($\overline{v}_y$) for those falling profiles that have been linearly fitted. The error for v_y is 0.25 mm/s, smaller than the symbols. We do not report the standard deviation for v_y here (whereas it is in (c) and (d)) as being also linked to the physical oscillation of the sphere, for small values of velocity it would make the plot unreadable. In (c) and (d) we separate those experiments that show a more irregular and chaotic motion ($\square$) from those that do not show any irregularities during the fall ($\bigcirc$) by plotting $std(v_y)/\overline{v}_y$. The dashed line is for $std(v_y)/\overline{v}_y$=0.15, from the Newtonian case. In (e) and (f) we separate the intermittent regime (3) ($\times$) from the other irregular regime (2) ($\square$) based on the amount of time t_s the sphere remains at $v_y \leqslant err(v_y)$. t_0 is the total time the sphere takes to descend h. The dashed line indicates t_s/t_0=0.05.

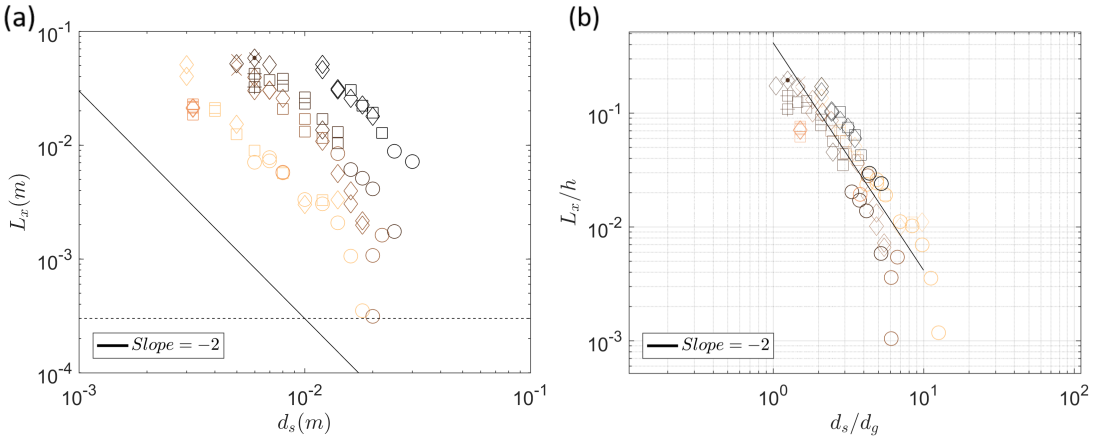

Figure 3.5: Total distance travelled in the horizontal direction, L_x. (a) L_x as function of the sphere diameter d_s. Dashed line indicates the uncertainty in position. (b) Same plot with y-axis normalized by the vertical falling distance h and x-axis by the gel grain size d_g. Colours indicate the different fluids as in Fig. 3.4. Symbols refer to the different motion regimes: ○ for the linear regime (1); □ for an irregular regime superimposed to a linear one (2); × for the intermittent regime (3) and ♢ for the logarithmic regime (4). Empty symbols are for steel spheres while the symbol with a point inside refers to ρ_s=7799 kg/m^3 and those filled with a plus sign are for ρ_s=14952 kg/m^3.

where $C_{exp} = 0.49 \pm 0.26$ (Fig. 3.6b).

In this way the total travelled distance in horizontal direction turns to be a good candidate to underline the strong interaction of the sphere and the gel grains that make up the fluid structure when those two have similar sizes.

3.3 Determination of the SAP gels effective rheology

The fall of a sphere within certain boundary conditions is described by the combination of a proper set of equations of motion and the constitutive relation. We have seen in section 1 that for yield stress fluids a commonly used rheological model that relates stress and strain in a non-linear way is the Herschel-Bulkley model, eq. (1.19).

Considering a fluid which can be described with such model, for small Reynolds numbers (Re≪1), the problem of a settling particle needs two parameters to be characterized (Tabuteau et al., 2007; Ansley and Smith, 1967). They are the Bingham number, Bi, eq. (1.37), which compares yield stress with viscous stresses, and the Yield number, Y, eq. (1.39), which compares the yield stress with the buoyancy stress.

As described in section 1, most of the experimental work done to investigate the yield of a viscoplastic fluid was carried out using Carbopol microgels due to their simplicity of preparation and because they are considered as simple yield stress fluids (i.e. shear stress, and hence viscosity, depends only on the applied shear rate and not on the shear rate history of the sample). The main difference between experiments done with Carbopol and the

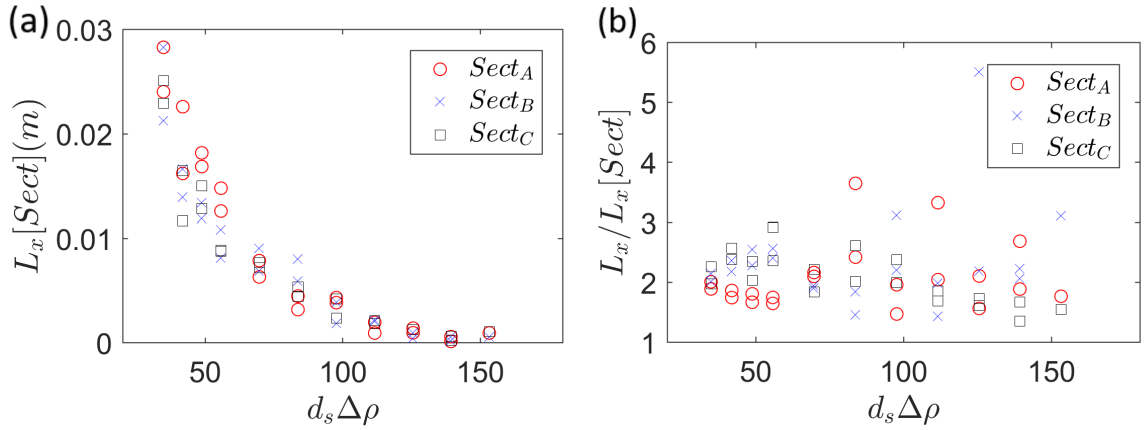

Figure 3.6: Distance travelled in the horizontal direction in gel C. (a) Distance travelled in different 15-cm-vertical-sections of h, $L_x[Sect]$, as function of spheres buoyancy. Sections are $Sect_A$=[h=0 cm, h=15 cm]; $Sect_B$=[h=15 cm, h=30 cm]; $Sect_C$=[h=7.5 cm, h=22.5 cm]. (b) Ratio between the total distance travelled in 30 cm, L_x, and the distance travelled in 15 cm, $L_x[Sect]$.

present work regards the typical size of the fluid structure compared to the dimension of the object that is moving through it. Carbopol corresponds to the case where the fluid structure (grains) is much smaller than the spheres. In this case, only regimes (1), (4) and (5) were reported (e.g. Tabuteau et al., 2007) whereas neither the irregular regime (our regime (2)) nor the intermittent regime (3) were observed; and the fall of the sphere was always described to be free of any sort of chaotic motion (Tabuteau et al., 2007; Putz et al., 2008; Holenberg et al., 2012).

In regime (1), that is when a constant terminal velocity can be determined, Tabuteau et al. (2007) showed that the settling of a sphere in Carbopol is well-fitted by the following equation

$$Y_{inv} = \frac{1}{Y} = 7 + \frac{8.52}{Bi} \tag{3.2}$$

with n=0.5, and that there is a critical value of Y above which there is no motion: Y_c=0.145 (Fig. 3.7).

For clarity, we rewrite eq. (3.2) as function of the rheological properties of the fluid, that is

$$\frac{g d_s \Delta\rho}{3} = 7\sigma_y + 8.52 K_v \left(\frac{v_y}{d_s}\right)^{0.5}. \tag{3.3}$$

Taking into account the differences between SAP and Carbopol, one can use eq. (3.2) or eq. (3.3), valid for $d_s \gg d_g$, and check its domain of validity in our case, namely for $d_s \to d_g$. To do so, we define an average falling velocity for all runs in regimes (1), (2) and (3) (circle and square symbols in Fig. 3.4c).

In this way, by fitting our data and comparing them with what eq. (3.3) predicts, we can

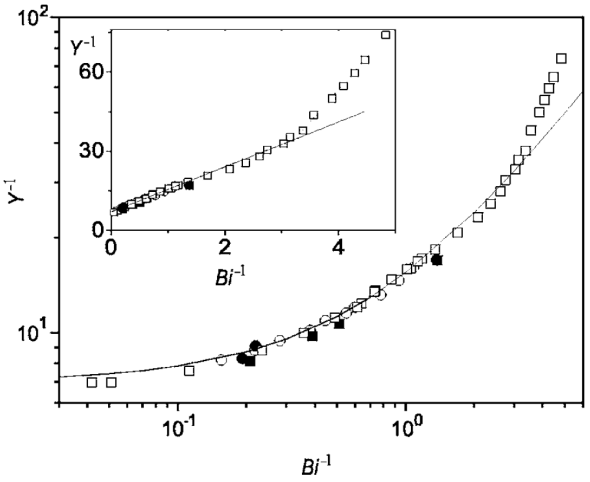

Figure 3.7: Adapted from Tabuteau et al. (2007). Experiments of a falling sphere in Carbopol microgels. Data are plotted as $1/Y$ as function of $1/Bi$. The insert shows the same with linear axes. Solid line is eq. (3.2).

find an effective rheology (i.e. the effective yield stress, $\sigma_y(eff)$, and the effective consistency, $K_v(eff)$) for each of our gel mixtures (Fig. 3.8).

The best fit is found for a shear-thinning index n between 0.50 and 0.70 (Fig. 3.9a). Unless otherwise indicated, in what follows we will use n=0.50 since it is with this value that eq. (3.2) is defined. For a given fluid, experiments in both linear and irregular regimes can be linear fitted by the same line (Fig. 3.8). We find that its intercept with y-axis, $\sigma_y(eff)$, and slope, $K_v(eff)$, increase with the gel grain size (Fig. 3.9b). These values are summarized in Table 3.2.

For experiments involving large spheres, it is opportune to check whether wall corrections are needed or not (Atapattu et al., 1990). For sufficiently small sphere-to-tube diameter ratio, d_s/D, we do not expect any reduction of the sphere's terminal velocity, and the measured velocity, v_y, is equal to the ideal terminal velocity of a sphere falling in an unbounded medium, v_∞. On the other hand, if d_s/D exceeds a critical value, d_s/D_c, the velocity decreases, leading to v_y/v_∞ <1. The critical diameter ratio for a yield stress fluid is given by Atapattu et al. (1990):

$$d_s/D_c = 0.055 + 1.114\,Y \qquad \text{if} \quad Y \leqslant Y_c. \tag{3.4}$$

In our case, d_s/D is smaller than d_s/D_c as long as d_s/D <0.1. The influence of walls causes a reduction in speed such that (Atapattu et al., 1990):

$$\frac{v_y}{v_\infty} = 1 - 1.7\,[(d_s/D) - (d_s/D_c)] \qquad \text{if} \quad d_s/D > d_s/D_c. \tag{3.5}$$

So, for 0.1$\leqslant$ d_s/D $\leqslant$0.17, wall effects lead to 0.8< v_y/v_∞ <1, i.e a maximum decrease of v_y/v_∞ of less than 20%. Considering only the experiments with $v_y/v_\infty > 0.8$, we recalculate the effective rheology in the same way as described above (Fig.3.10a). The new values of

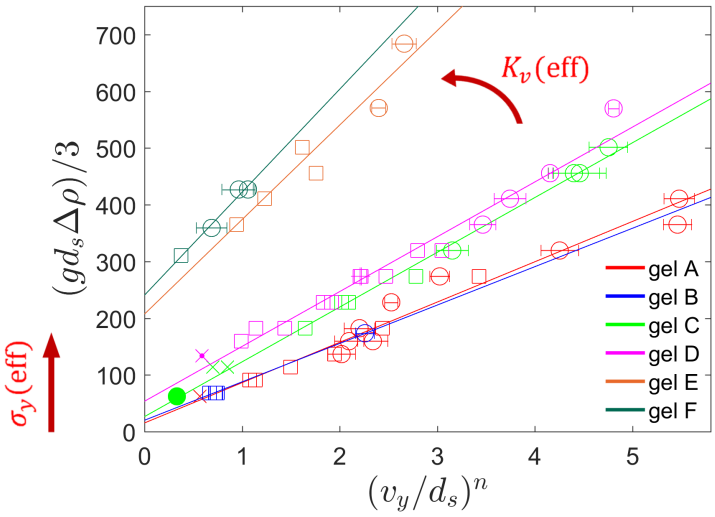

Figure 3.8: Effective yield stress and consistency for the fluids in exam. Following the approach of Tabuteau et al. (2007), v_y is the average falling velocity for those experiments where a steady decrease of the speed has not been observed (i.e. we do not consider regime (4)) and n=0.5 is the power-law index. Colours represent the fluids as in Fig. 3.4. Symbols represent the regimes: circles for regime (1), squares for regime (2) and crosses for regime (3). Empty symbols for steel sphere; symbol with a point inside for ρ_s=7799 kg/m^3; with a plus sign for ρ_s=14952 kg/m^3 and filled symbols for ρ_s=2200 kg/m^3. Solid lines are the linear data fits.

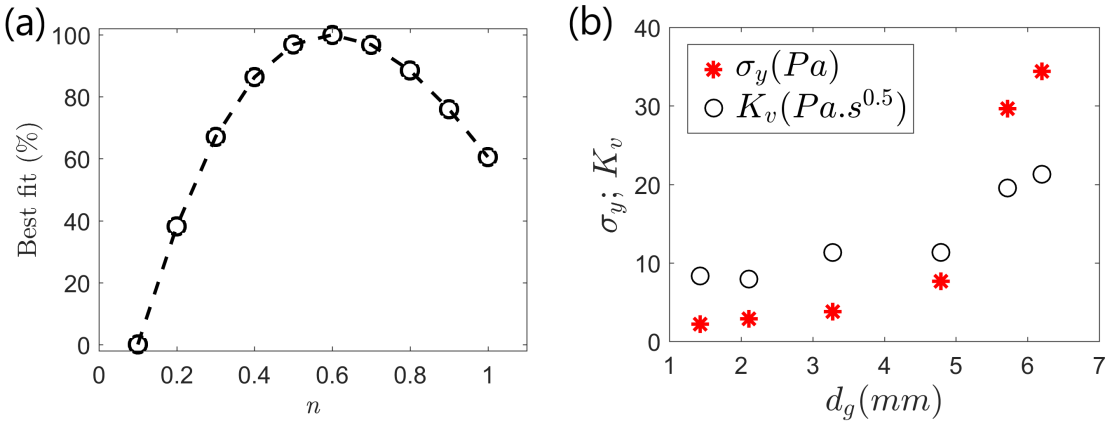

Figure 3.9: (a) Power law index, n, that best fits data in Fig. 3.8 for all gel samples. The best range of n is in between 0.50 and 0.70. (b) Effective yield stress (σ_y) and effective consistency (K_v) as function of gel grains size.

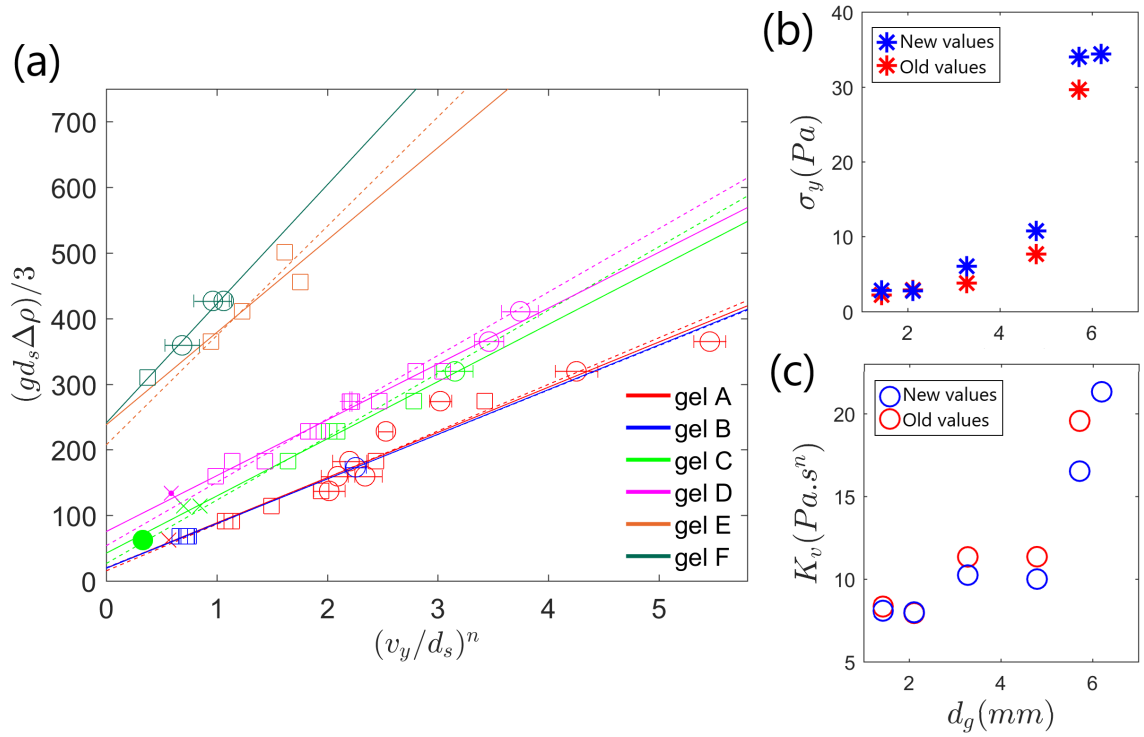

Figure 3.10: Influence of the velocity reduction due to wall effects on the effective rheology. n=0.5. (a) The new fit that considers only experiments with $v_y/v_\infty > 0.8$ (solid lines) is compared with the previous fit from Fig. 3.8 (dashed lines). Colours and symbols here are those described in Fig. 3.8. (b) Effective yield stress and consistency as function of gel grains size from the new fit (blue symbols). Red symbols are those in Fig. 3.8.

$\sigma_{Y(eff)}$ and $K_{v(eff)}$ vary at most by 20% from the previous ones (Fig.3.10b).

Once we got the effective yield stress and the consistency of each sample, we plot Y_{inv} as function of Bi^{-1} in Fig. 3.11. For values of Bi^{-1} >0 we achieve a good collapse along eq. (3.2) for experimental data that belong to regimes (1), (2) and (3). In this way, even considering the irregular (2) and the intermittent (3) regimes where the interaction between moving objects and fluid structure results in highly irregular falls of objects themselves, an effective rheology following the Hershel-Bulkley model with a classical shear-thinning index of 0.5 well represents the majority of our data.

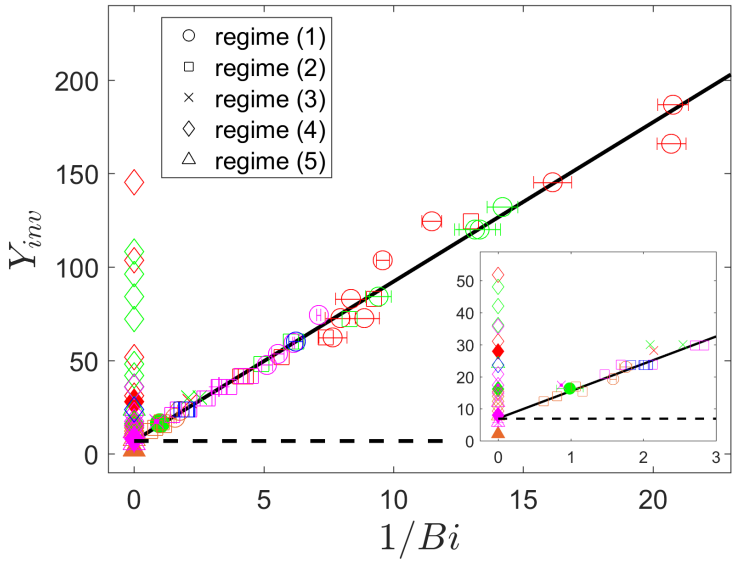

Figure 3.11: Y_{inv} as function of $1/Bi$. Colours are for the different fluids. The dashed line indicates Y_{inv_C}=6.9 (Tabuteau et al., 2007). Symbols are filled in a different way to distinguish between spheres of different materials: full-filled symbols are for light spheres (ρ_s =2200 kg/m^3), open-symbols for ρ_s =7970 kg/m^3, point-filled for ρ_s =7799 kg/m^3, asterisk-filled for ρ_s =3227 kg/m^3 and plus-filled for ρ_s =14952 kg/m^3. We show the good collapse of our data along eq. (3.2) (solid black line). The inset shows the data zoomed around the critical conditions. For v_y =0 the experimental data deviate from the theoretical curve, the stoppage regimes (no-motion regime (5) and logarithmic regime (4)) are not well predicted and they are observed also for $Y_{inv} > Y_{inv_C}$.

	σ_y(eff) (Pa)	K_v(eff) (Pa s^n)	G_0 (Pa)
gel A	2.07	8.44	103.5
gel B	2.88	7.95	144.0
gel C	3.79	11.34	189.5
gel D	7.67	11.35	383.5
gel E	29.63	19.56	1481.5
gel F	34.38	21.31	1719.0

Table 3.2: Effective rheology (yield stress and consistency) of the fluids in exam. The shear-thinning index is n=0.5. The shear modulus G_0 is defined from $\sigma_y = G_0\gamma_y$, with yield strain γ_y=0.02.

So far, our observations in SAP have been compared with experiments done in the Carbopol case. However, the Hershel-Bulkley model is used also to characterize the flow of other kind of materials. Pastes of soft particles, that is fluids made by deformable and soft spherical particles, are an example. Seth et al. (2011) show how the simulated flow curves of such pastes are well described by an Hershel-Bulkley model with the same shear thinning index n=0.50±0.02 as ours (Fig. 3.12). In this case, suspensions of soft particles undergo jamming transition and become solid when the particle volume fraction reaches the random close packing limit (or jamming limit) $\phi_c \simeq$0.64 (Bonn et al., 2017). An yield stress appears

then only for particle volume fraction $\phi > \phi_c$. This is the same situation we have in SAP gels where ϕ, estimated in between 0.63 and 0.70, is larger than the maximum packing fraction obtained from eq. (2.3). Above the ϕ_c threshold, particles are compressed together and adapt their shape by forming flat facets at contact (Fig. 3.12a). The interaction between two of those soft particles consists of two forces: an elastic force $\bar{F}_{\perp}$, perpendicular to the contact facet, and an elastohydrodynamic drag force $\bar{F}_{//}$, parallel to the facet, that makes particles glide along one another (Seth et al., 2011). During flow, the rheology of these pastes is dominated by the elastic component of the stress (σ^e) which is linked to the elastic deformation of particles during the rearrangement, and hence associated to $\bar{F}_{\perp}$. σ^e is found orders of magnitude larger than the viscous counterpart (σ^v) due to $\bar{F}_{//}$ (see insert in Fig. 3.12b). Both these forces depend on the elastic properties of the particles, on the contact radius, that represents how much particles overlap, and on the overlap distance, that is how much they are compressed. Increasing the particle volume fraction, the energy needed to deform the entire medium increase (Fig. 3.12b) and, consequently, increases also the value of rheological parameters of the Hershel-Bulkley law (i.e. σ_y and K_v).

In our case, an increment of the effective yield stress and consistency is observed with the increase of grain size d_g (Fig. 3.9b). Inside the framework of soft particles and assuming that ϕ remains constant for each d_g, an increment of grain size will mainly cause an increment of the overlay between particles that, in turn, it will lead to an increment of $\bar{F}_{\perp}$ and $\bar{F}_{//}$. Thus a growing gel size d_g will create a more solid network able to withstand the flow better. The emerging yield stress is then due to elasticity and relates to the critical deformation, γ_y, through $\sigma_y = G_0\gamma_y$, with G_0 the shear modulus associated to the rheological transition. Moreover, σ_y would increase more when the elastic component predominates in the system. This occurs either for an increasing d_g or for an increasing ϕ (or ϕ_m) due to the higher polydispersity of larger gels (Fig. 2.3). The same would occur for the consistency which is proportional to the normalized shear modulus G_0/E^*, where E^* is the contact modulus $E^* = E/2(1-\nu)^2$ (E: Young modulus; ν: Poissons ratio) (Seth et al., 2011, 2006).

The effective properties of our gels (Fig. 3.9b) that we have obtained for a framework valid for simple yield stress fluids would then mainly derive from the fluid elasticity. Using a critical strain of γ_y=0.02, generally measured in soft particles (Seth et al., 2011) (similar values are also reported directly for SAP, e.g. in Ramazani-Harandi et al. (2006)), one can calculate the shear modulus G_0 of each gel. Values are reported in Table 3.2. Finally, we can estimate the Deborah number, De, that is the ratio between relaxation time and flow time scale

$$De = \frac{\Delta\rho g d_s}{G_0}, \tag{3.6}$$

and evaluate how much the material elasticity influences the settling of a sphere. Values of De for each experiment are listed in section 2.4 and their influence on the critical conditions of motion are discussed in next section.

A further analysis on how the properties of a single elastic grain could influence the

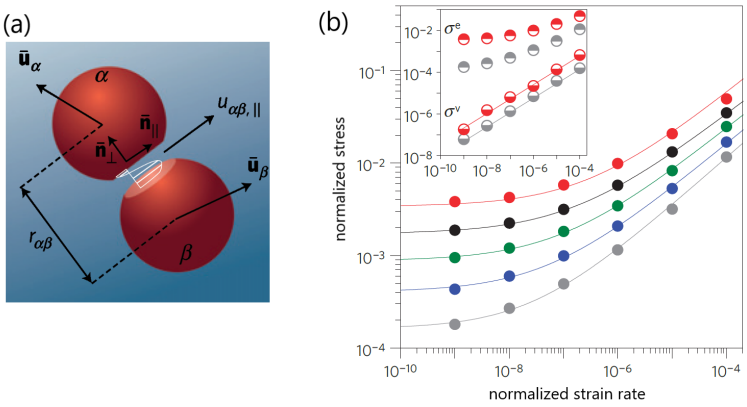

Figure 3.12: Modified from Seth et al. (2011). Computed flow curves for soft particles glasses. Each colour refers to a different particle volume fraction: ϕ=0.70 (grey), ϕ=0.75 (blue), ϕ=0.80 (green), ϕ=0.85 (black) and ϕ=0.90 (red). The inset displays the variations of the elastic stress and viscous stress for ϕ=0.70 and ϕ=0.90.

effective σ_y and K_v would be useful to quantify the role that its elasticity plays for the bulk rheology. However, the extreme softness of the material makes it very difficult. After several attempts to measure forces and penetration depth by using a microindenter with a minimum normal force of 20 mN, we have not been able to get any reliable measurement since slip or rupture of the grain always occurred even for such small values of normal force.

3.4 Entrapment conditions

Fig. 3.11 shows that for Bi^{-1}=0, spheres get entrapped also for $Y_{inv} > Y_{inv_C}$. From the experimental work of Tabuteau et al. (2007), the critical value of the (inverse) Yield number, Y_{inv_C}, below which spheres do not move in a simple yield stress fluid is Y_{inv_C}=6.90. This value is very close to 6.99, predicted in previous works of Beris et al. (1985) and Blackery and Mitsoulis (1997). On the other hand, a more recent study (Fraggedakis et al., 2016) points out that the critical value may increase as function of the Deborah number if elastic effects are taken into account. The expression they then derived to describe the critical conditions is:

$$Y_{inv_C} = 1.2 + \frac{1}{0.176 + 0.135\,De}. \tag{3.7}$$

For a material that is not elastic at all, i.e. De=0, eq. (3.7) returns the classical Y_{inv_C}=6.9. We plot $Y_{inv_C}(De)$ in Fig. 3.13 together with no-motion cases in SAP. According to the De values of our experiments (tables in section 2.4), elastic effects are particularly important only for large and/or heavy spheres (large $\Delta\rho d_s$) which fall fast through the fluid. For no-motion cases, De is found to be always very small (Fig. 3.13) and cannot explain the reason why arrest of small particles takes place at such large values of Y_{inv_C}.

Generally, the critical Y_{inv_C}=6.9 or $Y_{inv_C}(De)$ seem to work well in our cases only when

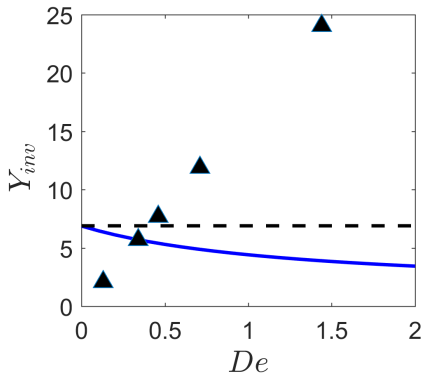

Figure 3.13: Inverse of Yield number, Y_{inv}, as function of Deborah number, De. Blue line is eq. (3.7). Black dashed line is the constant value Y_{inv_C}=6.90. Black triangles represent the no-motion cases obtained in SAP.

the intruder size is very large compared to the particle size that build up the fluid structure. As we highlighted at the beginning of this section, equation (3.2) was derived for Carbopol when the size of the moving object is much larger than the size of the particles than make up the fluid structure. Inside this assumption, the critical condition is well predicted in our case too. In gel E, for example, we had no-motion for a large glass sphere (d_s/d_g >2.5 and $\Delta\rho$=1200 kg/m^3) for Y_{inv}=2.09 (Fig. 3.14), smaller than Y_{inv_C}. For the smallest intruders in SAP this rheology clearly breaks down and we observe arrest also for $Y_{inv} > Y_{inv_C}$ (Fig. 3.14b). The larger value of Y_{inv} at which we had no-motion is for a 4-mm steel sphere falling in gel C (d_g=3.28 mm, $\Delta\rho$=6970 kg/m^3) in which Y_{inv}=24.05, more than three times Y_{inv_C}. In general, we observe good agreement with Y_{inv_C} for those experiments where d_s/d_g >2.5 whereas for $d_s \to d_g$ the critical condition moves toward larger Y_{inv} (Fig. 3.14a). The critical (inverse) Yield number is found to be

$$Y_{inv_C} = -28.93\,(d_s/d_g) + (52.50 \pm 9.36) \qquad for \quad d_s/d_g < 2.5. \tag{3.8}$$

Uncertainties in the scaling law are due to the difficulty to set up a clear limit between no-motion regime and intermittent regime (blue lines in Fig. 3.14b). For gel D, for example, there exists a small area between the transition in which the motion regime is either intermittent or logarithmic, and the spheres usually cannot make it to the bottom.

We attribute the increase of Y_{inv_C} to the interaction between spheres and the gel structure: when $d_s \to d_g$, the spheres "see" obstacles on their way. Arrest is not due anymore to the effective σ_y of the entire mixture but rather the sphere now see a different material consisting in only a few gel grains. It is in this case that the effective rheology described by eq. (3.2) breaks down.

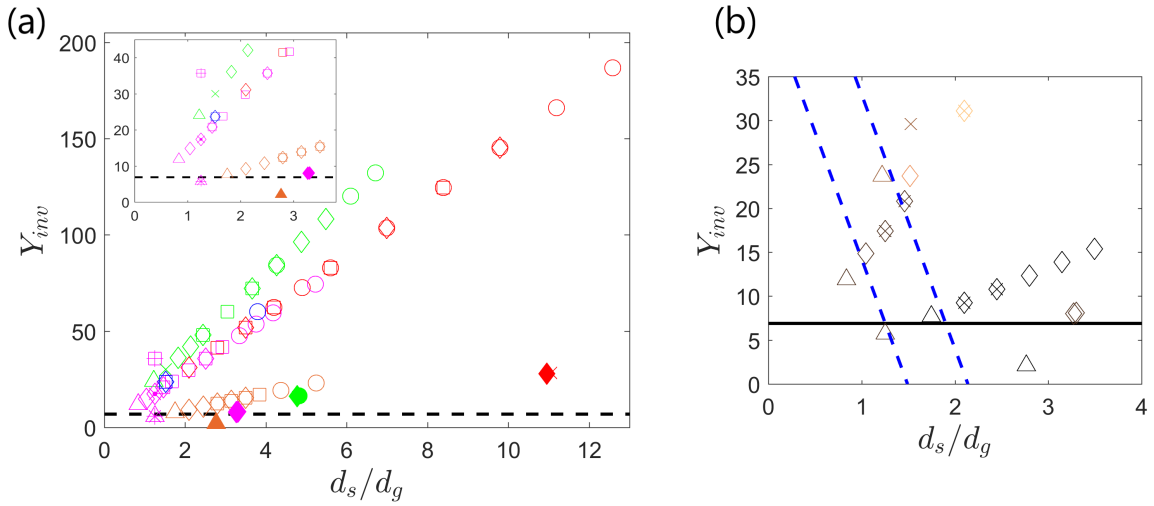

Figure 3.14: (a) Range of validity of the effective rheology. Colours are for the different fluids. Symbols are those used in Fig. 3.4. Black dashed line indicates Y_{inv_C}=6.90 (Tabuteau et al., 2007). For d_s/d_g <2.5, we have no motions (triangles), even for Y_{inv} larger than the critical one commonly used. Insert shows the same zoomed close to critical conditions. (b) Same plot of (a) in which we highlight the no motion limit that rises up in our case at d_s/d_g<2.5. The blue dashed lines are the upper and lower limits of eq. (3.8). Black line indicates Y_{inv_C}. To clarity, here we show the regimes with same symbols, i.e. independently from ρ_s. That is no-motion regime with triangles, logarithmic regime with diamonds and intermittent regime with crosses. The other regimes are not indicated.

3.5 Matrix deformation and PIV velocity field

3.5.1 Linear regime

To catch grains motion around the intruder and to identify the existence and extent of the fluidized region, we have analyzed fluid cross-sections, illuminated by a laser-sheet, using Particle Image Velocimetry (PIV package from LaVision). We treat fluid grains as tracer particles in the classical PIV framework (interrogation windows of 32x32 pixels), detecting the variation in light intensity between consecutive frames to calculate the velocity field. Given our setup where the tank is illuminated from the left side, we show here only the left side of the velocity field since the right one is perturbed by the shadow of the sphere.

We first focus on the linear regime by plotting the magnitude of velocity field for a 20-mm sphere falling in a fluid with d_g=5.72 mm. In Fig. 3.15 we show the magnitude of the instant velocity field in which we recognize an area of material that moves under the sphere passage while more peripheral areas remain motionless (i.e. undeformed). Fig. 3.16a and b display the vertical and horizontal components of velocity for the average velocity field. The figure is obtained averaging the velocity field in the referential of the sphere for 50 frames. However, from these figures the limit between yielded and unyielded region remains not very clear since isolines become more and more irregular moving away from the sphere. To better define the limit, in Fig. 3.16c we report the map of the second invariant of the strain rate tensor,

$\dot{\gamma}_2 = \sqrt{\frac{1}{2}\dot{\gamma}_{ij}^2}$. The figure shows the overall shape of the yielded region and the boundary of the yielded surface, that is the outline between undeformed (here set to $\dot{\gamma}_2$=0.2 s^{-1} because of the noise level in the PIV measurements) and deformed zone ($\dot{\gamma}_2$ >0.2 s^{-1}), pointing out the strong shear localization nearby the sphere as expected for yield stress fluids (e.g Gabard and Hulin, 2003). The small ring of low rates of strain immediately around the sphere's outline is an artifact due to light reflection which slightly widens the section of the sphere during the PIV analysis. The shape of the yield surface looks similar to the one reported for Carbopol by Putz et al. (2008) and Holenberg et al. (2012) (Fig. 3.17a and b, respectively). They found an yield surface that approximates the shape of an ovoid spheroid, a profile that can be used to describe also our Fig. 3.16. The size of the yielded region ahead the sphere in our case is about twice the sphere radius. Hence, the major axis of the spheroid, R_f, is more than three time larger than the sphere radius: $R_f \simeq 3.1R_s$, with R_s the radius of the sphere. A similar R_f is measured from Holenberg et al. (2012) experiments for a smooth and light sphere (Fig. 3.17b) where $R_f \simeq 3.4R_s$. However, in case of Putz et al. (2008) the yielded envelop ahead the sphere is found to be more pronounced, $R_f \simeq 5R_s$. Discrepancies might be due to the different sensibilities of the experimental techniques used to derive the yield surface. In Holenberg et al. (2012) a combination of PIV and PTV (particle tracking velocimetry) has been used whereas in our case and in the one of Putz et al. (2008) only PIV was used. Moreover, we have defined the limit between yielded and not-yielded regions at $\dot{\gamma}_2$=0.2 s^{-1} whereas Putz et al. (2008) set that limit to 0.1 s^{-1}. In any case a yielded surface based on the second invariant of the rate of shear has to be interpreted only as a first approximation of the real surface subjected to solid-liquid transition. This is because an yielded surface strain-rate based is calculated directly from velocity gradients of the flow field ignoring the stress field at which the fluid is subjected during the sphere passage.

Generally, any flow involving the movement of an object in a elasto-viscoplastic fluid, like the settling of a sphere in our case, is permitted if a specific "unjamming criterion" is satisfied. Ovarlez et al. (2010) demonstrated that when a flow is imposed in some direction, unjamming takes place simultaneously in all directions of space. This three dimensions unjamming criterion is found to be well described by the Von Mises criterion. The latter is traditionally used in plasticity theory and postulates that yielding of a ductile material begins when the second invariant of the deviatoric stress, J_2, reaches a critical value. According to it, the fluidization of a region of our fluid occurs when the fluid yield stress is overtaken by J_2, that is

$$\sqrt{\frac{1}{2}J_2} \geqslant Y. \tag{3.9}$$

However, as seen in Fig. 3.16c and Fig. 3.17, in experiments it is significantly easier to measure the velocity field and work with the rate of deformation tensor instead of measuring the stress field. A yield surface defined on $\dot{\gamma}_2$ (strain rate defined) and one based on J_2 (stress defined) are yet equivalent only for inelastic and unidirectional flow (Cheddadi et al., 2012; Fraggedakis et al., 2016). In our case the flow around the sphere is definitely more complex

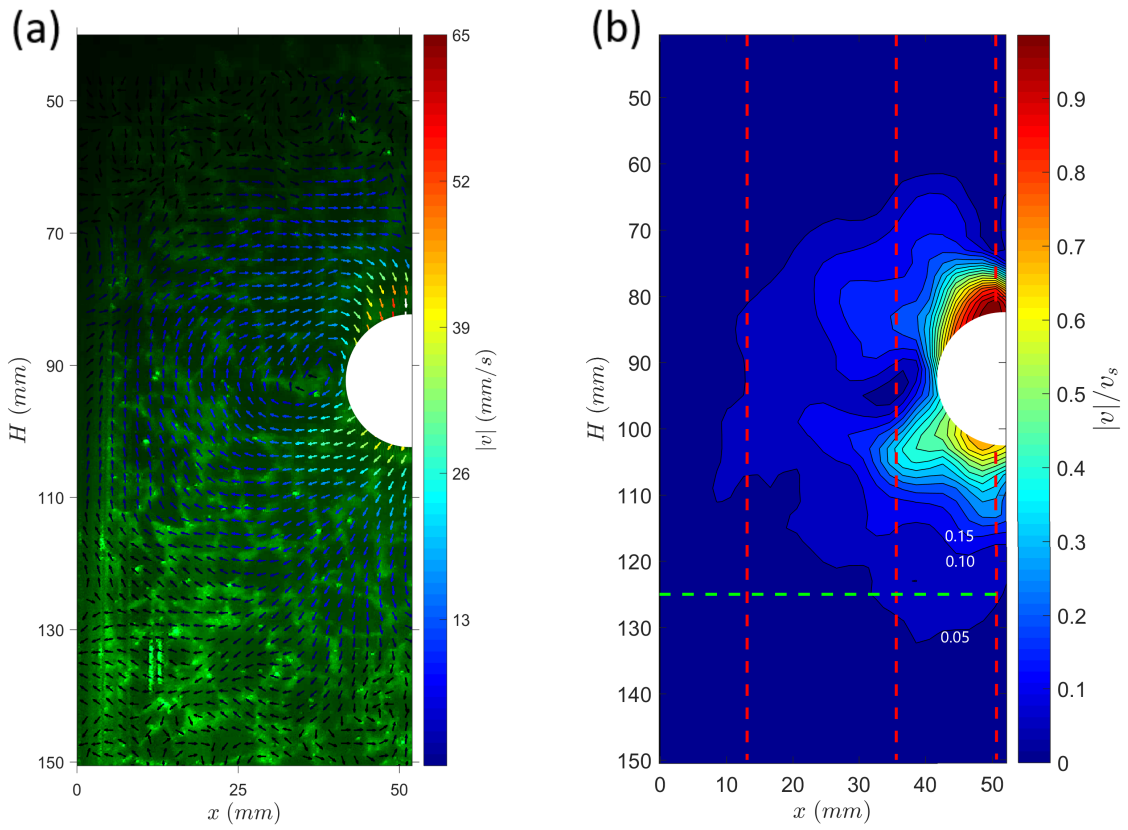

Figure 3.15: Linear regime, d_s=20 mm, d_g=5.72 mm, time t=6.24 s. (a) Instant velocity field superimposed the illuminated fluid structure. Colours refer to the magnitude of velocity. (b) Contour of the instant velocity magnitude normalized by the sphere velocity v_s. Dashed lines indicate sections in which spatio-temporal profiles are carried out.

and hides a stress tensor where several components might be not null (i.e. there exist elastic stresses throughout the material). If fluid elasticity can no longer be neglected, the elastic contribution to the deviatoric stress tensor that defines the fluidization (according to the Von Mises criterion) will be all the more significant.

Another efficient way to estimate the portion of fluid affected by the fall of the sphere is to plot horizontal spatio-temporal profiles, both for light intensity of the pixel line (Fig. 3.18a) and for the components of velocity (Fig. 3.18b and c). In this way one can observe how the sphere is preceded and followed by a deformation front that triggers the grains motion. Horizontal spatio-temporal profile also highlights the lateral extension (i.e. perpendicular to the falling direction) of the deformed area: bright bands on the side of the sphere are bent once the sphere appears and they move back to the original position once the sphere has passed. We define the maximum horizontal length of the deformed section from the outline of the sphere with l_d (Fig. 3.18a).

In viscoplastic fluids, a rough estimation of l_d can be made by looking at the wall effects. Traditionally, the influence of a moving object regards only a portion of fluid close to the object and it does not go further in the solid region. This means that beyond a critical tube

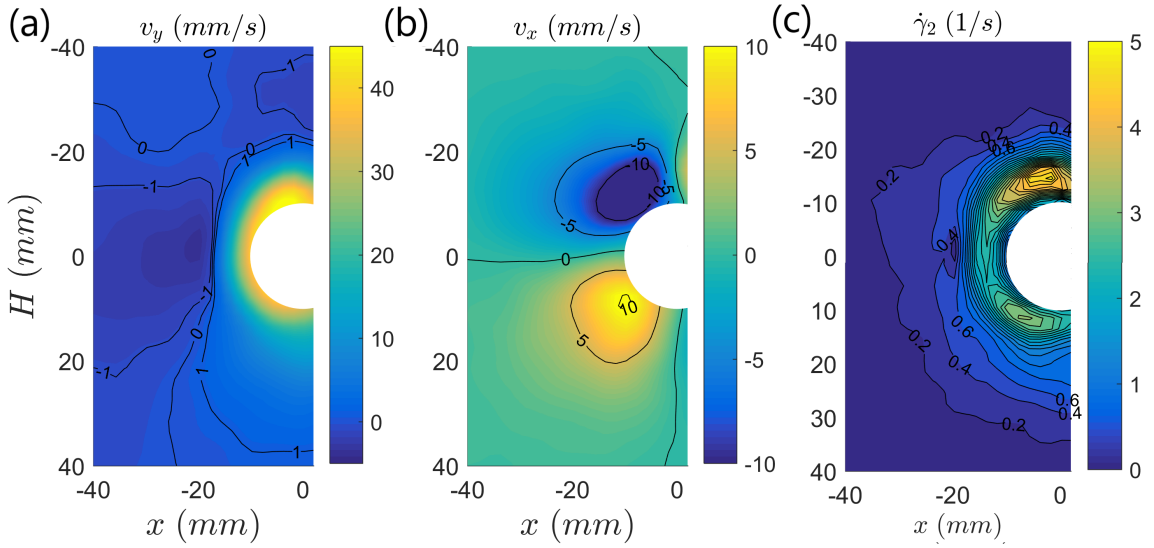

Figure 3.16: Linear regime, d_s=20 mm, d_g=5.72 mm. Vertical (a) and horizontal (b) component of the averaged velocity field. The figures are obtained by averaging the velocity field in the referential of the sphere for 50 frames. (c) Second invariant of rate-of-strain tensor obtained from the averaged velocity field. Contour lines show intervals of 0.2 s^{-1}.

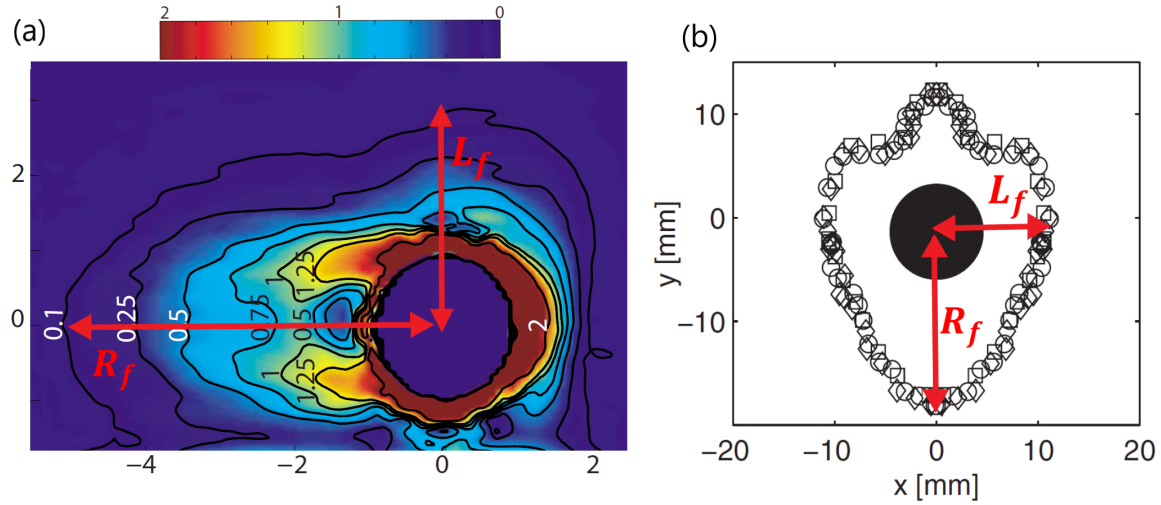

Figure 3.17: (a) Modified from Putz et al. (2008). Contour of the second invariant of the shear rate for the flow field generated by a sphere of radius R_s=3.2 mm falling in Carbopol (σ_y=1.4 Pa, K_v=5.5 Pa s^n, n=0.28). Sphere moves from right to left. (b) Modified from Holenberg et al. (2012). Solid-fluid boundary for a smooth light sphere (R_s=4.78 mm) settling in Carbopol (σ_y=9.07 Pa, K_v=1.322 Pa s^n, n=0.53).

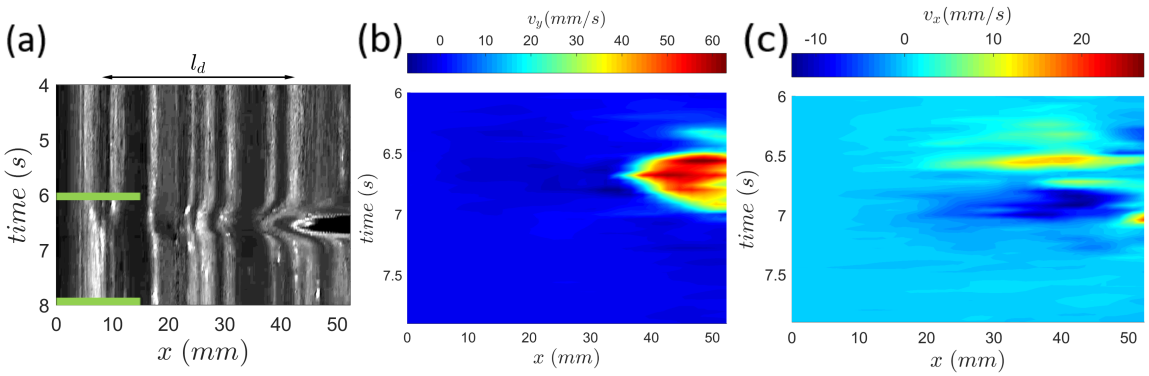

Figure 3.18: Linear regime, d_s=20 mm, d_g=5.72 mm. (a) Horizontal pixel line of light intensity (green line in Fig. 3.15b) plotted over time (time elapsed since the sphere was released). l_d indicates the deformed area at the sphere side. Vertical (b) and horizontal (c) components of the velocity field along the same horizontal pixel line as function of time (in between 6 and 8 seconds after the release of the sphere, as indicated by green lines in (a)).

size one does not expect wall effects. The critical conditions have been already reported in section 3.3: a reduction of sphere velocity in viscoplastic fluids occurs for $d_s/D > d_s/D_c$, where d_s/D_c is defined by eq. (3.4). Since wall effects arise when the sheared fluid envelope surrounding the sphere gets to the wall, d_s/D_c can be interpreted as the critical diameter ratio at which the lateral fluidized portion of fluid, l_d, extends exactly as much as the distance between the edge of the sphere and the wall. For those experiments in which we have been able to estimate l_d from the spatio-temporal profile (only in linear regime (1) and irregular regime (2)), we show in Fig. 3.19 the length of the experimental fluidized horizontal section from the center of the sphere, $l_d + d_s/2$, as function of the corresponding $D_c/2$ given by the wall effects estimation of Atapattu et al. (1990):

$$\frac{D_c}{2} = d_s \left(0.11 + 2.228\,\frac{3\sigma_y}{g d_s(\rho_s - \rho_f)}\right)^{-1}, \tag{3.10}$$

where σ_y and ρ_f are those of the gel. We find that the fluidized lateral section L_{fluid} scales as:

$$L_{fluid} = l_d + \frac{d_s}{2} \approx d_s\left[(1.86 \pm 0.37)\,(0.11 + 2.228\,Y)\right]^{-1}. \tag{3.11}$$

Using eq. (3.11) to obtain L_{fluid} for the experiments in Carbopol (Putz et al., 2008; Holenberg et al., 2012), we get a good estimation of the width of their yield surfaces. Values are reported in Table 3.3. Considering L_f as the distance between the sphere center and the maximal extension of the yielded envelope (as indicated in Fig. 3.17), for the case of Holenberg et al. (2012) we obtain a difference smaller than 15% between L_f and L_{fluid}. The difference between L_f and the minimum value of L_{fluid} is around 23% for the case of Putz et al. (2008). A larger discrepancy is expected in this case because their yield surface does not represent the extreme zero contour of strain rate but instead is defined at $0.1\dot{\gamma}_2$.

source	σ_y (Pa)	K_v (Pa s^n)	n	d_s (mm)	v_s (mm/s)	$\Delta\rho$ (kg/m^3)	Y_{inv}	R_f (mm)	L_f (mm)	L_{fluid} (mm)
a	29.63	19.56	0.50	20	66.30	6970	15.38	31.3	31.1	43.8 ± 11.9
b	1.4	5.5	0.28	6.4	3.3	1311	19.60	16.46	9.3	15.9 ± 4.4
c	9.07	1.32	0.53	9.6	0.24	2082*	7.18	16.25	11.1	12.7 ± 3.5

Table 3.3: Rheology, fluid conditions and extension of yield surface for three experiments. Source a refers to our case (Fig. 3.16c); source b to experiments of Putz et al. (2008) (their case 3); source c to experiments of Holenberg et al. (2012) (smooth and light bead). R_f and L_f are the vertical and lateral extensions of the yield surface, respectively. They have been measured directly from Fig. 3.17 and Fig. 3.16c. L_{fluid} is the fluidized lateral section obtained from eq. (3.11). *: the value of $\Delta\rho$ have been calculated from eq. (3.2) with their rheological parameters and velocity. It deviates from what one gets by using the reported sphere weight of 0.51 g. However, using the latter one gets Y_{inv}=0.41 which is much smaller than the critical value of Y_{invC}=6.9 under which the entrapment of the sphere occurs.

This leads to an underestimation of the real amplitude of the fluidized region. Values are similar when comparing the contour lateral extension of our case (Fig. 3.16c) with L_{fluid} predicted for the same sphere and fluid rheology (d_s=20 mm and gel E)(Table 3.3). The smaller value of L_f is again consistent with the fact that it comes from a yielded envelope defined at $\dot{\gamma}_2$=0.2 instead of zero because of the noise during PIV measurements.

Similarly, fluid deformation above and below the sphere can also be followed from vertical spatio-temporal profiles. Fig. 3.20 shows three examples taken at 33.19, 19.69 and 1.69 mm from the central sphere axis, respectively. In the farthest (Fig. 3.20a), bright bands only move slightly upward after the sphere has passed of about 10 pixels (that is less than 1.5 mm). For closest pixel lines (Fig. 3.20b and c), fluid is pushed downward before the arrival of the sphere and moves gently upward right after it has passed.

Another characteristic of the fluid flow regards the fore-aft asymmetry (Fig. 3.21) in which the flow field ahead the sphere differs from the one at its back. In Fig. 3.21c, plotting the vertical component of the fluid velocity, v_y, along the central axis and normalizing it by the sphere velocity, v_s, we see the fore fluidized zone being close to the sphere and vanishing when v_y/v_s=0.

To compare with Newtonian fluids, we define an effective viscosity $\eta_{eff}=\sigma/\dot{\gamma}$ with a characteristic strain rate of $\dot{\gamma}=v_s/d_s$. For the case without yield stress, stress writes $\sigma=K_v\dot{\gamma}^n$, leading to $\eta_{eff}=K_v\dot{\gamma}^{n-1}=K_v(v_s/d_s)^{-0.5}$ for n=0.5. The fluid velocity profile along the vertical y-axis for a Newtonian fluid is

$$v_y = v_{Stokes}\left(-\frac{1}{2}\frac{R_s^3}{y^3}+\frac{3}{2}\frac{R_s}{y}\right) \tag{3.12}$$

for a radial angle equal to 0, where v_{Stokes} is the Stokes velocity for a fluid with viscosity $\eta = \eta_{eff}$. We find in SAP a velocity profile more limited (red dashed line in Fig. 3.21c) compare to the one obtained from eq. (3.12) (gray dashed line in Fig. 3.21c). That is

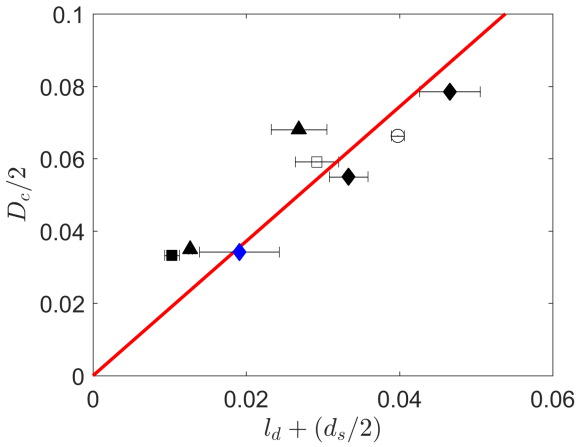

Figure 3.19: Measured yield surface width from the center of the sphere, $l_d + (d_s/2)$, *vs.* the critical radius $D_c/2$ at which wall effects are expected at given Y. Empty symbols are for experiments in regime (1), filled symbols for regime (2). Axes are in m. Symbols refer to gel A (■), gel C (▲), gel E (♦) and gel F (●). The solid line shows a linear fit with slope of 1.94.

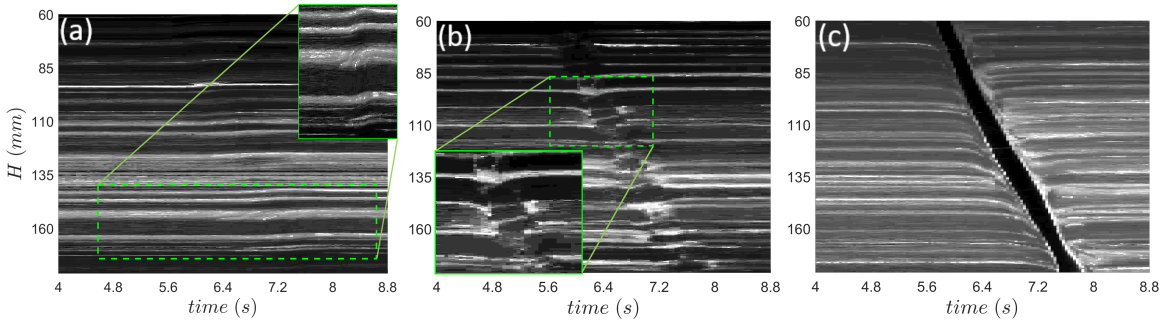

Figure 3.20: Spatio-temporal profiles of light intensity for vertical lines in Fig. 3.15b (red dashed lines). d_s=20 mm, d_g=5.72 mm. Distance between the pixel line and the sphere central axis: (a) 39.19 mm; (b) 19.69 mm; (c) 1.69 mm. Insets show zoomed areas where fluid deformation is more clear.

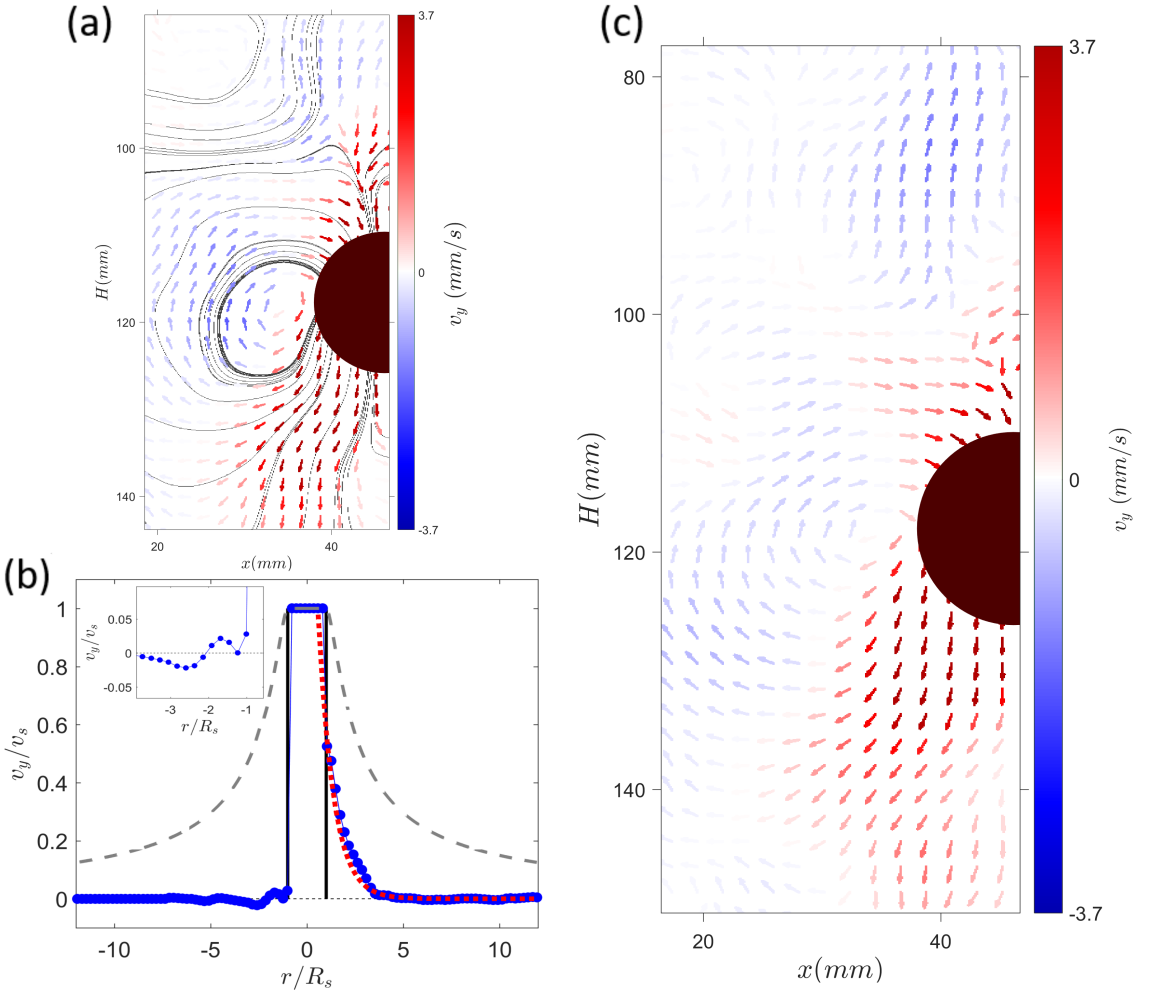

Figure 3.21: Linear regime, d_s=19 mm, d_g=6.2 mm. (a) Vertical component of instant velocity field. Full lines are streamlines. (b) Vertical component of velocity, v_y, normalized by the sphere velocity, v_s, as function of the ratio between distance, r, and sphere radius, R_s. Sphere moves here from left to right. v_y is the mean of velocities in a 2-mm-large band along the vertical axis. Black lines delimit the zone overlaid by the sphere. Red dotted line is the fit to eq. (3.13). For comparison, we show with gray dashed line the velocity vertical profile obtained from eq. (3.12) for a fluid with viscosity $\eta = \eta_{eff} = K_v\dot{\gamma}^{n-1}$. (c) Vertical component of velocity for the frame following that in (a).

expected since, unlike viscous sedimentation, in viscoplastic fluids the flow is always localized nearby the sphere because the stress applied by it on the surrounding fluid decays with distance (Beris et al., 1985). Velocity decay in the front region is exponential and can be fitted to

$$\frac{v_y}{v_s} = (2.51 \pm 0.28)\, e^{-(1.27\pm0.10)\,\frac{r}{R_s}}, \tag{3.13}$$

with a sum of squared estimate of errors of 0.038. A similar exponential decay in reported in Carbopol by Putz et al. (2008).

At the back of the sphere the velocity field is significantly different: fluid moves also upward creating a negative wake. The presence of such negative wake in viscoelastic or elasto-viscoplastic fluids have already been reported both in numerical studies (Harlen, 2002; Frank and Li, 2006; Kim et al., 2005; Kemiha et al., 2006) and in experiments (Kemiha et al., 2006; Putz et al., 2008; Holenberg et al., 2012; Fraggedakis et al., 2016). As in Putz et al. (2008), in cases where we carried out PIV measurements, Re is small and the possible influence of inertia on the creation of the negative wake is irrelevant ($Re \leq 0.12$ for the reported cases in Fig. 3.16 and Fig. 3.21, Table 2.8 and 2.5). In Harlen (2002) the nature of the negative wake is assumed to be linked to the elasticity of the fluid (elastic recoil of shear stresses) and its appearance to be due to the relaxation of shear stresses generated close to the side of the sphere. Similar conclusions are presented in Putz et al. (2008), according to which the fore-aft asymmetry has to be found in the elastic component of the fluid bulk rheology.

3.5.2 Intermittent regime

We move now to the intermittent case. Here the motion of the sphere is characterized by discontinued cycles of irregular motion at almost constant velocity suddenly broken off by periods where the sphere does not move at all. These "stop" intervals do not happen in the same way for every experiment: during the sphere fall, they show up at different heights in the fluid column and can last differently, up to involve almost the 60% of total time the sphere takes to descend 30 cm (blue line in Fig. 3.3a and Fig. 3.4f). In Fig. 3.22 we show the velocity field both during the "go" part and the "stop" part for a sphere to grain size ratio of d_s/d_g=2.1. Even though the velocity of the sphere is here more disturbed by fluid grains, during the "go" phase the fluid velocity fields is similar the one shown for the linear case (Fig. 3.22a): one also finds a fluid region that moves and one that does not, as well as a negative wake. Same conclusions can be deduced by looking at the evolution through time of a vertical cross section in Fig. 3.23. During a "go" event, fluid is pushed downward by the sphere and it will flow upstream immediately after the sphere transit, as highlighted by the shifting of bright and dark bands in the zoomed box in Fig. 3.23.

Similarly, for the same experiment in Fig. 3.24, we show the time evolution of the lateral extension of the fluidized region. Fig. 3.24a is the spatiotemporal evolution for a "go" phase. As we highlighted for the linear regime, bright bands on the side of the sphere are

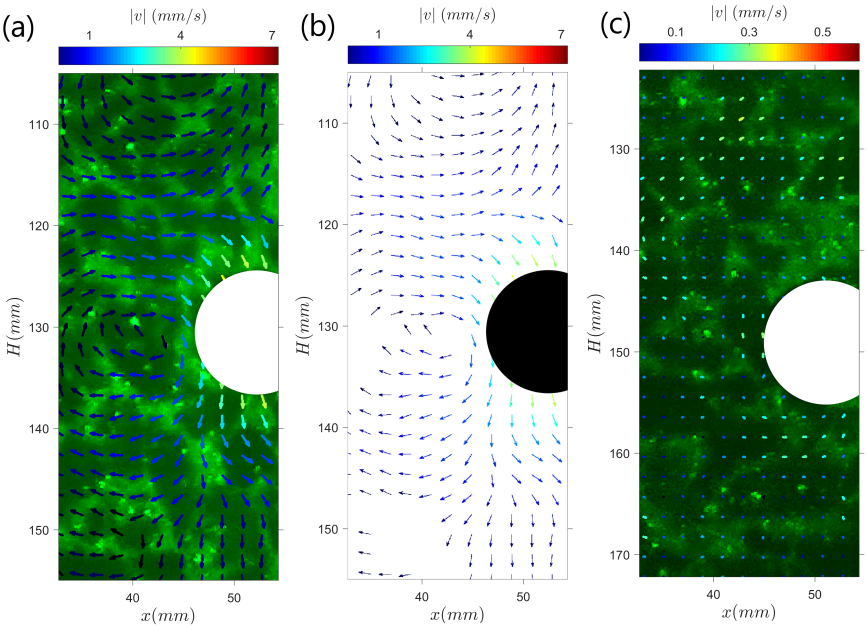

Figure 3.22: Intermittent regime, d_s=12 mm, d_g=5.72 mm. x-axis indicated the distance from the lateral wall. (a) and (b): moving fluid during the "go" part. Snapshot taken 39.4 s after the sphere was released. Vectors length is kept constant and velocity magnitude is shown by the colormap. (c) Motionless fluid in the "stop" part. Snapshot at time t=72 s. Here vectors length and colour refers to the magnitude of velocity field (vectors length is ten times the pixel displacement measured).

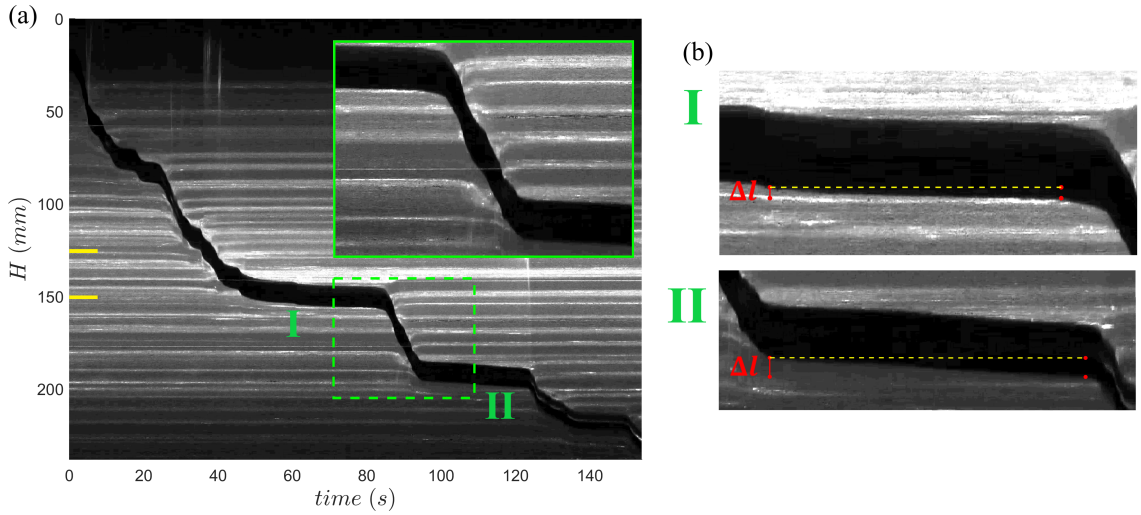

Figure 3.23: (a)Spatio-temporal profile of light intensity for a vertical line centred on the sphere for the intermittent regime. The experiment is the same of Fig. 3.22. Inset shows the motion of the sphere between two "stop" events. (b) Main stop events zoomed from (a) (I and II). Δl indicates the maximal compression of material in front of the sphere before motion starts again.

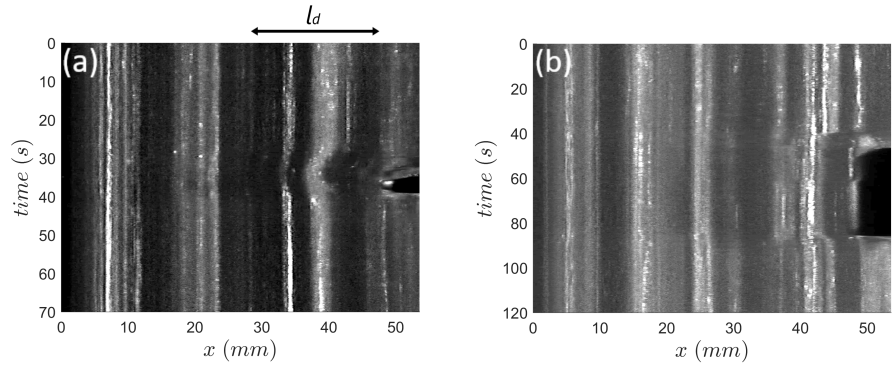

Figure 3.24: (a) Horizontal cross-sections at distance of 125 mm from the top during a "go" phase (height indicated by the upper yellow line in Fig. 3.23). (b) The same but at distance of 150 mm from the top where the sphere is in its "stop" phase (lower yellow line in Fig. 3.23). Same experiment of Fig. 3.22 and Fig. 3.23.

distorted once the sphere arrives. When the sphere leaves the horizontal pixel line in which the spatiotemporal plot is carried out, they go back to the initial position. The width of the fluidized region is estimated from the figure to be l_d=14.3 mm. Hence, given the sphere diameter d_s=12 mm, the width of yield surface from the center of the sphere is L_{fluid}=20.3 mm. For the same gel (i.e. same rheological properties), by calculating L_{fluid} from eq. (3.11), one gets L_{fluid}=19.1±5.2 mm, in agreement with the previous value measured directly from the spatiotemporal plot of a "go" event. However, the situation changes during the stop phase. Fig. 3.24b shows that once the sphere is arrested, the portion of fluid at its side seems to not move as well. Here in fact bright and dark lines do not show any evident time evolution during the period in which the sphere is at rest.

We can explain observations in the intermittent regime by recalling the characteristics of soft glassy materials. In this case the flow occurs through a sequence of elastic (reversible) deformations and local plastic (irreversible) rearrangement events during which stresses are relaxed (Mansard and Colin, 2012). The latter will be all the more common the higher the local shear stresses are (e.g. in the case of a larger sphere). Moreover, since they are elastically combined, i.e. the stress released after a plastic event is transmitted through the material by elastic interactions, a single event can trigger entire avalanches (Balmforth et al., 2014). In our case, from Fig. 3.23b, one can notice that during a "stop" phase a very slow motion in front of the sphere occurs. In a first stage, we consider this motion simply due to elastic compression of one grain under the weight of the sphere. The consequent deformation during the stop phase would be $\varepsilon = \Delta l/d_g$, where Δl indicates the total compression of the grain. The maximal percentage deformation measured is $\varepsilon \simeq 45\%$. This value is definitely too large to be associated only with the elastic compression of a single grain. On the other hand, the elastic deformation could affect several grains instead of a single one as hypothesized. And it can also occur simultaneously with a few rearrangements. We cannot access the number of plastic events during the "stop" phase because they occur in all directions and we only have information about the illuminated 2D plane. However, the change in dynamics is

evident once a threshold of maximal compression is reached or a sufficient number of plastic rearrangement events are triggered in the region under compression. When this occur, an avalanche-type of event takes place. It is then during this sudden event that stresses are relaxed and the sphere moves downward again.

3.6 Summary of the main results

In this chapter we have experimentally investigated the influence that the size of particles which build up the structure of an yield stress fluid has on the dynamics of a spherical intruder falling under gravity through it. As the typical size of the gel grains was varied between 1 and 6 mm and the sphere diameter was varied between 3 and 25 mm, there exists a range where they become comparable.

We have been able to expand from three (in Carbopol) to five (in SAP) the observed regimes of sphere motion: (1) a linear regime where the sphere has a steady-state motion; (2) an irregular regime superimposed to a linear one where spheres never stop during their way down but their velocity varies; (3) an intermittent regime in which periods of no-motion and periods of irregular falls follow one another; (4) a logarithmic regime where the sphere velocity progressively decreases; (5) no-motion. Beside the classical steady-state motion (1) and stoppage regimes (5), typical of viscoplastic fluids, the interaction between moving objects and the fluid structure results in two additional regimes ((2) and (3)) where the motion becomes more chaotic. The same strong interaction between the sphere and the gel grains is also observed from the sphere total travelled distance in the horizontal direction.

Moreover, we have shown that the effective rheology of SAP follows the Herschel-Bulkley model with a power index n=0.50, making this simple set-up a good rheometer for this type of fluids.

We also found that both yield stress and consistency of the gel increase with the gel grain size, suggesting that the effective rheology, due to the material heterogeneous properties, depends on the size of the particles which constitute the fluid structure. However, it is remarkable that the overall sphere motion predicted by the Herschel-Bulkley model begins break down because it "sees" the texture only for sphere diameters less than twice the SAP grain size.

The region of fluid subjected to the solid-liquid transition have also been discussed. We have compared the yield surface obtained from the velocity field with the fluid deformation detected by analyzing spatiotemporal sphere fall profiles. Finally, a scaling law for the lateral extension of the yielded surface has been provided and found in agreement with other published studies.

Chapter 4

Simulations of thermal plumes in an EVP fluid

In the previous chapters, we saw experimentally how the fluid structure could influence the solid-flowing transition. A related question is of course how to describe mathematically the rheology in order to model the onset of motion in a yield-stress fluid. In particular, when is the classical Hershel-Bulkley (viscosity-plastic "VP") formulation sufficient to generate all the observations? In this chapter, we investigate this question, comparing the regularized "VP" and the elasto-visco-plastic approaches in numerical simulations. To be able to probe the solid-flowing transition, we look at the onset and development of a thermal plume in a yield-stress fluid like Carbopol.

Thermal convection in yield stress fluids has been already introduced in section 1.4.2. Theoretically, in a Rayleigh-Benard Convection ("RBC") configuration where a layer of fluid is uniformly heated from below and cooled from above, the conductive regime in a yield stress fluid (modeled with a viscous-plastic rheology) is linearly stable for all Rayleigh numbers (e.g. Zhang et al., 2006). This is at odds with experiments which have reported the development of RBC without any applied finite-amplitude disturbance (Darbouli et al., 2013; Metivier et al., 2017; Kebiche et al., 2014). What is missing in the VP model to allow the development of RBC remains debated.

A better understood way to get a yield stress fluid to convect is by changing the heating configuration. If a localized heating source is used instead of heating the entire fluid's lower surface, this laterally heterogeneous heating constitutes a finite amplitude perturbation and thermal plumes can develop, even in a yield stress fluid (Davaille et al., 2013). The presence of a yield stress directly influences the onset of convection as well as the plume temperature, velocity and size. Following the experiments of Davaille et al. (2013), the development of thermal plumes has also been investigated using numerical simulations by Massmeyer et al. (2013) and Karimfazli et al. (2016). The difference between the two mainly regards the numerical technique used to deal with the singularity of the effective viscosity on the

yield surface (i.e. on the boundaries of the plume). Although both approaches capture some characteristics of plumes obtained in the laboratory, they also show some limitations. Moreover, in both cases the elasticity that is usually present in jamming fluids (e.g. chapters 3 for SAPs and Dinkgreve et al. (2017) for Carbopol) is ignored.

In this chapter we attempt to simulate numerically the development of plumes in Carbopol. We introduce elasticity in the problem and we explore the influence it has on plume dynamics. In order to do so, we use the StagYY code (Tackley, 2008), a well known code primarily used to model Earth's mantle dynamics. In fact, beside industrial applications (e.g. Hunt, 1991; Steffe, 1996, for food and glass industries), the problem of development of thermal plumes in a complex rheology fluid is also important in geodynamics. As seen in chapter 1, the Earth's mantle convects and mantle plumes are responsible for intraplate volcanism. The rheology in the lower mantle, where plumes might originate, might involve dislocations motions in solid crystalline material (e.g. in crystals of bridgmanite, as described by Boioli et al., 2017). These motions will occur only if the local stresses become larger than a critical value that depends on the dislocations density (i.e. the more dislocations, the more "jammed" the material could be). This would lead to lower mantle rocks with a rheology that could be described by a formalism similar to Carbopol's (Davaille et al., 2018).

A number of different convection codes already exist to study mantle dynamics, one of which is StagYY. It is the same code used by Massmeyer et al. (2013) which first attempt to study numerically thermal plumes in a viscoplastic fluid. Massmeyer et al. (2013) already modified StagYY to implement a regularized version of the Herschel-Bulkley model. More recently the code has been updated by implementing viscoelastic rheology (Patočka et al., 2017). Here we implement the Herschel-Bulkley viscoplatic model in the viscoelastic version of the code in order to make an elasto-visco-plastic (EVP) rheology available.

The work is done in collaboration with P. J. Tackley (Institute of Geophysics, Department of Earth Sciences, ETH Zurich, Switzerland) and V. Patočka (Institute for Planetary Research, German Aerospace Center, Berlin, Germany) and is not finished yet. More runs are needed to make a detailed analysis and to quantify how including elasticity affects the plume characteristics. In this perspective, we report and discuss here the preliminary results.

4.1 Previous studies

The problem of development of thermal instabilities in yield stress fluids has been recently approached both via experiments and numerical simulations. As introduced in section 1.4.2, when a yield stress fluid is heated, buoyancy stresses due to thermal expansion may not be large enough to exceed the yield stress. In this case, fluid motion is prevented and the fluid remains motionless until the yield stress is reached.

Davaille et al. (2013) investigated this problem experimentally by looking at the development of thermal plumes in Carbopol. In their experiments Carbopol filled a rectangular tank and was heated from a localized heating source placed on the center of the bottom of

the tank. They visualized the growth of thermal instabilities by using three different types of Thermo-Liquid Crystals (TLCs). Each TLC reflects the light at one specific temperature and allows to image the structure of the temperature field (e.g. Fig. 4.1 and Fig. 4.2). The three specific isotherms visible in Fig. 4.1 and Fig. 4.2 are 26.6±0.5 °C, 31.6±0.5 °C and 39.5±0.5 °C. For clarity, on the experimental isotherms we overlap isotherms that have been computed for a purely conductive regime. In addition to the thermal structure evolution recognizable in the spatiotemporal plot of Fig. 4.1, Fig. 4.2a-c show the front view of three specific stages of the development of the thermal instability. In fact, its growth can be described in three main steps: (1) a no-motion phase where a hot pocket grows up by thermal diffusion around the heater (Fig. 4.2a). At this stage, experimental and numerical isotherms show a good overlap. (2) Slow creep takes place within the growing hot pocket. It can be seen by following aggregates of TLCs which form reflecting particles that move slowly upward (e.g. in Fig. 4.1 where bright lines are not longer horizontal). At this stage the experimental isotherms start to deviate from the purely conductive regime as shown by the slight discrepancy in Fig. 4.2b. The mismatch between experimental and numerical isotherms highlights how the conductive regime is gradually lost starting from this stage. (3) A hot finger rises upward at time $t{=}t_{onset}$ (Fig 4.2c). Upwelling occurs only within the thermal anomaly and shear is strongly localized along plume boundaries. The fluid within the anomaly moves then as a plug and the overall plume shape resembles that of a finger.

These three different regimes can be bounded by the dimensionless yield parameter Y_0, defined as

$$Y_0 = \frac{\sigma_{th}}{\sigma_y} = \frac{\alpha \rho g P_w}{k \sigma_y}, \tag{4.1}$$

where α is the thermal expansion, ρ the fluid density at room temperature, k the thermal conductivity, and P_w the thermal power supplied by the heater. The yield parameter compares the thermally induced stress (σ_{th}) with the yield stress (Davaille et al., 2013) and has not to be mistaken with the Yield number, Y (eq. (1.39)), used so far. Fig. 4.3a shows that the transition between no-motion, stage (1), and cell regime, stage (2), is marked by the critical yield parameter Y_{0c1}. Similarly, the transition from cell regime to plume regimes, stage (3), occurs at an yield parameter Y_{0c2}. Therefore, for $Y_0 < Y_{0c1}$ =120±15 only a motionless hot pocket is formed. For $Y_{0c1} < Y_0 < Y_{0c2}$ =260±20 a small scale convection is confined inside the hot pocket. For $Y_0 > Y_{0c2}$ plumes can rise up.

In chapter 3 we used the inverse of the Yield number, $Y_{inv} = 1/Y$, which represents the ratio between the buoyancy stress and the yield stress, to describe the critical motion condition for a falling sphere or a rising bubble in yield stress fluid. The inverse of the Yield number writes as

$$Y_{inv} = \frac{g \Delta\rho \, d}{3 \sigma_y}. \tag{4.2}$$

Making an analogy between the falling sphere and the thermal instability, one can con-

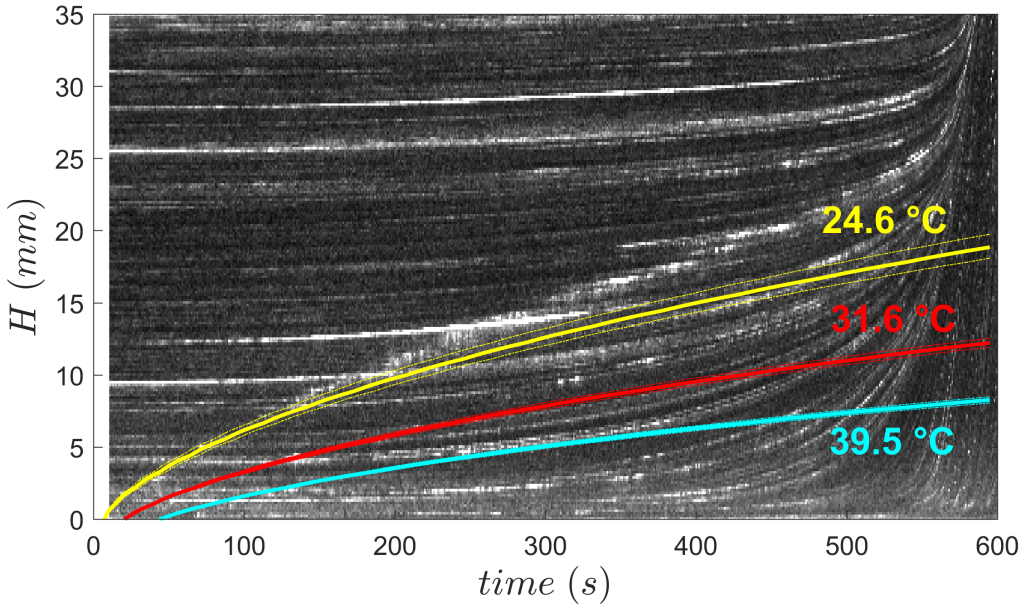

Figure 4.1: Thermal structure evolution in Carbopol for the case where the patch is bottom mounted (experiment from Davaille et al. (2013)). The figure shows the light intensity of the pixel line in the center of the tank as a function of time. The brighter lines are the TLCs isotherms. The same isotherms are reproduced numerically in the conductive regime and plotted with different colours: yellow (24.6±0.5 °C), red (31.6±0.5 °C) and blue (39.5±0.5 °C).

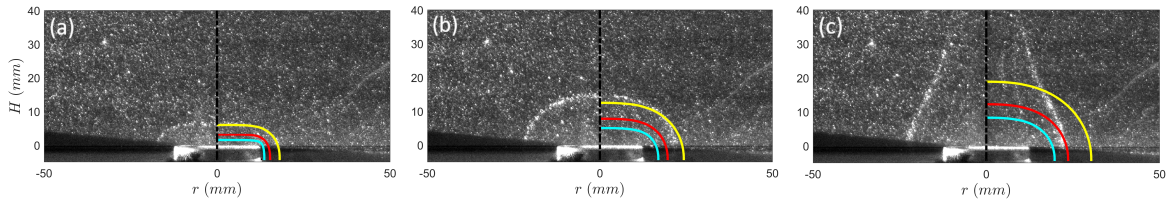

Figure 4.2: Front view of the growth of a hot pocket and the development of a plume in Carbopol. Same experiment and isotherms of Fig. 4.1. (a) t= 100 s, numerical isotherms fit well the experimental ones. (b) t= 300 s, a mismatch between isotherms is recognizable. (c) t= 600 s, rising of the hot plume.

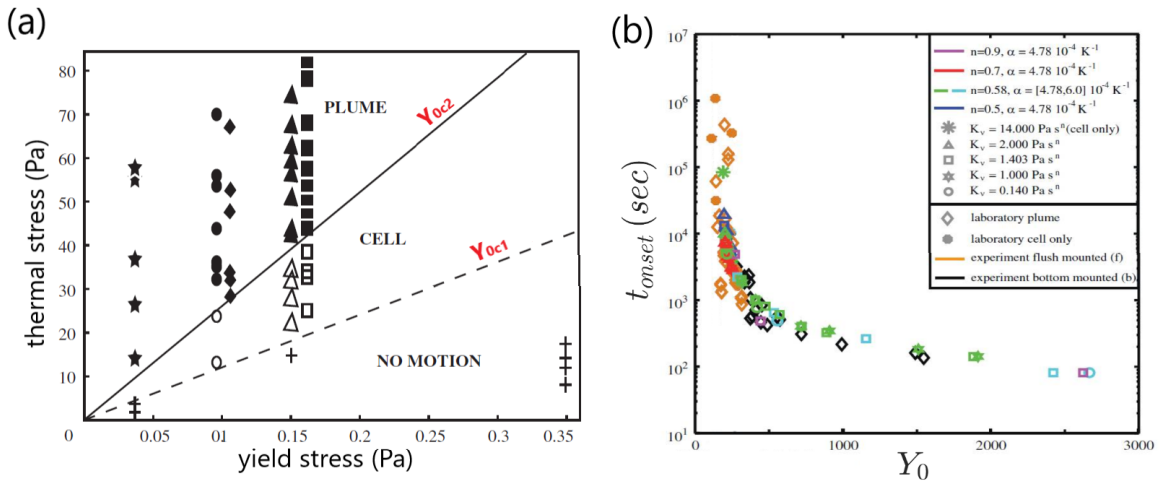

Figure 4.3: (a) Regime diagram for thermal instabilities generated from a localized heating point. Axis represent the yield stress, σ_y, and the thermally induced stress, σ_{th}. Y_{0c1} (dashed line) separates no-motion (crosses) from experiments where convection was confined around the heater (empty symbols). Y_{0c2} (solid line) separates cell convection from plumes (filled symbols). Modified from Davaille et al. (2013). (b) Modified from Massmeyer et al. (2013). Dependence of the onset time, t_{onset}, on the yield parameter Y_0.

sider the hot pocket forming around the heater before the plume rises as a buoyant "entity" that tries to go up but is kept anchored at the bottom surface by the fluid yield stress. Hence in eq. (4.2) d=$2r_{eq}$, with r_{eq} the equivalent radius of a sphere having same volume of the hot pocket. We can quantitatively define the hot pocket as bounded within the temperature field by the isotherm $T_{lim} = 0.1\,\Delta T$, where $\Delta T = T_{max} - T_{amb}$ and T_{max} is the maximum temperature at that moment. The hot pocket is therefore represented by the volume of fluid at $T \geqslant T_{lim}$. For the density difference term we refers to the mean $\Delta\rho$ within the fluid pocket, that is $\Delta\rho \simeq \overline{\Delta\rho} = \alpha\rho(\overline{T}_{hot\,pocket} - T_{amb})$ where $\overline{T}_{hot\,pocket}$ is the average temperature of the pocket. Davaille et al. (2013) found that the thermal instability will rise only if $Y_{inv} > Y_{inv_C} = 8.8 \pm 0.7$, a critical value very close to the one for the falling sphere discussed in previous chapters (i.e. $Y_{inv_C} = 6.99$).

Thermal plumes induced in a yield stress fluid by a localized heating have been investigated through numerical simulations as well. Massmeyer et al. (2013) tried to reproduce numerically experiments in Carbopol done with a configuration similar to Davaille et al. (2013). They simulated in 3-D a fluid with rheological properties of those of Carbopol being subjected to a localized heating. To solve the system governing equations they used a finite volume code (StagYY, Tackley (2008)) with a regularized Herschel-Bulkley model for the constitutive equation. The specific form of regularization will be described later on, but it simply considers a viscosity truncation for very small strain rates. In this way the code avoids the singularity coming from the Herschel-Bulkley model, which implies infinity viscosity as the shear rate goes to zero, by assuming a fluid with very high viscosity at $\sigma < \sigma_y$. However, this assumption leads to a purely viscous description of the fluid which will always

move, although very slowly, even for local stresses lower than the yield stress. Massmeyer et al. (2013) recover the essential features of plumes originated in laboratory. They obtained plumes with a finger-like shape and a strong shear localization on plume boundaries. The onset of convection is also similar to the experimental one: yielding and upward motion take place a long time after heating starts, and the plume onset time (t_{onset}) depends on Y_0 (Fig. 4.3b). They are two asymptotic limits: for Y_0 decreasing towards Y_{0c1}, the onset time increases rapidly to infinity, whereas for very large Y_0, it tends to the classical finite values obtained in absence of a yield stress. The influence of the yield stress is strongest for the first branch, and it is also where a small difference in Y_0 can have the largest influence on the onset time and maximum height reached by the plume. It is also where one can expect the influence of elasticity to be the strongest. Unfortunately, a more precise comparison between their numerical results and laboratory experiments was made difficult by the experimental uncertainties of 30% on the fluid properties. Nevertheless they find that beside a yield parameter larger than Y_{0c}, plume development also requires the Bingham number being supercritical (i.e. Bi <1). The Bingham number compares the yield stress to the viscous stress and writes:

$$Bi = \frac{\sigma_y}{K_v \dot{\gamma}^n}, \tag{4.3}$$

Motion is therefore expected only when local shear rates are larger than the critical strain rate corresponding to Bi=1, i.e. for $\dot{\gamma} > \dot{\gamma}_c = (\sigma_y/K_v)^{1/n}$. Note that when $Bi = 1$, the stress is $\sigma_c = 2\sigma_y$ and the viscosity $\eta_c = 2\sigma_y/\dot{\gamma}_c$.

Similar conclusions can be drawn from the numerical work of Karimfazli et al. (2016). Differently from Massmeyer et al. (2013), they investigated in two dimensions the development of thermal instabilities in a Bingham fluid with an augmented Lagrangian algorithm (see Ciarlet et al., 2010, for a review on the method). Therefore in their case the shear-thinning index is n=1 and the effective viscosity is $\eta_e = \sigma_y/\dot{\gamma} + \eta_p$, where η_p is the plastic viscosity of the fluid that in our convention reads as the consistency, K_v. They characterized the flow in terms of three dimensionless number (besides the length ratio): the Yield number, the Bingham number and the Rayleigh number, with the latter representing the ratio between time scales for advective and conductive heat transfer, that is $Ra = (\alpha g \rho \Delta T h^3)/(k\eta_p)$, where h is characteristic size of the tank. Taking for the strain rate in Bi formula the value of $\dot{\gamma}_{cond}$=κ/d^2, one can rewrite the Rayleigh number in terms of the other two dimensionless numbers:

$$Ra = 3Y_{inv}\frac{\sigma_y d^2}{\kappa\eta_p} = 3Y_{inv}Bi_{cond}, \tag{4.4}$$

with η_p=K_v and Bi_{cond} the Bingham number with $\dot{\gamma} = \dot{\gamma}_{cond}$. As in the previously cases, Karimfazli et al. (2016) found the start of convection to be controlled by Y_{inv}. Moreover, they found that once deformation starts, the convective flow depends also on Ra and strong buoyancy stresses compared to viscous stresses are needed to form the plume head as well as

to allow repeated pulsations. From their study, the Rayleigh number seems to be crucial in studying the transition between no plume pulsing (at large Ra), as the case in Massmeyer et al. (2013), and plume episodicity (at large Ra), as the case in Davaille et al. (2013). However, a separation between episodicity and non-episodicity based on the definition of Ra, which has the size of the box at the numerator, implies always having pulsations for an infinitely high tank. Pulsing, however, was not found to depend on tank height in the laboratory experiments of Davaille et al. (2013), but instead, it seems to depend on the fluid rheology. Although pulsations and plume episodicity remain an open topic, it is not the target of our work and it will not be discussed further.

4.2 Governing equations

We assume an incompressible fluid in the Boussinesq approximation with infinite Prandtl number (cf. chapter 1). Boussinesq approximation allows to ignore all density differences, because sufficiently small, except those linked to the buoyancy term and caused by the thermal expansion, α. In the buoyancy term the dependence of density ρ on temperature T is then given by

$$\rho - \rho_0 = \Delta\rho = -\rho_0\alpha(T - T_0), \tag{4.5}$$

where ρ_0 is the density at reference temperature T_0.

The system dynamics is then governed by the following equations of conservation of mass, momentum and energy:

$$\nabla \cdot \boldsymbol{v} = 0, \tag{4.6}$$

$$0 = -\nabla P + \nabla \cdot \boldsymbol{\sigma} + \rho\boldsymbol{g}, \tag{4.7}$$

$$\frac{\partial T}{\partial t} = \kappa\nabla^2 T - \boldsymbol{v} \cdot \nabla T, \tag{4.8}$$

where $\boldsymbol{v}$ is the velocity field, P the pressure, $\boldsymbol{g}$ the gravity acceleration, κ the thermal diffusivity, i.e. $\kappa = k/\rho C_p$, and $\boldsymbol{\sigma}$ the deviatoric part of the total Cauchy stress tensor $\boldsymbol{\sigma}_{tot}$=$-P\boldsymbol{I} + \boldsymbol{\sigma}$, where $\boldsymbol{I}$ is the identity tensor. Both thermal diffusivity and expansivity are assumed constant.

Together with these equations, to describe the fluid behaviour under applied stress, one has to define a proper stress-strain rate constitutive relation. Under the incompressible fluid approximation the classical simplified law of viscous friction is

$$\boldsymbol{\sigma} = 2\eta\mathbb{D}, \tag{4.9}$$

where η is the viscosity and $\mathbb{D}$ the deviatoric part of the strain rate tensor. For simple shear flow, the absolute value of shear rate is $\dot{\gamma}=2\,|\mathbb{D}|$, where $|\mathbb{D}|$ is the second invariant (i.e. the magnitude) of the tensor, $|\mathbb{D}|=\sqrt{\frac{1}{2}D_{ij}^2}$. Eq. (4.9) supposes a linear (Newtonian) dependence between applied stress and strain rate and obviously it cannot be used in our case where rheology is non-linear. Formulation and implementation of the proper constitutive law is discussed in the next two subsections.

4.2.1 Viscous approximation (VP)

We have first tried to reproduce the results presented in Massmeyer et al. (2013) by using their same approach but with an up-to-date version of StagYY code (Patočka, 2018). Massmeyer et al. (2013) carried out simulations of thermal convection in Carbopol in order to replicate their own experiments and those of Davaille et al. (2013). To avoid the theoretical singularity that appears in the Hershel-Bulkley formulation for $\dot{\gamma} \to 0$ (eq. (1.19)), they applied a viscous truncation by using the regularized model of de Souza Mendes and Dutra (Mendes and Dutra, 2004) in which a finite high effective viscosity is introduced for small strain rate values. In addition to a shear-rate dependent viscosity, their rheological measurements of Carbopol flow curve reveal a weak dependence on temperature. This dependence has shown up in the form of a temperature dependent consistency, that is

$$K_v(T) = K_{v0} * 1.6927\, e^{[-0.0257(T-293.15)]}. \tag{4.10}$$

with K_{v0} is the consistency at room temperature (T_{amb}) and temperature is expressed in Kelvins. On the other hand, both yield stress, σ_y, and shear-thinning index, n, were found constant with respect to temperature. Taking into account this temperature dependence, the regularized model becomes:

$$\boldsymbol{\sigma} = \left[1 - \exp\left(\frac{-\eta_{max}|\mathbb{D}|}{\sigma_y}\right)\right](\sigma_y + K_v(T)|\mathbb{D}|^n)\mathbb{D}|\mathbb{D}|^{-1}, \tag{4.11}$$

where η_{max} is the upper viscosity cut-off. The first bracket on the right side of eq. (4.11) represents the regularization term whereas the second one is the Hershel-Bulkley model (Saramito and Wachs, 2017). For large enough values of η_{max}, we do not expect it to play a significant role either in the plume dynamics or in its onset time. In fact, Massmeyer et al. (2013) reported no influence in plume behaviour for η_{max}=[10^8, 10^{10}, 10^{12}] Pa s. For this reason, we chose their lowest value, i.e. η_{max} is here always taken equal to 10^8 Pa.s. In addition to the upper viscosity cut-off, to avoid too large viscosity contrasts, we also use the lower cut-off for the viscosity η_0=0.01 Pa.s. This minimum cut-off of viscosity has never been reached during computations and therefore has never affected the fluid flow.

4.2.2 Visco-elastic rheology (VE)

Viscoelasticity in StagYY has been implemented by Patočka et al. (2017), using the rheological description of a viscoelastic Maxwell material. As seen in section 1.3.4, the Maxwell constitutive equation represents a viscoelastic fluid as a viscous dashpot and an elastic spring connected in series, that is:

$$\mathbb{D} = \mathbb{D}_{viscous} + \mathbb{D}_{elastic} = \frac{1}{2\eta}\boldsymbol{\sigma} + \frac{1}{2G}\overset{\triangledown}{\sigma}, \tag{4.12}$$

where G is the shear modulus and $\overset{\triangledown}{\sigma}$ is the objective stress tensor rate, namely the frame-invariant derivative. In fact, differently from the purely viscous case, here one has to include an invariant stress derivative which incorporates both stress rotation and advection. A general form of $\overset{\triangledown}{\sigma}$ writes

$$\overset{\triangledown}{\sigma} = \frac{\partial \boldsymbol{\sigma}}{\partial t} + \boldsymbol{v} \cdot \nabla\boldsymbol{\sigma} + (\boldsymbol{\sigma}\mathbb{W} - \mathbb{W}\boldsymbol{\sigma}) - m(\boldsymbol{\sigma}\mathbb{D} + \mathbb{D}\boldsymbol{\sigma}), \tag{4.13}$$

where the spin $\mathbb{W} = W(\boldsymbol{v}) = \frac{1}{2}(\nabla\boldsymbol{v} - (\nabla\boldsymbol{v})^T)$ is the antisymmetric part of the velocity gradient, that is the non-objective vorticity tensor. Here the symbol T indicates the transpose operation. The symmetric part of the velocity gradient is instead the already introduced rate-of-deformation tensor (or stretching) $\mathbb{D} = D(\boldsymbol{v}) = \frac{1}{2}(\nabla\boldsymbol{v} + (\nabla\boldsymbol{v})^T)$. m symbol in eq. (4.13) is a parameter of the derivative, $m \in [-1,1]$ and it can be chosen arbitrarily since it is objective and its product with $\mathbb{D}$ does not affect the transformation properties of the frame-invariant $\overset{\triangledown}{\sigma}$. Using m=0 one obtains the Jaumann rate, the typical rate used in viscoelastic convection and geodynamics contexts. This is because it is the only one among the others objective stress rate formulations (e.g. the Oldroyd rate, the Green-Naghdi rate, etc.) that preserves the deviatoric property of the tensor needed in a framework where stress in divided into its deviatoric and hydrostatic part (Gerya, 2019; Muhlhaus and Regenauer-Lieb, 2005; Beuchert and Podladchikov, 2010).

The Jaumann objective stress tensor rate in this case writes:

$$\overset{\triangledown}{\sigma}_{(Jau)} = \frac{\partial \boldsymbol{\sigma}}{\partial t} + \boldsymbol{v} \cdot \nabla\boldsymbol{\sigma} + (\boldsymbol{\sigma}\mathbb{W} - \mathbb{W}\boldsymbol{\sigma}) \tag{4.14}$$

and using eq. (4.14) in eq. (4.12), the constitutive equation becomes:

$$2\mathbb{D} = \frac{1}{\eta}\boldsymbol{\sigma} + \frac{1}{G}\left[\frac{\partial \boldsymbol{\sigma}}{\partial t} + \boldsymbol{v} \cdot \nabla\boldsymbol{\sigma} + (\boldsymbol{\sigma}\mathbb{W} - \mathbb{W}\boldsymbol{\sigma})\right]. \tag{4.15}$$

In Earth's mantle dynamics, the role of elasticity on the overall mantle convection have been recently investigated by Thielmann et al. (2015) and Patočka et al. (2017, 2019) by assuming a viscoelastic mantle. In either cases, the implementation of viscoelasticity rather than viscous or viscoplastic rheologies to investigate the evolution of a rigid planetary lid seems not to affect significantly the general style of convection and convective forces (Thiel-

mann et al., 2015). On the other hand, however, it has a definite impact on the lithosphere, which being colder is also more viscous than the mantle. The use of elasticity is found to decrease lithospheric stresses (if lithosphere can bend and build topography) and to notably alter the spatial distribution of stress within it. Lithosphere deformation and consecutive topographic response are also anticipated when viscoelastic and a sufficient large relaxation time are considered.

The choice $m = 0$ in eq. (4.13) remains valid as long as the Weissenberg number $We = \eta\dot{\gamma}/G$ is smaller than 1. This is the case for lithosphere and mantle dynamics. For higher values, numerical instabilities and non-physical strain softening is observed (Beuchert and Podladchikov, 2010; Thielmann et al., 2015). For plumes motion in our carbopol experiments, we can take η_c and $\dot{\gamma}_c$ as viscosity and strain rate scales, respectively. Then We will remain less than 1 for $G > 0.3$.

4.2.3 Elasto-visco-plastic rheology (EVP)

The second rheological model we test combines viscoplasticity (section 4.2.1) together with viscoelasticity (section 4.2.2).

As we have seen for the falling sphere in SAP, the simple viscoplastic approximation fails to describe the overall deformation of a Hershel-Bulkley fluid since it does not account for elastic stresses, although they become important at small deformations. To take into account elasticity, we formulate an elasto-visco-plastic (EVP) rheology by including plastic effects in the viscoelastic Maxwell formulation. The approach is similar to the EVP model of Saramito and Wachs (2017), used by Fraggedakis et al. (2016) to study elastic effects during the fall of a ball in Carbopol.

In the viscoelastic constitutive equation, eq. (4.15), a proper viscosity law has to be chosen and expressed either in the form of $\eta = \eta(\boldsymbol{\sigma})$ or $\eta = \eta(\mathbb{D})$. In our case the Hershel-Bulkley rheology is implemented in the viscous component (i.e. the dashpot) whereby viscosity depends on both strain-rate and temperature. We use then the same de Souza Mendes and Dutra formulation of eq. (4.11), which rewritten in form of $\eta = \eta(\mathbb{D})$ reads

$$\eta = \frac{1}{2}\left[1 - \exp\left(\frac{-\eta_{max}|\mathbb{D}|}{\sigma_y}\right)\right](\sigma_y + K_v(T)|\mathbb{D}|^n)|\mathbb{D}|^{-1}. \tag{4.16}$$

Since this term only enters in the viscous part ($\mathbb{D}_{viscous}$) of the bulk rate of deformation ($\mathbb{D}$), the strain rate used to solve eq. (4.16) is only the viscous one, i.e. $\mathbb{D}_{viscous} = \mathbb{D} - \mathbb{D}_{elastic}$. In other words, the non-linear viscoplastic rheology based on $\eta = \eta(\mathbb{D})$ in the viscoelastic case becomes $\eta = \eta(\mathbb{D}_{viscous})$ and the final constitutive equation writes

$$2\mathbb{D} = \frac{1}{\eta(\mathbb{D}_{viscous}, T)}\boldsymbol{\sigma} + \frac{1}{G}\left[\frac{\partial\boldsymbol{\sigma}}{\partial t} + \boldsymbol{v}\cdot\nabla\boldsymbol{\sigma} + (\boldsymbol{\sigma}\mathbb{W} - \mathbb{W}\boldsymbol{\sigma})\right] \tag{4.17}$$

where $\eta(\mathbb{D}_{viscous}, T)$ indicates a viscosity which is a function of temperature and the viscous

part of the total rate-of-deformation and is given by eq. (4.16) for $\mathbb{D} = \mathbb{D}_{viscous}$.

For clarity, we report here the discretization work done by Patočka et al. (2017), based on the formulation by Moresi et al. (2002), for the viscoelastic version of StagYY. Eq. (4.17) is discretized in time with a mixed Euler first-order accurate scheme: implicit to respect to $\mathbb{D}$, $\boldsymbol{\sigma}$ and η, and explicit with respect to $\boldsymbol{v} \cdot \nabla\boldsymbol{\sigma}$ and $(\boldsymbol{\sigma}\mathbb{W} - \mathbb{W}\boldsymbol{\sigma})$. Given the computational time step of $\Delta t{=}t^n - t^{n-1}$, the stress at the n-th time step is

$$\boldsymbol{\sigma}^n = 2Z^n\eta^n\mathbb{D}^n + (1 - Z^n)\left[\boldsymbol{\sigma}^{n-1} - \Delta t\,(\boldsymbol{v} \cdot \nabla\boldsymbol{\sigma} + (\boldsymbol{\sigma}\mathbb{W} - \mathbb{W}\boldsymbol{\sigma}))^{n-1}\right], \tag{4.18}$$

with

$$Z^n = \frac{\Delta t}{\Delta t + \lambda^n}, \tag{4.19}$$

where Z is the viscoelastic factor (Gerya, 2019) and $\lambda = \eta/G$ is the relaxation time, that is the time it takes for the medium to adapt to applied stresses or deformations. The product between $(1 - Z)$ and the quantities contained in the square bracket of eq. (4.18), i.e. the relaxed stress, $\boldsymbol{\sigma}^{n-1}$, the advection term and $(\boldsymbol{\sigma}\mathbb{W} - \mathbb{W}\boldsymbol{\sigma})$, corresponds to the part of energy that has not been dissipated during Δt and has remained in the system at the time t^n. Since the dissipated energy is the energy lost during the viscous deformation, the preserved part is clearly stored in the form of elastic energy.

The viscoelastic factor Z is linked with the relaxation time and evaluates the impact of elastic effects. When relaxation time is short compared to the time step ($\lambda \ll \Delta t$) then $Z \to 1$ and the material responds mostly as a viscous fluid. On the other hand, when $\lambda \gg \Delta t$, $Z \to 0$ and only the elastic contribution remains in eq. (4.18). Another way to evaluate the fluidity of a viscoelastic material is by using the Deborah number (De) already defined in eq. (1.9). In geodynamics De is usually taken as the ratio between the relaxation time and the characteristic diffusion time k/h^2, namely $De = \lambda k/h^2$, with h the characteristic length scale (for example the lithosphere thickness). When the relaxation time is much larger than the time-scale of the flow ($De \to \infty$) elastic effects dominate whereas in the opposite case ($De \to 0$) viscous effects dominate. On the other hand, De can also be formulated by using $\Delta\rho g d_s/\eta$ as flow scale, as already done in eq. (3.6) for the case of a falling sphere in SAP, a problem quite similar to the uplift of a hot plume in the mantle (cf. chapter 1). However, this latter formulation needs a length scale to be defined. In this case we can proceed as done for the yield number, that is by using the dimension that the hot pocket reaches right before the departure of the plume as length scale. The Deborah number then becomes:

$$De = \frac{\eta}{G}\frac{\Delta\rho g d_s}{\eta} = \frac{\alpha\rho(\overline{T}_{hot\,pocket} - T_{amb})g(2r_{eq})}{G}, \tag{4.20}$$

where r_{eq} indicates the radius of an equivalent sphere having the same volume of the hot pocket. For the density difference term we refers to the mean $\Delta\rho$ within the fluid pocket,

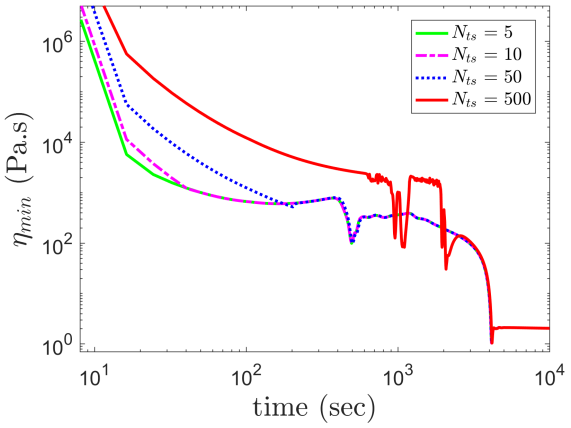

Figure 4.4: Number of time steps, N_{ts}, in which an infinity shear modulus G is brought to G=2 Pa. Lines represent the minimum of viscosity along the tank central axis of different simulations carried out only by changing N_{ts}.

that is $\Delta\rho \simeq \overline{\Delta\rho} = \alpha\rho(\overline{T}_{hot\,pocket} - T_{amb})$ where $\overline{T}_{hot\,pocket}$ is the average temperature of the pocket.

In codes that solve for velocity and not for displacement, e.g. all those designed to model viscous fluids instead of elastic solids, as it is for StagYY, a viscoelastic medium will always responds to an input with an immediate deformation of the body and this always results in a singularity. A way to avoid it, is by starting with a non-elastic rheology (i.e. $G \to \infty$ in eq. (4.12)) and only afterwards slowly decrease the shear modulus to the desired value. This is the same as gradually increase the Deborah number De from zero to its real value in non-dimensional studies. In StagYY this procedure is done within an arbitrary number of time steps, N_{ts}. In Fig. 4.4 we plot the evolution of the minimum of viscosity, η_{min}, as a function of time for plume simulations in which we only vary N_{ts}. The onset of convection that corresponds to the minimum pick of η_{min} is not influenced by N_{ts}. However, a too large number of time steps might hide early dynamics. For this reason we choose N_{ts}=10 and we keep it constant for all other simulations.

4.3 Numerical setup

The simulations we carried out are based on the experimental work already carried out in our team (Massmeyer (2013), Davaille et al. (2013)). Carbopol fills a rectangular tank and is heated from below by a localized heat source. The heater is a circular element of radius r_{hp}=1.25 cm, and is placed at the center of the bottom surface. Experiments are characterized by two different bottom configurations. In Davaille et al. (2013) the heater element is bottom mounted and gives to the bottom surface a specific topography. In Massmeyer et al. (2013) the patch is flush mounted, so that the bottom surface has no topography. In all our simulations we use the latter configuration.

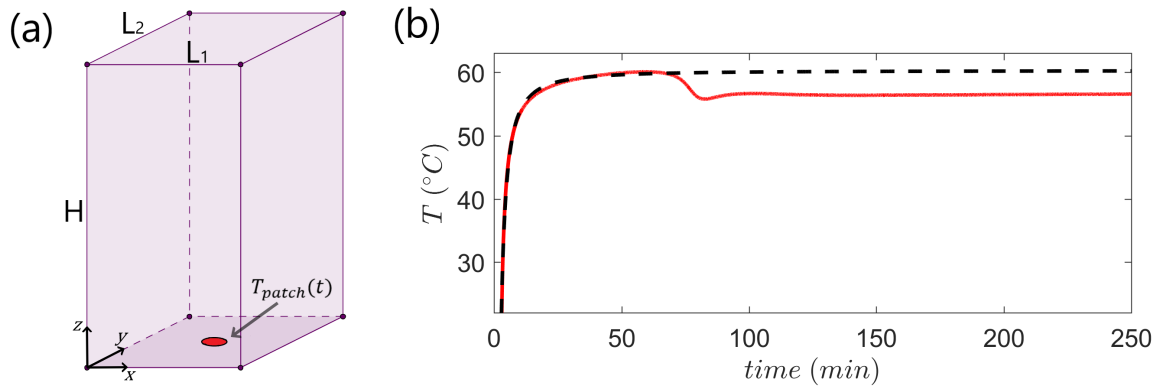

Figure 4.5: (a) Illustration of the 3-D numerical domain. L_1 is the length, L_2 the width and H the height. The patch on the bottom surface represents the heating point which follows the prescribed temperature evolution $T_{patch}(t)$. (b) Example of thermal history from laboratory experiments of Massmeyer et al. (2013) (red line). The temperature drop around 75 minutes is caused by the plume lift off. The generalized temperature used in input in our simulations is the black dashed line.

Most of our computations are made using a fluid height, H, of 40 cm but some tests have been made with H = 18.6 cm as well. For H=40 cm, the numerical configuration consists in a 3D Cartesian tank of 20x20x40 cm^3 (length L_1, width L_2 and height H, respectively) with a resolution of 64x64x128 grid points whereas for H=18.6 cm, the resolution in vertical direction is decreased by half (Fig. 4.5a).

The governing equations are solved with StagYY (Tackley, 2008). The code discretizes differential equations using a finite volume technique on a orthogonal staggered grid and solve them with an iterative multigrid method. In the staggered numerical grind, scalar variables are defined at the grid cell centre while derivatives which involve adjacent points are located at the face of the grid cells. In the multigrid method, starting from a principal and thinner grid, a series of wider grids are assembled by the interpolation of field variables and residuals. These coarser grids are used to find corrections at different wavelengths to the principal solution on the main grid. These corrections are then interpolated back to the principal grid to update the corrected solution. Simulations in 3D last roughly one day, depending on the temperature history given in input and fluid rheology.

4.3.1 Boundaries conditions

The boundary conditions are defined as follows: sidewalls and bottom surface have no-slip and no-flux boundary conditions whereas the top surface is free-slip and is kept at ambient temperature, T_{amb}=20.5 °C. The mathematical expressions of the boundary conditions in Cartesian coordinates are summarized in Table 4.1.

	Temperature	Velocity
Sidewalls:	$\frac{dT}{dx}$=0 or $\frac{dT}{dy}$=0;	$v_{x,y,z}$=0
Bottom surface:	$\frac{dT}{dz}$=0	$v_{x,y,z}$=0
Top surface:	$\frac{dT}{dz}$=0	$\frac{dv_{x,y}}{dz}$=0; v_z=0

Table 4.1: Boundary conditions used for all simulations. v is the velocity and T the temperature.

4.3.2 Fluid properties

The fluid we model is the so called "sample CBP6" in Massmeyer (2013); Massmeyer et al. (2013). It is Carbopol, with a shear-rate-dependent viscosity described by a Herschel-Bulkley model. According to their laboratory measurements, the yield stress is σ_y=0.09 Pa with 30% of uncertainty, the consistency is K_{v0}=1.403 Pa.s^n, the shear-thinning index is n=0.58, the elastic modulus is G=2.083 Pa, density ρ_f=1151 kg/m^3, thermal expansion α=4.78x10^{-4} K^{-1}, heat capacity C_p=3286 Jkg^{-1}K^{-1} and thermal conductivity k_c=0.435 Wm^{-1}K^{-1}. Thermal and rheological properties of the specific mixture have been measured at T=20 °C (Massmeyer, 2013). Her rheological measurements also points out a dependence of rheology on the temperature. Although both yield stress and shear-thinning index are found constant, this dependence has shown up in the form of a temperature dependent consistency. The latter is described by eq. (4.10).

4.3.3 Temperature history

The temperature difference applied by the heater is not constant and follows a prescribed temperature evolution that we indicate here with $T_{patch}(t)$. The temperature is measured experimentally on top of the heating patch and since experiments were made at constant thermal power P_w, the rise of the thermal plume immediately leads to a drop of the recorded temperature. Therefore, directly using as input in our simulations the temperature recorded during their experiments will force the onset of convection and its subsequent development. This limits the range of rheological properties that one can test numerically, forcing to ignore those that would start convection later. So in order to have onset times of convection (t_{onset}) that do not depend on temperature drops within the prescribed thermal history used in input, one must provide a $T_{patch}(t)$ that is independent from the registered onset time. We generalized the thermal history by fitting temperature data until the experimental plume onset and projecting the trend afterwards (e.g. the case in Fig. 4.5b). The use of a generalized temperature evolution instead of the real one may lead to discrepancies on the height reached by the plume when compared with experiments. The difference is due to the fact that in experiments the drop in heat supply is reflected in a less buoyant plume which would then rise to a slightly lower height. However, since we are here mainly interested on how the onset of convection varies for different rheological properties, the use of one temperature history or the other has no impact if kept constant for the various tests. Thus,

in our simulations we directly use the generalized $T_{patch}(t)$ as thermal history (i.e. the black dashed line rather than the red one for the example in Fig. 4.5b).

4.3.4 Thermal power estimate

For a given $T_{patch}(t)$, we first calculate the thermal power, P_w, needed in eq. (4.1) to calculate the yield parameter. The thermal power is defined as the surface integral of the amount of flux of heat

$$P_w = \int Q \, dS, \tag{4.21}$$

where Q is the heat-flux, $Q = -k_c \nabla T$, and dS the surface through which Q is calculated. In Fig. 4.6a the heat-flux generated from the patch is shown splitted in its three Cartesian components. In vertical direction Q is calculated with the temperature gradient between the first grid cell above the surface and the temperature at the bottom surface (Fig. 4.6b).

Given the time dependence of the input temperature which increases up to a plateau value (black line in Fig. 4.6b), thermal power also varies over time. The temporal evolution of P_w for the corresponding $T_{patch}(t)$ is shown in the inset of Fig. 4.6b. After the first sharp rise in temperature, the thermal power is roughly constant until the onset of convection and increases when plume lifts off. This latter increment is due to the fact that Q is now removed more efficiently than before by conduction and therefore P_w must necessarily be increased to keep ∇T constant. In what follows, we will usually refer to the minimum P_w value prior to the onset as the "heater power".

4.3.5 Tables of all simulations

The majority of simulations reported here are made by using the elasto-visco-plastic (EVP) version of StagYY described in section 4.2.3. Fluid properties that are not present in the tables are kept constant and given in section 4.3.2. Only those properties listed have been varied and systematically studied. We tested three different configurations referring to as many experimental setups in Massmeyer (2013). Experiments we refer to are "20110404", "20110502" and "20110429" in Massmeyer (2013) (see her Table 3.1). We indicate them here with "CBP6-A", "CBP6-B" and "CBP6-C", respectively.

We choose to focus our analysis within the narrow range of yield parameter Y_0 close to the critical value Y_{0c2} (for $Y_0 > Y_{0c2}$) since that is where we expect the elastic part to be important. We varied G between 20 and 0.2. Note that for the latter value, the simulation crashed as expected since the Weissenberg number is that case was greater than 1.

Below is the list of all simulations together with relevant parameters needed for the discussion in the next sections. Parameters and dimensionless numbers not already introduced will be explained in the next sections when relevant.

Table's columns refer to: name of the simulation; model version (VP: viscous approx-

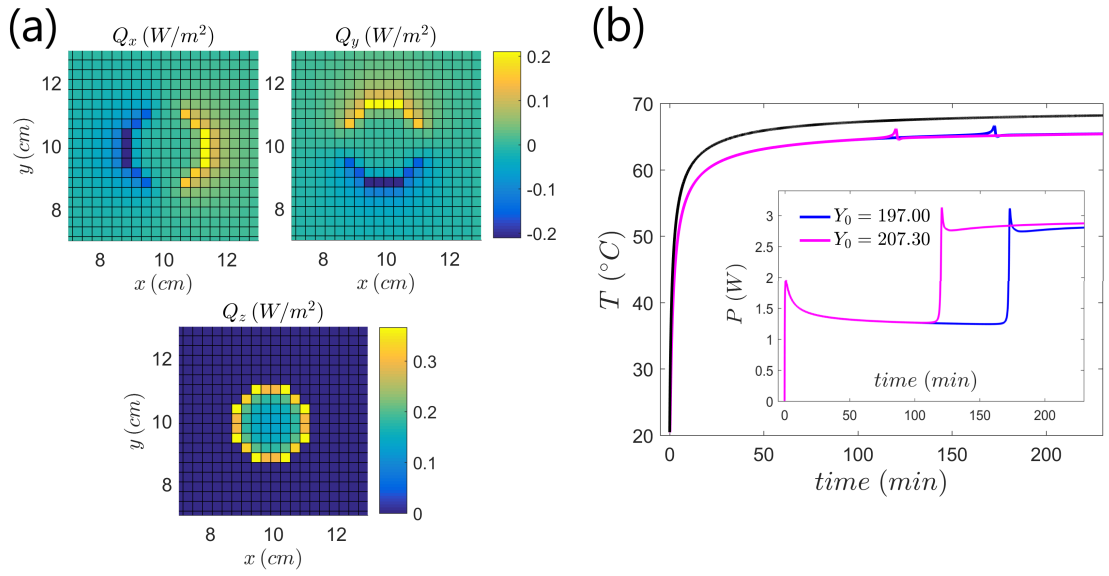

Figure 4.6: (a) Heat-flux Q out from the heating patch in x, y, z directions. (b) Example of thermal difference between the temperature $T_{patch}(t)$ prescribed for the patch (black line) and temperature of the first grid node along the central axis (color lines). The inset shows the power needed by the system to guarantee the prescribed temperature trend.

imation with elasticity turned off, EVP: elasto-visco-plastic); the reference experiment in Massmeyer (2013); thermal power P_w; yield stress σ_y; shear modulus G; plume onset time, t_{onset}, defined when the Bingham number becomes equal to 1; maximum temperature, T_{hp}, reached inside the hot pocket before plume onset; equivalent radius, r_{eq}, of a sphere having same volume of the hot pocket; yield parameter Y_0; and the inverse of the critical yield number Y_{inv_C}.

Table 4.2: Summary of simulations. For simulations *T-38* and *T-42* the plume never took off.

#	Version	Ref. Exp	P_w (W)	σ_y (Pa)	G (Pa)	t_{onset} (min)	max T (K)	r_{eq} (mm)	Y_0	Y_{inv_C}
T-27	VP	CBP6-A	1.27	0.068	-	-	-	-	231.70	-
T-28	VP	CBP6-A	1.27	0.068	-	65.0950	-	-	231.70	-
T-33	VP	CBP6-A	1.27	0.080	-	170.6333	-	-	197.00	-
T-34	VP	CBP6-A	1.27	0.076	-	120.2000	-	-	207.30	-
T-35	EVP	CBP6-A	1.27	0.076	2.0	66.8877	337.51	28.70	207.30	7.44
T-36	EVP	CBP6-A	1.27	0.076	20.0	103.9497	338.25	31.85	207.30	8.14
T-38	EVP	CBP6-A	1.27	0.076	0.2	crashed	-	-	207.30	-
T-39	EVP	CBP6-A	1.27	0.076	2.0	66.8877	337.51	28.70	207.30	7.44
T-40	EVP	CBP6-A	1.27	0.076	2.0	66.8877	337.51	28.70	207.30	7.44
T-41	EVP	CBP6-A	1.27	0.076	2.0	67.2933	337.51	28.76	207.30	7.46
T-42	EVP	CBP6-A	1.27	0.105	2.0	-	-	-	150.10	-
T-43	EVP	CBP6-A	1.27	0.090	2.0	211.6192	339.27	36.64	175.10	7.79
T-44	EVP	CBP6-A	1.27	0.079	2.0	79.7377	337.86	29.92	199.50	7.48
T-45	EVP	CBP6-A	1.27	0.083	2.0	103.9497	338.33	31.66	189.80	7.44
T-46	EVP	CBP6-A	1.27	0.087	2.0	144.1228	338.81	33.90	181.10	7.58
T-47	EVP	CBP6-A	1.27	0.079	3.0	90.9645	338.08	30.72	199.50	7.67
T-48	EVP	CBP6-A	1.27	0.083	3.0	122.0750	338.57	32.70	189.80	7.71
T-49	EVP	CBP6-A	1.27	0.087	3.0	179.9677	339.03	35.50	181.10	7.87
T-50	EVP	CBP6-A	1.27	0.079	1.0	56.2018	337.17	27.53	199.50	6.89
T-51	EVP	CBP6-A	1.27	0.083	1.0	68.7813	337.61	28.86	189.80	6.81
T-52	EVP	CBP6-A	1.27	0.087	1.0	86.6360	338.05	30.42	181.10	6.92
T-53	EVP	CBP6-A	1.27	0.084	2.0	109.3602	338.40	32.09	188.30	7.48

Table 4.3: Summary of simulations (second part). For simulations *T-B04* and *T-C05* the plume never took off.

#	Version	Ref. Exp	P_w (W)	σ_y (Pa)	G (Pa)	t_{onset} (s)	max T (K)	r_{eq} (mm)	Y_0	Y_{inv_C}
T-B04	EVP	CBP6-B	1.07	0.079	1.0	-	-	-	168.05	-
T-B05	EVP	CBP6-B	1.07	0.076	1.0	120.6595	331.57	30.68	174.68	6.78
T-B06	EVP	CBP6-B	1.07	0.066	2.1	73.9640	331.28	27.69	201.15	7.36
T-B07	EVP	CBP6-B	1.07	0.066	1.0	53.5275	331.04	25.84	201.15	7.04
T-B08	EVP	CBP6-B	1.07	0.066	1.5	64.9340	331.20	26.97	201.15	7.10
T-C04	EVP	CBP6-C	1.16	0.079	1.0	97.0147	333.85	30.71	182.19	6.92
T-C05	EVP	CBP6-C	1.16	0.090	3.0	-	-	-	159.92	-
T-C06	EVP	CBP6-C	1.16	0.072	2.0	82.2813	333.80	29.71	199.90	7.49
T-C07	EVP	CBP6-C	1.16	0.072	1.0	54.1215	333.73	27.04	199.90	6.94
T-C08	EVP	CBP6-C	1.16	0.072	1.5	69.3302	333.77	28.57	199.90	7.22
T-C09	EVP	CBP6-C	1.16	0.071	2.0	77.1722	333.78	29.34	201.86	7.41

4.4 Results without elasticity

We start by trying to replicate the results of Massmeyer et al. (2013) and testing the new version of the code with elasticity turned off. This brings us back to the purely viscous approach in which fluid rheological properties are expressed by the regularized model in eq. (4.11). In this case, we obtain a plume morphology and an evolution of convection that do not differ much from what Massmeyer et al. (2013) have already proposed. For instance, although the onset time of convection has been proved to be strongly dependent on the yield parameter Y_0 and the entire system to be highly sensitive to small variations in the rheological parameters, with reasonable values of σ_y, K_{v0} and n, one can get an onset time by using a regularized model which is about the same of the experimental one. In the experiment "20110404" done with the fluid "CBP6" by Massmeyer (2013) (see her Table 3.1), the experimental onset time was estimated around t_{onset}^{Exp}=119.9 min with an experimental thermal power of P_w^{Exp}=1.850±0.185 W and a fluid with σ_y=0.090±0.015 Pa, K_{v0}=1.403±0.2 Pa s^n and n=0.58±0.01. In our case we get an onset time derived from numerical simulation of t_{onset}=120.2 min by setting σ_y=0.076 Pa, K_{v0}=1.403 Pa s^n and n=0.58. In our case the thermal power is P_w=1.27 W, slightly higher than P_w=1.14 W used for the same system in the numerical simulations of Massmeyer et al. (2013). An higher P_w than the one used by Massmeyer et al. (2013) in her numerical part, allows us to increase the yield stress towards values included in the experimental uncertainty (unlike in was for Massmeyer et al. (2013)), keeping, in the meantime, a value of Y_0 similar to the one used in Massmeyer et al. (2013).

4.4.1 Description of the flow

Fig. 4.7 displays the typical spatio-temporal evolution of a plume for temperature and strain-rate along the plume central axis. Similarly to Massmeyer's runs, the transition from the first stage of deformation (solid-like behaviour) to the flowing behaviour can be highlighted looking at the main heat transfer mechanism active at that moment. The heat transferred by conduction corresponds to the hypothetical elastic phase, here represented by the first highly viscous ($\eta \to \eta_{max}$, Fig. 4.7c) and unyielded ($\dot{\gamma}$=0) part of the spatiotemporal plot (Fig. 4.7b). The transfer by convection is achieved with a viscosity drop in the center of the box (Fig. 4.7c). A zoom on Fig. 4.7b shows how small strain rates are present even before the main upwelling event although they occur not much earlier. Similar behaviour is present in laboratory experiments (Fig. 4.1 and 4.2) where the fluid within the growing hot pocket is not totally at rest but it slowly moves around the heater. It is only when shear rate reaches a certain threshold that this heat pocket evolves into a plume. This value is here represented by the critical shear rate, $\dot{\gamma}_c$, defined at Bingham number Bi=1, that is $\dot{\gamma}_c = \left(\frac{\sigma_y}{K_v}\right)^{(1/n)}$. From the velocity field, we can plot the time evolution of the velocity maximum along the plume axis (Fig. 4.7e). It reaches a maximum at take off, because this is when the hot pocket buoyancy is maximum. Then it decreases to the steady-state regime

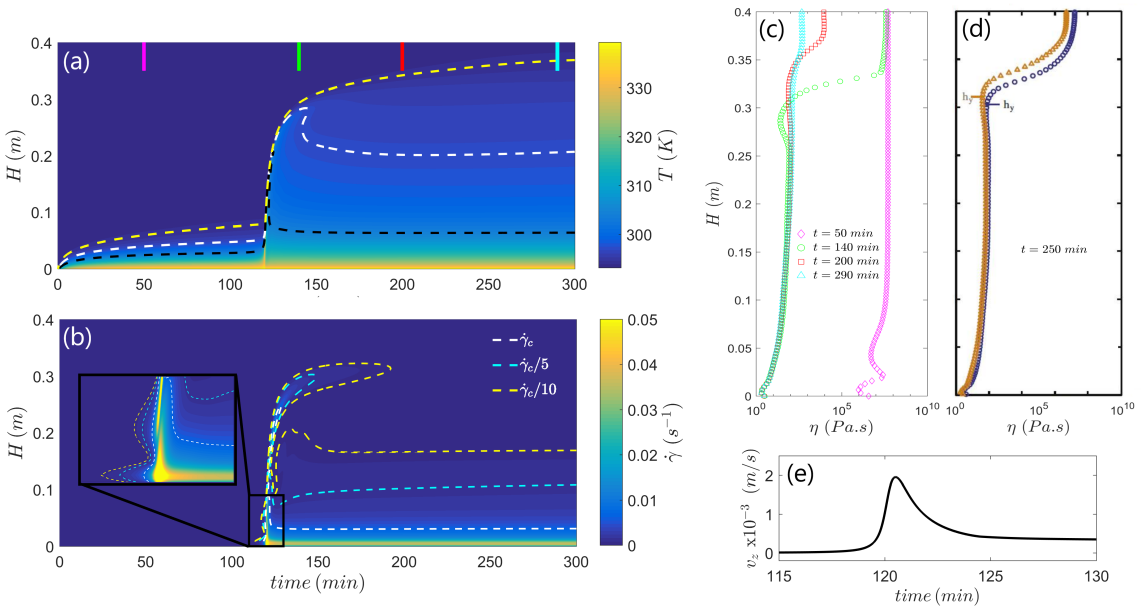

Figure 4.7: Development of a plume in simulations with viscous truncation and by using the regularized model of eq. (4.11) (Y_0=207.3, De=0). Evolution along the central axis of (a) temperature field where three isotherms have been highlighted in yellow (21.0 °C), white (23.9 °C) and black (31.1 °C) and (b) shear rate. Contours in the shear rate statiotemporal evolution indicate the critical shear rate, $\dot{\gamma}_c$, defined at Bi=1 and $\dot{\gamma}_c/5$ and $\dot{\gamma}_c/10$. The inset shows the zoomed portion around plume onset. (c) Viscosity profiles along the cross sections indicated on the top of (a) by the four similarly colored lines. Profiles are taken at times t=50 min, t=140 min, t=200 min and t=290 min. (d) Viscosity profiles at t=250 min from Massmeyer et al. (2013). Simulations had the same parameters used in our case. (e) Maximum rising velocity, v_z, along the plume central axis.

value. The same evolution is also seen in Newtonian fluids (e.g. Davaille et al., 2011).

Once the plume develops (Fig. 4.8), the shear rate is strongly localized along the plume boundaries (Fig. 4.8b). This results in a thermal instability with an quasi-plug flow within it, and an overall thermal shape that looks like a finger (Fig. 4.8a). However, we do not observe any consecutive pulses as reported in some cases for thermal anomalies rising in viscoplastic material. Within the plume regime, thermal instabilities develop a proper head and are repeated in successive pulsations only if buoyancy stresses are strong compare to viscous stresses. If this is not the case, like here, advection is predicted to be weak and these phenomena are prevented (Karimfazli et al., 2016).

4.4.2 Comparison with Massmeyer's simulations

Fig. 4.9 compares the trend of the minimum of viscosity along the tank central axis for two of our simulations with an old one from Massmeyer et al. (2013). Viscosity decreases smoothly in time in our case, and although curves trajectories and onset time between old and new runs are found about the same for same initial conditions, the first part of calculations show

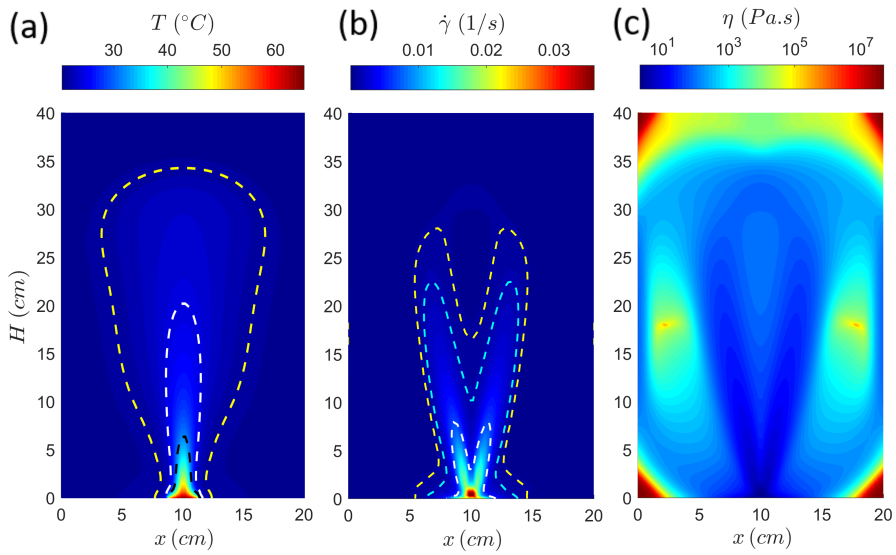

Figure 4.8: Vertical cross-section of the plane through the plume axis at t=200 min (Y_0=207.3, De=0). (a) Temperature field. Isotherms at 21.0 °C (yellow line), 23.9 °C (white line) and 31.1 °C (black line). (b) Deformation field. Lines refer to the critical shear rate $\dot{\gamma}_c$ (white), $\dot{\gamma}_c/5$ (light blue) and $\dot{\gamma}_c/10$ (yellow). (c) Viscosity field.

a quite important shift. Large steps in their case might either correspond to actual time steps that take long compared to the newer run, or, more likely, the viscosity field was not updated every step.

The most evident difference concerns the viscosity at the top of the column fluid. Massmeyer et al. (2013) observed an almost undeformed zone close to the top surface: this unyielded area, very clear in their experiments, is achieved in simulations by very high viscosities and almost null shear rates (e.g. in Fig. 4.7d where it is visible more than 100 minutes after the plume onset). The fluid there seems to be at the rest along the 10 cm below the top surface. In our simulations, the plume head always reaches the top surface. Time evolution can be followed in Fig. 4.7c where the viscosity contrast between top and bottom surfaces tend to flatten out over time. Consequently, viscosity in the highest part of the fluid column always decreases with time (Fig. 4.7c and Fig. 4.8c), preventing the formation of a non-deformed layer close to the top surface.

4.5 Results with EVP

Once elasticity is turned on the rheological model becomes the one presented in section 4.2.1. Here we concentrate on the effects that viscoelasticity has on the start of convection and demonstrate how it affects the take off of the plume.

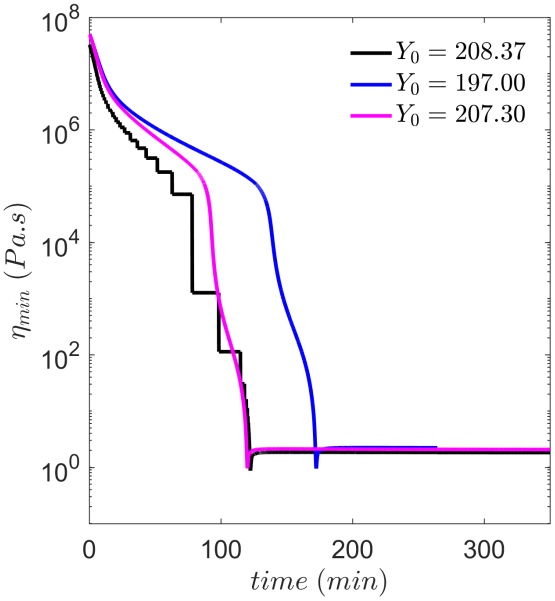

Figure 4.9: Minimum of viscosity along the tank central axis as function of time. Black line refers to simulation #47 in Table 1 of Massmeyer et al. (2013). Blue and magenta lines refer to two new simulations at different Y_0 and De=0. For the same configuration and initial conditions of the simulations, plume onset time in the laboratory experiment is t_0=119.9 min (Massmeyer et al., 2013).

4.5.1 Description of the flow

Fig. 4.10 shows the development of a thermal instability in the EVP case for the same Y_0 as the VP case previously shown on Fig. 4.7. Both temperature and strain-rate evolutions over time are very similar. In both cases, a single strong event suddenly takes place and the ascent of the plume is preceded only by small deformations close to the heating point. As before, in the shear rate fields we highlights contour of the critical shear rate obtained at Bi=1. Although lower shear rates than $\dot{\gamma}_c$ are reached around the heater before onset, the instability rises only once the maximum strain rate reaches $\dot{\gamma}_c$ (see the zoomed view in Fig. 4.10b).

EVP simulations also succeed in reproducing the development of the finger shape observed in the laboratory experiments, as seen in the temperature field (Fig. 4.11), the shear rate field (Fig. 4.12) or the viscosity field (Fig. 4.13). The three snapshots are taken at three different times corresponding to the three motion regimes described in Davaille et al. (2013): no-motion, small convective cell and the developed plume. During the no-motion stage, viscosity is relatively large everywhere (Fig. 4.13a) whereas it starts to decrease when small, but not null, shear strain appears around the heater (Fig. 4.13b). Once the plume rises (Fig. 4.13c), the strong shear localization on plume boundaries and the consequent drop in viscosity marks the plume morphology and gives it the finger-like shape observed in the laboratory Davaille et al. (2013).

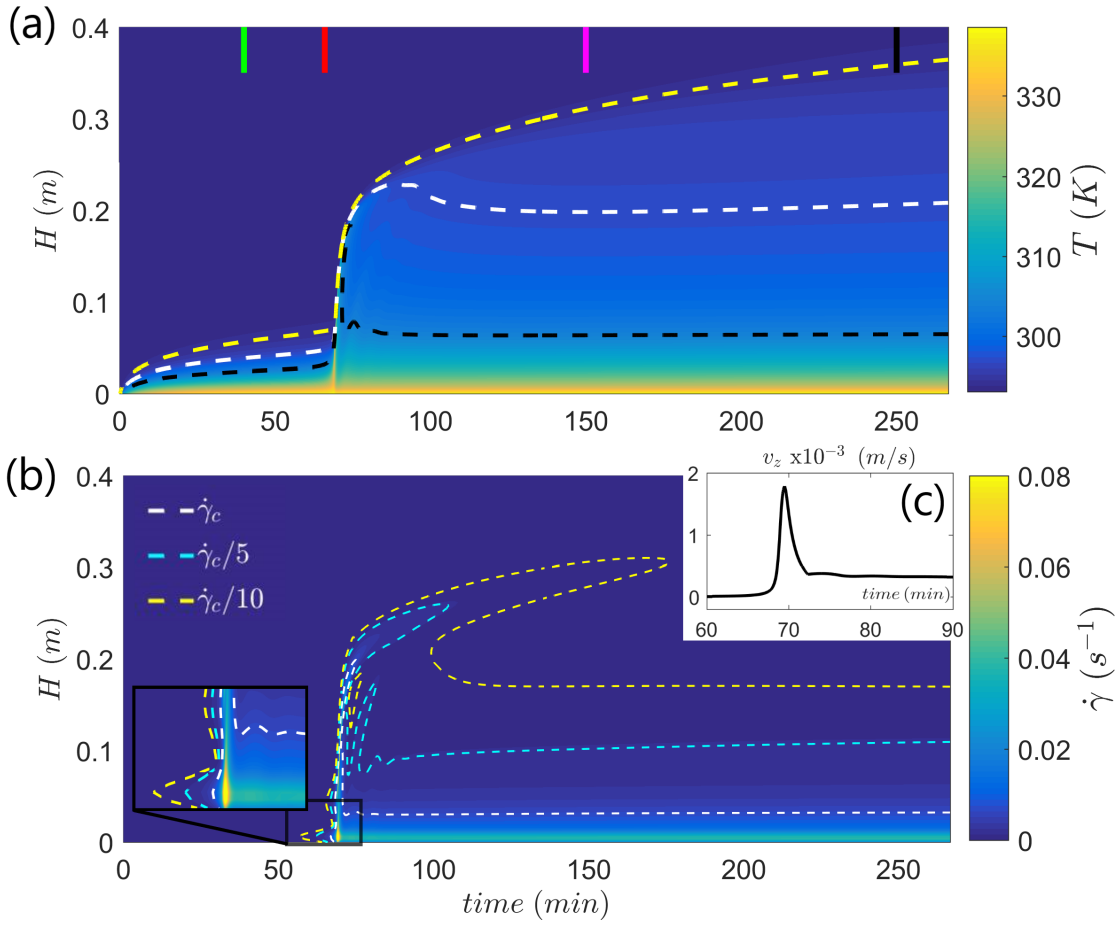

Figure 4.10: Development of a plume with an elasto-viscolastic model for Y_0=207.30 and De=0.85. Evolution along the central axis of (a) temperature field, where three isotherms have been highlighted: 21.0 °C (in yellow), 23.9 °C (in white) and 31.1 °C (in black), and (b) shear rate, where $\dot{\gamma}_c$ is the critical shear rate defined for Bi=1. (c) Maximum rising velocity, v_z, along the plume central axis.

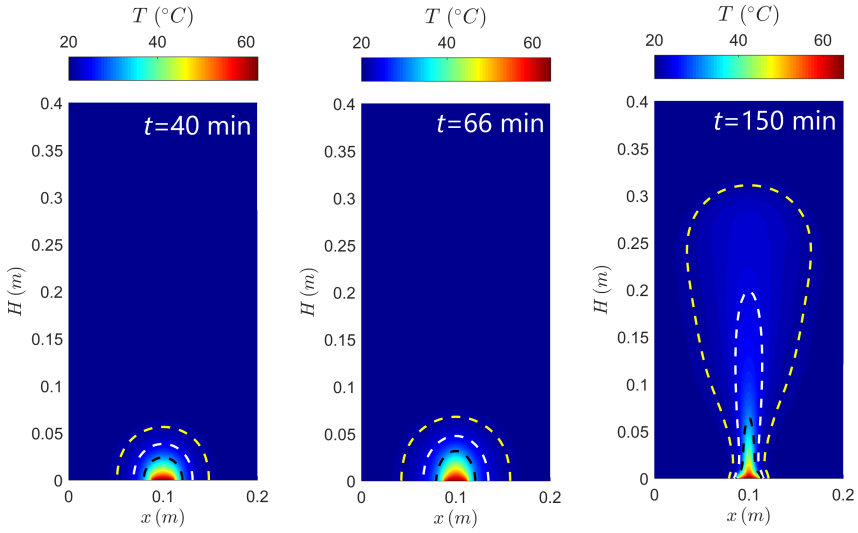

Figure 4.11: Temperature field of vertical cross-sections of the plane through the plume axis at t=40 min, t=66 min and t=150 min. Isotherms at 21.0 °C (in yellow), 23.9 °C (in white) and 31.1 °C (in black). Y_0=207.3 and De=0.85.

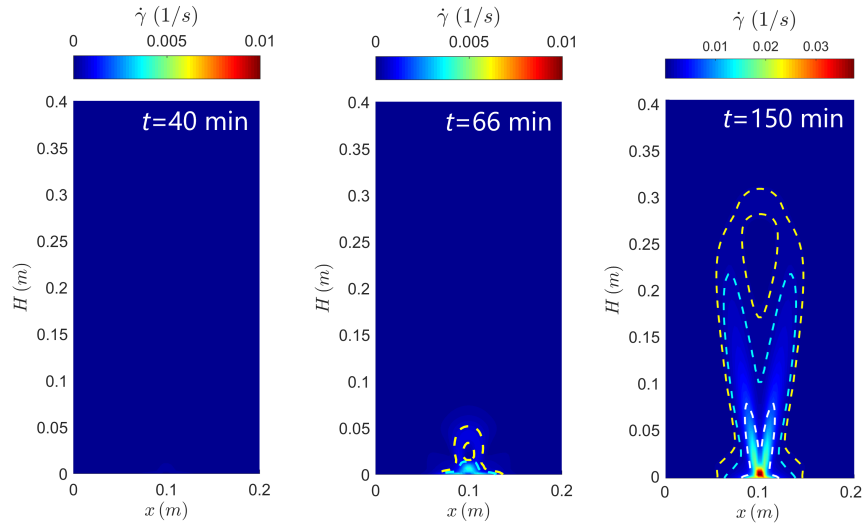

Figure 4.12: Deformation field of vertical cross-sections of the plane through the plume axis at t=40 min, t=66 min and t=150 min. Isolines at critical shear rate $\dot{\gamma}_c$, $\dot{\gamma}_c/5$ and $\dot{\gamma}_c/10$. Y_0=207.3 and De=0.85.

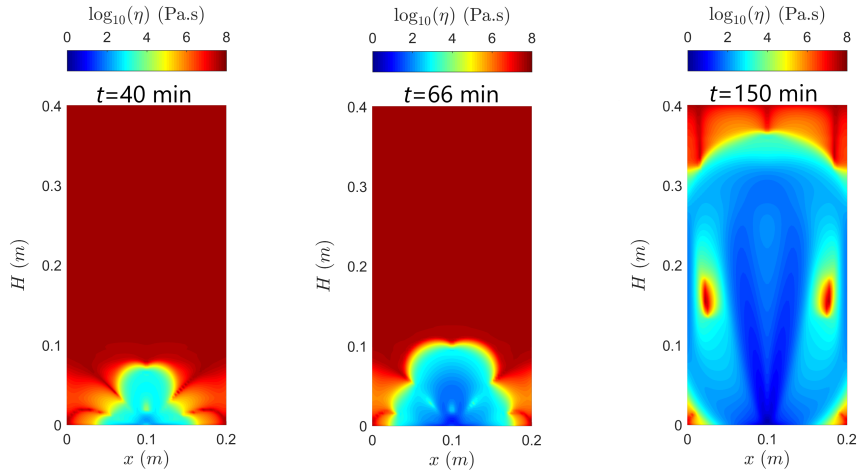

Figure 4.13: Viscosity field along the vertical plane through the plume axis at t=40 min, t=66 min and t=150 min. Y_0=207.3 and De=0.85.

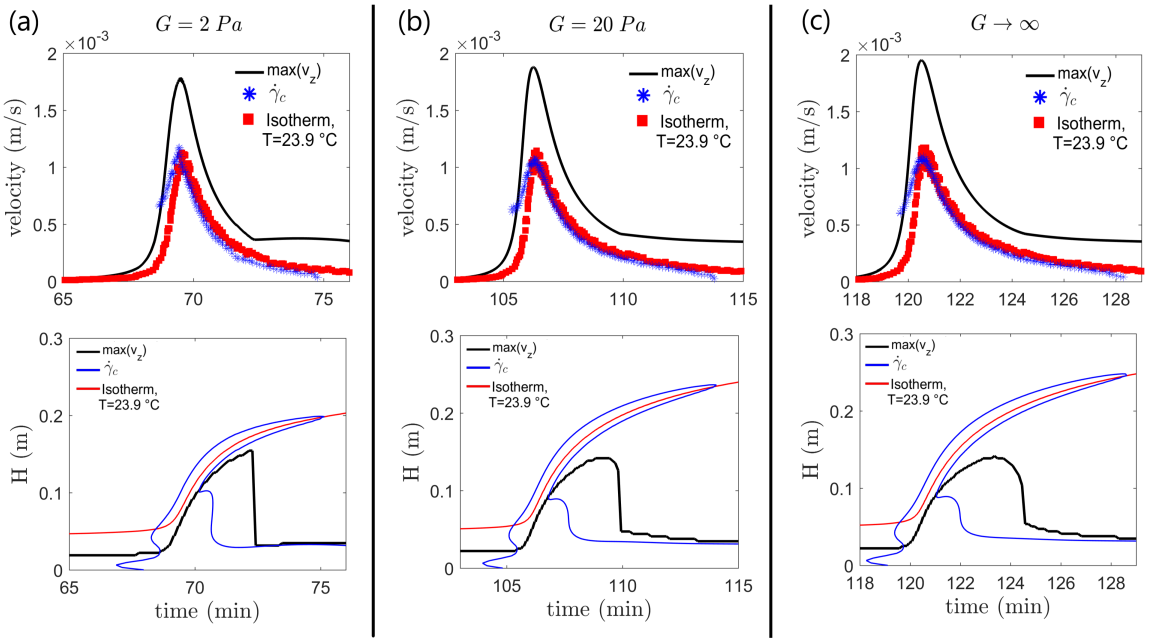

Figure 4.14: Zoom around the onset time for Y_0=207.30. Top: Velocity as a function of time. The solid black line indicates the maximal vertical velocity (v_z) along the plume axis. Red squares represent the rising velocity of the T=23.9 °C isotherm. Blue crosses represent the rising velocity of the point where $\dot{\gamma}$=$\dot{\gamma}_c$. (a) EVP model with G=2 Pa; (b) EVP model with G=20 Pa; (c) VP model. Bottom: Time evolution of the height of the point with maximum v_z (black), with T=23.9 °C (red), and with $\dot{\gamma}$=$\dot{\gamma}_c$ (blue).

Fig. 4.14 shows the evolution of the uplift through time. Here we display the maximal flow velocity together with the rising velocity along the central axis for the isotherm T=23.9 °C and the point where $\dot{\gamma}$=$\dot{\gamma}_c$. The plume rises in two stages (Fig. 4.10): right after onset, the uplift is fast with a maximum strain rate $\dot{\gamma}_{max}$ localized at the top of the plume, and larger than $\dot{\gamma}_c$. This first stage is due to the release and uplift of the hot pocket build up during the conductive stage. It is followed by a second, much slower uplift. A local maximum in strain rate can still be followed at the top of the plume but it is now smaller than $\dot{\gamma}_c$ (Fig. 4.14bottom). This local $\dot{\gamma}_{max}$ corresponds to the local stagnation point in the plume head referential, where the upwelling flow inside the plume head encounters the downwelling flow outside the plume head (Fig. 4.15e). It also corresponds to a local viscosity minimum allowing us to follow the "plume height" by looking at the time evolution of the viscosity along the central axis (Fig. 4.15; Massmeyer et al. (2013)). The plume velocity during the first stage is larger than the velocity maintained during the the following steady-state stage because the plume must initially penetrate an unyielded medium by developing enough buoyancy stress to overcome the fluid yield stress (i.e. $Y_{inv} > Y_{inv_C}$). Once the fluid is yielded by the plume, fluid flow within it does not need to overtake any yield stress and hence motion can be sustained by smaller buoyancy. Smaller buoyancy means also lower values of velocities. Maximal vertical velocity starts to decrease when the plume loses part of its buoyancy for heat conduction and it drops down to the steady-state value when the plume buoyancy is held back again by the yield stress. The steady-state motion after the release of the plume is the constant flow supplied by the heater. During this stage both the height of those isotherms away from the highest plume regions where heat is lost by conduction and height of the critical strain rate remain constant and velocity drops to zero. Fig. 4.14(bottom) tracks the position of the maximal velocity. In all cases it firstly rises with the plume and only after plume has lost most of its energy it descends back on a thermal boundary layer about 3 cm above the bottom surface.

4.5.2 Influence of the elasticity

However, few differences between viscoplastic and elasto-viscoplastic cases are present. For the same initial conditions, i.e. for the same Y_0, temperature history and Hershel-Bulkley fluid's properties, Fig. 4.16 shows the main discrepancies we found.

Onset time

The strong shift from a regime mainly dominated by conduction to one where heat is transported by advection takes place when the strain rate approaches its critical value $\dot{\gamma}_c$ defined by Bi=1 (Fig. 4.16b). The Bingham number Bi is calculated by using the maximum shear rate along the plume axis at each time step. In this way one can track its evolution over time (Fig. 4.16c) and use it to define the onset time once it becomes equal to one.

As the level of elasticity decreases from small shear modulus (i.e. large rigidity $1/G$) to

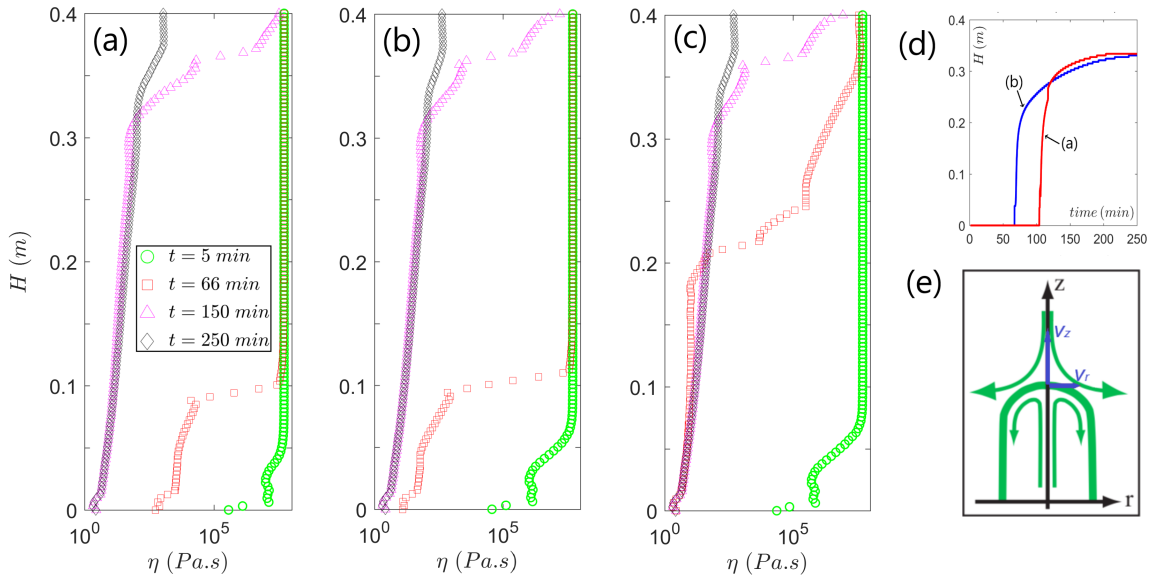

Figure 4.15: Viscosity profile along the central axis. Profiles are taken before plume onset at t=5 min (green circles), close to the onset time or right after at t=66 min (red squares) and at t=150 min (magenta triangles) and long after departure at t=250 min (black diamonds). Position of same profiles are indicated in the example of Fig. 4.10 by small color lines. (a) Y_0=207.3, G=20 Pa. (b) Y_0=207.3, G=2 Pa. (c) Y_0=199.5, G=1 Pa. In (d) we track the plume height h_z over time for the two simulations (a) and (b). (e) Cartoon that shows the link between the local minimum of viscosity in the plume head and the maximum in strain rate. The latter corresponds to a local maximum in dv_z/dr and is a stagnation point in the plume referential. Modified from Davaille et al. (2013).

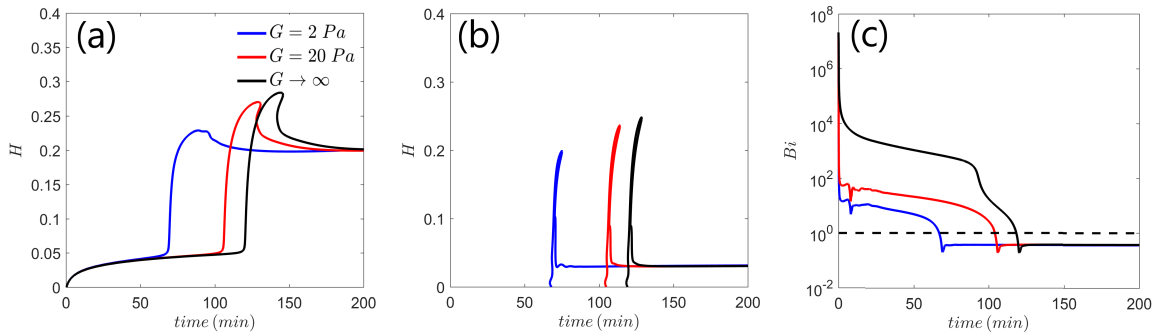

Figure 4.16: Results for simulations with Y_0=207.30. Black line is for the VP model. Color lines for EVP model with shear modulus G of 2 Pa (blue line) and 20 Pa (red line). Time evolution along the plume axis of: (a) height of the T=23.9 °C isotherm; (b) height at which $\dot{\gamma} = \dot{\gamma}_c$; (c) Bingham number, Bi. The dashed line indicates Bi=1.

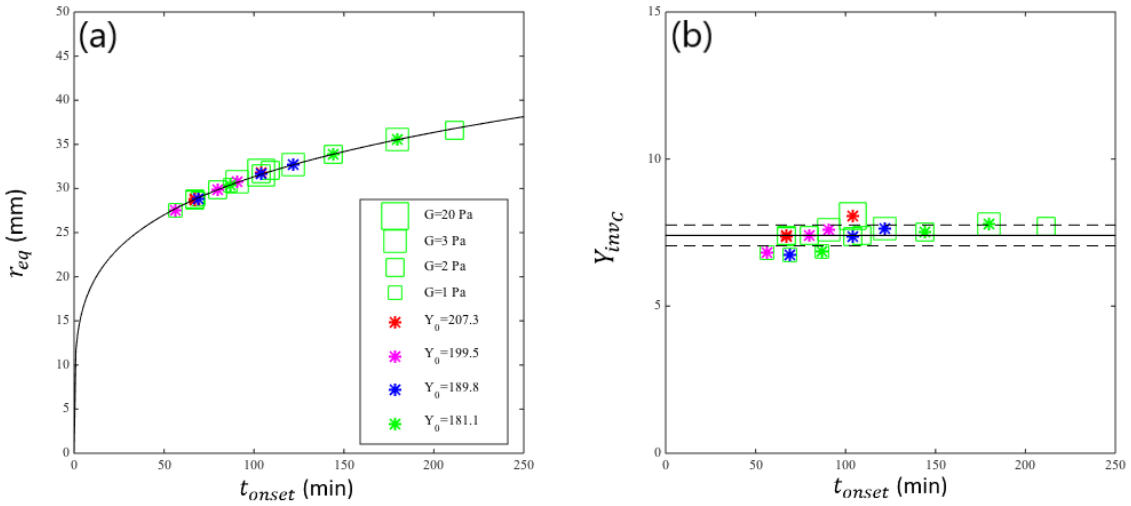

Figure 4.17: (a) Effective hot pocket radius at onset as a function of the onset time, for all the simulations of table 1. The solid line shows the best power law fit, with an exponent of 0.214 (R=0.998). (b) Local Yield number at onset. The solid line represents its mean value, and the dashed lines show the standard deviation.

the case where elasticity is not taken into account (no rigidity, i.e. $G \to \infty$), the plume onset time increases. This is seen on the temperature field, as well as on the velocity and strain rate fields (Fig. 4.16). Generally, an increment of G leads to a more viscous response of the elasto-viscoplastic medium. By increasing G the evolution over time of the isotherm goes toward the non-elastic case obtained with the VP model (Fig. 4.16a).

Plume size and buoyancy

As already described in section 4.1, we can determine the effective radius of the hot pocket r_{eq} from the temperature field when the plume takes off at t_{onset}. For a given temperature history, Fig. 4.17a shows that r_{eq} only depends on the onset time, i.e. how long the heat has accumulated before take off, irrespective of the elasticity of the fluid. The local buoyancy number can also be estimated at the onset time and it is found to be constant, with a value $Y_{inv_C} = 7.28 \pm 0.35$ (Fig. 4.17b), very close to what is found theoretically (6.99), and experimentally (8.8 ± 0.7).

Maximum plume height reached in the first uplift stage

We define this maximum height H_{max} reached by the hot plume in the first uplift stage as the maximum position of $\dot{\gamma} = \dot{\gamma}_c$, i.e. the highest position where $Bi = 1$ (Massmeyer et al., 2013). Figure 4.18 shows that H_{max} again mainly depends on the onset time, i.e. on the buoyancy stored in the hot pocket during the conductive stage. However, a small

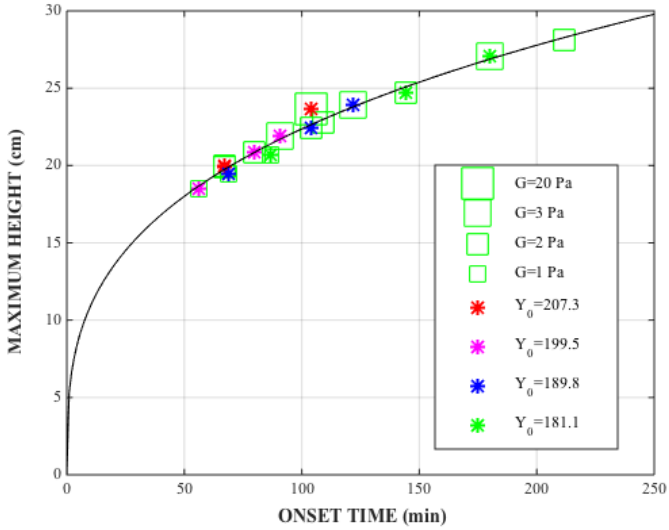

Figure 4.18: Maximum height reached by the plume in the first stage as a function of onset time. The solid line shows the best power law fit, with an exponent of 0.312 (R=0.98).

extra-dependence on the elasticity begins to appear, the data points with smaller G being below the curve fit, while larger G rise above the curve fit.

Plume maximum velocity

The plume reaches its maximum velocity very close after the onset time (Fig. 4.10). We choose here to define the plume velocity as the uplift rate of the location where $Bi = 1$ on the plume axis. Figure 4.19a shows that the maximum velocity v_{max} also depends on the onset time, i.e. on the buoyancy stored in the plume hot pocket during the conductive stage. But there is also an additional dependence on elasticity, with increasing v_{max} with increasing elasticity (i.e. decreasing G).

For a visco-plastic fluid, a scaling for v_{max} can be derived from the balance between the buoyancy force of the hot plume $F_b = 4\pi g \Delta\rho r_{eq}^3/3$ and the drag $F_d \sim \pi r_{eq}^2(\sigma_y + K_v(v_{max}/2r_{eq})^n)$:

$$v_{max} = r_{eq}\dot{\gamma}_c \left(C_0 \frac{g\Delta\rho r_{eq}}{3\sigma_y} - 1 \right)^{1/n} \tag{4.22}$$

where C_0 is an experimental constant. As we showed that the local (inverse) Yield number $g\Delta\rho r_{eq}/3\sigma_y$ was a constant at onset, we find that $v_{max} \sim r_{eq}\dot{\gamma}_c$.

The effect of elasticity can be a priori estimated through a global Deborah number. As already seen, the definition of the Deborah number requires a relaxation time of form of $\lambda = \eta_c/G$ and the formulation of an "experimental" time. For the rising plume, we can take

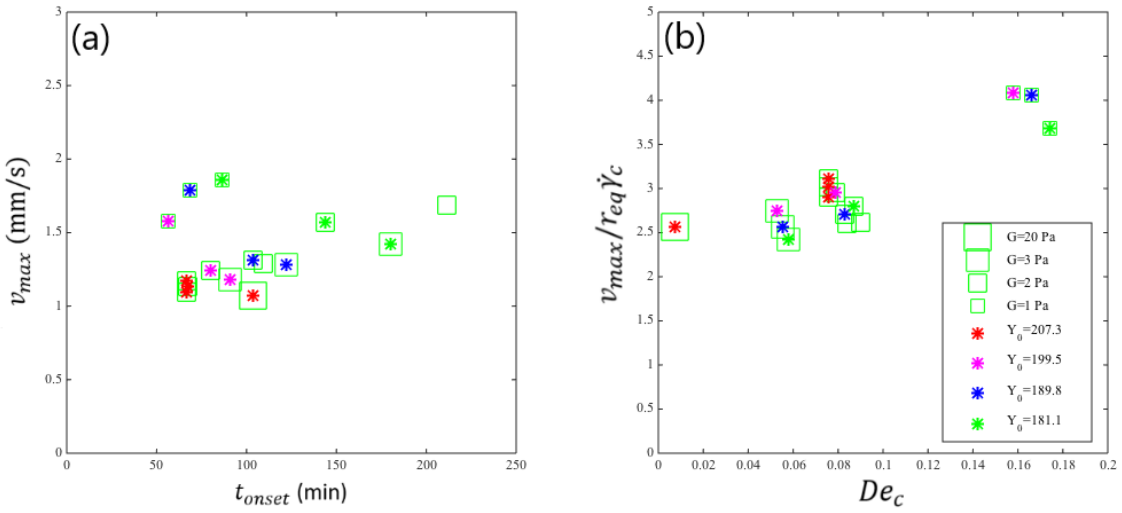

Figure 4.19: (a) Maximum velocity of the hot pocket measured as the maximum uplift rate of the point where $Bi = 1$ on the plume axis as a function of the onset time, for all the simulations of Table 4.2. (b) Maximum plume velocity normalized by the scaling $r_{eq}\dot{\gamma}_c$ as a function of the global Deborah number $De_c = \dot{\gamma}_c \eta_c / G$.

as experimental time (t_p) the inverse of the critical strain rate, so that:

$$De_c = \frac{\eta_c}{G}\frac{1}{t_p} = \frac{2\sigma_y}{G}. \tag{4.23}$$

With this definition, De_c is similar to the Weissenberg number. Figure 4.19b shows that the normalized velocity increases with increasing De_c. But we need more simulations to determine the full scaling.

4.5.3 Discussion

Estimate of the onset time from the external parameters

The previous section has shown the importance of the onset time in determining the characteristics of the plume uplift. Fig. 4.20a shows the relationship between De_c and the onset time t_{onset} for different yield parameters. The onset time has been normalized by a conductive time scale based on the Peltier heater diameter, $t_{cond} = D_p^2/\kappa$.

At constant Y_0, data can be fitted by a logarithmic curve, that is $De_c = a_c \log(t_{onset}\,\kappa/D_p^2) + b_c$. And coefficients a_c and b_c are found to increase linearly with Y_0. The final expression for the onset time writes:

$$\frac{t_{onset}}{D_p^2/\kappa} = 0.232 \exp\left(\frac{127.1712 - 181.717(De_c + 0.0093)^{1/2}}{Y_0 - Y_{0c}}\right) \tag{4.24}$$

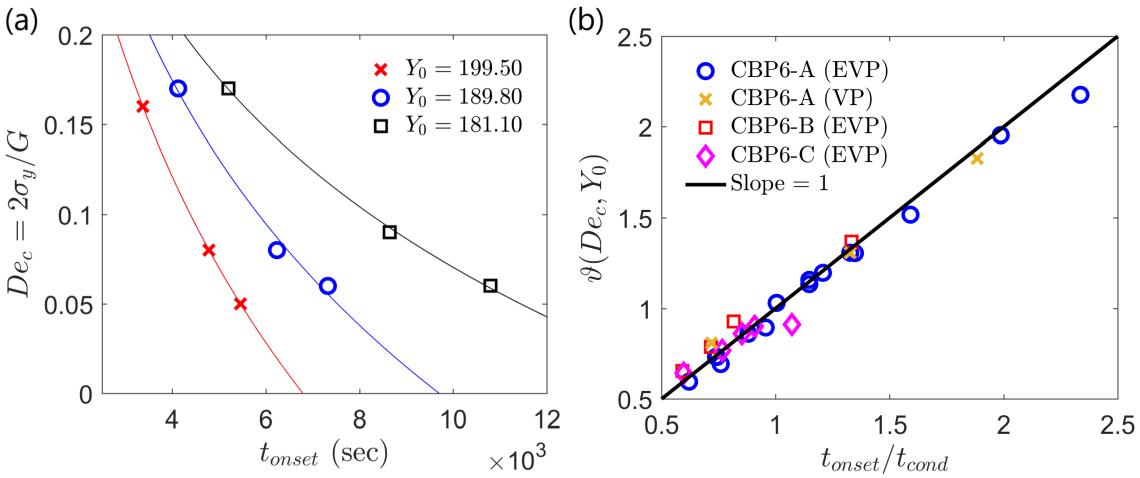

Figure 4.20: (a) Global Deborah number, De_c, defined in eq. (4.23), as function of plume onset time, t_{onset}, for three values of yield parameter Y_0. Color lines indicate a fit of form De_c=$a\log(t_{onset}) + b$. For Y_0=199.50 (red crosses) a=-0.2285 and b=2.0162. For Y_0=189.80 (blue circles) a=-0.1969 and b=1.8076. For Y_0=181.10 (black squares) a=-0.1516 and b=1.4667. (b) Normalized plume onset time as a function of $\vartheta(De_c, Y_0)$. ϑ is a function of De_c and Y_0 that represents the right side of eq. (4.24). All simulations are reported. Symbols indicate different initial conditions (i.e. fluid height and temperature history, see Table 4.2, 4.3) or different rheological models (VP: viscoplastic, EVP: elasto-visco-plastic).

where $Y_{0c} = 143.8736$. The latter value is very close to the critical Y_0 value under which no plume can develop. The different numerical coefficients comes from the fit of all the data. We have kept all the digits because the exponential function is very sensitive. This relation describes well not only the onset times obtained with the EVP model but also those obtained for the VP case where $De_c = 0$ (as shown by the orange crosses in Fig. 4.20b).

Local Deborah number

It could be useful to evaluate the local Deborah number (De) defined by eq. (4.20) at the onset time. Fig. 4.21a shows that the local Deborah number is not a constant (contrarily to the local Yield number) but varies with both Y_0 and t_{onset}. All the data can be fitted with:

$$De = 0.506\,\zeta^{1.467}, \tag{4.25}$$

with ζ being a function of plume onset time, t_{onset}, and yield parameter, Y_0 (Fig. 4.21b):

$$\begin{cases} \zeta = b_0 - a_0\,\log(t_{onset}) \\ b_0 = 0.20\,Y_0 - 21.24 \\ a_0 = 0.03\,Y_0 - 3.95 \end{cases} \tag{4.26}$$

Eq. (4.25) is found to describe quite well the entire set of simulations done in the EVP

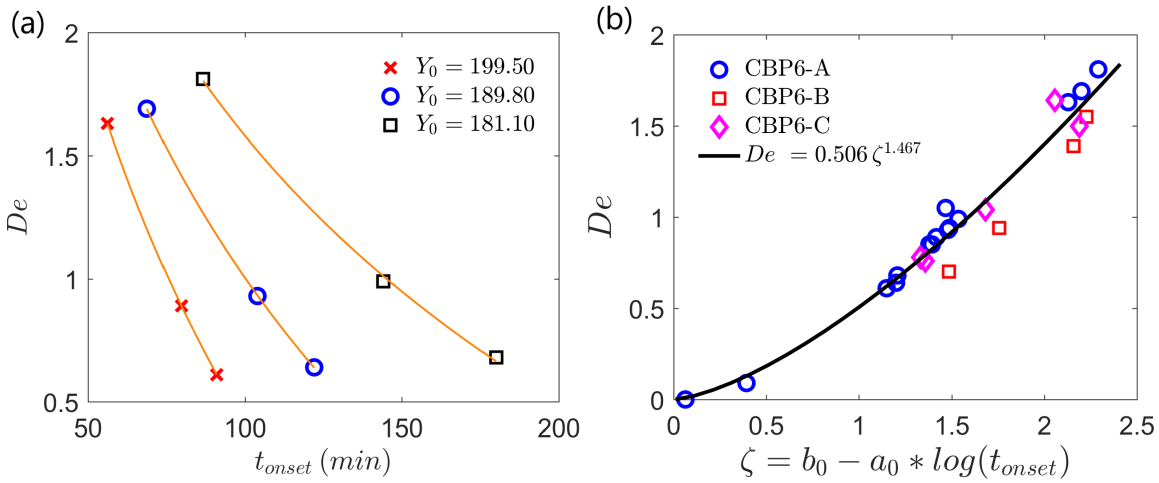

Figure 4.21: (a) Deborah number, De, as function of plume onset time, t_{onset}, for three values of yield parameter Y_0. Orange lines indicate a fit of form De=$a\log(t_{onset})+b$. For Y_0=199.50 (red crosses) a=-2.1177 and b=10.162. For Y_0=189.80 (blue circles) a=-1.8322 and b=9.4412. For Y_0=181.10 (black squares) a=-1.557 and b=8.7507. (b) Deborah number as function of ζ, where $\zeta = b_0 - a_0\log(t_{onset})$. Both a_0 and b_0 are functions of Y_0, see eq. (4.26). All simulations with EVP model are reported. Symbols indicate different initial conditions (i.e. fluid height and temperature history, see Table 4.2, 4.3). Black line represents a power-law fit of form of De=$0.506\zeta^{1.467}$.

framework (Fig. 4.21b), even with different fluid heights and thermal histories. It also describes well the limit cases for the VP rheology. For the viscoplastic case (VP) having infinite shear modulus and hence $De \to 0$, ζ results equal zero and the onset time is only a function of the yield parameter, that is $\log(t_{onset})$=b_0/a_0, as it is for Massmeyer et al. (2013) (Fig. 4.3b). For simulation *"T-34"* carried out with a VP model (Table 4.2), eq. (4.25) leads to an onset time of 123.6 min, very close to the onset of 120.2 min obtained from the calculation. Similarly, for the purely elastic case ($De \to \infty$), ζ and hence t_{onset} go to infinity and convection does not occur.

4.6 Summary of the main results

In this chapter we have shown simulations of thermal plumes in an elasto-viscoplastic medium triggered by a difference of temperature applied in a localized heating point. We have found a good agreement with laboratory experiments (Davaille et al., 2013; Massmeyer, 2013) and previous numerical works carried out with simplified rheological models (Massmeyer et al., 2013; Karimfazli et al., 2016). However some differences are present as well, concerning the onset time of convection and the fluid flow in areas of low strain rate. Depending on material rigidity, the addition of an elastic component results in a more rapid deformation of the fluid so that the emergence of thermal plumes in a "Maxwelliam-Hershel-Bulkley" fluid slightly differs from the one in which elasticity is not considered. In terms of classifying the flow, we find that besides the global yield parameter Y_0 and local parameters Bi and Y_{inv}, the rising of

the plume and its subsequent growth is also affected by the Deborah number De. As already seen experimentally (Davaille et al., 2013), and numerically in the VP model (Massmeyer et al., 2013), the yield parameter remains also for the EVP model the key-parameter to describe the development of a thermal plume: small variations of it strongly affect to onset time. Local conditions are needed to keep the flow active as well: the Bingham number, which takes into account the fluid yield stress and compares it with viscous stresses, has to be supercritical (i.e. $Bi<1$) to ensure the ascent of the plume. Making then an analogy between the thermal instability during its early growth stages and a sphere, we find that also in the EVP case the inverse of Yield number Y_{inv} has to be larger than a critical value for the plume to rise. This critical condition is $Y_{inv_C}= 7.35 \pm 0.35$, apparently independent from the shear modulus (Table 4.2 and 4.3) and similar to Y_{inv_C}=6.99, the value for a settling sphere (Tabuteau et al., 2007; Beris et al., 1985), and Y_{inv_C}=8.8 $\pm$ 0.7 found experimentally for plumes in Carbopol (Davaille et al., 2013). The role of elasticity has been evaluated through the Deborah number. We found a dependence between De and the plume onset time in which the more elastic the material is, the shorter is the onset time. These variations in onset time directly influence the plume buoyancy, and therefore its uplift velocity and the height it will reach. In addition, elasticity also influences the local rheology of the fluid, which will alter furthermore the plume characteristics.

Further work is needed to fully evaluate the influence of elasticity. We need more runs to explore different initial conditions and different fluids properties, to extent the domain of validity of the scalings we presented here, as well as to determine completely the elasticity influence. Moreover, we would like to modify the calculation of the stress tensor, by adding the upper convected rate (e.g. m=1 instead of m=0 in eq. (4.13)), to extend the domain of elasticity that we can explore.

A next step will then be to try the EVP model for a Rayleigh-Benard setup and see whether the model is able to reproduce those experiments which achieve RBC in absence of any perturbations in Carbopol. The latter situation is of particular interest also in geodynamic, where a yield stress together with a viscoelastic rheology might become fundamental for modeling a more realist mantle convection.

Chapter 5

Implications for magma chambers

Many geological processes, such as the settling of crystals and nodules in a magma chamber, or of iron drops in a partially molten magma ocean, as well as the upwelling of magma bodies in the lithosphere, take place in heterogeneous systems. The heterogeneities in material properties (composition, density and rheology) give rise to a medium of complex effective rheology that controls the dynamics of these phenomena. In this chapter we focus on magmatic systems. We shall see that they can present mechanical behaviors and rheological transitions similar to those in SAP gels. So we shall use the results of Chapter 3 to explore what can happen when the size of the magma structure becomes relevant to the flow.

5.1 The mush-magma transition

A good description of the dynamics of magmatic systems is crucial to understand their mobility, lifetime and internal structure (Massol and Jaupart, 2009; Gonnermann and Manga, 2007; Caricchi et al., 2007; Turner and Costa, 2007). Magmatic systems are large scale environments that develop across the whole crust (Cashman et al., 2017; Sparks et al., 2019). They consist in a set of magmatic reservoirs that differ from each other based on the proportions of melt, crystals and exolved volatiles (Bachmann and Bergantz, 2008). A magmatic system can be subdivided in three interacting main domains: magma, mush and host rocks (Sparks et al., 2019). The first two are regions of partially or totally molten material that are then, by definition, above the solidus. Differently from host rocks which do not contain melt, magma and mush are multi-phases systems that include solid parts (crystals) together with melts and exolved volatiles. The dynamics of these heterogeneous domains are strongly affected by their rheology (Mader et al., 2013): for example, viscosity, η, can span up to 25 orders of magnitude between highly viscous hot sub-solidus rocks (η up to 10^{20} Pa s) and exsolved magmatic fluids (down to 10^{-5} Pa s) (Sparks et al., 2019). Due to this large viscosity range, instabilities develop over a large range of time scales: from minutes, during gas release in explosive eruption, to 10^4 years for Rayleigh-Taylor instabilities arising

from a magma layer (Seropian et al., 2018).

We focus here on the dynamics of two of the three domains: mush and magma.

Mushes are not eruptible (in their entirety) magmatic reservoirs that dominate volumetrically the magmatic system (Bachmann and Huber, 2016; Sinton and Detrick, 1992). They are characterized by high crystal contents with a crystal-dominated mechanical behaviour (Sparks et al., 2019; McKenzie, 1985). The solid components form a semi-rigid framework in which melt is dispersed at the porous scale, between crystals, or on a mesoscale, as pockets, lenses and veins (Sparks et al., 2019; Edmonds et al., 2019). Even though the bulk mush rheology is controlled by the crystalline network, and at short time-scale has a solid-like behaviour (Sparks et al., 2019), the mush solid framework can also face viscous deformation through different processes at the grain scale. At low melt fraction and under gravitational loading, it deforms similarly to host rocks, that is through dislocation creep (non-Newtonian power law rheology) or by diffusive processes (Newtonian rheology) (Holness et al., 2019). Effective viscosity is typically around 10^{18} Pa s but under higher temperatures and for a melt fraction of 40% it can decrease to 10^{14} Pa s for both deformation mechanisms (Sparks et al., 2019; Schmeling et al., 2012). On the other hand, in a melt-rich mush, stresses are transmitted within the crystal network through force chains. This gives it the ability to sustain stress until the breakage of the network and subsequent flow if a critical stress is applied (Bergantz et al., 2017; Bonn et al., 2017).

Magma has higher melt fractions; its rheology is controlled by the deformation of the melt and depends strongly on temperature, composition and physical properties of suspended crystals and bubbles (Mader et al., 2013; Costa et al., 2009). At low concentration of suspended material it behaves as a Newtonian fluid (crystal-poor magma) whereas a crystal-rich magma can show complex elasto-viscoplastic rheologies with shear-thinning flow curves (Mader et al., 2013; Vona et al., 2011). Magma viscosity (or effective viscosity) is generally within the range of 1-10^6 Pa s (Sparks et al., 2019). It can move and be transported through mush and sub-solidus rocks and subsequently erupted (Marsh, 1981).

Progression between a self-sustained (jammed) solid-like domain and a flowing liquid-like domain marks the strong rheological jump occurring during the mush-magma transition (MMT) (Bergantz et al., 2017; Burgisser and Bergantz, 2011; Karlstrom et al., 2012). From this point of view, the MMT becomes a rheological boundary between a system that is jammed and one that is not. It occurs over a very small region of strain rate or crystal content (Caricchi et al., 2007; Costa et al., 2009; Burgisser and Bergantz, 2011). The crystal volume fraction that usually marks the transition is around 50-70%, although it can vary significantly due to crystal shape and size (Sparks et al., 2019; Mueller et al., 2009).

Several mechanisms have been proposed to explain how a magma reservoir might form in shallow crust (i.e. magma chambers) or how magma enriched layers can be assembled below or within a mush. For large intrusions such as dykes and sills there are evidences, either geophysical (White et al., 2011; Greenfield and White, 2015; Magee et al., 2018) or geological (Scaillet et al., 1995; Ruprecht and Plank, 2013), that they can move magma throughout the

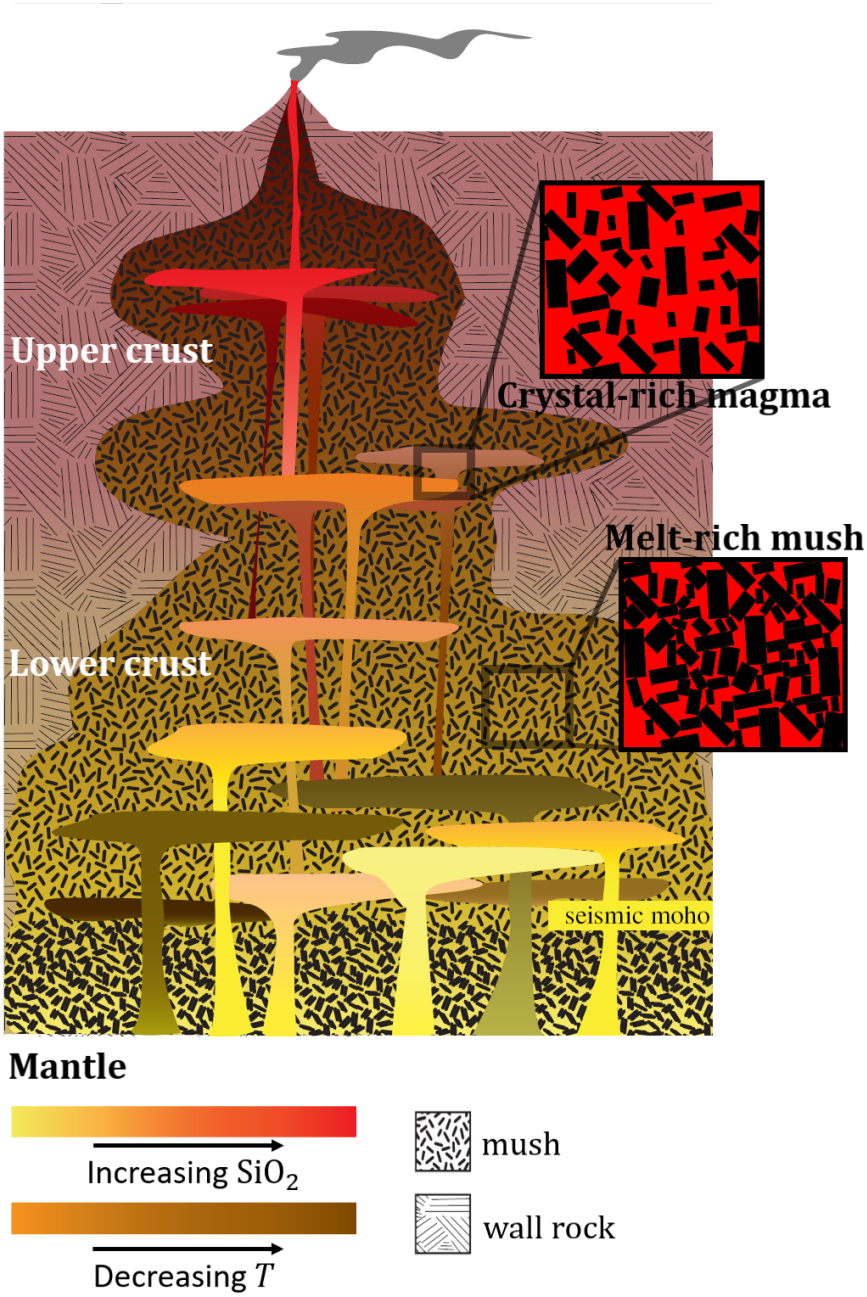

Figure 5.1: Modified from Cashman et al. (2017). Sketch of a transcrustal magmatic system. The magmatic system is largely composed by a mush in which layers enriched in melt form ephemeral magma chambers. The two boxes show a possible example of the structure of a crystal-dominated mush, where the rheology is controlled by the crystalline network, and a melt-rich magma, where rheology is controlled by melt.

crust during eruptions, however, they cannot provide the large magma volumes needed to form plutonic rocks or to supply prolongated volcanic activities (Karakas et al., 2017). For these reasons, to supply shallow magma chambers, melt might have to travel through the underlying mush or to be concentrated in specific enriched layers by other processes.

A way to transport melt through the mush is via porous flow (McKenzie, 1985). During its upward journey, melt comes in contact with crystalline matrix with which it is not in chemical equilibrium. This gives rise to a series of reactions between melt and crystals at the grains scale (reactive flow), leading to physical changes in the matrix which can either be dissolved or precipitated (Lissenberg and MacLeod, 2016; Jackson et al., 2018). Such porous medium approach is also important for the migration of exolved volatile phase which also influences significantly physical and rheological properties of the mush. Numerical models show how viscous fingering might take place in mush with intermediate melt fractions (Parmigiani et al., 2014; Cardoso and Woods, 1999). For lower melt concentrations, fracture-like channels can instead be opened cyclically even when a steady flux of gas is supplied to the bottom of the crystal-rich domain, suggesting that, in this way, mush can acts as a valve (Barth et al., 2019). However, porous flow alone might not be enough to describe all the processes that take place within the reservoir. For instance, it cannot explains observations in the Oman ophiolite (Kelemen et al., 1997) and at Hess Deep (Lissenberg and MacLeod, 2016), where melt has been quickly extracted and moved for kilometers in a time not sufficient to react with the surrounding mush. A way to get around this is by rapid channelized buoyant flows that can occur once sufficiently large melt-rich bodies are formed (Lissenberg and MacLeod, 2016; Jackson et al., 2018; Bachmann and Bergantz, 2004). Formation of such melt-rich layers does not necessary need an input heat flux: the increment of melt fraction in specific areas of the mush can trigger the MMT without any increments in temperature if the moving interstitial melt is enriched in low melting point components (Jackson et al., 2018).

A way a mush has to allow the formation of magma lenses is being remobilized. Remobilization acts as a fluidization mechanism through which solid-like areas of the mush are destabilized, leading to a rapid rise of melt. Typical examples are defrosting processes where heat and fluids coming from new magma intruded at the base of the mush bring it above the solidus until the MMT is reached (Parmigiani et al., 2014; Mahood, 1990). Simulations of mush remobilization due to melt intrusions highlight how the unlocked system can be mixed well and crystals can be efficiently entrained by the intruding melt (Bergantz et al., 2017; Burgisser and Bergantz, 2011; Bergantz et al., 2015; Schleicher et al., 2016). However, fluidization events may not concern the whole mush domain but only the portions where stresses exceed the strength of the crystalline network, leaving the remaining zone in their unyielded state (Karlstrom et al., 2012).

All these evidences show how to have an appropriate rheology to describe flow of crystal-rich magmas or mushes is a crucial point in volcanology and geodynamics. All processes that involve the motion of one of these magmatic systems, such as eruptions or the formation of magma chambers, require a proper description of the stress-strain constitutive equation and

its domain of validity. Their high solid fractions make them similar to concentrated suspensions in which solid touching particles can form a self sustained network that guarantees to the material the ability to resist local stresses. The presence of a network of particles does not characterize the fluid only by setting up a solid-liquid transition but, once the material is put in motion, it also influences the resulting flow. Flow characteristics will depend then on the particle-particle interactions since particles are not completely free to move or rotate: for a suspension of particles, in fact, the resulting effective fluid viscosity is always larger than the case where there are no particles (Mueller et al., 2009; Manga et al., 1998). The motion of intruders in a crystal-rich magmatic body, like the settling of crystals or country rock blocks as well as the ascent of bubbles or melt pockets, is generally treated in two distinct ways that can be view as end-members of a larger spectrum of behaviors. When intruders or deformable gas bubbles are very small compare to the crystals that make up the mush structure ($d_s \ll d_g$, where now d_s indicates the diameter of the intruder and d_g the characteristic diameter of crystals), they will see the surrounding material as a solid porous medium and they will be transported through its channels and connected porous not deforming the crystal network itself (Belien et al., 2010; Parmigiani et al., 2016). On the other hand, a large intruder ($d_s \gg d_g$) relates with the fluid structure as a continuum and will interact with the network depending on its rheology. Considering only those two scenarios, however, can lead to underestimate intermediate behaviours that strongly influence the critical conditions at which the motion is permitted. Hence, it is crucial to know when a particle-rich system is better described either as an undeformable porous medium or as a continuum, in which it is the bulk effective rheology that define the mechanical response of the system, or when this latter rheology breaks down and is not any more able to fully describe the flow.

5.2 Mush properties

In order to make a comparison between a magmatic system and the experiments presented in chapter 3, we have first to describe the geometric characteristics and mechanical and rheological properties usually assumed for a crystal mush. In the previous section we have seen how a magmatic system is volumetrically dominated by a mush reservoir and how it involves areas where the ratio of melt to crystals can varies significantly. Mush can extend throughout the entire crust and, within it, melt-rich layers can develop at different depths: from only few kilometers below the surface down to the limit with the mantle. The classic view of a magma chamber right below a volcano as a stationary (for long periods of time) and large melt-dominated body is unlikely. Even in the uppermost parts of the system, the magmatic reservoir is probably dominated by igneous mushes.

However, the issue of defining the geometry of such environments rises up from the difficulty in constraining the spatial melt distribution in lower and mid crustal reservoirs. The problem is due to the resolution of seismic tomography that is not able to detect large melt bodies even in regions that are active nowadays or have produced large eruptions in the

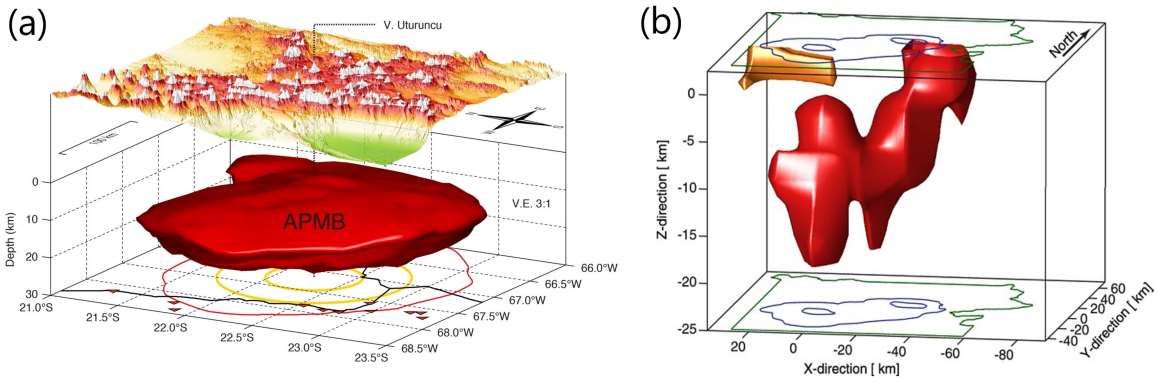

Figure 5.2: 3-D seismic images of crustal magmatic reservoirs where a low velocity body is shown through the contour (in red) of a seismic wave velocity isosurface. (a) Image of the Altiplano-Puna Magma Body (APMB), from Ward et al. (2014). (b) Magmatic reservoir beneath Yellowstone, from Farrell et al. (2014).

Quaternary (Cashman et al., 2017). What seismic tomographies usually show are areas of reduced seismic velocities that are interpreted as hotter zones compared to the surrounding material and hence with probably a higher melt content. For example, at Puna Magma Body (central Andes) seismic tomography shows a very large low-velocity zone at depth less than 25 km that might represent a melt-rich mush of $5\text{x}10^5$ km^3, Fig. 5.2a (Ward et al., 2014; Comeau et al., 2015). Likewise, underneath Yellowstone caldera (USA) a $1\text{x}10^4$ km^3 low-velocity body lays out between 5 and 17 km and overtops an even larger lower crustal anomaly of $4.6\text{x}10^4$ km^3, Fig. 5.2b (Farrell et al., 2014; Humphreys and Hager, 1990).

Fig. 5.1 summaries these observations and sketches a vertical cross-section of a partially molten magmatic system in which several melt-rich layers can form at different depths within a crystal mush that extends for the entire thickness of the crust. In the same figure we also show an example of a possible range of crystals sizes and shapes for both mush and magmas. In this case, a typical range of grain sizes can be set in between 1 and 5 mm. This range corresponds to what have been used in numerical simulations and several analog experiments of mush dynamics. For example, Bergantz et al. (2017) use in their simulations a particle diameter of 1 mm for felsic magma and 4 mm for mafic magma. Similarly, in analog experiments, particle diameters of d_g=[0.1, 1.5] mm and d_g=[1, 4] mm are used in Castruccio et al. (2010) and Forien et al. (2015), respectively. Other works have employed a maximum particle diameter of 1 mm (Hoover et al., 2001) and 5 mm (Boudreau, 2016). Crystal size of natural samples of Etna and Kilauea basaltic magmas show also same values: in Etna's lava flow larger crystals have a size of 4 mm (Pinkerton and Sparks, 1978; Castruccio et al., 2014) and should not be larger than few millimeters in the case of Kilauea basalt (Ryerson et al., 1988). These studies report the magma rheological properties as well (Table 5.1). In Etna basalts and lava flows yield stress and consistency have been measured equal to σ_y=78 Pa, $K_v \simeq$ 3000 Pa.s^n (Pinkerton and Norton, 1995) and σ_y=181 Pa, K_v=8000 Pa.s^n (Pinkerton and Sparks, 1978) with a shear-thinning exponents of $n \simeq$0.5 and n=0.76, respectively. Values of the same order of magnitude have been reported for Kilauea basalts and lava lakes: σ_y=10-

Table 5.1: Rheological properties for basaltic magmas. Shaw et al. (1968) analyzed tholeiitic lava from Makaopuchi lava lake (Hawaii); Ryerson et al. (1988) picritic basalts from Kilauea Iki lava lake (Hawaii); Pinkerton and Sparks (1978) lava flow from Etna volcano (Italy); Pinkerton and Norton (1995) basalts from Etna volcano (Italy); Ishibashi (2009) basalt from Fuji volcano (Japan); Vona et al. (2011) basalts from (a) Stromboli and (b) Etna volcano (Italy).

	σ_y (Pa)	K_v (Pa.s^n)	n	d_{cryst} (m)
Shaw et al. (1968)	70-120	6.5-7.5x10^2	1	-
Ryerson et al. (1988)	100-800	$\sim$10^1-10^2	0.7-0.9	-
Pinkerton and Sparks (1978)*	181	8x10^3	0.76	4x10^3
Pinkerton and Norton (1995)*	78	$\sim$ 3x10^3	$\sim$0.5-0.8	-
Ishibashi (2009)	-	7.65x10^2	0.82	1x10^3
Vona et al. (2011)a	-	$\sim$ 4x10^2 - 4x10^3	$\sim$0.9	$\sim$1x10^4
Vona et al. (2011)b	-	1-5x10^3	0.90-0.95	$\sim$1x10^4

* after Castruccio et al. (2014)

10^3 Pa, K_v=10-100 Pa.s^n, n=0.7-0.9 for the first case (Ryerson et al., 1988) and $\sigma_y \simeq 10^2$ Pa, $K_v \simeq$700 Pa.s^n, n=1 (i.e. magma is supposed to be a Bingham fluid in this latter case) for in-situ measurements in lava lake (Shaw et al., 1968). Other natural datasets are those of Caricchi et al. (2007); Ishibashi (2009); Champallier et al. (2008); Pistone et al. (2012). In all these cases rheological measurements show a non-Newtonian, predominantly shear-thinning, behaviour of crystal-rich magmas. However, although a yield strength is assumed to appear as soon as an interconnected framework of crystals develops, the experimental quantification of yield stress of natural samples is still quite complex because viscosity measurements are usually carried out at very high torque (e.g. Champallier et al. (2008)). In these cases, to fit the flow curves with a yield stress power-law model and to be able to extrapolate the proper value of σ_y analysis at much lower stress would be necessary. Ultimately, even though a precise value of yield stress for such systems is not straightforward to get, different rheological behaviours have been observed and are expected during transition from mush to magma. Therefore, we will evaluate experimental results within a range of yield stress for a magmatic system between 0.1 and 100 Pa.

In section 2.1 we have also introduced the importance of crystals shape and maximum packing fraction, ϕ_m, for particle suspensions. For crystal-rich reservoirs, a ratio of ϕ/ϕ_m >0.8 leads to a non-Newtonian rheology in which yield stress and shear thinning behaviours become stronger as the ratio increases (Mader et al., 2013). With an average particle aspect ratio of β=1.81, according with eq. (2.3), our SAP samples have a maximum packing fraction ϕ_m=0.638, leading to ϕ/ϕ_m >1 and making SAP a good candidate for the analogy with a crystal-rich magma or melt-rich mush.

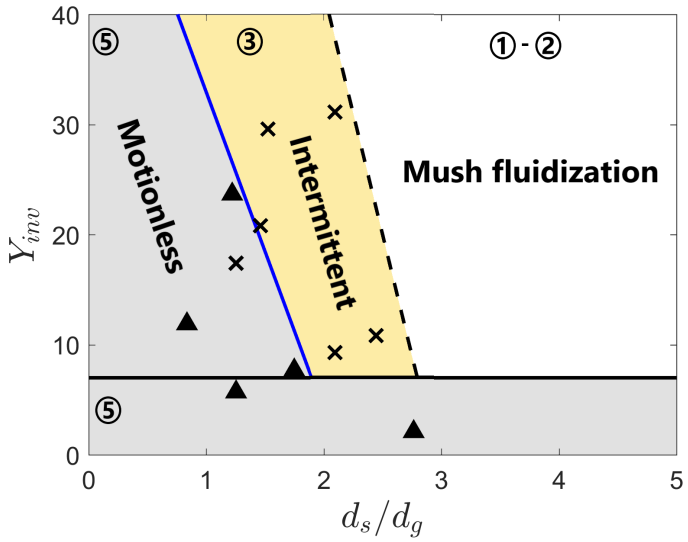

Figure 5.3: Regime diagram adapted from Fig. 3.14. Zones in gray represent the motionless regime (5), and are bounded by the black solid line, Y_{inv_C}=6.99, which identifies the classical boundary in the limit of large d_s/d_g, and by the blue line, eq. (3.8), which identifies the boundary due to the fluid structure. The zone in white where the fluidization is expected (motion regime (1) and (2)) is separated from motionless by the region where we observe intermittent behaviour (regime (3), in yellow). Symbols indicate our experiments: triangles for no-motion and crosses for the intermittent regime.

5.3 Magma pockets rising in a mush

We investigate here the different regimes of intrusion through a crystal-dominated mush of a buoyant magma pocket. The latter could be due to replenishment of the magma chamber by influx of mantle-derived hot basaltic melt. The mush is considered to be an Hershel-Bulkley fluid (that is, it has an yield stress and a strain-rate dependent viscosity) with rheological properties within the range of those described in the previous section.

Conditions for motion: influence of the crystal size

Based on our observations in SAP, we recall in Fig. 5.3 the motion-motionless boundary by indicating the upper limit of Y_{inv_C} for small d_s/d_g and the region where we get the intermittent regime. Together with the classical Y_{inv_C}=6.99 valid for large d_s/d_g, the final expression of the critical (inverse) Yield number divides the (Y_{inv}, d_s/d_g)-space in two regions as shown by solid lines in Fig. 5.3. In the motionless regime (5) the new incoming material does not intrude the surrounding medium.

We can now use the rheological characteristics of a mush (e.g. Table 1) to translate Fig. 5.3 depending on the mush yield stress and crystal size (Fig. 5.4). We consider a less dense melt pocket ($\Delta\rho$=600 kg/m^3) intruding in a magmatic reservoir with density 3300 kg/m^3 and crystal diameter d_c=1 mm (Fig. 5.4a) or d_c=4 mm (Fig. 5.4b). According with section

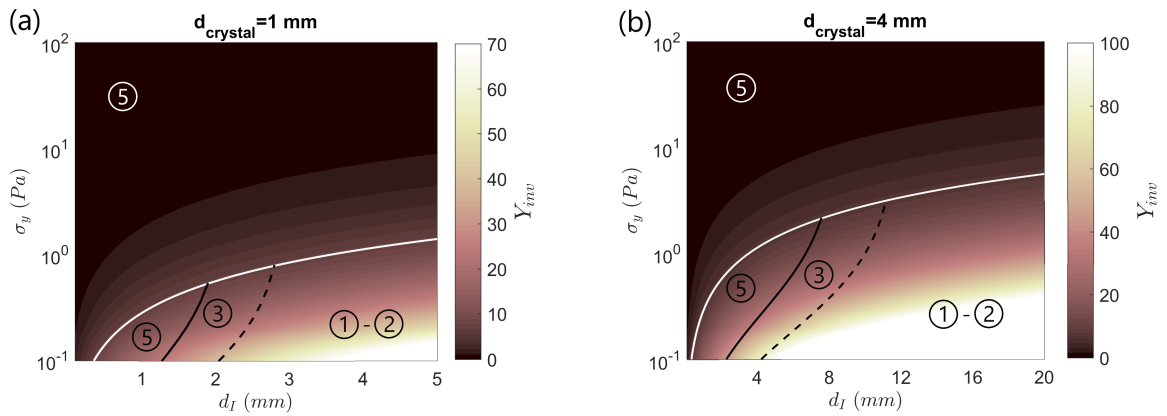

Figure 5.4: Influence of the intermittent regime and new Y_{inv_C} in crystal-rich magmatic reservoirs. $\Delta\rho$=600 kg/m^3. The crystal diameter is 1 mm (a) and 4 mm (b). White line is Y_{inv_C}=6.99. Black solid line is eq. (3.8). Black dashed line is the intermittent regime boundary as in Fig. 5.3. Numbers indicate the same mush's states as in Fig. 5.3.

5.2, we choose a not excessively large interval of yield stress for the hypothetical mush, that is we vary σ_y between 0.1 and 100 Pa. In the case of a mush with d_c=1 mm, small intruders ($d_I \leqslant$5 mm) can move only for very small values of σ_y, i.e. $\sigma_y \leqslant$1.5 Pa. The intermittent regime and the new Y_{inv_C} limit concern mainly very small melt drops. And although the zone where the mush structure influences the intrusion dynamics increases with the crystal size (Fig. 5.4), it shall not play a role for natural crystal sizes (1-4 mm) and yield stresses (Table 1). Only large pockets ($\gg d_c$) would make it through natural mushes where σ_y is larger than 10^1-10^2 Pa: 35 cm for σ_y=100 Pa and 2.85 m for σ_y=800 Pa.

Then, within the so called mush fluidization zone (regime (1) and (2)) the intruder is able to move upward interacting and deforming the mush.

Ascent rate

As we saw earlier, the ascent rate depends on the intruder buoyancy and the mush rheology. It writes:

$$v_I = \left[\left(\frac{g d_I \Delta\rho}{3} - 7\sigma_y\right)\frac{d_I^n}{8.52 K_v}\right]^{1/n}. \tag{5.1}$$

Fig. 5.5 shows the velocity at which a less dense melt pocket ($\Delta\rho$=600 kg/m^3) of size d_I rises through a mush with yield stress in between 0.1 and 10^3 Pa. We consider an interval of K_v in between 700 and 3000 Pa.s^n and n=0.5 (Fig. 5.5a) or n=0.9 (Fig. 5.5b). Although the influence of σ_y prevails at small d_I, for large intruders the difference in velocity within this specific range of yield stress is mainly due to the consistency. Thus, if we assume valid the Hershel-Bulkley model for a magmatic system, a 1-m-wide spherical pocket of basaltic melt would be able to travel, for instance, a 25-km-thick crustal mush (with a yield stress of

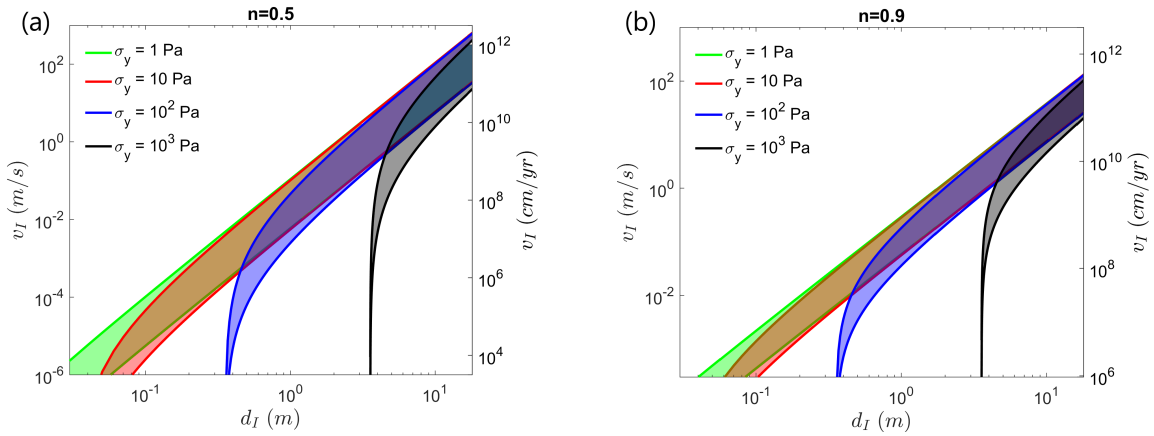

Figure 5.5: Velocity v_I of a rising melt pocket of diameter d_I in a Hershel-Bulkley mush. (a) Shear-thinning index n=0.5. (b) Shear-thinning index n=0.9. Colors refer to different yield stresses as indicated in legend. Bands thickness depend on the interval of consistency which is taken in between 700 and 3000 Pa.s^n.

100 Pa, n=0.5 and K_v=[700, 3000] Pa.s^n) in 1.8x10^{-2} - 3.3x10^{-1} years, that is in about a week to months.

Extent of the fluidized region

As we have reported in section 3.5, the deformation around the intruder for the linear and irregular regimes in SAP involves a section of material that scale as eq. (3.11). This volume of fluidized material responds mainly as a viscoplastic fluid: when the melt pocket goes up the mush, an area of it will be subjected to solid-liquid transition, here the MMT, in which the self sustained network of crystals loses it strength. For a mush at the same conditions of those described above (σ_y=100 Pa and $\Delta\rho$=600 kg/m^3), the 1-m-wide melt pocket, according with eq. (3.11), would also fluidize a lateral section L_{fluid} of 2.4 m, leading to a volume of fludized mush V_{fl}=58.3 m^3, where V_{fl} indicates the volume of a sphere of radius L_{fluid}. Within this volume the stress field won't be transmitted any more by force chains but by a combination of viscous and elastic stresses, depending on the rheological properties of the fluid. In this way, the newly fluidized zone also helps to trigger further motion by mobilizing other small inclusions, such as small bubbles that can be previously entrapped in the mush and that now can move along streamlines until eventually colliding with the main inclusion, further increasing its buoyancy and size. For example, in our experiments, few small bubbles, were trapped in the fluid column during the fluid preparation. They were able to move upward only when the material around them were fluidized, for instance by the passage of a large sphere during a run or simply stirring the fluid during the preparation.

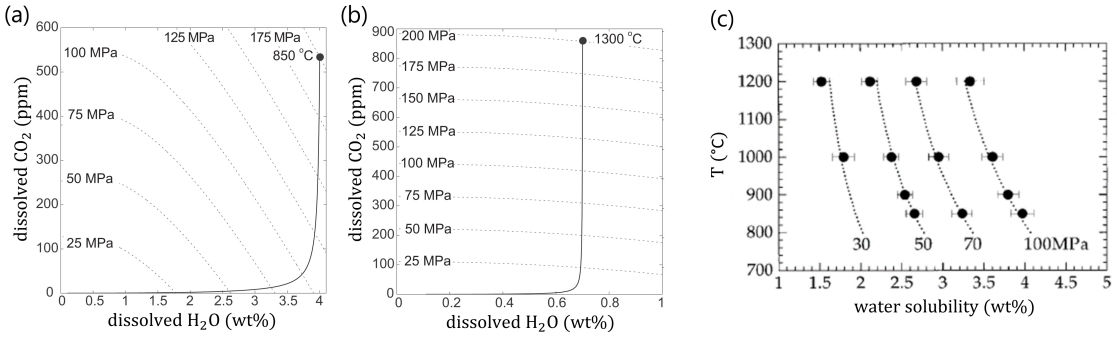

Figure 5.6: Solubility of CO_2 and H_2O. (a) and (b) are modified from Gonnermann and Manga (2013). (a) Solid line shows a closed-system degassing path of a rhyolite magma. Starting conditions are: no initial exsolved volatiles, T=850 °C, initial pressure of 200 MPa, initial dissolved H_2O content of 4 wt%. (b) Degassing path of a basaltic magma. Starting conditions are: no initial exsolved volatiles, T=1300 °C, initial pressure of 200 MPa, initial dissolved H_2O content of 0.7 wt%. (c) Modified from Yamashita (1999). Water solubility in rhyolite as a function of temperature.

5.4 Bubbles rising in a mush

Bubbles and dissolved volatiles, especially water, play a very important role in varying magma viscosity, compressibility and buoyancy, and in helping its ascent (Pyle and Pyle, 1995). The presence of bubbles together with their ability to escape and move inside the magma body, has also a direct impact on the dynamics of explosive eruptions. Evaluate their mobility is then of extreme interest also for natural hazard.

Bubbles commonly nucleate within magma during its decompression and/or heating. It occurs because the solubility of volatile phases increases with pressure and decreases with temperature (Yamashita, 1999; Schmidt and Behrens, 2008). Consequently, as pressure decreases and temperature increases, gas or vapor bubbles can nucleate and grow. If external fluids are not involved, these gas bubbles are mainly made by the principal magmatic volatiles, that is H_2O and CO_2. In silicate melts, for example, solubility of CO_2 is proportional to partial pressure, p_i, whereas solubility of H_2O has a square root dependence on p_i (Gonnermann and Manga, 2013). Fig. 5.6a and b show an example of how solubility of the main volatiles evolves in basaltic magma and in rhyolite as the pressure varies. One can note that almost all CO_2 exsolves at pressure larger than 25 MPa for basalt and larger than 100 MPa for rhyolite. On the other hand, H_2O dissolves from the magma at pressure lower than 25 MPa and 100 MPa for basalt and rhyolite, respectively. Within the same range of pressure, Fig. 5.6c shows the decrease of water solubility in rhyolite when temperature increases.

When buoyant bubbles form by exsolution of volatiles within a crystal-dominated mush, then they may or may not be able to move through it, similarly to the rising melt pocket case. We plot this condition in Fig. 5.7a, where we consider bubbles of diameter d_b within a mush with similar yield stress and crystal size ranges as in the previous section. We consider

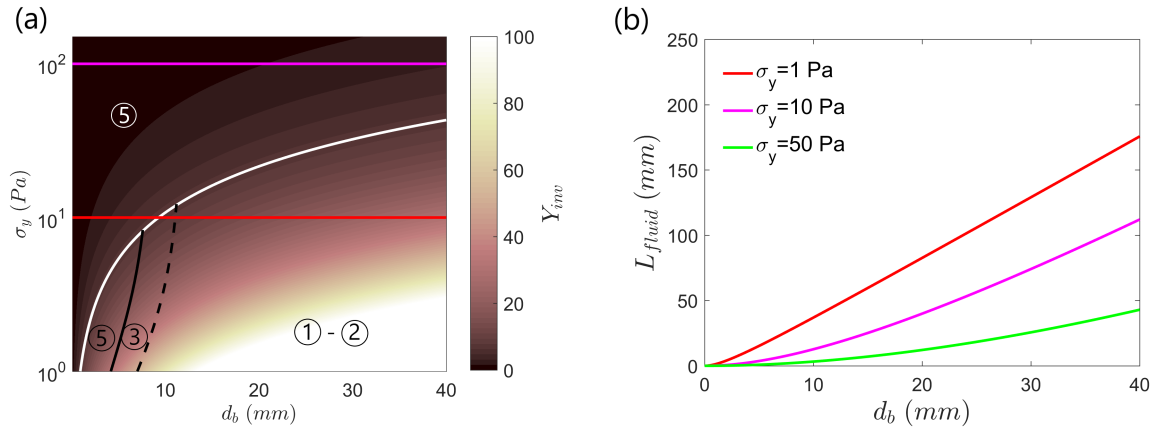

Figure 5.7: (a) Motion and no-motion conditions for a bubble of diameter d_b moving through a crystal-rich magmatic reservoirs with yield stress. $\Delta\rho$=2300 kg/m^3 and crystal diameter is 4 mm. White line is Y_{inv_C}=6.99. Black solid line is eq. (3.8). Black dashed line is the intermittent regime boundary as in Fig. 5.3. Magenta (σ_y=100 Pa) and red (σ_y=10 Pa) lines indicate conditions described in the text. (b) Fluidized region as function of bubble diameter for three values of yield stress which can allow the bubble motion.

a density ratio between bubble and magma of $\Delta\rho$=2300 kg/m^3 and that the bubbles retain their shape constant due to surface tension. From Fig. 5.7a one can recognize once again the limit that bounds bubbles able to move from those that are unable and remain entrapped into the mush. Fundamental is the region in which motion is not expected: there is a broad area in the (σ_y, d_b)-space in which even quite large bubbles are trapped and cannot move and deform the mush. For instance, in the case of σ_y=100 Pa (magenta line in Fig. 5.7a), small bubbles are always stuck in the mush and only those with a diameter of $d_b \sim 10$ cm are buoyant enough to rise. We see that for the bubble case, the influence of the mush structure significantly increases the domain of parameters where the bubbles remain stuck in the mush. These conditions are therefore crucial because can allow the accumulation of all these small bubbles in specific portions of the mush. The presence of portions or layers enriched in motionless bubbles directly impacts the possible re-mobilization scenarios described in the introduction to this chapter (sect. 5.1).

On the other hand, a weaker mush, e.g. σ_y=10 Pa (red line in Fig. 5.7a), allows more bubbles (i.e. also those with smaller sizes) to move upward fluidizing a region around them. According to eq. (3.11), Fig. 5.7b shows the portion of mush around a single bubble which undergoes fluidization as function of bubble diameter and yield stress. For a crystal size of d_c=4 mm, the minimum bubble diameter needed for $Y_{inv} > Y_{inv_C}$ is here d_b=0.9 cm (Fig. 5.7a). A bubble of such diameter would be buoyant enough to rise through the mush, leading in turn to a fluidized lateral section L_{fluid}= 11 mm and a fluidized volume of material equal to $V_{fl} \simeq$5.6x10^3 mm^3. Bubbles would travel upward with velocity v_b in between 4.3 cm/yr, for n=0.5 and K_v=700 Pa.s^n, and 2x10^{-1} cm/yr, for same n but K_v=3000 Pa.s^n.

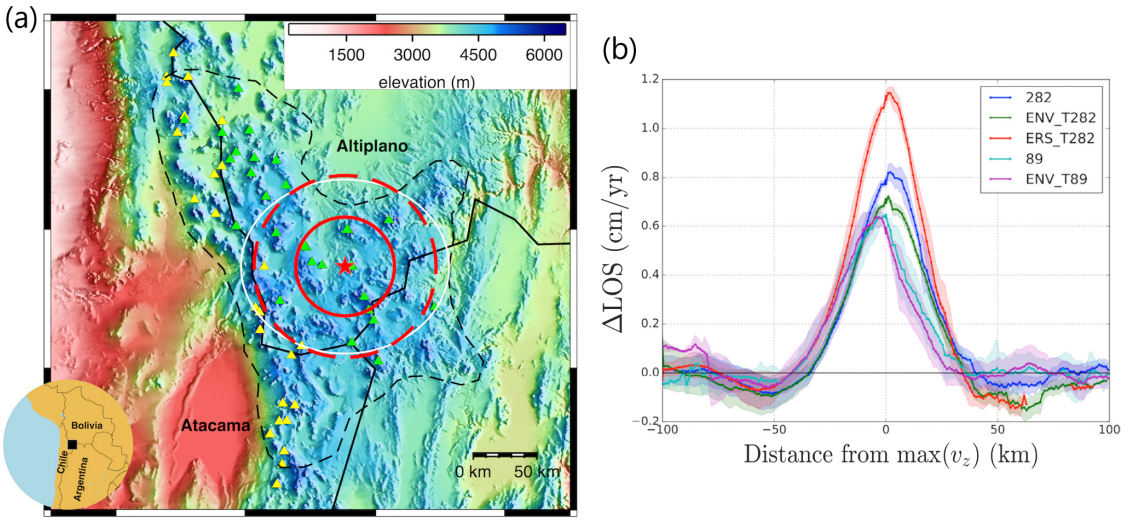

Figure 5.8: (a) Map view of the Altipiano-Puna region (southern Bolivia). The center of the regional uplift is indicated by a red star. The uplift involves the region within the red solid circle (radius of about 40 km). The region of subsidence is restricted by the red dashed circle (from InSAR data). White ellipse bounds the spatial extent of the seismic anomaly at 20 km below sea level of Ward et al. (2014). Figure modified from Gottsmann et al. (2017). (b) Average velocities of line of sight (LOS) along sections crossing the center of the uplift. Modified from Gottsmann et al. (2017).

5.5 Diapirism

At larger scale, upwelling of buoyant material within the crust translates in diapirism. Typically, diapirism is associated to salt domes which being lighter than surrounding sedimentary rocks can slowly flow upward and deform through solid-state creep processes. However, diapirism is also involved in magmatic systems. Here a diapir represents a large portion (of the order of tens of kilometers in diameter) of buoyant and very viscous crustal rocks which rises slowly forming a dome shaped structure. The process involves long time-scales and hence is usually associated with viscous and plastic deformations of the crust and not only with its elastic response.

An active and rising diapir may be the cause of the uplift observed above the Altiplano-Puna Magma Body (APMB, Fig. 5.2a) (Fialko and Pearse, 2012; Comeau et al., 2015). Geodesy data (InSAR) and leveling data show in fact a continuous (since 1960s), nearly constant and slow uplifting of an about 100-km-wide region of the Altiplano-Puna volcanic complex (Fialko and Pearse, 2012; Henderson and Pritchard, 2013; del Potro et al., 2013) (Fig. 5.8a). The central area which is being uplifted at about 1 cm/yr is also surrounded by a broad ring of subsidence (Fig. 5.8b). This forms a global sombrero-shape uplift which is consistent with the presence of a diapir deep inside the crust. In this case the diapir would develop from the APMB within a framework of an heterogeneous crust and at a greater depth than the brittle-ductile transition. The latter is reported between 4.5 and 10 km below the Altiplano (Jay et al., 2012) whereas the APMB extends from a depth of ∼20 km below the

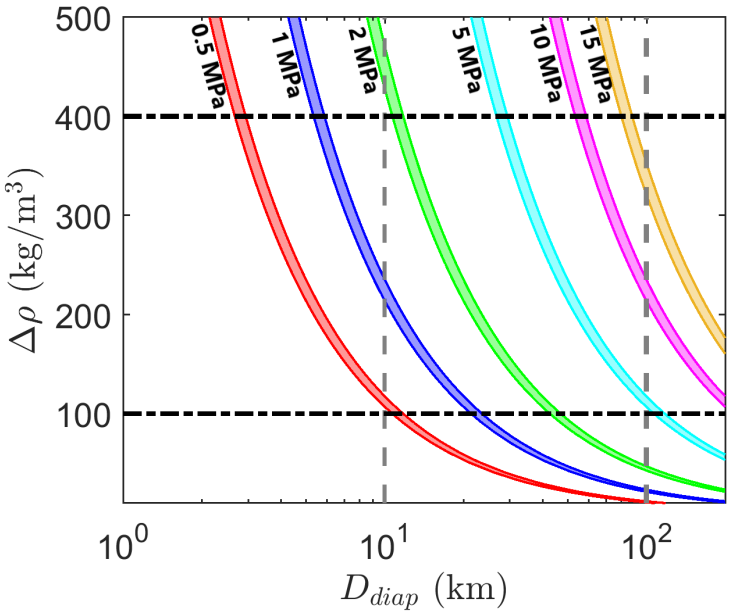

Figure 5.9: Yield stress (color lines) allowing the development of a diapir from the APMB in the lower part of the crust as function of diapir diameter and density contrast within the crust and according to $Y_{inv_C} = 7.35 \pm 0.35$.

surface (based on magnetotelluric images, Comeau et al. (2015)).

In the previous chapter 4 we shown that two main conditions need to be satisfied to allow the ascent of a buoyant instability in a yield stress medium. The first one regards the inverse of the yield number, that is $Y_{inv} > Y_{inv_C} = 7.35 \pm 0.35$, and the second one is accounted by a supercritical Bingham number, i.e. $Bi \leqslant 1$. Given these two conditions, one can evaluate the emplacement conditions for buoyant instabilities (e.g. a diapir) in a crust with complex rheology. We do that for the case of APMB, assuming for the rising diapir a vertical velocity of v_z=1 cm/yr (Fialko and Pearse, 2012).

In Fig. 5.9 we show the conditions which lead to $Y_{inv} = Y_{inv_C}$. We take as characteristic diapirs diameter, D_{diap}, the range between 10-100 km, according to Fig. 5.8b. The density contrast between diapir and surrounding crust is not well constrained and varies between different geodynamics models. Fialko and Pearse (2012) use in their numerical simulations a density difference of $\Delta\rho$=400 kg/m^3, whereas smaller values of $\sim$100 kg/m^3 are employed by Gottsmann et al. (2017) and Spang et al. (2019). Within these ranges of diapirs size and density, we find that the diapir could move, deforming the surrounding ductile crust if the latter has a yield stress in between 0.5 and 15 MPa (Fig. 5.9). Larger values of yield stress clearly need either a larger instability or an unlikely larger density contrast. Similar values of σ_y have been reported for crustal granitic rocks on the western Arabian Peninsula, where the rock strength is estimated between 1-3 MPa (Jónsson, 2012). Also Gerya and Burg (2007) use a plastic strength of the crust equal to 1 MPa to model ultramafic magmatic intrusions in continental crust. Slightly larger yield strengths have been measured by Caricchi et al. (2007)

during their laboratory experiments. Here water bearing (2.7 wt.% H_2O) rhyolitic melts with particles of quartz have shown yield strengths in the order of 20-100 MPa, depending on temperature and crystal fractions.

In our case, assuming a crust with a yield stress larger than 15 MPa would result in a buoyant instability stuck within it. A simple Stokes flow for a viscous approximation is therefore not sufficient to explain the observed uplift at such high σ_y and other ingredients have to been invoked. A way to decrease locally the yield stress requires, for instance, an increment in temperature such as to remelt crystals and facilitate the MMT. In this way some portions of the magma body could face more easily the rheological transition which let them to move through the crust. Another avenue consists of accumulation and growth of bubbles. Given the large hypothetical yield stress bubbles will grow in situ making portions of the magmatic reservoir volatile-saturated. If these regions are also cooling down because close to colder crustal rocks, the continued exsolution of volatiles leads to a significant pressure increase due to the expansion of the volatile-rich melt-crystal mixture (Edmonds and Woods, 2018). A drastic increase in pressure would in turn lead to fractures and fast intrusions of magma into the surrounding brittle crust through dykes. The development of the dyke then releases the pressure in the volatile-saturated portions of the magma body and the dyke will slow down.

Beside $Y_{inv} > Y_{inv_C}$, the other condition needed for motion is $Bi \leqslant 1$. As previously seen, this critical condition translate into a critical (and minimum) strain rate needed for motion. In chapter 4 we show that for an Hershel-Bulkley fluid, it writes as $\dot{\gamma}_c = (\sigma_y/K_v)^{(1/n)}$ and that it further implies a stress of $\sigma = \sigma_y + K_v(\dot{\gamma}_c)^n = 2\sigma_y$. The effective viscosity is then given by $\eta_c = 2\sigma_y/\dot{\gamma}_c$. In Fig. 5.10 we display this viscosity as a function of fluid consistency and the range of yield stress found previously (i.e. σ_y in between 0.5 and 15 MPa). We take two limit values for the shear thinning index, namely n=0.25 (Fig. 5.10a) and n=0.5 (Fig. 5.10b). They correspond to stress exponents n_E=1/n of 4 and 2, respectively; as expected for rocks (Ranalli, 1995). The viscosity reported in Fig. 5.10 corresponds to the maximum viscosity, calculated from the minimum strain rate that guarantees Bi=1, that the crust must have to allow the displacement due to the rising diapir. Moreover, from the recorded uplift velocity (v_z) one can further bound the minimum value of consistency for the specific case at APMB. From the condition $Bi \leq 1$ one can in fact relate the measured maximum rising velocity to the size of the instability and the critical strain rate. As found for plume simulations in previous chapter, the maximum velocity scales as (Fig. 5.11):

$$\max(v_z) \sim 3.7 D_{eq} \dot{\gamma}_c, \tag{5.2}$$

where v_z was the plume velocity and D_{eq} the equivalent diameter of the hot pocket before the onset. This scaling translates to $v_z \sim 3.7 D_{diap} \dot{\gamma}_c$ for the case of APMB, leading to a critical strain rate of $\dot{\gamma}_c = v_z/3.7 D_{diap}$. The resulting consistency is therefore $K_v = \sigma_y \dot{\gamma}_c^{-n} = \sigma_y (\frac{3.7 D_{diap}}{v_z})^n$.

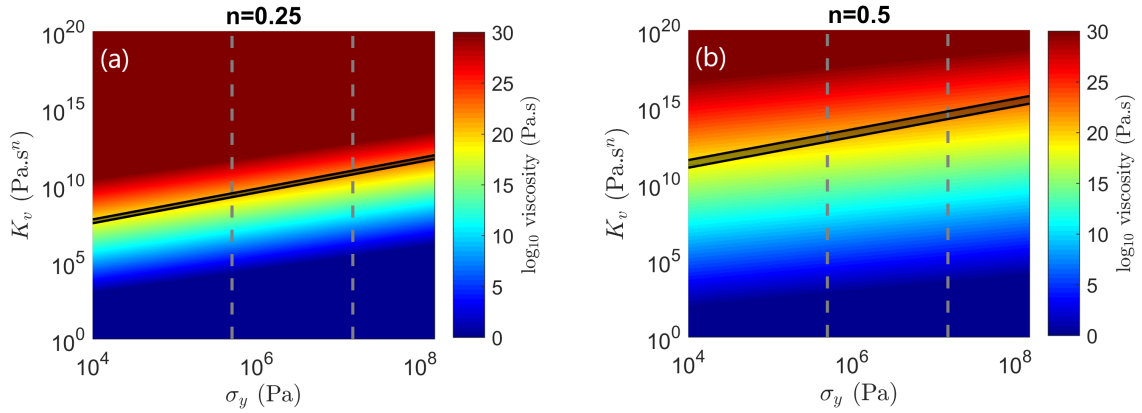

Figure 5.10: Maximum viscosity η_c at Bi=1 as function of consistency K_v and yield stress σ_y. Grey dashed lines bound the range of yield stress after Fig. 5.9. Black bands indicate $K_v = \sigma_y(D_{diap}/v_z)^n$, with D_{diap} between 10 and 100 km and an uplift velocity of v_z=1 cm/yr (Fialko and Pearse, 2012). (a) Shear thinning exponent n=0.25 and (b) n=0.5.

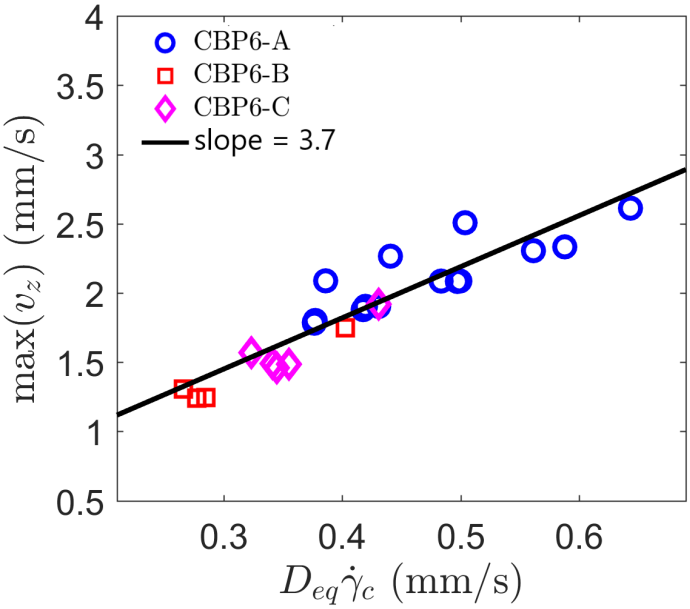

Figure 5.11: Maximum plume rising velocity as a function of the product between equivalent diameter D_{eq} (where $D_{eq} = 2r_{eq}$) and critical strain rate. The line indicates a fit with slope of 3.7.

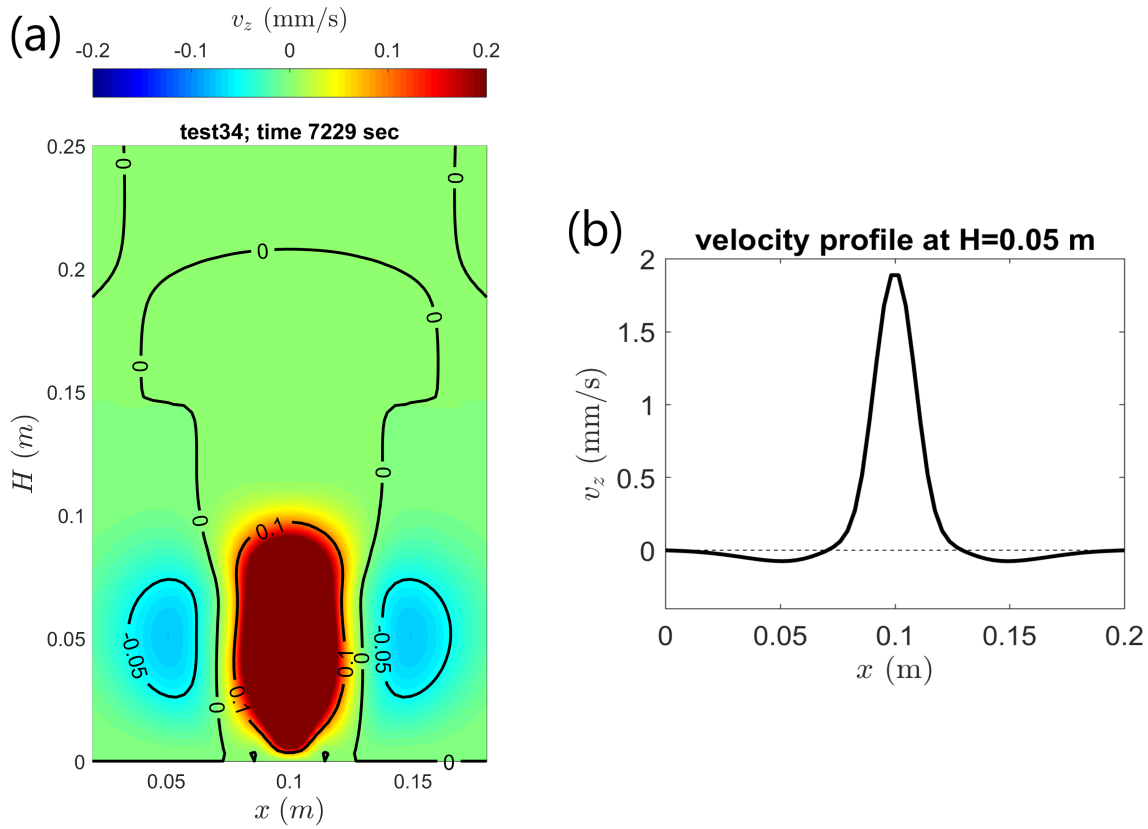

Figure 5.12: (a) Example of velocity field of a thermal plume generated in a viscoplastic fluid at time t=7229 seconds (simulation T-34 in Table 4.2, chapter 4). Colors and contour refer to the vertical component of the velocity. (b) Velocity profile for the same simulation in (a) taken at a height of H=0.05 m. Dashed line indicates v_z=0.

This value of K_v is reported in Fig. 5.10 for the chosen interval of diapirs sizes.

In this way, according to Fig. 5.9, a diapir of D_{diap}=50 km and $\Delta\rho$=100 kg/m^3 would set on motion in a lower crust with yield stress of around σ_y=2.2 MPa and n=0.5. These conditions would lead to a consistency of $K_v \sim$ 5x10^{13} Pa.s^n and finally to an effective maximum viscosity for the crustal rocks around the diapir of about $\eta_c \sim$2.6x10^{21} Pa.s. Such an high viscosity corresponds in order of magnitudes to the one of hot sub-solidus host rocks (Sparks et al., 2019) inside which magma bodies are usually emplaced.

The other features that the diapir model is capable to reproduce regards the ring of negative velocities close to the upwelling body. We show it in Fig. 5.12 by proposing the case of a thermal plume simulated in a viscoplastic medium (simulation T-34 in Table 4.2, chapter 4). From the velocity field (Fig. 5.12a) one can notice how, at the lifting of the plume, the sides of the hot pocket empty themselves in the rising plume, producing a downwards flow of material. The velocity profile along at a height of H=5 cm (Fig. 5.12b) qualitatively recalls the sombrero shape of the uplift velocity registered at APMB. However, this comparison must be taken only as a qualitative one since either initial conditions (e.g. the aspect ratio) and rheological properties between the natural case at APMB and the

simulation in Fig. 5.12 are different.

5.6 Summary of the volcanological applications

In section 5.3 we have investigated the different regimes of intrusion through a Hershel-Bulkley crystal-dominated mush of a buoyant magma pocket. We have shown that small intruders (diameter $\leqslant$5 mm) move only in mushes with a very small yield stress (σ_y <1.5 Pa). The intermittent regime discussed in chapter 3, where the fluid structure strongly influences the rising dynamics, concerns here only very small melt drops and, although a dependence on the crystal size was found, it seems to be not particularly relevant for natural crystal sizes and yield stresses. On the other hand, larger intrusions (e.g. one meter wide) can move quite quickly and travel through a mush extending throughout the entire crust in weeks/months.

Similarly, in section 5.4 we found that there are conditions at which bubbles can remain entrapped, and hence accumulate, within specific portions of the mush. And others where buoyant bubbles move efficiently and are able to fluidize an area of mush around them. These conditions can therefore become fundamental for the subsequent dynamic evolution of the entire mush, contributing or not to the remobilization of large parts of the mush.

Lastly, in section 5.5 we have discussed the natural case at APMB by applying results from our plume simulations. To allow the lifting of a 10-100 km-wide diapir with a density contrast with respect to surrounding rocks of 100-400 kg/m^3, the lower ductile crust needs a yield stress of ∼0.5 - 15 MPa to respect conditions of $Y_{inv} \geqslant Y_{inv_C}$. In addition to that, from $Bi \leqslant 1$ we can bound the maximum effective viscosity (η_c) for a lower crust which would allow the emerge of a diapir. For an uplift velocity of 1 cm/yr at APMB, we find the effective viscosity η_c being around 10^{21} Pa.s.

Chapter 6

Conclusions

In this thesis we investigated the role of elasticity and fluid structure on motions of yield stress fluids. Both laboratory experiments and numerical simulations have been used to analyze and characterize fluids deformation. We applied afterwards the scaling laws found in this way to evaluate their influences and impacts on different geological systems.

Regarding the experiments, we have investigated the influence of the size of grains which build up the structure of a mixture of water and swollen superabsorbent polymer (SAP) on the dynamics of a sphere falling under gravity through it. As the sphere to structure sizes ratio d_s/d_g was varied between 0.8 and 13, we were able to explore the range where fluid structure and intruder sizes become comparable. Besides the classical steady-state motion and the stoppage regimes already reported in viscoplastic fluids for $d_s/d_g \gg 1$, the interaction between sphere and the fluid structure results in two additional regimes where the motion becomes more chaotic. We found that this strong interaction can be appreciated in the first place by the signature on the sphere total travelled distance in the horizontal direction. Furthermore, we proved that the effective rheology of our SAP fluids is described by an Herschel-Bulkley model with shear-thinning index of 1/2, making this simple set-up a good rheometer for this type of fluids. The fluid rheological properties (i.e. yield stress and consistency) are found to increase with the gel grain size. However, the overall sphere motion predicted with an Herschel-Bulkley rheology begins to break down when it "sees" the texture only for sphere diameters less than twice the SAP grain size. This happens because when the sphere diameter becomes less than twice the SAP grain size, the sphere does not see anymore the collective properties of the SAP fluid, but rather the properties of each individual grain. This can explain the complete arrest of the spheres that we recorded even for Yield number (Y) much lower than the critical one (Y_c). Next, we analyzed the flow around the sphere using Particle Image Velocimetry (PIV). This technique allowed us to identify the flow fore-aft asymmetry in which a negative wake forms at the back of the sphere during the fall. PIV also helped us to recognize the possible region of fluid subjected to the solid-liquid transition. We further investigated this yielded region by comparing the yield surface obtained from the velocity field with the fluid deformation detected by analyzing spatiotemporal fall profiles.

A scaling law for the lateral extension of the yield surface has been provided and found in agreement with other published studies. Regarding these experiments, more work would be necessary to measure the mechanical properties of individual SAP grains. In this way, an interesting route for the future could be to try to relate quantitatively the rheological properties of SAP to its internal structure.

The second topic covered regards the development of thermal plumes in a elasto-visco-plastic (EVP) material and triggered by a difference of temperature applied in a localized heating point. We approached the problem via numerical modeling with a modified version of the code StagYY that combines viscoplastic and viscoelastic aspects together. Simulations succeed in reproducing plumes with a finger-like shape and with a take off a long time after the start of heating, as it was in experiments (Davaille et al., 2013). Similarly to Massmeyer et al. (2013), we found the flow being described by the global yield parameter Y_0 and local parameters Bi (the Bingham number) and Y_{inv} (the inverse of the Yield number). However, we have also shown how the rising of the plume and its subsequent growth is also affected by the employment of elasticity. Generally, with a EVP rheology the key parameter to trigger a plume remains the yield parameter since small variations of it strongly affects the plume onset time. Local conditions that allow plume takes off and growth require the ratio between yield stress and viscous stress being smaller than 1 (i.e. $Bi < 1$), and the ratio between the buoyancy of the hot pocket and the yield stress being equal to $Y_{inv_C} = 7.35 \pm 0.35$. We found a dependence between the local Deborah number and the plume onset time in which the more the material is elastic, the shorter the onset time is. Elasticity also affects the flow in regions of fluid where strain is small. With an EVP model plumes do not reach the top of the numerical domain and an unyielded layer of fluid always remains above the plume head.

This last part would benefit from more simulations in order to better constrain the plume dynamics at different initial conditions as well as the conditions needed to guarantee the plume episodicity showed in laboratory experiments. Moreover, we would like to modify the frame-invariant stress derivative by adding the upper convected rate in the constitutive model, to extend the domain of elasticity that we can explore.

Another topic equally interesting is the Rayleigh-Benard convection (RBC). In this case a model which considers elasticity could help to better understand the processes that hide behind the origin of RBC in yield stress fluids (e.g. Metivier et al., 2017; Darbouli et al., 2013; Kebiche et al., 2014). From a more geological prospective, an interesting avenue for the future would be the employment of the EVP model in simulations of mantle convection. Yield stress together with a viscoelastic rheology can become fundamental for modeling a more realist mantle convection and could help, for instance, to link recent developments in determining bridgmanite rheology, which characterizes the lower mantle and seems to deform as a viscoplastic fluid (Boioli et al., 2017; Davaille et al., 2018), with the broad mantle plumes imagined in the mantle by global seismic tomography (e.g. French and Romanowicz, 2015).

These results were applied to transcrustal magmatic reservoirs where the rheological transition between mush and magma (MMT) takes place. In this view we considered the

crystal mush as a jammed material with a rheology and a structure similar to SAP. Two situations have been investigated. The first regards the upward journey of a buoyant mantle-derived basaltic melt pocket. We have shown that small intruders (diameter $\leqslant$5 mm) move only in mushes with a very small yield stress (σ_y <1.5 Pa). The intermittent regime discussed above, where the fluid structure strongly influences the rising dynamics, concerns here only very small melt drops and, although a dependence on the crystal size was found, it seems to be not particularly relevant for natural crystal sizes and yield stresses. On the other hand, larger intrusions (e.g. one meter wide) can move quite quickly and travel through a mush extending throughout the entire crust in weeks/months.

The second application regards bubbles dynamics. We found that bubbles which nucleate within a crystal mush may or may not move through it depending on their buoyancy and the rheological properties of the mush. Therefore there are conditions under which bubbles can remain entrapped, and hence accumulate, within specific portions of the mush. And others where buoyant bubbles move efficiently and are able to fluidize an area of mush around them. These conditions can in turn become fundamental for the subsequent dynamic evolution of the entire mush, contributing or not to the remobilization of large parts of the mush. We concluded discussing the natural case at the Altiplano-Puna Magma Body (APMB). For this case we find that in order to allow the lifting of a 10-100 km-wide diapir with a density contrast with respect to surrounding rocks of 100-400 kg/m^3, the lower ductile crust needs a yield stress of $\sim$0.5 - 15 MPa to respect conditions of $Y_{inv} \geqslant Y_{inv_C}$. Moreover, from $Bi \leqslant 1$ and based on an uplift velocity of 1 cm/yr, we bounded the maximum effective viscosity (η_c) for a lower crust which would allow the emerge of a diapir at $\eta_c \sim 10^{21}$ Pa.s.

Chapter 7

Appendix

Appx. 1

The work presented in this thesis benefited from two collaborations and an internship. It has been also presented in a number of international conferences. We briefly summarize them below.

Internship at *Rockfield* (Swansea, UK)

The internship took place in February 2019 and lasted for one month. In this period I was introduced to their finite element and discrete element software *Elfen* by Dr. Fen Pan and Dr. Daniel Roberts. The main goal was to use their code to reproduce experiments involving fluids wit complex rheology. The simulations we carried out concerned both the onset of thermal convection (with the fluid being heated by a localized heating point) and the motion of a sphere through a yield stress fluid. In the first case we investigated the influence of the thermo-elastic stresses on the onset of convective motion in Carbopol. Thermo-elastic stresses are generated by the thermal expansion of the fluid which follows a change in temperature. By comparing the obtained stress fields with experiments of Davaille et al. (2013), we found that the stress around the heater reaches the fluid yield stress in a period of time that depends on the shear modulus (Fig. 7.1) and that matches the slow-motion stage recorded in the experiments before the plume onset (e.g. Fig. 4.2b).

In the second case, the interest was turned to the motion of a sphere through gels characterized by a complex rheology. We estimated the effective stress and strain fields, temperature field in the case of the variation of temperature was involved and the velocity field once the fluid starts to flow (Fig. 7.2).

Collaborations and conferences

Chapter 4 benefited from a sojourn at the Institute of Geophysics, ETH (Zurich, Switzerland). From June 23th to July 7th 2019 I have been able to start working with the code

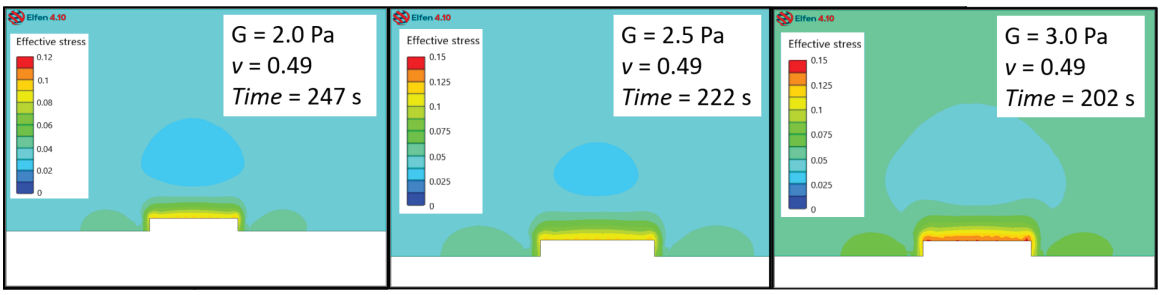

Figure 7.1: Zoomed snapshots of the effective stress field (Pa) resulting for three different simulations. Configuration and fluid properties are the same of Fig. 4.2. Here G indicates the shear modulus and v the Poisson's ratio. The yield stress (σ_y=0.1 Pa) is reached around the heater earlier for the largest shear modulus. And it is achieved when the corresponding experiment is in the slow creep stage (see Fig. 4.1 or Fig. 4.2).

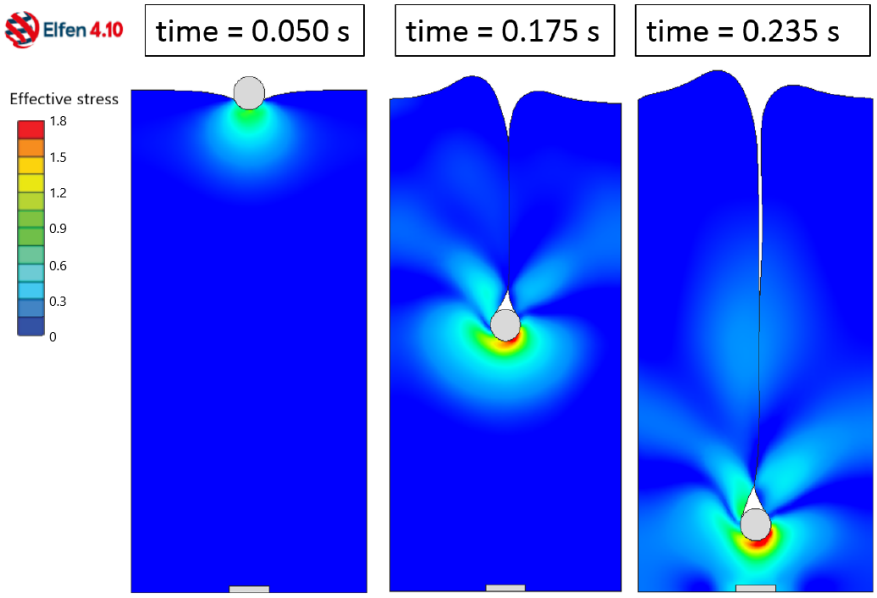

Figure 7.2: Effective stresses (Pa) during the fall of a sphere in a simple yield stress fluid.

StagYY thanks to the patient supervision of Paul Tackley. Here I had the chance to get used to the code and had the first simulations with the viscoplastic approximation running.

Chapter 3 and 5 benefited from discussions with Ichiro Kumagai and Kei Kurita during a sojourn (from November 16th to November 26th 2019) in Japan to attend the "Kitchen Earth Science" workshop at the Earthquake Research Institute (Tokyo).

The following is the list of conferences and related abstract titles where the results of the thesis have been presented.

- From viscous plumes to dikes and fractures: Influence of the thermo-elastic stresses on the onset of motion. Nethermod 2017, XIV International conference on numerical modeling in geodynamics, Utrecht, Netherlands, 27-31 August. (Poster presentation).

- Influence of the thermo-elastic stresses on the onset of convective motion in carbopol

initially at rest and heated from below. Viscoplastic Fluids Workshop: From Theory to Applications. Rotorua, New Zealand, 30-03 November 2017. (Oral presentation).

- Influence of the thermo-elastic stresses on the onset of convective motion in Carbopol. Journee de Dynamique des Fluides. 05/02/2018, Orsay, France. (Oral presentation) .

- Scale-dependent brittle-ductile rheology: Interaction between a falling sphere and the structure of a non-Newtonian yield-stress fluid. German-swiss geodynamics workshop 2018. Noer, Germany, 19-22 August (Poster presentation).

- Scale-dependent brittle-ductile rheology: Interaction between a falling sphere and the structure of a non-Newtonian yield-stress fluid. GeoMod2018. Barcelona, Spain, 01-04 October. (Poster presentation).

- Scale-dependent brittle-ductile rheology: insights from laboratory experiments. AGU Fall Meeting. Washington DC, USA, 10-14 December 2018. (Poster presentation).

- Scale-dependent magma rheology: insights from laboratory experiments. EGU General Assembly. Vienna, Austria, 7-12 April 2019. (Poster presentation).

- Scale-dependent rheology: insights from laboratory experiments. Ada Lovelace Workshop on numerical modeling of mantle and lithosphere dynamics. Siena, Italy, 25-30 August 2019. (Poster presentation).

- Interaction between a falling sphere and the structure of a non-Newtonian yield stress fluid. Viscoplastic Fluids Workshop: From Theory to Applications. Cambridge, UK, 15-19 September 2019. (Oral presentation).

- Probing the characteristics of mush-magma transition: insights from laboratory experiments. EGU General Assembly. Online, 4-8 May 2020.

Appx. 2

Appx1. Interaction between a falling sphere and the structure of a non-Newtonian yield-stress fluid

Nicolò R. Sgreva[a,*], Anne Davaille[a], Ichiro Kumagai[b], Kei Kurita[c]

[a] *Université Paris-Saclay, CNRS, FAST, 91405, Orsay, France.*
[b] *School of Science and Engineering, Meisei University, Hino, Tokyo 191-8506, Japan*
[c] *Earthquake Research Institute, University of Tokyo, Tokyo, Japan*

Abstract

We present an experimental study using mixtures of aqueous superabsorbent polymers (SAP) where we systematically investigate the influence of the size of grains that make up the fluid structure on the mixture effective rheology and its domain of validity. In water, SAP powder grains can swell up to 200 times and form gel grains whose sizes (d_g typically between 1 and 8 mm) can be controlled by choosing the size of the initial powder grains. The rheology of this mixture (water and touching grains) combines viscous, elastic and plastic aspects. Here, they are characterized using the free-fall of spheres of different densities and diameters (d_s). The latter were varied between 3 and 30 mm, therefore providing a range where they become comparable to the the fluid gel grains.

We observe five different regimes of motion: (1) A linear regime where the sphere has a rapid and straight fall and reaches a constant terminal velocity. (2) An irregular regime where the sphere's velocity varies around a constant value. (3) An intermittent regime where periods of no-motion and periods of irregular falls follow one another. (4) A slow fall regime where the sphere's speed progressively decreases in a logarithmic way. (5) A no-motion regime when spheres are not heavy enough to overcome the yield stress of the mixture, or are too small compared to the grain size.

The sphere falls in regimes (1), (2) and (3) are all following a same trend which, in the framework of an Hershel-Bulkley fluid, allows to estimate the effective yield stress σ_Y and consistency K_v of the SAP mixtures. Both σ_Y and K_v increase with increasing gel grain size. Regimes (2) and (3) are due to the interactions between the falling sphere and individual gel grains, i.e. the fluid structure. Moreover, the critical Yield number (Y_c, which compares σ_Y to the sphere buoyancy stress) above which there is no motion decreases as d_s/d_g becomes smaller than 2. So although the characteristic size of the fluid structure influences the magnitude of its rheological properties, the use of an Herschel-Bulkley rheology to describe spheres free fall breaks down only when the sphere diameter becomes very close to the SAP structure size.

Keywords: Yield stress, Falling sphere, SAP, Irregular motion, Intermittent motion

1. Introduction

Yield-stress fluids are a broad category of fluids which have been intensively studied in the last decades due to their key roles both in industry (e.g. drilling fluids, cement pastes, foams) and in natural phenomena (e.g. lava and mud flows, avalanches, landslides). A so-called yield-stress fluid does flow only when the applied stresses become larger than a threshold value, the yield stress (σ_Y). For example, for a suspension of particles in a liquid, the particles become in close contact as the particle volume fraction increases, and the material undergoes jamming. It can then support stresses without flowing. σ_Y represents the critical stress needed to unjam the structure. It introduces a non-linearity into the material rheology, which strongly impacts on the material dynamics [1, 2, 3, 4]. An example of these materials are soft particle glasses. Above the yield stress, their flow results from particles elastic deformations and plastic events during which particles rearrange [5]. Plastic local events can influence each other and lead to non-local elastic relaxation. This collective rearrangement can be the reason for spatial variation of viscosity in an homogeneous stress field in emulsions [6, 7]. Similar

*nicolo.sgreva@u-psud.fr

finite size effects can appear due to concentration gradients of particles in non-Brownian particle suspensions [8] or due to structural heterogeneities in polymers [9].

Several rheological models have been proposed to describe the rheology for stresses above the yield stress, such as the Bingham and the Herschel-Bulkley "HB" models. One issue is the domain of validity of these rheology models: how well do they describe the fluid behavior close to the yield stress? How do they depend on the microstructure typical lengthscale (e.g. the size of the particles d_g in suspension in the liquid)? How much larger than d_g must be the flow length scale for them to apply? For example, if we take the simple (and well known in Newtonian fluids) problem of a solid sphere settling in a fluid, when and how will the fluid microstructure interact with the sphere motion? There are two end-members depending on the size ratio between the fluid microstructure d_g and the falling sphere d_s. When $d_g/d_s >> 1$, the sphere will fall through a porous medium, moving along the liquid channels between particles, and when $d_g/d_s << 1$, the sphere will see a continuum with an effective rheology (e.g. "HB" model). But what happens for intermediate d_g/d_s?

The $d_g/d_s << 1$ case has been well studied for viscoplastic fluids, such as Carbopol [2]: the sphere reaches a steady-state downward motion only if a critical force is overcome, otherwise the fall is prevented [10, 11, 12]. However, the value of this critical force is still debated and it changes when the material elasticity is considered [13]. Once the sphere is set in motion, crucial aspects are the determination of the drag coefficient [10, 11, 14, 15] and the determination of the shape and position of the yield surface that separates the solid-like region from the fluid-like one [10, 13]. The yield surface and the drag force on the sphere have first been determined numerically and analytically for a Bingham fluid by Beris *et al.* [10] and subsequently for an HB fluid numerically [14, 16, 15] and experimentally [11] in Carbopol. In the liquid-like region, the flow in Carbopol is confined nearby the sphere, within an area which size depends on the yield stress of the fluid [17], and can be either symmetric [18] or asymmetric [17], depending on the sample preparation. Similar results had been found in viscoelastic aqueous polyacrylamide solutions [19], and in Laponite, a very thixotropic colloidal suspension [20], where the asymmetry of the flow pattern increases with the age of the fluid. This flow asymmetry is due to the appearance of a negative wake, i.e. upward fluid motion in the sphere's wake [21]. Another peculiar characteristic of a falling sphere in these fluids is that its velocity can depart from a constant value and show oscillations and irregularities. One of the first observations of an oscillatory particle settling has been in hydroxyl propyl guar (HPG) polymer gels [22], where the irregularities in the sphere descending motion were linked to the elasticity of the gels [23, 24]. Similar behavior was reported in entangled wormlike micellar fluids [25, 26], and in Laponite [27], where the vertical velocity can oscillate in bursts. In cornstarch suspensions [28, 29], the sphere velocity never approaches a steady terminal velocity but instead it oscillates, and decreases with time, to reach a series of stop-and-go cycles as the sphere becomes close to the experimental tank bottom. In wormlike micellar fluids, the oscillations originate from the formation and breakage of flow-induced structures [25, 26]; in cornstarch suspensions, in the formation and dissolution of a jammed layer that, under sufficient stress, increases drag and slows the sphere down [28, 29]; while the irregular motion in laponite is due to the existence of flow instabilities and shear banding [27].

In this paper, we investigate the free fall of spheres in aqueous suspensions of soft gel grains. We place ourselves in between the two end-members described above, using macroscopic super absorbent gels. Varying independently the size of the gels grains and the size of the falling spheres allows us to investigate the influence of the gel grain size on the effective rheology of the fluid and on the motion of spheres. The paper is organized as follow: in section 2 we describe the experimental set-up and the fluids used during the experiments. Section 3 presents the different regimes of motions that were observed. Results and their implications are discussed in section 4 and summarized in section 5.

2. Experimental set-up and fluids

2.1. The fluids

According to the product company (Omiya Green Service Co., Ltd), the fluid used is a polyacrylamide polymer made by copolymerization of acrylic acid and acrylamide. It is part of the family of aqueous dispersions of superabsorbent polymers (SAPs), with a large capacity of water absorption [30, 31]. They are used in many different water absorbing applications in agriculture [32], in health care industry (e.g. in sanitary pads and baby diapers), in sealants and in air-fresheners [33, 34].

The dry material is a white granular powder of particles with different irregular shapes. In water, the original small particles can swell up to 200 times and form gel grains whose size can be controlled by controlling the size of the initially dry grains.

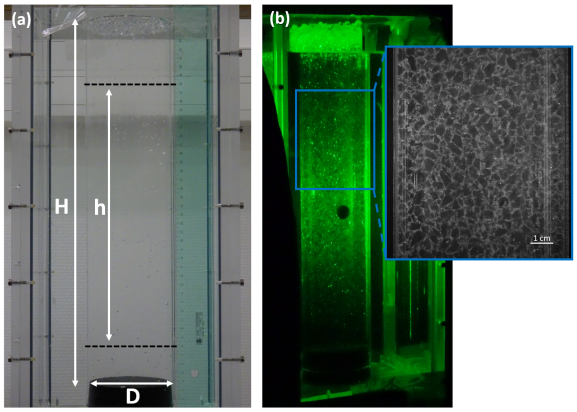

Figure 1: (a) Experimental set up. The cylindrical vessel containing the fluid is 50 cm high (H) and 10 cm wide (D). Videos are recorded in the tube section between the two black dotted lines (h). (b) Black and white image of the fluid structure illuminated by a laser sheet. The gel grains are in dark grey and the thin water film around them is in light grey.

name	Mean d_g (mm)	std (mm)	Median (mm)	Max d_g (mm)	Mean d_g^* (mm)
Gel A	1.4	0.3	1.4	2.3	1.4
Gel B	2.1	0.5	2.1	3.5	2.2
Gel C	3.3	0.9	3.0	5.8	3.4
Gel D	4.8	1.2	4.5	9.5	4.9
Gel E	5.7	1.2	5.5	9.6	5.8

Table 1: Characteristics of the five gels, obtained from image analysis: the mean grain diameter d_g, the standard deviation (std), the median and the maximum diameter for the 2-D distributions of circles; and the mean diameter d_g^* for the calculated 3-D grain size distributions.

Beside the general behaviour of such materials that combines viscoelastic [31] and shear-thinning aspects [35], the measurement of appropriate rheological properties in the swollen state is still quite complicated as typical commercial SAPs have large (up to few millimeters) and irregular swollen particles that render classical rheological methods difficult to use [31].

Starting from the provided raw material as the largest grains size end-member, we gradually ground the dry particles to form four thinner powders. All the final gel samples were then obtained by letting 17.5 ± 0.1 g of dry product react with 3.5 l of distilled water for one night. The resulting swollen mixture have been gently stirred (100 rpm) for 2-3 days with an electric stirrer in order to remove air bubbles and to homogenize the mixture. Careful weight measurements of a given volume of the final aqueous suspension before and after it was completely drained from the free water allowed to estimate a particle volume fraction of 62±2%.

As it was for the starting dry powders, the five final fluids under scrutiny differ from each other in the size of the grains that make up their structure. To obtain the grains size distribution of the swollen gel samples, we analyzed several high resolution images (4288 x 2848 pixels) of a laser-illuminated vertical cross-section of the experimental tank (Fig.1) by using Multispec, an image analysis software [36]. The sample was stirred between each image, so that each image shows a different organization of the fluid structure. Fig.1b shows an example of how the fluid structure looks like. The arrangement of the grains is easily recognizable and the sampling of each of them during the images analysis can be automatically or manually done directly from black and white images without needing more complex adjustments. Once the outline of the grains is defined from the image, the grain surface comes by counting the number of pixels of which it is composed. We describe each grain by the equivalent diameter, d_g, of a disk with the same area as the measured surface. Fig.2 presents the measured 2-D grains size distributions, $h(d)$, and their characteristics are given in Table 1. The distributions can be fitted by normal distributions (Fig.2f). To infer the real 3-D parent size distribution from the the 2-D measurements is a tricky problem, because it is underdetermined if the shape of the particles is unknown. Assuming that the gel grains are spheres, we estimate the numerical density histograms of these spheres diameters, $h(d^*)$, from $h(d)$, using the software StripStar [37] (Fig.2). To obtain the equivalent diameter of spheres, the measured $h(d)$ is compared to an ideal distribution $h_I(d)$ of disks obtained from an known distribution $h_I(d^*)$ of uniform distributed spheres of diameter d^*. The software derives the distribution of $h(d^*)$ by creating a proportionally higher or lower number of spheres in it, depending on the difference between the ideal distribution $h_I(d)$ and the measured distribution $h(d)$ (for details, see [37, 38]). Table 1 shows that the 3-D estimates are quite close to the 2D-measurements. In what follows, we take as the "gel grain size" the mean value of the 2-D measurements for each gel.

2.2. Setup

All the spheres are released in a 50 cm deep (H) and 10 cm wide (D) cylindrical Plexiglas vessel, previously filled with approximately 3.5 liters of fluid (Fig.1a). In order to reduce optical distortion on the images, the vessel was placed in a rectangular tank filled with water. Two illumination systems were used. Most of the experiments were carried out with a white light behind a

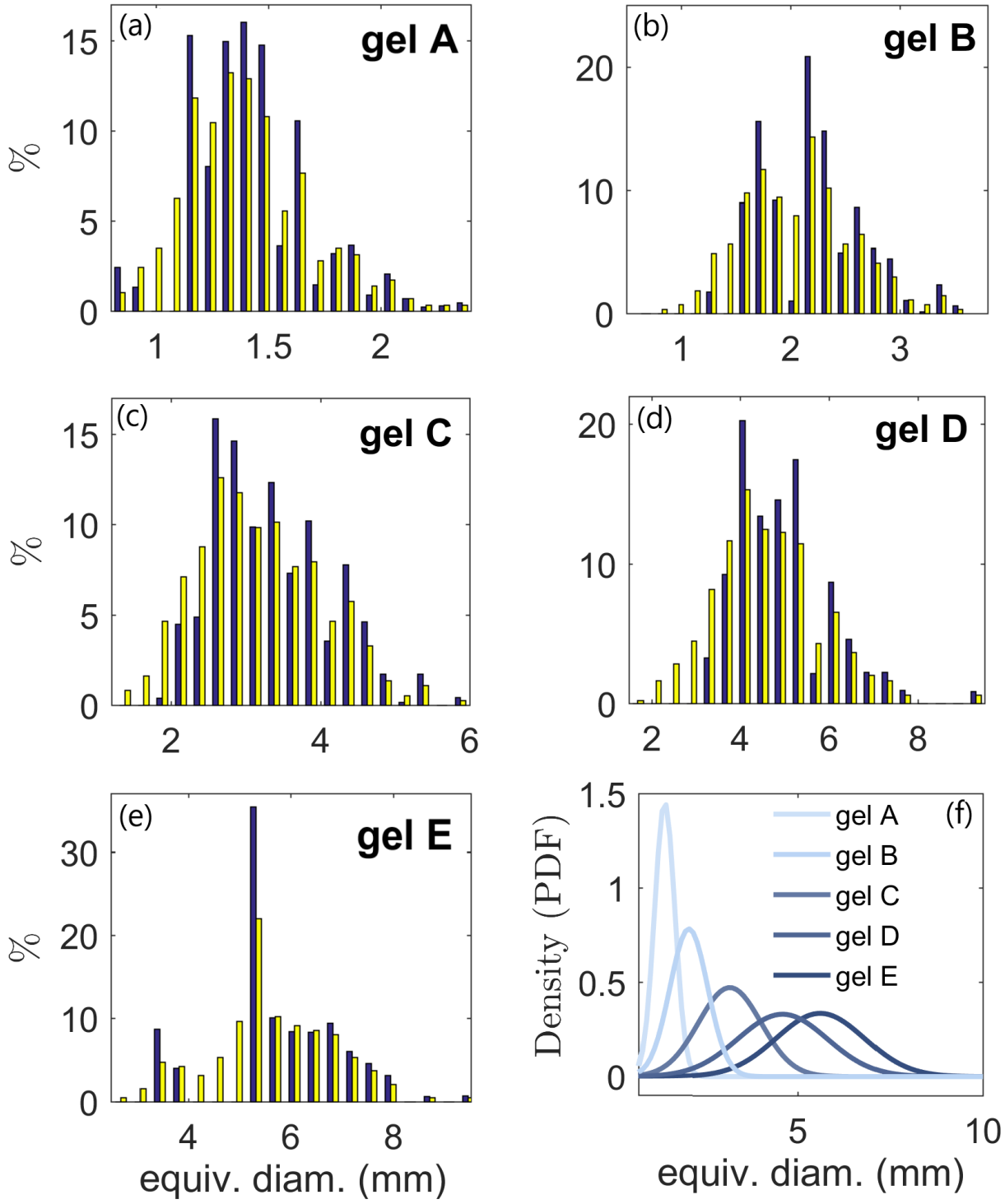

Figure 2: Histograms of measured 2-D grain size (yellow) and of calculated 3-D grain size (blue) for the five gels used in the experiments: gel A (a), gel B (b), gel C (c), gel D (d) and gel E (e). (f) Normal distribution fits for all gels.

diffusive screen placed on the back of the tank (Fig.1a). A subset of experiments were run when a vertical cross-section of the tank was illuminated by a 532 nm laser sheet, allowing to image the individual gel grains, as well as the descending sphere (Fig.1b). In this configuration, velocity fields were also recovered using the Davis software from LaVision. Images were recorded using a video camera (Canon Legria HF S21 1080p) with a frame rate of 25 frames/s. The position of the center of the sphere on each frame was determined by plotting the spatio-temporal evolution of a vertical pixel line centered on the sphere, or by using the blob analysis method in Matlab [39] (Fig.4 and 5a). Both methods allow the derivation of the local vertical velocity of the sphere through time. And the blob analysis also provides the measurements of the horizontal position and velocity of the sphere.

We run experiments with spheres of different materials and sizes. Their densities and diameters are summarized in Table 2. All the steel spheres (density of 7980 and 7970 kg/m^3) have been painted with black spray paint to avoid strong reflections, while the other spheres have been left with their original surfaces. The use of spray paint could increase the surface roughness, which in turn can affect the velocity field in the fluid around the object as well as the shape of the yielded region [40]. However, we did not observe any discrepancies when we compared the descent of a painted sphere and of a bare one of same density and diameter.

Before each experiment, we gently stirred the fluid to remove any preferential path that might have been formed during previous runs. SAP show some hysteresis whereby the fluid structure does not recover its original state after it has been deformed. This is observed when a second sphere is dropped from the same position as the previous one without stirring the fluid in between the two runs. For identical spheres, we have always measured higher velocities for spheres released second and falling through an already deformed path. Stirring the fluid between runs prevents this issue and allowed us to get reproducible velocities for identical spheres.

3. Experimental results

3.1. Calibration with a Newtonian fluid

We first tested the reproducibility and the accuracy of the experimental techniques, as well as the limitations arising from the dimensions of our setup. To do so, we measured the terminal velocities (v_y) of spheres settling in a Newtonian fluid at ambient temperature T_c=15.2±0.3 °C. The fluid is glucose syrup (Glucor 60/80) with density ρ_{fluid}=1394.66 kg/m^3 and viscosity η=12.3±0.7 Pa.s, at T_c. Spherical objects falling in a Newtonian fluid at low Reynolds number reach a terminal velocity given by the Stokes velocity

ρ_s (kg/m^3)	d_s (mm)
14952	6.00
7980	6.00; 12.00; 14.00; 16.00; 18.00
7970	3.00; 4.00; 5.00; 7.00; 8.00;
7970	10.00; 20.00; 22.00; 25.00
7799	6.00
7782	14.00
7621	8.00
7519	3.20
3227	6.00
2200	15.66; 15.81

Table 2: Spheres density ρ_s and diameter d_s.

$$v_{Stokes} = \frac{1}{18}\frac{d_s^2(\rho_s - \rho_{fluid})}{\eta}g, \qquad (1)$$

where g the acceleration due to gravity.

In Fig.3, we plot the velocities measured for spheres with diameters ranging between 3 and 18 mm, together with the Stokes relationship. The larger spheres depart from the Stokes velocity because of wall effects. But in this case, their terminal velocity can be written as $v_y = v_{Stokes} K_1^{-1}$ with:

$$K_1^{-1} = 1 + \alpha_1\left(\frac{d_s}{D}\right) + \alpha_2\left(\frac{d_s}{D}\right)^3 + \alpha_3\left(\frac{d_s}{D}\right)^5, \qquad (2)$$

where $\alpha_1 = -2.104443$, $\alpha_2 = 2.08877$, $\alpha_3 = -0.94813$ and D is the tube diameter [41]. These corrected Stokes velocities predict well the measured velocities (Fig.3), showing that our measurements set up is adequate.

3.2. Five different regimes of motion in SAPs

About 100 falling sphere experiments were run, with d_s/d_g ranging from 0.8 to 13. Fig.4 presents a selection of falling profiles in gel C (grains mean diameter d_g=3.3 mm) for four falling spheres with same density but different diameters. The same type of plot is also showed in Fig.5a where this time we track spheres having same size but different densities settling in gel D (d_g=4.8 mm). In both figures, the starting position along y-axis, h=0, does not refer to the top fluid surface but to the upper limit of the camera view at which movies were recorded (Fig.1a). All movies have been taken for

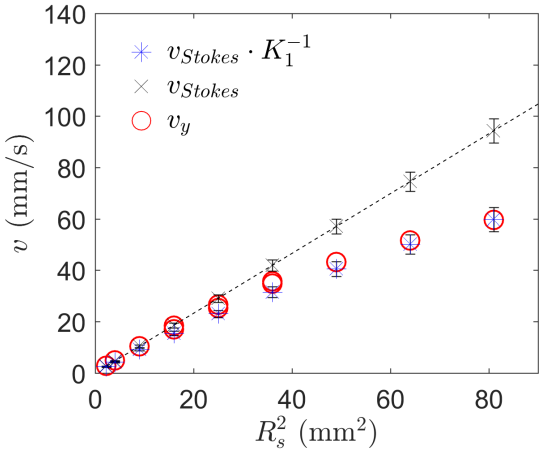

Figure 3: Measured terminal velocities, v_y, in syrup (circles) and Stokes velocities, v_{Stokes}, (crosses and dashed line) as a function of spheres squared radius, $R_s^2 = d_s^2/4$. Uncertainties for Stokes velocities come from the uncertainties in determining the syrup viscosity whereas the error for v_y is 0.25 mm/s, smaller than the symbols. Star symbols are the predicted velocities considering the wall correction, eq. (2).

a magnified portion of tube h=300 mm, starting from 70 mm under the surface. Camera position and therefore size of the view are kept constant for each run done in the same fluid.

For each gel, depending on the diameter and density of the sphere, we distinguish the following five regimes (Fig.4 and Fig.5):

(1) A linear regime: rapid and linear fall in which spheres reach a constant terminal velocity;

(2) an irregular regime superimposed to a linear one where spheres never stop during their way down (v_y >0) but their local velocity fluctuates around a constant value;

(3) an intermittent regime: another irregular regime but here periods of no-motion, where the sphere's vertical velocity goes to zero, and periods of irregular falls follow one another;

(4) a logarithmic regime where the sphere's speed progressively decreases (inset in Fig.4) and never reaches steady state; and

(5) a no-motion regime in which spheres do not move at all from their initial positions.

Regimes (1) and (5) have already been reported in yield stress fluids [11, 27, 42] and one can interpret them based on the state of the medium that surrounds the object. In the linear regime (1) the fluid around the sphere has a liquid-like behaviour that allows spheres to go down. In regime (5) local stresses are below the yield stress (σ_Y) and the material around the sphere re-

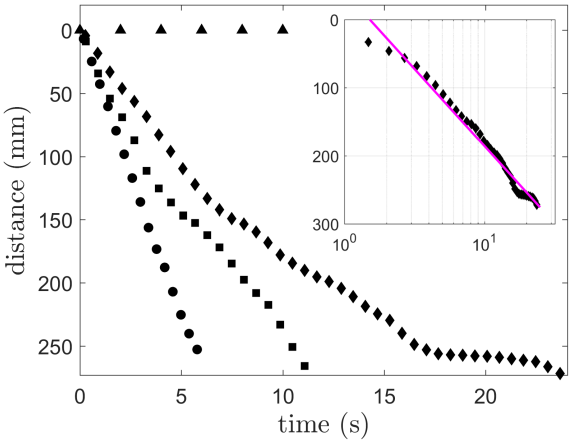

Figure 4: Depth of spheres settling through gel C as a function of time. The spheres have a density ρ_s=7980±10 kg/m^3. Varying sphere's diameter, one can recognize the following motion regimes: linear regime (circles •, d_s=10 mm), irregular motion superimposed to a linear trend (squares ■, d_s=8 mm), logarithmic regime (diamonds ♦, d_s=7 mm) and no-motion (upward-pointing triangles ▲, d_s=4 mm), i.e. regimes (1), (2), (4) and (5) described in the text, respectively. The insert shows the distance as a function of time for regime (4) with a semi-log scale. The color line is the fit $y(x)$=a log($b\,x$), where a=98.34 and b=0.66. The correlation coefficient is R=0.980.

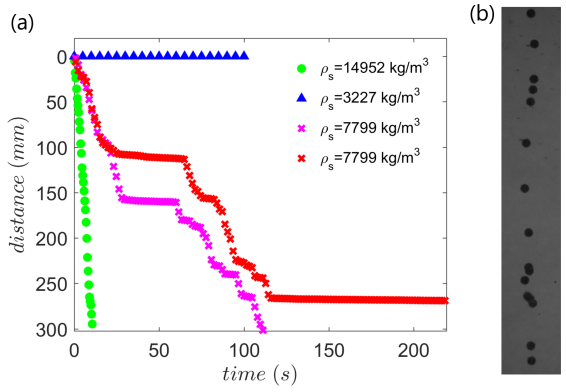

Figure 5: (a) Depth of spheres settling through gel D as a function of time. Here spheres have a constant diameter d_s=6 mm, but different densities. As in Fig.4, we report the case of linear regime (circles), no-motion (upward-pointing triangles) and, in addition, the intermittent regime (crosses). (b) Sequence of snapshots every 100 frames showing the irregular motion in gel D for a sphere with d_s=7 mm and ρ_s=7970 kg/m^3.

mains in the solid state, so that the object cannot move. Here the stress field is generated by the weight of the sphere and the no-motion regime is always observed for the smallest diameters d_s (Fig.4) or density contrasts $\Delta\rho$ (Fig.5a, as in [11]). We observed no-motion whether the sphere was placed on the surface of the fluid column, or gently pushed within it and released deeper in the fluid. In both cases, the spheres were left in that position for days (up to a week for one run) and they never moved away from their starting positions.

Although the distinction between the two end-member cases (1) and (5) is easy to establish, to discern quantitatively between the first steady-state motion regime (1) and the more irregular ones is more delicate. We summarize how we define the different motion regimes in Table 3. From the falling profiles one can notice that, although sometimes it is still possible to identify an almost constant falling speed superimposed on fluctuations (circle symbols both in Fig.4 and Fig.5a), in some other cases, spheres seem to slow down logarithmically during their way to the bottom (square symbols in Fig.4), making impossible the determination of a constant terminal velocity. We report this aspect in Fig.6a by plotting the mean squared variations (MSE) obtained by fitting the falling profiles with a linear or a semilog fit as function of spheres buoyancy. The logarithmic regime (4) is defined for $\mathrm{MSE}_{linear} > \mathrm{MSE}_{log}$, that is when falls are better represented by a logarithmic fit. Hence, this regime describes a continuous decrease in sphere's speed which never reaches a steady-state. In the case of Carbopol, velocity decreases following a power law [11], but in most of our cases, it best fits a logarithmic curve. Although the logarithmic behaviour appears more often at lower buoyancies (Fig.6a), we observed sometimes for a same buoyancy the coexistence of the logarithmic regime with the other ones (1) to (3). This suggests that this velocity decrease could be due to heterogeneities in the gel grains packing, like a denser packing closer to the tank bottom.

Once the separation between the stoppage cases (logarithmic regime (4) and no-motion (5)) and the other cases is established, one can identify the differences between the steady-state motion (regime (1)) and the more irregular and chaotic regimes (2) and (3). Depending on the buoyancy of the object and hence on its velocity, the irregularities show up as fluctuations in the sphere local vertical velocity and in a progressive increase of its horizontal motion (Fig.5b). Regimes (2) and (3) show some similarities: in both of them, spheres have a long term constant falling velocity on which is superimposed a more complex and irregular pattern of fluctuations. The latter are characterized by accelerations and subsequent decelerations in a short period of time and, in some cases, they can result in a succession of stops of the sphere.

	Regimes				
	(1)	(2)	(3)	(4)	(5)
$\overline{v}_y = 0 \pm err(v_y)$					x
$\mathrm{MSE}_{lin} > \mathrm{MSE}_{log}$				x	
$\mathrm{MSE}_{lin} < \mathrm{MSE}_{log}$ & $std(v_y)/\overline{v}_y < 0.15$	x				
$\mathrm{MSE}_{lin} < \mathrm{MSE}_{log}$ & $std(v_y)/\overline{v}_y \geqslant 0.15$		x	x		
$\mathrm{MSE}_{lin} < \mathrm{MSE}_{log}$ & $t_s/t_0 \geq 5\%$			x		

Table 3: Summary of the observed motion regimes and the way they are classified

To determine the boundaries between the irregular regimes (2) and (3) and regime (1), one can look, as a first approximation, at the ratio between the standard deviation (*std*) of the local falling velocity and its mean value. Variations of the local velocity for spheres in irregular regimes are much larger than the experimental uncertainty (Fig.6c-d). The latter is due to the precision of the technique we used to detect the sphere position in time (hereafter $err(v_y)$). It is estimated to be 0.25 mm/s from the syrup-case measurements and from local velocity measurements in the no motion regime. In the Newtonian case, $std(v_y)/\overline{v}_y$ always remains smaller than 0.15. We define the linear regime (1) using this threshold value, so that the velocity measurements obey $std(v_y)/\overline{v}_y < 0.15$ (dashed line in Fig.6c-d). This limit represents therefore a boundary between the steady-state motion and the regimes showing a broader distribution of velocities.

Once the linear regime is bounded in this way, we distinguish between the irregular regime (2) and the intermittent regime (3) as follows. In the intermittent case the sphere remains during a certain cumulative amount of time, t_s, at $v_y \leqslant err(v_y)$. We then compare t_s to the total time, t_0, the sphere takes to descend 30 cm. The intermittent regime is defined as $t_s/t_0 \geq 5\%$. The remaining irregular regime (2) is therefore defined as $t_s/t_0 < 5\%$ and $std(v_y)/\overline{v}_y > 0.15$ (Fig.6e-f).

The irregular motions we have observed are not only present and visible in the vertical direction but it also affects the horizontal motion. Along this direction, they collect a certain amount of traveled distance (L_x) with respect to their initial position, depending on their diameter (Fig.7a), on the gel grains size (Fig.7b), and on the vertical falling distance h (Fig. 8a). Fig. 8b shows

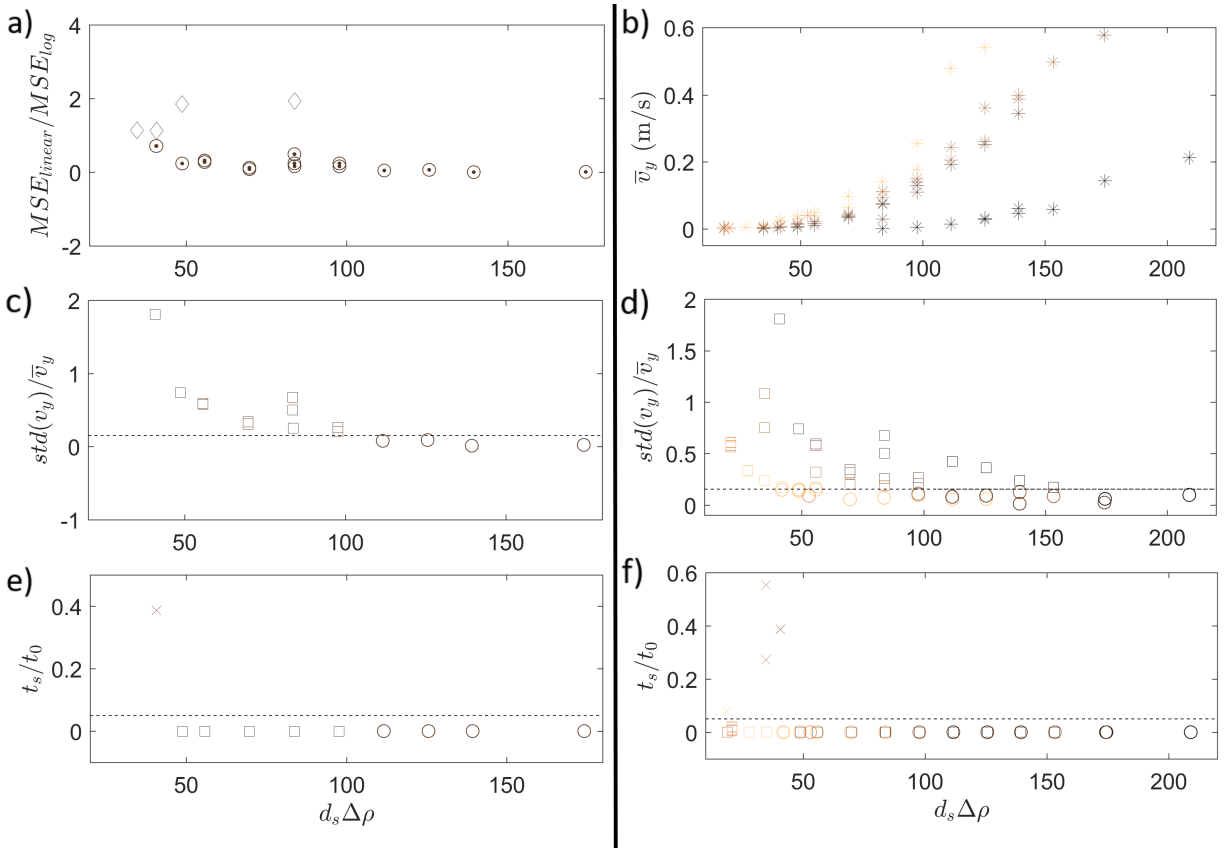

Figure 6: Determination of the different regimes of motion. In (a), (c) and (e) data refer to experiments carried out in gel E. In (b), (d) and (f) data are for all fluids and colours indicate the grain size as in Fig.2. (a) best fit (MSE_{linear}/MSE_{log}) of the falling profiles. ⊙ indicates a better linear fit whereas ♢ a better semilog fit (logarithmic regime (4), in the text). (b) mean falling velocities ($\overline{v}_y$) for those falling profiles that have been linearly fitted. The error for v_y is 0.25 mm/s, smaller than the symbols. We do not report the standard deviation for v_y here (whereas it is in (c) and (d)) as being also linked to the physical fluctuation of the sphere, for small values of velocity it would make the plot unreadable. In (c) and (d) we separate those experiments that show a more irregular and chaotic motion (□) from those that do not show any irregularities during the fall (○) by plotting $std(v_y)/\overline{v}_y$. The dashed line is for $std(v_y)/\overline{v}_y = 0.15$, from the Newtonian case. In (e) and (f) we separate the intermittent regime (3) (×) from the other irregular regime (2) (□) based on the amount of time t_s the sphere remains at $v_y \leqslant err(v_y)$. t_0 is the total time the sphere takes to descend h. The dashed line indicates t_s/t_0=5.

that for each run, L_x is roughly proportional to h. Fig.7 shows that small spheres change frequently their horizontal position, oscillating continuously around the vertical axis, and traveling for larger distances L_x than the large spheres. If we normalize L_x by h and d_s by the diameter of the gel grains (d_g), we can collapse all the data on the following master curve:

$$L_x/h = C_{exp}\left(d_s/d_g\right)^{-2}. \tag{3}$$

where $C_{exp} = 0.49 \pm 0.26$. So the total travelled distance in the horizontal direction proves to be a good witness of the strong interaction between the sphere and the gel grains that make up the fluid structure when those two have similar sizes ($1 < d_s/d_g < 10$).

4. Discussion

4.1. Determination of SAP effective rheology

The rheology of yield stress fluids is often modeled using the Herschel-Bulkley model [2, 12, 43]:

$$\begin{cases} \sigma = \sigma_Y + K_v\dot{\gamma}^n & \text{if} \quad \sigma > \sigma_Y \\ \dot{\gamma} = 0 & \text{if} \quad \sigma \leq \sigma_Y \end{cases} \tag{4}$$

where σ is the stress, σ_Y the yield stress, $\dot{\gamma}$ the shear rate, K_v the consistency and n the shear-thinning index. For small Reynolds numbers (Re$\ll$1), the flow resulting from a settling particle in a fluid following such a rheology depends on two key-parameters [11, 44]. The Bingham number compares the yield stress to the viscous stresses:

$$Bi = \frac{\sigma_Y}{K_v(v_y/d_s)^n}, \tag{5}$$

and the Yield number compares the yield stress to the buoyancy stress due to the sphere:

$$Y = \frac{3\sigma_Y}{gd_s\Delta\rho}. \tag{6}$$

As recalled in section 1, most of the experimental work to study this problem has been so far carried out in Carbopol. The main difference between experiments done in Carbopol and the present work regards the typical size of the fluid structure compared to the dimension of the object that is moving through it. Carbopol corresponds to the case where the fluid structure (with grains of tens of microns) is much smaller than the spheres ($d_s >> d_g$). In this case, only regimes (1), (4) and (5) were reported (e.g. [11]) while neither the irregular regime (2) nor the intermittent regime (3) were observed. Moreover, the fall of the sphere is always reported to be free of any sort of chaotic motion [11, 17, 40].

In regime (1), that is when a constant terminal velocity can be determined, Tabuteau *et al.* [11] showed that their data were well described by the following equation:

$$\frac{1}{Y} = 7 + \frac{8.52}{Bi} \tag{7}$$

with n=0.5. In addition, there is a critical value of Y, Y_c=0.145, above which there is no motion.

Equation (7) has been shown to apply for $d_s \gg d_g$ [11]. We are now going to check whether it also applies for a fluid with a much larger structure. We can rewrite eq.(7) as

$$\frac{gd_s\Delta\rho}{3} = 7\sigma_{Y(eff)} + 8.52K_{v(eff)}\left(\frac{v_y}{d_s}\right)^n, \tag{8}$$

where $\sigma_{Y(eff)}$ and $K_{v(eff)}$ represent the effective yield stress and consistency of the SAP through which the sphere is falling. v_y is the average falling velocity defined for those experiments which do not show a decrease in speed, i.e. those in regime (1), (2) and (3). By plotting the buoyancy stress ($gd_s\Delta\rho/3$) as a function of the effective strain rate, i.e. $(v_y/d_s)^n$, we show on Fig. 9 that SAP obeys the same linear relationship found for Carbopol [11]. Interestingly, experiments in both regime (1), (2) and (3) can be linear-fitted by the same line.

We then use our falling sphere set up as a rheometer. For each SAP mixture, we can found the coefficients of the linear fit shown in Fig.9. Using eq.(8), the slope will give us the effective consistency ($K_{v(eff)} = slope/8.52$) and the intercept at zero effective strain rate, the effective yield stress ($\sigma_{Y(eff)} = intercep/7$). Fits in Fig.9 depend on the shear thinning exponent n used to calculate the effective shear rate. Minimum mean squared values for the linear fit are found for n ranging between 0.5 and 0.7 (Fig.10). Unless otherwise indicated, in what follows we will use n=0.5 since it is with this value that eq. (7) was tested in Carbopol [11]. Fig.11 further shows that the effective yield stress and consistency increase with increasing gel grain size.

For experiments involving large spheres, it is opportune to check whether wall corrections are needed or not [45]. For sufficiently small sphere-to-tube diameter ratio, d_s/D, we do not expect any reduction of the sphere's terminal velocity, and the measured velocity, v_y, is equal to the ideal terminal velocity of a sphere falling in an unbounded medium, v_∞. On the other hand, if d_s/D exceeds a critical value, $(d_s/D)_{crit}$, the velocity decreases,

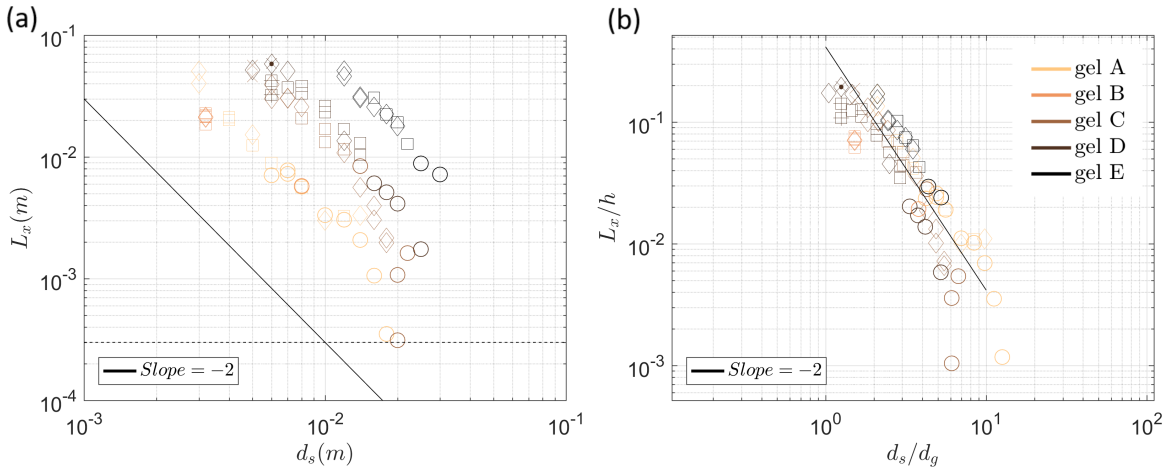

Figure 7: Total distance traveled in the horizontal direction (L_x). (a) L_x as function of the sphere diameter d_s for the different gels. The dashed line indicates the uncertainty in position. (b) Same plot with y-axis normalized by the vertical falling distance h and x-axis by the gel grain size d_g. Colours indicate the different fluids as indicated in the legend. Symbols refer to the different motion regimes: ○ for the linear regime (1); □ for an irregular regime superimposed to a linear one (2); × for the intermittent regime (3) and ◊ for the logarithmic regime (4). Empty symbols are for steel spheres while the symbol filled with a point refers to ρ_s=7799 kg/m^3 and those filled with a plus sign are for ρ_s=14952 kg/m^3.

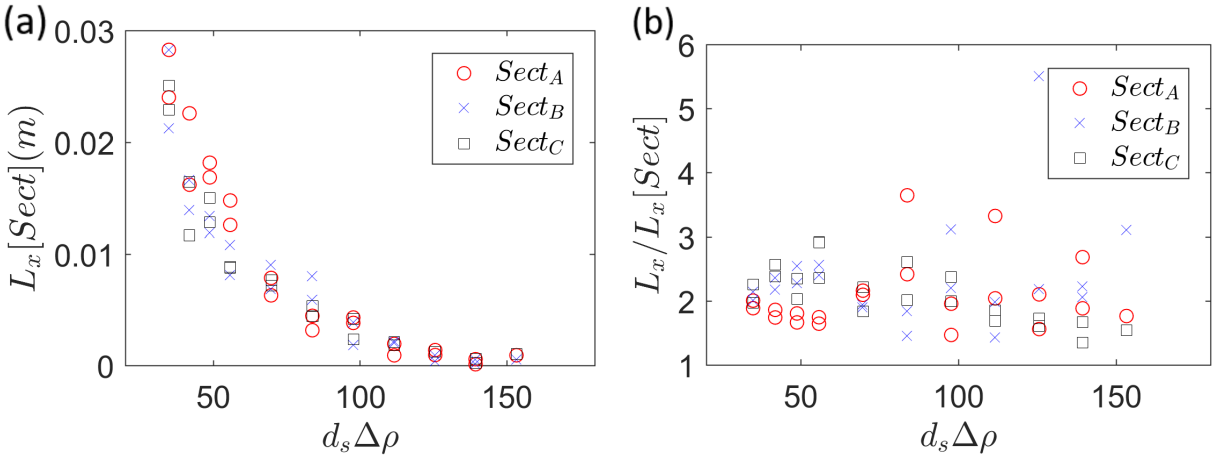

Figure 8: Distance traveled in the horizontal direction in gel C. (a) Distance traveled in different 15-cm-vertical-sections of h, $L_x[Sect]$, as function of spheres buoyancy. Sections are $Sect_A$=[h=0 cm, h=15 cm]; $Sect_B$=[h=15 cm, h=30 cm]; $Sect_C$=[h=7.5 cm, h=22.5 cm]. (b) Ratio between the total distance traveled in 30 cm, L_x, and the distance travelled in 15 cm, $L_x[Sect]$.

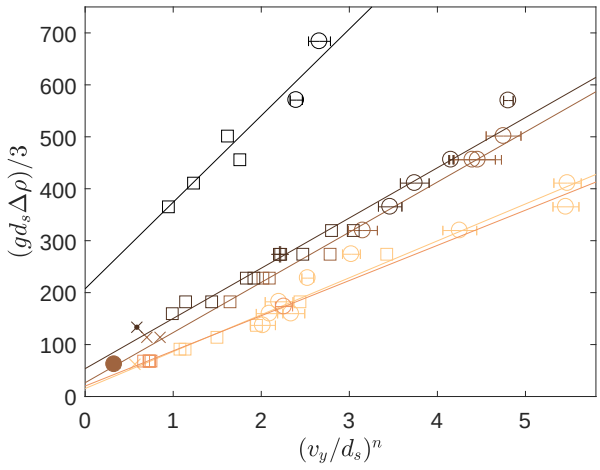

Figure 9: Sphere buoyancy as a function of effective shear rate, $(v_y/d_s)^n$. Following Tabuteau *et al.* [11] approach, v_y is the average falling velocity experiments in regimes (1), (2) and (3), and n=0.5 is the power-law index. Colours represent the fluids (same as Fig.7) while symbols represent the regimes (circles for regime (1), squares for regime (2) and crosses for regime (3)). Empty symbols for steel sphere; symbol with a point inside for ρ_s=7799 kg/m^3; with a plus sign for ρ_s=14952 kg/m^3 and filled symbols for ρ_s=2200 kg/m^3. Solid lines are the linear data fits.

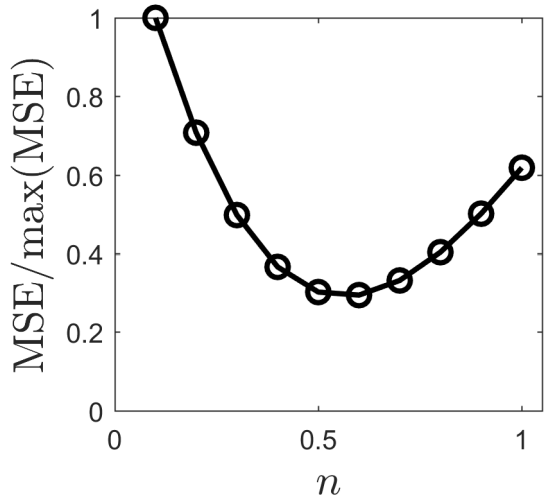

Figure 10: Power law index (n) that best linearly fits data in Fig.9 for all gel samples. y-axis represents the mean squared errors (MSE) of the linear fit normalized by the maximum MSE found. The best range of n is in between 0.50 and 0.70.

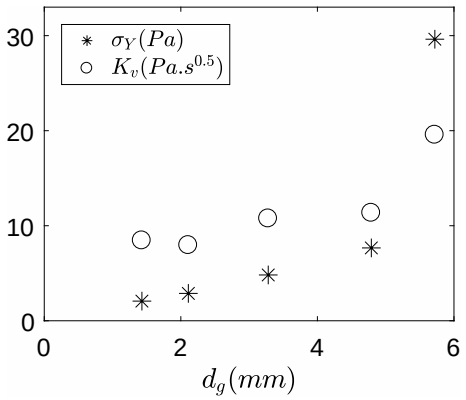

Figure 11: Effective yield stress (σ_Y) and effective consistency (K_v) as function of gel grains size.

leading to v_y/v_∞ <1. The critical diameter ratio for a yield stress fluid is given by [45]:

$$(d_s/D)_{crit} = 0.055 + 1.114\,Y \qquad \text{if} \quad Y \leqslant Y_c. \tag{9}$$

In our case, d_s/D is smaller than $(d_s/D)_{crit}$ as long as d_s/D <0.1. The influence of walls causes a reduction in speed such that [45]:

$$\frac{v_y}{v_\infty} = 1-1.7\,[(d_s/D) - (d_s/D)_{crit}] \qquad \text{if} \quad d_s/D > (d_s/D)_{crit}. \tag{10}$$

So, for 0.1$\leqslant$ d_s/D $\leqslant$0.17, wall effects lead to 0.8< v_y/v_∞ <1, i.e a maximum decrease of v_y/v_∞ of less than 20%. Considering only the experiments with v_y/v_∞ > 0.8, we recalculate the effective rheology in the same way as described above (Fig.12a). The new values of $\sigma_{Y(eff)}$ and $K_{v(eff)}$ vary at most by 20% from the previous ones (Fig.12b).

Once we got the yield stress and the consistency of each SAP gel, we plot Y^{-1} as function of Bi^{-1} in Fig.13. For values of Bi^{-1} >0, we achieve a good collapse along eq.(7) for all experimental data that belong to regimes (1), (2) and (3). It is remarkable that a same HB rheology allows to describe the flow from $d_s \gg d_g$ all the way down to when the sphere size becomes very close to the microstructure typical length scale $d_s \sim d_g$.

4.2. Arrest conditions

From the experimental work of Tabuteau *et al.* [11], the critical value of the Yield number (Y_c) above which spheres do not move in a simple yield stress fluid is 0.145. This value is very close to 0.143, predicted in previous works [10, 14]. On the other hand, Fraggedakis *et al.* [13] more recently pointed out that the critical value may increase if elastic effects are taken

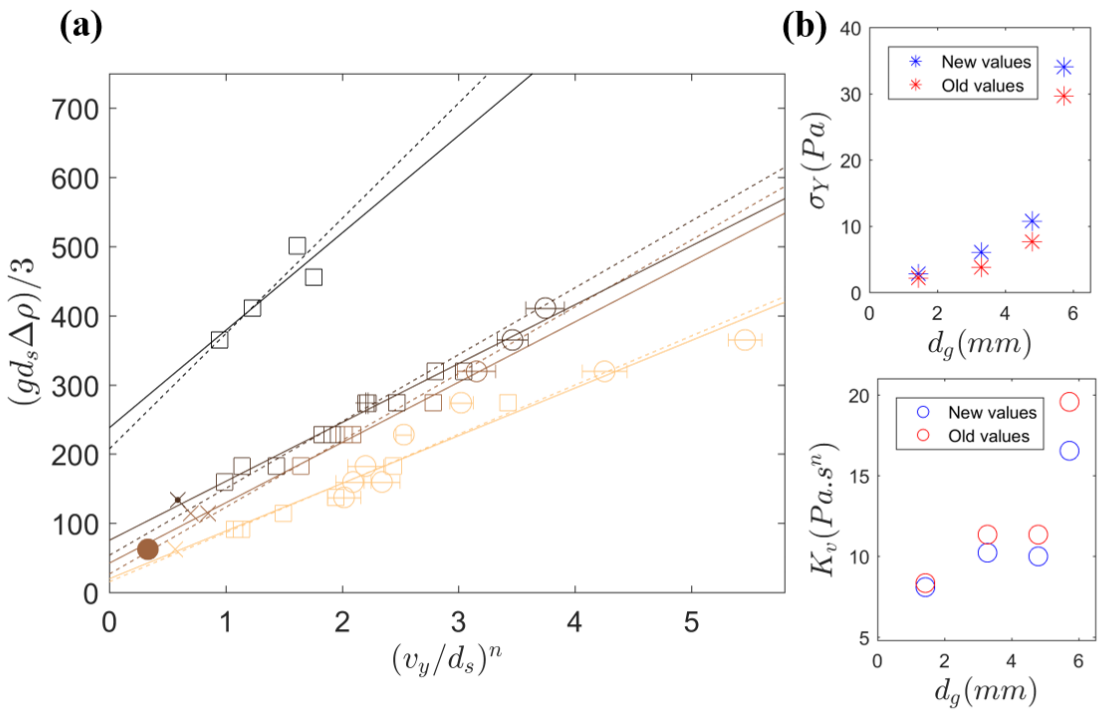

Figure 12: Influence of the velocity reduction due to wall effects on the effective rheology. n=0.5. (a) The new fit that considers only experiments with $v_y/v_\infty > 0.8$ (solid lines) is compared with the previous fit from Fig.9 (dashed lines). Colours and symbols here are those described in Fig.9. (b) Effective yield stress and consistency as function of gel grains size from the new fit (blue symbols). Red symbols are those in Fig.11.

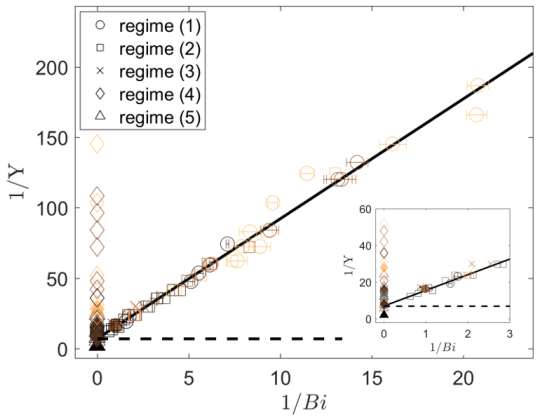

Figure 13: $1/Y$ as a function of $1/Bi$. Colours are for the different fluids. The dashed line indicates Y_c^{-1}=0.145^{-1} [11]. Symbols are filled in a different way to distinguish between spheres of different materials: full-filled symbols are for light spheres (ρ_s =2200 kg/m^3), open-symbols for ρ_s =7970 kg/m^3, point-filled for ρ_s =7799 kg/m^3, asterisk-filled for ρ_s =3227 kg/m^3 and plus-filled for ρ_s =14952 kg/m^3. We show the good collapse of our data along eq.(7) (solid black line). The inset shows the data zoomed around the critical conditions in order to better display the entrapment conditions.

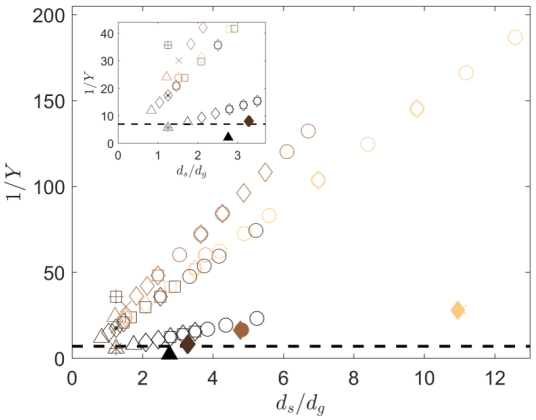

Figure 14: Range of validity of the effective rheology. Colours are for the different fluids. Symbols are those used in Fig.13. The dashed line indicates Y_c^{-1}=0.145^{-1} [11]. For d_s/d_g approaching the value of 2, we have no motions (triangles), even for Yield numbers lower than the critical one commonly used.

into account. In all these studies, the size of the moving object is much larger than the size of the particles than make up the fluid structure. In SAP, Fig.13 shows that sphere arrest (corresponding to Bi^{-1}=0) can also occur for $Y < Y_c$ when the diameter of the sphere becomes comparable to the diameter of the gel particles. For example, in gel C (d_g =3.3 mm), we observed arrest for values as low as $Y = 0.042 \approx Y_c/3$ (d_s =4 mm, steel sphere). This cannot be explained by the elasticity of the SAP mixture, which would give the opposite trend [13]. We attribute this anomalous arrest in SAP to the interaction between the sphere and the gel structure: when d_s becomes close to d_g, the spheres "see" the individual gel grains as obstacles on their way and the effective HB rheology breaks down.

4.3. Grains elasticity and rearrangements

Given the high volume grain fraction of our SAP solution, the emergence of a yield stress can be related to the jamming of soft grains. SAP gel grains act as athermal elastic particles that interact by compressing each other and by gliding along one another. In this case flow occurs through a sequence of elastic (reversible) deformations and local plastic (irreversible) rearrangement events which induce a long ranged relaxation of stress [6, 46, 47]. Seth and collaborators [5, 48] showed that the collective behaviour of a fluid made up by elastic grains can show elasto-viscoplastic responses and is well described by an Hershel-Bulkley rheology [5, 48]. Their micro-mechanical model based on the interactions of elastic spheres displays a shear thinning exponent of 1/2, as they observed in experiments with concentrated emulsions or polyelectrolyte micro gel pastes [5]. Such a 1/2 exponent would also fit well our SAP experiments (section 4.1). Moreover, the individual gel grain elastic deformations during flow were shown to strongly influence the mixture yield stress and consistency [5]. In SAPs, we observe that both yield stress and consistency increase when the SAP mean grain size increases. An increasing grain size at constant particle volume fraction would increase the grains overlap, and therefore the elastic repulsive force between the grains [5]: hence, this would indeed increase the yield stress and consistency. But this increase could also be due to an increasing elastic modulus of the individual grains [48], so we tried to measure the mechanical properties of individual grains. However, the extreme softness of the SAP grains made it very difficult. After several attempts to measure forces and penetration depth by using a microindenter with a minimum normal force of 20 mN, we have not been able to get any reliable measurements since slip or rupture of the grain always occurred even for such small values of normal force. More work in clearly needed to relate quantitatively the rheological properties of SAP to its internal structure.

Anyway, there is no doubt that elasticity is an important component of SAP mechanical behaviour. And as there are no polymer chains between SAP grains that could form system-spanning networks as time goes on,

there is no aging of the fluid during an experiment. However, we observed fore-aft symmetry breaking in the velocity field around the sphere and the formation of a negative wake (Fig.15), at least in the linear regime (1). This was also observed in Carbopol [e.g. 17, 40], and associated either with fluid elasticity [13, 17], or with the emergence of thixotropy and aging [18]. In SAP, visco-elasticity seems the most probable reason for the occurrence of the negative wake.

The long term motion of a sphere in SAP necessitates grains rearrangements. These are all the more common the higher the local shear stresses are (e.g. in the case of a larger sphere). And since the number of plastic events per unit of time controls fluid flow and relaxation [6], a sufficiently high number of them leads the system to be more fluid, resulting in sphere motion being in the linear regime (1). Decreasing the sphere size at constant density, results in decreasing its buoyancy, therefore also the stresses it exerts on the SAP, and eventually the number of rearrangements per unit of time. So the sphere will began to "see" individual rearrangements and its velocity will fluctuate accordingly, leading to regimes (2) and (3). However, as already reported in section 4.1, the sphere average velocity in these regimes still follows the same trend as in regime (1), which suggests that the rearrangements statistics over the sphere fall duration in regimes (2) and (3) may have the same overall properties as the rearrangements statistics at any given time in regime (1). In addition, when the sphere diameter becomes less than twice the SAP grain size, the sphere does not see anymore the "collective" properties of the SAP fluid, but rather the properties of each individual grain. This would explain the complete arrest of the spheres even though their Yield number is much lower than the critical value (section 4.2).

5. Conclusion

In this work, we have experimentally investigated the influence of the size of particles which build up the structure of a SAP fluid on the dynamics of a spherical intruder falling under gravity through it. As the sphere to structure sizes ratio d_s/d_g was varied between 0.8 and 13, we were able to explore the range where fluid structure and intruder sizes become comparable.

Besides the classical steady-state motion and the stoppage regimes already reported in viscoplastic fluids for $d_s/d_g >> 1$, the interaction between moving objects and the fluid structure results in two additional regimes where the motion becomes more chaotic. This strong interaction between the sphere and the gel grains has a

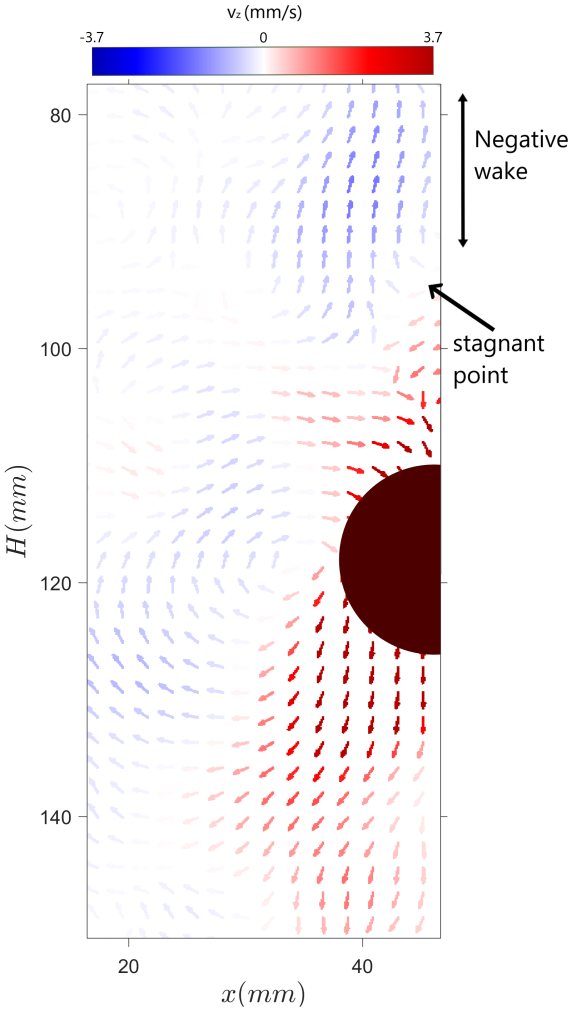

Figure 15: Fluid flow from PIV measurements. We display the vertical component of the right half part of instant velocity field (v_z) for a sphere (d_s=19 mm) falling in the linear regime (1) through SAP.

clear signature on the sphere total travelled distance in the horizontal direction.

Moreover, we have shown that the effective rheology of SAP follows the Herschel-Bulkley model with a power index n=0.50, making this simple set-up a good rheometer for this type of fluids. Both the yield stress and consistency are found to increase with the gel grain size. However, it is remarkable that the overall sphere motion predicted with an Herschel-Bulkley rheology begins to break down when it "sees" the texture only for sphere diameters less than twice the SAP grain size. More work is now underway to study SAP elasticity and the break up of the fore-aft symmetry of the flow around the sphere.

Acknowledgments

N.R. Sgreva was supported by the Initial Training Network No 642029-ITN CREEP, an Horizon 2020 - Marie Sklodowska-Curie Action. This research was also supported by LabEx PALM (ANR-10-LABX-0039-PALM). The manuscript was improved thanks to the in-depth comments of two anonymous reviewers.

References

[1] H. A. Makse, J. Brujic, S. F. Edwards, Statistical mechanics of jammed matter, arXiv preprint cond-mat/0503081 (2005).

[2] D. Bonn, M. M. Denn, L. Berthier, T. Divoux, S. Manneville, Yield stress materials in soft condensed matter, Reviews of Modern Physics 89 (3) (2017) 035005.

[3] P. Coussot, Rheometry of pastes, suspensions, and granular materials: applications in industry and environment, John Wiley & Sons, 2005.

[4] H. A. Barnes, A review of the slip (wall depletion) of polymer solutions, emulsions and particle suspensions in viscometers: its cause, character, and cure, Journal of Non-Newtonian Fluid Mechanics 56 (3) (1995) 221–251.

[5] J. R. Seth, L. Mohan, C. Locatelli-Champagne, M. Cloitre, R. T. Bonnecaze, A micromechanical model to predict the flow of soft particle glasses, Nature Materials 10 (11) (2011) 838–843.

[6] J. Goyon, A. Colin, G. Ovarlez, A. Ajdari, L. Bocquet, Spatial cooperativity in soft glassy flows, Nature 454 (7200) (2008) 84–87.

[7] J. Goyon, A. Colin, L. Bocquet, How does a soft glassy material flow: finite size effects, non local rheology, and flow cooperativity, Soft Matter 6 (12) (2010) 2668–2678.

[8] H. de Cagny, A. Fall, M. M. Denn, D. Bonn, Local rheology of suspensions and dry granular materials, Journal of Rheology 59 (4) (2015) 957–969.

[9] D. W. De Kort, S. J. Veen, H. Van As, D. Bonn, K. P. Velikov, J. P. Van Duynhoven, Yielding and flow of cellulose microfibril dispersions in the presence of a charged polymer, Soft Matter 12 (21) (2016) 4739–4744.

[10] A. Beris, J. Tsamopoulos, R. Armstrong, R. Brown, Creeping motion of a sphere through a bingham plastic, Journal of Fluid Mechanics 158 (1985) 219–244.

[11] H. Tabuteau, P. Coussot, J. R. de Bruyn, Drag force on a sphere in steady motion through a yield-stress fluid, Journal of Rheology 51 (1) (2007) 125–137.

[12] N. J. Balmforth, I. A. Frigaard, G. Ovarlez, Yielding to stress: recent developments in viscoplastic fluid mechanics, Annual Review of Fluid Mechanics 46 (2014) 121–146.

[13] D. Fraggedakis, Y. Dimakopoulos, J. Tsamopoulos, Yielding the yield-stress analysis: a study focused on the effects of elasticity on the settling of a single spherical particle in simple yield-stress fluids, Soft Matter 12 (24) (2016) 5378–5401.

[14] J. Blackery, E. Mitsoulis, Creeping motion of a sphere in tubes filled with a bingham plastic material, Journal of Non-Newtonian Fluid Mechanics 70 (1-2) (1997) 59–77.

[15] B. Deglo de Besses, A. Magnin, P. Jay, Sphere drag in a viscoplastic fluid, AIChE Journal 50 (10) (2004) 2627–2629.

[16] B. T. Liu, S. J. Muller, M. M. Denn, Convergence of a regularization method for creeping flow of a bingham material about a rigid sphere, Journal of Non-Newtonian Fluid Mechanics 102 (2) (2002) 179–191.

[17] A. Putz, T. Burghelea, I. Frigaard, D. Martinez, Settling of an isolated spherical particle in a yield stress shear thinning fluid, Physics of Fluids 20 (3) (2008) 033102.
[18] M. Dinkgreve, M. Fazilati, M. Denn, D. Bonn, Carbopol: From a simple to a thixotropic yield stress fluid, Journal of Rheology 62 (3) (2018) 773–780.
[19] M. T. Arigo, G. H. McKinley, An experimental investigation of negative wakes behind spheres settling in a shear-thinning viscoelastic fluid, Rheologica Acta 37 (4) (1998) 307–327.
[20] B. Gueslin, L. Talini, Y. Peysson, Sphere settling in an aging yield stress fluid: link between the induced flows and the rheological behavior, Rheologica Acta 48 (9) (2009) 961.
[21] O. Hassager, Negative wake behind bubbles in non-newtonian liquids, Nature 279 (5712) (1979) 402.
[22] A. Mollinger, E. Cornelissen, B. Van den Brule, An unexpected phenomenon observed in particle settling: oscillating falling spheres, Journal of Non-Newtonian Fluid Mechanics 86 (3) (1999) 389–393.
[23] T. Jiang, A. Young, A. Metzner, The rheological characterization of hpg gels: Measurement of slip velocities in capillary tubes, Rheologica Acta 25 (4) (1986) 397–404.
[24] P. Weidman, B. Roberts, S. Eisen, On the instability of spheres settling through a vertical pipe filled with hpg., Journal of Applied Fluid Mechanics 5 (4) (2012).
[25] A. Jayaraman, A. Belmonte, Oscillations of a solid sphere falling through a wormlike micellar fluid, Physical Review E 67 (6) (2003) 065301.
[26] N. Kumar, S. Majumdar, A. Sood, R. Govindarajan, S. Ramaswamy, A. Sood, Oscillatory settling in wormlike-micelle solutions: bursts and a long time scale, Soft Matter 8 (16) (2012) 4310–4313.
[27] M. Fazilati, N. Maleki-Jirsaraei, S. Rouhani, D. Bonn, Quasi-periodic and irregular motion of a solid sphere falling through a thixotropic yield-stress fluid, Applied Physics Express 10 (11) (2017) 117301.
[28] S. von Kann, J. H. Snoeijer, D. Lohse, D. van der Meer, Nonmonotonic settling of a sphere in a cornstarch suspension, Physical Review E 84 (6) (2011) 060401.
[29] S. Von Kann, J. H. Snoeijer, D. Van Der Meer, Velocity oscillations and stop-go cycles: The trajectory of an object settling in a cornstarch suspension, Physical Review E 87 (4) (2013) 042301.
[30] M. J. Zohuriaan-Mehr, K. Kabiri, Superabsorbent polymer materials: a review, Iranian Polymer Journal 17 (6) (2008) 451.
[31] M. Ramazani-Harandi, M. Zohuriaan-Mehr, A. Yousefi, A. Ershad-Langroudi, K. Kabiri, Rheological determination of the swollen gel strength of superabsorbent polymer hydrogels, Polymer Testing 25 (4) (2006) 470–474.
[32] M. R. Guilherme, F. A. Aouada, A. R. Fajardo, A. F. Martins, A. T. Paulino, M. F. Davi, A. F. Rubira, E. C. Muniz, Superabsorbent hydrogels based on polysaccharides for application in agriculture as soil conditioner and nutrient carrier: A review, European Polymer Journal 72 (2015) 365–385.
[33] R. Po, Water-absorbent polymers: a patent survey, Journal of Macromolecular Science, Part C: Polymer Reviews 34 (4) (1994) 607–662.
[34] A. T. Graham, F. L. Buchholz, Modern superabsorbent polymer technology, Wiley-vch, 1998.
[35] H. Zhang, R. S. Challa, B. Bai, X. Tang, J. Wang, Using screening test results to predict the effective viscosity of swollen superabsorbent polymer particles extrusion through an open fracture, Industrial & Engineering Chemistry Research 49 (23) (2010) 12284–12293.
[36] L. Biehl, D. Landgrebe, Multispeca tool for multispectral–hyperspectral image data analysis, Computers & Geosciences 28 (10) (2002) 1153–1159.
[37] R. Heilbronner, S. Barrett, Image analysis in Earth sciences: microstructures and textures of Earth materials, Vol. 129, Springer Science & Business Media, 2013.
[38] R. Heilbronner, D. Bruhn, The influence of three-dimensional grain size distributions on the rheology of polyphase rocks, Journal of Structural Geology 20 (6) (1998) 695–705.
[39] Blob analysis in computer vision system TM MATLAB (2019), `https://www.mathworks.com/help/vision/ref/blobanalysis.html?s_tid=doc_ta`.
[40] Y. Holenberg, O. M. Lavrenteva, U. Shavit, A. Nir, Particle tracking velocimetry and particle image velocimetry study of the slow motion of rough and smooth solid spheres in a yield-stress fluid, Physical Review E 86 (6) (2012) 066301.
[41] J. Happel, B. Howard, Low Reynolds number hydrodynamics: with special applications to particulate media, Springer Science and Business Media, 2012.
[42] T. Ferroir, H. Huynh, X. Chateau, P. Coussot, Motion of a solid object through a pasty (thixotropic) fluid, Physics of Fluids 16 (3) (2004) 594–601.
[43] P. Coussot, Yield stress fluid flows: A review of experimental data, Journal of Non-Newtonian Fluid Mechanics 211 (2014) 31–49.
[44] R. W. Ansley, T. N. Smith, Motion of spherical particles in a bingham plastic, AIChE Journal 13 (6) (1967) 1193–1196.
[45] D. Atapattu, R. Chhabra, P. Uhlherr, Wall effect for spheres falling at small Reynolds number in a viscoplastic medium, Journal of Non-Newtonian Fluid Mechanics 38 (1) (1990) 31–42.
[46] V. Mansard, A. Colin, Local and non local rheology of concentrated particles, Soft Matter 8 (15) (2012) 4025–4043.
[47] J.-L. Barrat, A. Lemaitre, Heterogeneities in amorphous systems under shear, Dynamical Heterogeneities in Glasses, Colloids, and Granular Media 150 (2011) 264.
[48] J. R. Seth, M. Cloitre, R. T. Bonnecaze, Elastic properties of soft particle pastes, Journal of Rheology 50 (3) (2006) 353–376.

Chapter 8

Résumé en français

Cette thèse étudie la transition solide/fluide dans les fluides à contrainte-seuil, en utilisant des expériences de laboratoire et des simulations numériques. Les résultats obtenus à partir de l'étude de mécanique des fluides sont ensuite appliqués à la dynamique des systèmes magmatiques. Les objectifs sont d'évaluer comment la transition dépend de la structure du fluide et de son élasticité, quels sont les ingrédients nécessaires pour décrire mathématiquement cette transition et le mouvement du fluide, et dans quelles conditions cette description n'est plus valide.

8.1 La rhéologie complexe des systèmes géologiques

L'intérieur de la Terre est constitué de plusieurs réservoirs d'agrégats polycristallins de compositions et propriétés physiques différentes. Ceux-ci sont les acteurs principaux de tous les processus ayant modelé notre planète au cours de son histoire. Leur déformation et leurs mouvements se font sur une large gamme d'échelle de temps et de taille, donnant lieu à dif-

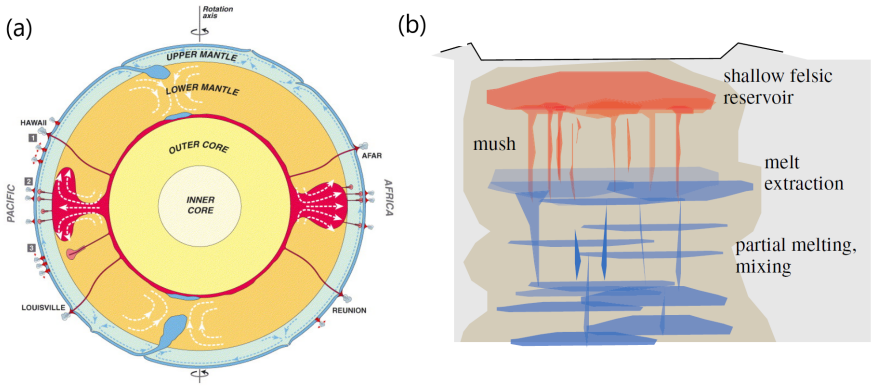

Figure 8.1: (a) Coupe de la Terre montrant les différentes composantes impliquées dans la dynamique du manteau (Courtillot et al., 2003). (b) Schéma d'un réservoir transcrustal (modifié à partir de Edmonds et al. (2019)).

férents comportements mécaniques. Un exemple typique en est le comportement rhéologique du manteau terrestre: à "courte" (humaine) échelle de temps, le manteau est se comporte comme un solide élastique et par exemple transmet les ondes sismiques de cisaillement; mais aux échelles des temps géologiques (millions d'années), le manteau s'écoule comme un fluide visqueux. Ainsi, refroidi à la surface par l'univers froid et chauffé par en dessous et de façon interne, le manteau est soumis à la convection thermique (Fig. 8.1a). Le volcanisme, la formation des plaques le long des dorsales océaniques, le mouvement des plaques et leur subduction dans les fosses océaniques, sont autant de signatures de la convection mantellique.

Par contre, la convection dans le manteau est définitivement plus complexe que dans un fluide isovisqueux. Par exemple, la Tectonique des plaques ne pourrait pas se développer dans un fluide Newtonien parce que ce dernier ne permet pas la forte localisation de la déformation, nécessaire à la formation des limites de plaques. Un comportement en plaques requiert une relation contrainte-déformation différente: la rhéologie viscoplastique est un moyen de localiser la déformation et de générer des zones faibles.

De même, il est fondamental d'utiliser un cadre rhéologique approprié pour modéliser et interpréter les processus ignés dans les chambres magmatiques et les complexes ignés dans la croûte terrestre (Fig. 8.1b). Les systèmes magmatiques transcrustaux sont dominés par de larges regions de roches partiellement fondus (des "mush" cristallins) dans lesquelles la rhéologie est controlée par la déformation du réseau cristallin solide. Néanmoins, lors d'une éruption, le matériau éruptif est à l'état d'une suspension fluide de cristaux dans un liquide fondu. Il existe donc une transition rhéologique par laquelle un domaine de mush à comportement solide développe un comportement fluide et peut rapidement faire éruption.

Dans tous les cas, le comportement des matériaux géologiques fait intervenir des processus allant de la réponse élastique à différents types d'écoulements. Ce sont donc des "fluides complexes" et plusieurs questions se posent:

- Dans quelle mesure la déformation est-elle localisée? Quelle est la taille de la région qui s'écoule comme un fluide, par rapport à celle qui se déforme comme un solide élastique? Comment les instabilités thermo-convectives et leur évolution sont-elles affectées par ce comportement?

- Comment le mouvement démarre-t'il? En effet, dans l'exemple de la Tectonique des plaques et de la convection mantellique, la transition solide-liquide dépend fortement de la structure thermique de la lithosphère et de la rhéologie associée.

Pour explorer ces questions, deux systèmes ont été choisis pour la simplicité de leur dynamique dans le cas Newtonien et leur pertinence pour les systèmes géologiques: (1) le mouvement d'une sphère solide, et (2) le développement des panaches thermiques.

8.2 Sphère en chute libre dans un fluide à seuil

La première partie de cette thèse concerne la chute libre d'une sphère dans un mélange aqueux de gels superabsorbants (SAP). Ce mélange a une rhéologie élasto-visco-plastique. L'objectif est ici d'étudier l'influence de la taille des grains de gel qui constituent la structure du fluide sur la dynamique de l'intrusion sphérique. Comme la taille typique des grains de gel varie entre 1 et 6 mm et le diamètre des sphères varie entre 3 et 25 mm, il existe une gamme de recouvrement entre les deux tailles. Dans ce cas, la sphère peut décrire 5 différents régimes dynamiques de chute dans les SAP, contre 3 dans le Carbopol (où la structure du fluide est très petite par rapport à la taille de la sphère):

(1) un régime linéaire où la sphère chute à vitesse constante;

(2) un régime irrégulier superposé sur le linéaire, où la vitesse de chute varie autour d'une valeur constante;

(3) un régime intermittent avec une alternance de régime irrégulier et de périodes où la sphère s'arrête quasiment complètement;

(4) un régime logarithmique où la vitesse de la sphère décroît progressivement;

(5) un régime où la sphère reste à l'arrêt.

Outre les régimes (1) et (5), typiques des fluides visco-plastiques, l'interaction entre la sphère et la structure du fluide génère deux régimes supplémentaires (2) et (3) où le mouvement devient plus chaotique. La même interaction forte entre la sphère et le gel est aussi retrouvée sur la distance totale parcourue par la sphère dans la direction horizontale. De plus, nous avons démontré que la rhéologie effective des SAP est bien décrite par le modèle de Herschel-Bulkley avec un exposant n=0.5, et que ce système à chute de billes pouvait servir de rhéomètre pour ce type de fluide (Fig. 8.2a). La contrainte-seuil et la consistance effective des gels augmentent avec la taille des grains de gel. Ceci suggère que la rhéologie effective, due aux propriétés de ce matériau hétérogène, dépend de la taille des particules qui constituent la structure du fluide. Par contre, le mouvement de la sphère prédit par le modèle d'Herschel-Bulkley commence à ne plus être valide lorsque le diamètre de la sphère devient inférieur à deux fois la taille des grains de gel: la sphère "voit" alors directement les grains individuels au lieu de ne voir que leurs effets collectifs.

Les caractéristiques de l'écoulement induit par la sphère en chute libre ont été aussi étudiés par PIV (Particle Image Velocimetry). L'écoulement autour de la sphère montre une asymétrie amont-aval, avec l'apparition d'une trainée négative derrière la sphère (Fig. 8.2b). A partir des champs de vitesse, nous avons aussi déterminé l'interface entre la région se déformant comme un solide élastique et la région d'écoulement fluide ("yield surface"). Celle-ci a ensuite été comparée avec le champ de déformation observé directement à partir de l'analyse des profils spatio-temporels de la chute. Une loi d'échelle pour l'extension latérale de la région fluidisée a été proposée, en bon accord avec les données déjà publiées dans la litterature.

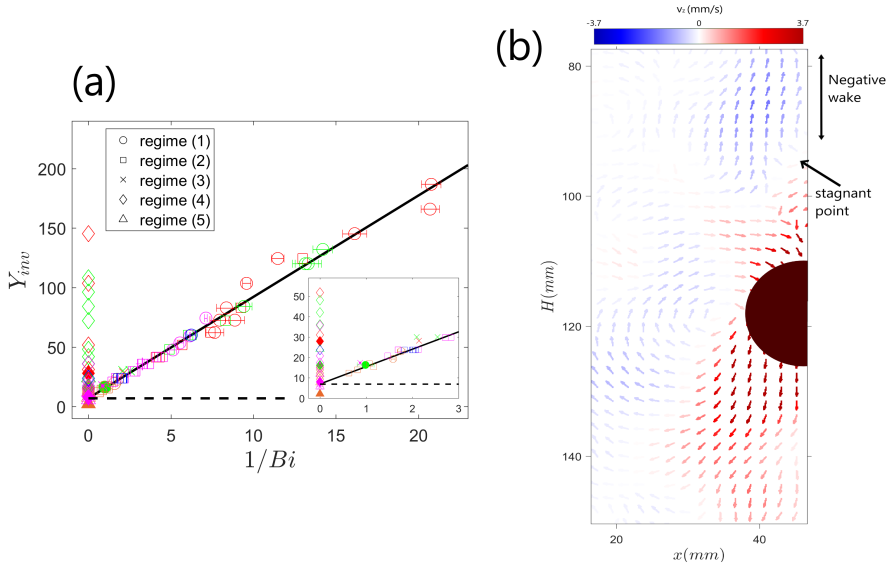

Figure 8.2: Chute libre d'une sphère rigide dans les SAP. (a) Y_{inv} en fonction de Bi. Les couleurs désignent les différentes tailles de SAP. Le remplissage des symboles indiquent les différents types de sphères. The solid black line représente la loi d'échelle obtenue dans le Carbopol (Tabuteau et al., 2007). L'insert montre un zoom des données autour des conditions critiques détaillant les conditions d'arrêt. (b) Ecoulement d'après les mesures de PIV. Composante verticale du champs de vitesse instantanée pour une sphère en chute libre à travers les SAP dans le régime linéaire.

8.3 Panaches thermiques dans un fluide élasto-visco-plastique

La seconde partie de cette thèse concerne le développement à partir d'une source ponctuelle de chaleur des panaches thermiques dans un milieu elasto-visco-plastique initialement au repos. Pour ce faire, nous avons utilisé des simulations numériques qui combinent visco-élasticité et visco-plasticité dans un cadre "Maxwell-Hershel-Bulkley". La morphologie des panaches simulés est en bon accord avec les observations des expériences de laboratoire et les études numériques utilisant une rhéologie viscoplastique simplifiée. Par contre, l'introduction de l'élasticité génère des différences quantitatives sur le temps de démarrage de la convection et sur l'écoulement dans les régions à faible taux de cisaillement. Suivant la rigidité du matériau, l'addition de la composante élastique produit une déformation plus rapide du fluide (Fig. 8.3a,b).

Le paramètre-clef pour prédire le type d'écoulement est le paramètre global Y_0, rapport entre les contraintes d'origine thermique et la contrainte-seuil. Pour des valeurs croissantes de Y_0, on observe (1) pas d'écoulement et croissance conductive d'une poche de fluide chaud autour de l'élément chauffant, (2) une cellule convective autour de l'élément chauffant, ou enfin (3) la montée d'un panache thermique. Une faible variation de Y_0 près du seuil d'écoulement entraîne de grandes variations du temps de démarrage de l'écoulement. D'autre part, au démarrage du panache, deux paramètres locaux prennent une valeur critique: le nombre de Bingham, Bi, rapport entre la contrainte seuil et les contraintes visqueuses, devient inférieur

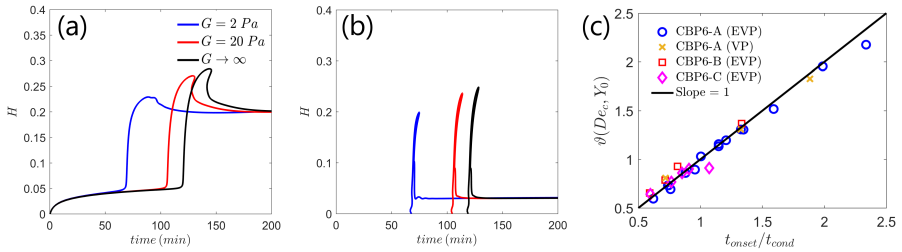

Figure 8.3: Evolution temporelle le long de l'axe du panache: (a) hauteur de l'isotherme $T = 23.9$ °C; (b) hauteur à laquelle $\dot{\gamma} = \dot{\gamma}_c$, où $\dot{\gamma}_c$ est le taux de cisaillement critique auquel $Bi = 1$, i.e. $\dot{\gamma}_c = \left(\frac{\sigma_y}{K_v}\right)^{(1/n)}$. Résultats pour les simulations avec $Y_0 = 207.30$. La ligne noire présente le modèle viscoplastique (VP), tandis que les lignes de couleur sont pour le modèle elasto-viscoplastique (EVP). (c) Temps de démarrage du panache normalisé par le temps conductif en fonction de $\vartheta(De_c, Y_0)$ pour toutes les simulations effectuées. ϑ est une fonction de De_c et Y_0.

à 1; et le rapport Y_{inv} entre les contraintes dues à la flottabilité de la poche de fluide chaud et la contrainte-seuil devient supérieur à une valeur critique $Y_{inv_C} = 7.35 \pm 0.35$, très proche de la valeur-seuil pour la chute libre d'une sphère rigide 6.99. Nos résultats suggèrent que ces deux conditions locales sont indépendantes du module élastique.

Le rôle de l'élasticité peut être estimé à travers le nombre de Deborah, De, rapport entre le temps de relaxation et le temps d'observation. Le temps de démarrage du panache dépend de De (Fig. 8.3c): plus le matériau est élastique, plus le temps de démarrage est court. Ces variations influent directement sur la quantité de chaleur emmagasinée par le panache au démarrage, et donc sur sa flottabilité, et sur les contraintes emmagasinnées dans le système, ce qui va conditionner la vitesse de montée du panache et la hauteur qu'il va atteindre. L'espace des paramètres étudiés reste à étendre pour caractériser complètement le phénomène.

8.4 Implications pour les systèmes magmatiques

La dernière partie de cette thèse s'intéresse à la dynamique des réservoirs magmatiques transcrustaux, où les résultats obtenus dans les deux parties précédentes sont utilisés.

Tout d'abord à petite échelle, nous avons examiné le mouvement des bulles de gaz et des poches de liquide fondu dans la chambre magmatique en supposant que le "mush" dominé par les cristaux suivait un comportement rhéologique Hershel-Bulkley. Les intrusions millimétriques seront viables uniquement pour de très faibles valeurs de contrainte-seuil dans le mush (inférieure à 1.5 Pa), et le régime de montée intermittente (dans lequel la structure du mush influencerait fortement la dynamique de l'intrusion) ne concernera que les très petites gouttes de liquide fondu. Par contre les intrusions métriques pourront s'écouler assez rapidement et traverser un mush faisant l'épaisseur de la croûte en semaines/mois. De même, il existe des gammes de contrainte-seuil du mush et de tailles pour lesquelles les bulles res-

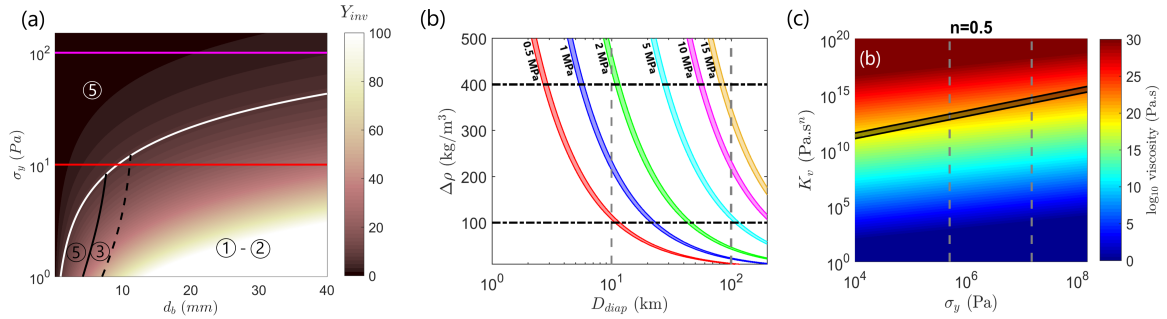

Figure 8.4: (a) Conditions d'écoulement et d'arrêt pour une bulle de diamètre d_b se déplacant à travers un réservoir magmatique riche en cristaux ayant une contrainte-seuil. Différence de densité $\Delta\rho$=2300 kg/m^3 ; diamètre des cristaux de 4 mm. La ligne blanche correspond au critère Y_{inv_C}=6.99. La ligne noire pleine représente la nouvelle limite critique tenant compte de l'influence de la taille caractéristique de la structure d'après notre étude in SAP. La ligne de tirets noirs représente la frontière du régime intermittent. (b) Contrainte-seuil (lignes de couleur) permettant le développement d'un diapir à partir de l'APMB dans la partie intférieure de la croute en fonction du diamètre du diapir et de son contraste de densité (critère Y_{inv_C}= 7.35 ± 0.35). (c) Viscosité effective maximum pour Bi = 1 en fonction de la consistence et de la contrainte seuil. Les lignes de tirets gris bornent les gammes de yield stress comme sur (b). Les bandes noires indiquent la condition Bi = 1, c'est-à-dire $K_v = \sigma_y(D_{diap}/v_z)^n$, avec D_{diap} entre 10 et 100 km et une vitesse de remontée v_z=1 cm/an. L'exposant d'adoucissement est n=0.5.

teront piégées et pourront s'accumuler dans certaines régions du mush, et des conditions dans lesquelles ces bulles pourront remonter efficacement et fluidifier une région de mush autour d'elles (Fig. 8.4a). Ces conditions peuvent devenir fondamentales pour l'évolution dynamique du mush tout entier, contribuant ou non à le remobiliser en entier ou en partie, et à générer des eruptions.

A plus grande échelle, nous avons discuté la dynamique du réservoir magmatique "Altipiano-Puna Magma Body" (APMB) et ses conditions de remontée à l'intérieur de la croûte. Ainsi nous montrons que la flottabilité d'un diapir de 10-100km de diamètre ne peut le faire remonter dans la croûte ductile inférieure que si la contrainte-seuil de celle-ci est entre 0.5 et 15 MPa (critère sur Y_{inv_C}; Fig. 8.4b). En outre, une vitesse de remontée de 1 cm/an de la surface implique alors une viscosité effective de la croûte inférieure de l'ordre de 10^{21} Pa.s (critère sur Bi; Fig. 8.4c).

Bibliography

S. Androvandi, A. Davaille, A. Limare, A. Foucquier, and C. Marais. At least three scales of convection in a mantle with strongly temperature-dependent viscosity. *Physics of the Earth and Planetary Interiors*, 188(3-4):132–141, 2011.

R. W. Ansley and T. N. Smith. Motion of spherical particles in a bingham plastic. *AIChE Journal*, 13(6):1193–1196, 1967.

M. T. Arigo and G. H. McKinley. An experimental investigation of negative wakes behind spheres settling in a shear-thinning viscoelastic fluid. *Rheologica Acta*, 37(4):307–327, 1998.

D. Atapattu, R. Chhabra, and P. Uhlherr. Wall effect for spheres falling at small reynolds number in a viscoplastic medium. *Journal of Non-Newtonian Fluid Mechanics*, 38(1): 31–42, 1990.

O. Bachmann and G. W. Bergantz. On the origin of crystal-poor rhyolites: extracted from batholithic crystal mushes. *Journal of Petrology*, 45(8):1565–1582, 2004.

O. Bachmann and G. W. Bergantz. Rhyolites and their source mushes across tectonic settings. *Journal of Petrology*, 49(12):2277–2285, 2008.

O. Bachmann and C. Huber. Silicic magma reservoirs in the Earth's crust. *American Mineralogist*, 101(11):2377–2404, 2016.

N. J. Balmforth and A. C. Rust. Weakly nonlinear viscoplastic convection. *Journal of Non-Newtonian Fluid Mechanics*, 158(1):36–45, 2009.

N. J. Balmforth, I. A. Frigaard, and G. Ovarlez. Yielding to stress: recent developments in viscoplastic fluid mechanics. *Annual Review of Fluid Mechanics*, 46:121–146, 2014.

H. A. Barnes. A review of the slip (wall depletion) of polymer solutions, emulsions and particle suspensions in viscometers: its cause, character, and cure. *Journal of Non-Newtonian Fluid Mechanics*, 56(3):221–251, 1995.

A. Barth, M. Edmonds, and A. Woods. Valve-like dynamics of gas flow through a packed crystal mush and cyclic strombolian explosions. *Scientific Reports*, 9(1):821, 2019.

M. Beaulne and E. Mitsoulis. Creeping motion of a sphere in tubes filled with Herschel–Bulkley fluids. *Journal of Non-Newtonian Fluid Mechanics*, 72(1):55–71, 1997.

I. B. Belien, K. V. Cashman, and A. W. Rempel. Gas accumulation in particle-rich suspensions and implications for bubble populations in crystal-rich magma. *Earth and Planetary Science Letters*, 297(1-2):133–140, 2010.

D. Bercovici. The generation of plate tectonics from mantle convection. *Earth and Planetary Science Letters*, 205(3-4):107–121, 2003.

G. Bergantz, J. Schleicher, and A. Burgisser. Open-system dynamics and mixing in magma mushes. *Nature Geoscience*, 8(10):793, 2015.

G. W. Bergantz, J. M. Schleicher, and A. Burgisser. On the kinematics and dynamics of crystal-rich systems. *Journal of Geophysical Research: Solid Earth*, 122(8):6131–6159, 2017.

A. Beris, J. Tsamopoulos, R. Armstrong, and R. Brown. Creeping motion of a sphere through a bingham plastic. *Journal of Fluid Mechanics*, 158:219–244, 1985.

M. J. Beuchert and Y. Y. Podladchikov. Viscoelastic mantle convection and lithospheric stresses. *Geophysical Journal International*, 183(1):35–63, 2010.

L. Biehl and D. Landgrebe. Multispec: a tool for multispectral–hyperspectral image data analysis. *Computers & Geosciences*, 28(10):1153–1159, 2002.

F. Birch. Density and composition of mantle and core. *Journal of Geophysical Research*, 69 (20):4377–4388, 1964.

J. Blackery and E. Mitsoulis. Creeping motion of a sphere in tubes filled with a bingham plastic material. *Journal of Non-Newtonian Fluid Mechanics*, 70(1-2):59–77, 1997.

F. Boioli, P. Carrez, P. Cordier, B. Devincre, K. Gouriet, P. Hirel, A. Kraych, and S. Ritterbex. Pure climb creep mechanism drives flow in Earth's lower mantle. *Science Advances*, 3(3):e1601958, 2017.

D. Bonn, M. M. Denn, L. Berthier, T. Divoux, and S. Manneville. Yield stress materials in soft condensed matter. *Reviews of Modern Physics*, 89(3):035005, 2017.

A. Boudreau. Bubble migration in a compacting crystal-liquid mush. *Contributions to Mineralogy and Petrology*, 171(4):32, 2016.

A. Burgisser and G. W. Bergantz. A rapid mechanism to remobilize and homogenize highly crystalline magma bodies. *Nature*, 471(7337):212, 2011.

S. S. Cardoso and A. W. Woods. On convection in a volatile-saturated magma. *Earth and Planetary Science Letters*, 168(3-4):301–310, 1999.

L. Caricchi, L. Burlini, P. Ulmer, T. Gerya, M. Vassalli, and P. Papale. Non-newtonian rheology of crystal-bearing magmas and implications for magma ascent dynamics. *Earth and Planetary Science Letters*, 264(3-4):402–419, 2007.

K. V. Cashman, R. S. J. Sparks, and J. D. Blundy. Vertically extensive and unstable magmatic systems: a unified view of igneous processes. *Science*, 355(6331):eaag3055, 2017.

A. Castruccio, A. Rust, and R. Sparks. Rheology and flow of crystal-bearing lavas: Insights from analogue gravity currents. *Earth and Planetary Science Letters*, 297(3-4):471–480, 2010.

A. Castruccio, A. Rust, and R. Sparks. Assessing lava flow evolution from post-eruption field data using herschel–bulkley rheology. *Journal of Volcanology and Geothermal Research*, 275:71–84, 2014.

R. Champallier, M. Bystricky, and L. Arbaret. Experimental investigation of magma rheology at 300 MPa: From pure hydrous melt to 76 vol.% of crystals. *Earth and Planetary Science Letters*, 267(3-4):571–583, 2008.

S. Chandrasekhar. *Hydrodynamic and hydromagnetic stability*. Courier Corporation, 2013.

I. Cheddadi, P. Saramito, and F. Graner. Steady couette flows of elastoviscoplastic fluids are nonunique. *Journal of Rheology*, 56(1):213–239, 2012.

P. G. Ciarlet, R. Glowinski, and J. Xu. *Numerical Methods for Non-Newtonian Fluids: Special Volume*. Elsevier, 2010. Chapter: On the numerical simulation of viscoplastic fluid flow.

M. J. Comeau, M. J. Unsworth, F. Ticona, and M. Sunagua. Magnetotelluric images of magma distribution beneath volcán uturuncu, bolivia: Implications for magma dynamics. *Geology*, 43(3):243–246, 2015.

A. Costa, L. Caricchi, and N. Bagdassarov. A model for the rheology of particle-bearing suspensions and partially molten rocks (2009). *Geochemistry, Geophysics, Geosystems*, 10 (3), 2009.

V. Courtillot, A. Davaille, J. Besse, and J. Stock. Three distinct types of hotspots in the earth's mantle. *Earth and Planetary Science Letters*, 205(3-4):295–308, 2003.

P. Coussot. *Rheometry of pastes, suspensions, and granular materials: applications in industry and environment*. John Wiley & Sons, 2005.

P. Coussot. Introduction to the rheology of complex fluids. In *Understanding the rheology of concrete*, pages 3–22. Elsevier, 2012.

V. Dansereau, J. Weiss, P. Saramito, and P. Lattes. A Maxwell elasto-brittle rheology for sea ice modelling. *The Cryosphere*, 10:1339–1359, 2016.

M. Darbouli, C. Métivier, J.-M. Piau, A. Magnin, and A. Abdelali. Rayleigh-Bénard convection for viscoplastic fluids. *Physics of Fluids*, 25(2):023101, 2013.

A. Davaille and C. Jaupart. Onset of thermal convection in fluids with temperature-dependent viscosity: Application to the oceanic mantle. *Journal of Geophysical Research: Solid Earth*, 99(B10):19853–19866, 1994.

A. Davaille and A. Limare. Laboratory studies of mantle convection. *Treatise on Geophysics, Volume 7: Mantle Dynamics, chapter 3*, 2015.

A. Davaille, A. Limare, F. Touitou, I. Kumagai, and J. Vatteville. Anatomy of a laminar starting thermal plume at high prandtl number. *Experiments in Fluids*, 50(2):285–300, 2011.

A. Davaille, B. Gueslin, A. Massmeyer, and E. Di Giuseppe. Thermal instabilities in a yield stress fluid: existence and morphology. *Journal of Non-Newtonian Fluid Mechanics*, 193: 144–153, 2013.

A. Davaille, P. Carrez, and P. Cordier. Fat plumes may reflect the complex rheology of the lower mantle. *Geophysical Research Letters*, 45(3):1349–1354, 2018.

G. F. Davies. *Dynamic Earth: Plates, plumes and mantle convection.* American Association of Physics Teachers, 2001.

R. del Potro, M. Díez, J. Blundy, A. G. Camacho, and J. Gottsmann. Diapiric ascent of silicic magma beneath the Bolivian Altiplano. *Geophysical Research Letters*, 40(10):2044–2048, 2013.

M. Dinkgreve, M. M. Denn, and D. Bonn. Everything flows?: elastic effects on startup flows of yield-stress fluids. *Rheologica Acta*, 56(3):189–194, 2017.

D. P. Dobson, N. Miyajima, F. Nestola, M. Alvaro, N. Casati, C. Liebske, I. G. Wood, and A. M. Walker. Strong inheritance of texture between perovskite and post-perovskite in the D" layer. *Nature Geoscience*, 6(7):575–578, 2013.

M. Edmonds and A. W. Woods. Exsolved volatiles in magma reservoirs. *Journal of Volcanology and Geothermal Research*, 368:13–30, 2018.

M. Edmonds, K. V. Cashman, M. Holness, and M. Jackson. Architecture and dynamics of magma reservoirs, 2019.

E. Engdahl, E. A. Flinn, and R. P. Massé. Differential pkikp travel times and the radius of the inner core. *Geophysical Journal International*, 39(3):457–463, 1974.

J. Farrell, R. B. Smith, S. Husen, and T. Diehl. Tomography from 26 years of seismicity revealing that the spatial extent of the yellowstone crustal magma reservoir extends well beyond the yellowstone caldera. *Geophysical Research Letters*, 41(9):3068–3073, 2014.

M. Fazilati, N. Maleki-Jirsaraei, S. Rouhani, and D. Bonn. Quasi-periodic and irregular motion of a solid sphere falling through a thixotropic yield-stress fluid. *Applied Physics Express*, 10(11):117301, 2017.

T. Ferroir, H. Huynh, X. Chateau, and P. Coussot. Motion of a solid object through a pasty (thixotropic) fluid. *Physics of Fluids*, 16(3):594–601, 2004.

Y. Fialko and J. Pearse. Sombrero uplift above the Altiplano-Puna magma body: Evidence of a ballooning mid-crustal diapir. *Science*, 338(6104):250–252, 2012.

M. Forien, J. Tremblay, S.-J. Barnes, A. Burgisser, and P. Page. The role of viscous particle segregation in forming chromite layers from slumped crystal slurries: insights from analogue experiments. *Journal of Petrology*, 56(12):2425–2444, 2015.

D. Fraggedakis, Y. Dimakopoulos, and J. Tsamopoulos. Yielding the yield-stress analysis: a study focused on the effects of elasticity on the settling of a single spherical particle in simple yield-stress fluids. *Soft Matter*, 12(24):5378–5401, 2016.

X. Frank and H. Z. Li. Negative wake behind a sphere rising in viscoelastic fluids: A lattice boltzmann investigation. *Physical Review E*, 74(5):056307, 2006.

S. W. French and B. Romanowicz. Broad plumes rooted at the base of the Earth's mantle beneath major hotspots. *Nature*, 525(7567):95–99, 2015.

I. Frigaard and C. Nouar. On the usage of viscosity regularisation methods for visco-plastic fluid flow computation. *Journal of Non-Newtonian Fluid Mechanics*, 127(1):1–26, 2005.

C. Gabard and J.-P. Hulin. Miscible displacement of non-newtonian fluids in a vertical tube. *The European Physical Journal E*, 11(3):231–241, 2003.

T. Gerya. *Introduction to numerical geodynamic modelling*. Cambridge University Press, 2019.

T. V. Gerya and J.-P. Burg. Intrusion of ultramafic magmatic bodies into the continental crust: numerical simulation. *Physics of the Earth and Planetary Interiors*, 160(2):124–142, 2007.

H. M. Gonnermann and M. Manga. The fluid mechanics inside a volcano. *Annual Review of Fluid Mechanics*, 39(1):321–356, 2007.

H. M. Gonnermann and M. Manga. Dynamics of magma ascent in the. *Modeling volcanic processes: The physics and mathematics of volcanism*, page 55, 2013.

J. Gottsmann, J. Blundy, S. Henderson, M. Pritchard, and R. Sparks. Thermomechanical modeling of the Altiplano-Puna deformation anomaly: Multiparameter insights into magma mush reorganization. *Geosphere*, 13(4):1042–1065, 2017.

A. T. Graham and F. L. Buchholz. *Modern superabsorbent polymer technology*. Wiley-vch, 1998.

T. Greenfield and R. S. White. Building Icelandic igneous crust by repeated melt injections. *Journal of Geophysical Research: Solid Earth*, 120(11):7771–7788, 2015.

B. Gueslin, L. Talini, and Y. Peysson. Sphere settling in an aging yield stress fluid: link between the induced flows and the rheological behavior. *Rheologica Acta*, 48(9):961, 2009.

M. R. Guilherme, F. A. Aouada, A. R. Fajardo, A. F. Martins, A. T. Paulino, M. F. Davi, A. F. Rubira, and E. C. Muniz. Superabsorbent hydrogels based on polysaccharides for application in agriculture as soil conditioner and nutrient carrier: A review. *European Polymer Journal*, 72:365–385, 2015.

L. Guillou and C. Jaupart. On the effect of continents on mantle convection. *Journal of Geophysical Research: Solid Earth*, 100(B12):24217–24238, 1995.

I. A. Gutowski, D. Lee, J. R. de Bruyn, and B. J. Frisken. Scaling and mesostructure of carbopol dispersions. *Rheologica Acta*, 51(5):441–450, 2012.

J. Happel and B. Howard. *Low Reynolds number hydrodynamics: with special applications to particulate media*. Springer Science and Business Media, 2012.

O. G. Harlen. The negative wake behind a sphere sedimenting through a viscoelastic fluid. *Journal of Non-Newtonian Fluid Mechanics*, 108(1-3):411–430, 2002.

O. Hassager. Negative wake behind bubbles in non-newtonian liquids. *Nature*, 279(5712): 402, 1979.

R. Heilbronner and S. Barrett. *Image analysis in Earth sciences: microstructures and textures of Earth materials*, volume 129. Springer Science & Business Media, 2013.

R. Heilbronner and D. Bruhn. The influence of three-dimensional grain size distributions on the rheology of polyphase rocks. *Journal of Structural Geology*, 20(6):695–705, 1998.

S. Henderson and M. Pritchard. Decadal volcanic deformation in the Central Andes Volcanic Zone revealed by InSAR time series. *Geochemistry, Geophysics, Geosystems*, 14(5):1358–1374, 2013.

W. Hibler. A viscous sea ice law as a stochastic average of plasticity. *Journal of Geophysical Research*, 82(27):3932–3938, 1977.

W. Hibler. A dynamic thermodynamic sea ice model. *Journal of Physical Oceanography*, 9 (4):815–846, 1979.

G. Hirth and D. Kohlstedf. Rheology of the upper mantle and the mantle wedge: A view from the experimentalists. *Geophysical Monograph. American Geophysical Union*, 138: 83–106, 2003.

Y. Holenberg, O. M. Lavrenteva, U. Shavit, and A. Nir. Particle tracking velocimetry and particle image velocimetry study of the slow motion of rough and smooth solid spheres in a yield-stress fluid. *Physical Review E*, 86(6):066301, 2012.

M. B. Holness, M. J. Stock, and D. Geist. Magma chambers versus mush zones: constraining the architecture of sub-volcanic plumbing systems from microstructural analysis of crystalline enclaves. *Philosophical Transactions of the Royal Society A*, 377(2139):20180006, 2019.

S. Hoover, K. Cashman, and M. Manga. The yield strength of subliquidus basalts-experimental results. *Journal of Volcanology and Geothermal Research*, 107(1-3):1–18, 2001.

E. D. Humphreys and B. H. Hager. A kinematic model for the late cenozoic development of southern california crust and upper mantle. *Journal of Geophysical Research: Solid Earth*, 95(B12):19747–19762, 1990.

J. Hunt. Industrial and environmental fluid mechanics. *Annual Review of Fluid Mechanics*, 23(1):1–42, 1991.

H. Ishibashi. Non-newtonian behavior of plagioclase-bearing basaltic magma: Subliquidus viscosity measurement of the 1707 basalt of Fuji volcano, Japan. *Journal of Volcanology and Geothermal Research*, 181(1-2):78–88, 2009.

M. Jackson, J. Blundy, and R. Sparks. Chemical differentiation, cold storage and remobilization of magma in the Earth's crust. *Nature*, 564(7736):405, 2018.

J. A. Jay, M. E. Pritchard, M. E. West, D. Christensen, M. Haney, E. Minaya, M. Sunagua, S. R. McNutt, and M. Zabala. Shallow seismicity, triggered seismicity, and ambient noise tomography at the long-dormant Uturuncu Volcano, Bolivia. *Bulletin of Volcanology*, 74 (4):817–837, 2012.

A. Jayaraman and A. Belmonte. Oscillations of a solid sphere falling through a wormlike micellar fluid. *Physical Review E*, 67(6):065301, 2003.

T. Jiang, A. Young, and A. Metzner. The rheological characterization of hpg gels: Measurement of slip velocities in capillary tubes. *Rheologica Acta*, 25(4):397–404, 1986.

S. Jónsson. Tensile rock mass strength estimated using InSAR. *Geophysical Research Letters*, 39(21), 2012.

O. Karakas, W. Degruyter, O. Bachmann, and J. Dufek. Lifetime and size of shallow magma bodies controlled by crustal-scale magmatism. *Nature Geoscience*, 10(6):446, 2017.

I. Karimfazli, I. Frigaard, and A. Wachs. Thermal plumes in viscoplastic fluids: flow onset and development. *Journal of Fluid Mechanics*, 787:474–507, 2016.

L. Karlstrom, M. L. Rudolph, and M. Manga. Caldera size modulated by the yield stress within a crystal-rich magma reservoir. *Nature Geoscience*, 5(6):402, 2012.

Z. Kebiche, C. Castelain, and T. Burghelea. Experimental investigation of the Rayleigh–Bénard convection in a yield stress fluid. *Journal of Non-Newtonian Fluid Mechanics*, 203: 9–23, 2014.

P. B. Kelemen, K. Koga, and N. Shimizu. Geochemistry of gabbro sills in the crust-mantle transition zone of the oman ophiolite: Implications for the origin of the oceanic lower crust. *Earth and Planetary Science Letters*, 146(3-4):475–488, 1997.

M. Kemiha, X. Frank, S. Poncin, and H. Z. Li. Origin of the negative wake behind a bubble rising in non-Newtonian fluids. *Chemical Engineering Science*, 61(12):4041–4047, 2006.

J. M. Kim, C. Kim, C. Chung, K. H. Ahn, and S. J. Lee. Negative wake generation of fene-cr fluids in uniform and poiseuille flows past a cylinder. *Rheologica Acta*, 44(6):600–613, 2005.

D. Kohlstedt, B. Evans, and S. Mackwell. Strength of the lithosphere: Constraints imposed by laboratory experiments. *Journal of Geophysical Research: Solid Earth*, 100(B9):17587–17602, 1995.

R. Krishnamurti. On the transition to turbulent convection. part 1. the transition from two-to three-dimensional flow. *Journal of Fluid Mechanics*, 42(2):295–307, 1970a.

R. Krishnamurti. On the transition to turbulent convection. part 2. the transition to time-dependent flow. *Journal of Fluid Mechanics*, 42(2):309–320, 1970b.

R. Krishnamurti. Theory and experiment in cellular convection. *NATO Advanced Study Institute on Continental Drift and the Mechaniscm of Plate Tectonics, University of Newcastl upon Tyne, England*, pages 245–257, 1979.

N. Kumar, S. Majumdar, A. Sood, R. Govindarajan, S. Ramaswamy, and A. Sood. Oscillatory settling in wormlike-micelle solutions: bursts and a long time scale. *Soft Matter*, 8 (16):4310–4313, 2012.

K. Lejcuś, J. Dąbrowska, D. Garlikowski, and M. Śpitalniak. Innovative water absorbing geocomposite for anti-erosion protection. *Environmental Connections, Portland (OR)*, 2015.

C. Li, A. Magnin, and C. Métivier. Natural convection in shear-thinning yield stress fluids in a square enclosure. *AIChE Journal*, 62(4):1347–1355, 2016.

C. J. Lissenberg and C. J. MacLeod. A reactive porous flow control on mid-ocean ridge magmatic evolution. *Journal of Petrology*, 57(11-12):2195–2220, 2016.

W. Lowrie. *Fundamentals of Geophysics*. Cambridge university press, 2007.

H. Mader, E. Llewellin, and S. Mueller. The rheology of two-phase magmas: A review and analysis. *Journal of Volcanology and Geothermal Research*, 257:135–158, 2013.

C. Magee, C. T. Stevenson, S. K. Ebmeier, D. Keir, J. O. Hammond, J. H. Gottsmann, K. A. Whaler, N. Schofield, C. A. Jackson, M. S. Petronis, et al. Magma plumbing systems: a geophysical perspective. *Journal of Petrology*, 59(6):1217–1251, 2018.

G. Mahood. Second reply to comment of RSJ Sparks, HE Huppert and CJN Wilson on 'Evidence for long residence times of rhyolitic magma in the Long Valley magmatic system: the isotopic record in the precaldera lavas of Glass Mountain'. *Earth and Planetary Science Letters*, 99(4):395–399, 1990.

H. A. Makse, J. Brujic, and S. F. Edwards. Statistical mechanics of jammed matter (2005). *arXiv preprint cond-mat/0503081*, 2005.

M. Manga and D. Weeraratne. Experimental study of non-Boussinesq Rayleigh–Bénard convection at high Rayleigh and Prandtl numbers. *Physics of Fluids*, 11(10):2969–2976, 1999.

M. Manga, J. Castro, K. V. Cashman, and M. Loewenberg. Rheology of bubble-bearing magmas. *Journal of Volcanology and Geothermal Research*, 87(1-4):15–28, 1998.

V. Mansard and A. Colin. Local and non local rheology of concentrated particles. *Soft Matter*, 8(15):4025–4043, 2012.

B. Marsh. On the crystallinity, probability of occurrence, and rheology of lava and magma. *Contributions to Mineralogy and Petrology*, 78(1):85–98, 1981.

A. Massmeyer, E. Di Giuseppe, A. Davaille, T. Rolf, and P. J. Tackley. Numerical simulation of thermal plumes in a herschel–bulkley fluid. *Journal of Non-Newtonian Fluid Mechanics*, 195:32–45, 2013.

A. M. Massmeyer. *Thermal instabilities in a yield-stress fluid: from the laboratory to the planetary scale*. Theses, Université Paris Sud - Paris XI, May 2013.

H. Massol and C. Jaupart. Dynamics of magma flow near the vent: Implications for dome eruptions. *Earth and Planetary Science Letters*, 279(3):185 – 196, 2009.

MathWorks. Blob analysis in computer vision system tm (2019). *MATLAB*, 2019.

D. McKenzie. The extraction of magma from the crust and mantle. *Earth and Planetary Science Letters*, 74(1):81–91, 1985.

P. R. S. Mendes and E. S. Dutra. Viscosity function for yield-stress liquids. *Applied Rheology*, 14(6):296–302, 2004.

C. Metivier, C. Li, and A. Magnin. Origin of the onset of Rayleigh-Bénard convection in a concentrated suspension of microgels with a yield stress behavior. *Physics of Fluids*, 29 (10):104102, 2017.

P. Møller, A. Fall, and D. Bonn. Origin of apparent viscosity in yield stress fluids below yielding. *EPL (Europhysics Letters)*, 87(3):38004, 2009.

A. Mollinger, E. Cornelissen, and B. Van den Brule. An unexpected phenomenon observed in particle settling: oscillating falling spheres. *Journal of Non-Newtonian Fluid Mechanics*, 86(3):389–393, 1999.

L. Moresi, F. Dufour, and H.-B. Mühlhaus. Mantle convection modeling with viscoelastic/brittle lithosphere: Numerical methodology and plate tectonic modeling. *Pure and Applied Geophysics*, 159(10):2335–2356, 2002.

S. Mueller, E. Llewellin, and H. Mader. The rheology of suspensions of solid particles. *Proceedings of the Royal Society A: Mathematical, Physical and Engineering Sciences*, 466 (2116):1201–1228, 2009.

H.-B. Muhlhaus and K. Regenauer-Lieb. Towards a self-consistent plate mantle model that includes elasticity: simple benchmarks and application to basic modes of convection. *Geophysical Journal International*, 163(2):788–800, 2005.

M. Murakami, K. Hirose, K. Kawamura, N. Sata, and Y. Ohishi. Post-perovskite phase transition in $MgSiO_3$. *Science*, 304(5672):855–858, 2004.

H.-C. Nataf, B. Hager, and R. Scott. Convection experiments in a centrifuge and the generation of plumes in a very viscous fluid. In *Annales Geophysicae*, volume 2, pages 303–309. European Geosciences Union, 1984.

G. Ovarlez, Q. Barral, and P. Coussot. Three-dimensional jamming and flows of soft glassy materials. *Nature materials*, 9(2):115–119, 2010.

A. Parmigiani, C. Huber, and O. Bachmann. Mush microphysics and the reactivation of crystal-rich magma reservoirs. *Journal of Geophysical Research: Solid Earth*, 119(8): 6308–6322, 2014.

A. Parmigiani, S. Faroughi, C. Huber, O. Bachmann, and Y. Su. Bubble accumulation and its role in the evolution of magma reservoirs in the upper crust. *Nature*, 532(7600):492, 2016.

V. Patočka. *Maxwell-type viscoelasticity in small and large deformations of planetary mantles*. Theses, Univerzita Karlova, Matematicko-fyzikální fakulta, 2018.

V. Patočka, O. Čadek, P. J. Tackley, and H. Čížková. Stress memory effect in viscoelastic stagnant lid convection. *Geophysical Journal International*, 209(3):1462–1475, 2017.

V. Patočka, H. Čížková, and P. Tackley. Do elasticity and a free surface affect lithospheric stresses caused by upper-mantle convection? *Geophysical Journal International*, 216(3): 1740–1760, 2019.

H. Pinkerton and G. Norton. Rheological properties of basaltic lavas at sub-liquidus temperatures: laboratory and field measurements on lavas from mount etna. *Journal of Volcanology and Geothermal Research*, 68(4):307–323, 1995.

H. Pinkerton and R. Sparks. Field measurements of the rheology of lava. *Nature*, 276(5686): 383–385, 1978.

M. Pistone, L. Caricchi, P. Ulmer, L. Burlini, P. Ardia, E. Reusser, F. Marone, and L. Arbaret. Deformation experiments of bubble-and crystal-bearing magmas: Rheological and microstructural analysis. *Journal of Geophysical Research: Solid Earth*, 117(B5), 2012.

R. Po. Water-absorbent polymers: a patent survey. *Journal of Macromolecular Science, Part C: Polymer Reviews*, 34(4):607–662, 1994.

A. Putz, T. Burghelea, I. Frigaard, and D. Martinez. Settling of an isolated spherical particle in a yield stress shear thinning fluid. *Physics of Fluids*, 20(3):033102, 2008.

D. Pyle and D. Pyle. Bubble migration and the initiation of volcanic eruptions. *Journal of Volcanology and Geothermal Research*, 67(4):227–232, 1995.

M. Ramazani-Harandi, M. Zohuriaan-Mehr, A. Yousefi, A. Ershad-Langroudi, and K. Kabiri. Rheological determination of the swollen gel strength of superabsorbent polymer hydrogels. *Polymer Testing*, 25(4):470–474, 2006.

G. Ranalli. *Rheology of the Earth*. Springer Science & Business Media, 1995.

T. Rolf and P. Tackley. Focussing of stress by continents in 3d spherical mantle convection with self-consistent plate tectonics. *Geophysical Research Letters*, 38(18), 2011.

X. Ruan, Y. Li, Z. Jin, Z. Pan, and Z. Yin. Modeling method of concrete material at mesoscale with refined aggregate shapes based on image recognition. *Construction and Building Materials*, 204:562–575, 2019.

P. Ruprecht and T. Plank. Feeding andesitic eruptions with a high-speed connection from the mantle. *Nature*, 500(7460):68, 2013.

F. Ryerson, H. Weed, and A. Piwinskii. Rheology of subliquidus magmas: 1. picritic compositions. *Journal of Geophysical Research: Solid Earth*, 93(B4):3421–3436, 1988.

R. Sakaguchi, T. Shiraiwa, P. Chivavibul, T. Kasuya, M. Enoki, N. Yamashita, H. Yokota, Y. Matsui, A. Kazama, K. Ozaki, et al. Multiscale analysis of mns inclusion distributions in high strength steel. *ISIJ International*, pages ISIJINT–2019, 2020.

P. Saramito. A new constitutive equation for elastoviscoplastic fluid flows. *Journal of Non-Newtonian Fluid Mechanics*, 145(1):1–14, 2007.

P. Saramito. A new elastoviscoplastic model based on the herschel–bulkley viscoplastic model. *Journal of Non-Newtonian Fluid Mechanics*, 158(1-3):154–161, 2009.

P. Saramito and A. Wachs. Progress in numerical simulation of yield stress fluid flows. *Rheologica Acta*, 56(3):211–230, 2017.

B. Scaillet, A. Pêcher, P. Rochette, and M. Champenois. The gangotri granite (garhwal himalaya): laccolithic emplacement in an extending collisional belt. *Journal of Geophysical Research: Solid Earth*, 100(B1):585–607, 1995.

J. M. Schleicher, G. W. Bergantz, R. E. Breidenthal, and A. Burgisser. Time scales of crystal mixing in magma mushes. *Geophysical Research Letters*, 43(4):1543–1550, 2016.

H. Schmeling, J. P. Kruse, and G. Richard. Effective shear and bulk viscosity of partially molten rock based on elastic moduli theory of a fluid filled poroelastic medium. *Geophysical Journal International*, 190(3):1571–1578, 2012.

B. C. Schmidt and H. Behrens. Water solubility in phonolite melts: Influence of melt composition and temperature. *Chemical Geology*, 256(3-4):259–268, 2008.

G. Seropian, A. Rust, and R. Sparks. The gravitational stability of lenses in magma mushes: Confined Rayleigh-Taylor instabilities. *Journal of Geophysical Research: Solid Earth*, 123 (5):3593–3607, 2018.

J. R. Seth, M. Cloitre, and R. T. Bonnecaze. Elastic properties of soft particle pastes. *Journal of Rheology*, 50(3):353–376, 2006.

J. R. Seth, L. Mohan, C. Locatelli-Champagne, M. Cloitre, and R. T. Bonnecaze. A micromechanical model to predict the flow of soft particle glasses. *Nature Materials*, 10(11): 838–843, 2011.

H. Shaw, T. Wright, D. Peck, and R. Okamura. The viscosity of basaltic magma; an analysis of field measurements in makaopuhi lava lake, hawaii. *American Journal of Science*, 266 (4):225–264, 1968.

J. M. Sinton and R. S. Detrick. Mid-ocean ridge magma chambers. *Journal of Geophysical Research: Solid Earth*, 97(B1):197–216, 1992.

V. Solomatov. Scaling of temperature-and stress-dependent viscosity convection. *Physics of Fluids*, 7(2):266–274, 1995.

A. Spang, T. Baumann, and B. J. Kaus. 3D geodynamic models of the present-day Altiplano-Puna magmatic system. *AGUFM*, 2019:V23H–0194, 2019.

R. Sparks, C. Annen, J. Blundy, K. Cashman, A. Rust, and M. Jackson. Formation and dynamics of magma reservoirs. *Philosophical Transactions of the Royal Society A*, 377 (2139):20180019, 2019.

J. F. Steffe. *Rheological methods in food process engineering.* Freeman press, 1996.

C. Stein, J. Schmalzl, and U. Hansen. The effect of rheological parameters on plate behaviour in a self-consistent model of mantle convection. *Physics of the Earth and Planetary Interiors*, 142(3-4):225–255, 2004.

C. Stein, A. Finnenkötter, J. Lowman, and U. Hansen. The pressure-weakening effect in super-earths: Consequences of a decrease in lower mantle viscosity on surface dynamics. *Geophysical Research Letters*, 38(21), 2011.

C. Stein, J. Lowman, and U. Hansen. The influence of mantle internal heating on lithospheric mobility: Implications for super-earths. *Earth and Planetary Science Letters*, 361:448–459, 2013.

H. Tabuteau, P. Coussot, and J. R. de Bruyn. Drag force on a sphere in steady motion through a yield-stress fluid. *Journal of Rheology*, 51(1):125–137, 2007.

P. J. Tackley. Self-consistent generation of tectonic plates in time-dependent, three-dimensional mantle convection simulations. *Geochemistry, Geophysics, Geosystems*, 1(8), 2000.

P. J. Tackley. Modelling compressible mantle convection with large viscosity contrasts in a three-dimensional spherical shell using the yin-yang grid. *Physics of the Earth and Planetary Interiors*, 171(1-4):7–18, 2008.

M. Thielmann, B. J. Kaus, and A. A. Popov. Lithospheric stresses in Rayleigh–Bénard convection: effects of a free surface and a viscoelastic Maxwell rheology. *Geophysical Supplements to the Monthly Notices of the Royal Astronomical Society*, 203(3):2200–2219, 2015.

M. Tiryakioğlu. Statistical distributions for the size of fatigue-initiating defects in Al–7% Si–0.3% Mg alloy castings: A comparative study. *Materials Science and Engineering: A*, 497(1-2):119–125, 2008.

R. Trompert and U. Hansen. Mantle convection simulations with rheologies that generate plate-like behaviour. *Nature*, 395(6703):686–689, 1998.

D. L. Turcotte and G. Schubert. *Geodynamics*. Cambridge university press, 2002.

S. Turner and F. Costa. Measuring timescales of magmatic evolution. *Elements*, 3(4):267–272, 08 2007.

A. Vikhansky. Thermal convection of a viscoplastic liquid with high Rayleigh and Bingham numbers. *Physics of Fluids*, 21(10):103103, 2009.

S. von Kann, J. H. Snoeijer, D. Lohse, and D. van der Meer. Nonmonotonic settling of a sphere in a cornstarch suspension. *Physical Review E*, 84(6):060401, 2011.

S. Von Kann, J. H. Snoeijer, and D. Van Der Meer. Velocity oscillations and stop-go cycles: The trajectory of an object settling in a cornstarch suspension. *Physical Review E*, 87(4): 042301, 2013.

A. Vona, C. Romano, D. Dingwell, and D. Giordano. The rheology of crystal-bearing basaltic magmas from Stromboli and Etna. *Geochimica et Cosmochimica Acta*, 75(11):3214–3236, 2011.

K. M. Ward, G. Zandt, S. L. Beck, D. H. Christensen, and H. McFarlin. Seismic imaging of the magmatic underpinnings beneath the altiplano-puna volcanic complex from the joint inversion of surface wave dispersion and receiver functions. *Earth and Planetary Science Letters*, 404:43–53, 2014.

P. Weidman, B. Roberts, and S. Eisen. On the instability of spheres settling through a vertical pipe filled with hpg. *Journal of Applied Fluid Mechanics*, 5(4), 2012.

R. S. White, J. Drew, H. R. Martens, J. Key, H. Soosalu, and S. S. Jakobsdóttir. Dynamics of dyke intrusion in the mid-crust of Iceland. *Earth and Planetary Science Letters*, 304 (3-4):300–312, 2011.

J. A. Whitehead Jr and B. Parsons. Observations of convection at rayleigh numbers up to 760,000 in a fluid with large prandtl number. *Geophysical & Astrophysical Fluid Dynamics*, 9(1):201–217, 1977.

H.-D. Xi, S. Lam, and K.-Q. Xia. From laminar plumes to organized flows: the onset of large-scale circulation in turbulent thermal convection. *Journal of Fluid Mechanics*, 503: 47–56, 2004.

S. Yamashita. Experimental study of the effect of temperature on water solubility in natural rhyolite melt to 100 MPa. *Journal of Petrology*, 40(10):1497–1507, 1999.

H. Zhang, R. S. Challa, B. Bai, X. Tang, and J. Wang. Using screening test results to predict the effective viscosity of swollen superabsorbent polymer particles extrusion through an open fracture. *Industrial & Engineering Chemistry Research*, 49(23):12284–12293, 2010.

J. Zhang, S. Childress, and A. Libchaber. Non-Boussinesq effect: Thermal convection with broken symmetry. *Physics of Fluids*, 9(4):1034–1042, 1997.

J. Zhang, D. Vola, and I. Frigaard. Yield stress effects on Rayleigh–Bénard convection. *Journal of Fluid Mechanics*, 566:389–419, 2006.

M. J. Zohuriaan-Mehr and K. Kabiri. Superabsorbent polymer materials: a review. *Iranian Polymer Journal*, 17(6):451, 2008.